

**SPACE CHARGE DISTRIBUTION MEASUREMENTS IN
POLYMERS BY AN IMPROVED PULSED
ELECTRO-ACOUSTIC METHOD**

by

YUE LIU

A thesis

presented to the University of Waterloo

in fulfillment of the

thesis requirement for the degree of

Doctor of Philosophy

in

Electrical Engineering

Waterloo, Ontario, Canada, 1996

© Yue Liu, 1996



National Library
of Canada

Acquisitions and
Bibliographic Services

395 Wellington Street
Ottawa ON K1A 0N4
Canada

Bibliothèque nationale
du Canada

Acquisitions et
services bibliographiques

395, rue Wellington
Ottawa ON K1A 0N4
Canada

Your file *Votre référence*

Our file *Notre référence*

The author has granted a non-exclusive licence allowing the National Library of Canada to reproduce, loan, distribute or sell copies of his/her thesis by any means and in any form or format, making this thesis available to interested persons.

The author retains ownership of the copyright in his/her thesis. Neither the thesis nor substantial extracts from it may be printed or otherwise reproduced with the author's permission.

L'auteur a accordé une licence non exclusive permettant à la Bibliothèque nationale du Canada de reproduire, prêter, distribuer ou vendre des copies de sa thèse de quelque manière et sous quelque forme que ce soit pour mettre des exemplaires de cette thèse à la disposition des personnes intéressées.

L'auteur conserve la propriété du droit d'auteur qui protège sa thèse. Ni la thèse ni des extraits substantiels de celle-ci ne doivent être imprimés ou autrement reproduits sans son autorisation.

0-612-21366-8

The University requires the signatures of all persons using or photocopying this thesis. Please sign below, and give address and date.

ABSTRACT

This study presents a novel method of processing measured signals from the Pulsed Electro-Acoustic(PEA) method in order to obtain space charge distributions with improved resolution and accuracy. The proposed method (i.e. the simulation model method) enables surface charges to be distinguished from space charge distributions. Therefore, space charge distributions can be processed separately from surface charges without surface charges being mixed into the obtained space charge distributions. In addition, a nonlinear detection and optimization process in the simulation model is proposed as an option for even better charge distribution results. A brief review of solid breakdown mechanisms and space charge effects illustrates the importance of space charge distribution measurements. A literature review of the available space charge distribution measuring techniques shows the advantages of the PEA method for space charge distribution measurements. Furthermore, the deconvolution procedure(DCON) and the direct method(DM), the two previous methods used to obtain space charge distributions from the PEA measured signals, are critically reviewed and re-analyzed in order to gain a better appreciation of the proposed simulation model method. The obtained results of four sets of synthetic signals by the DM, the DCON, and the point matching simulation model(PMSM) methods; and the obtained results of two sets of experimental signals by the PMSM method demonstrate the advantages associated with the use of the simulation model method. Also presented are experimental studies designed and conducted to determine the dynamic changes of space charge distributions under HVDC uniform field voltage applications for sheet specimens made of LDPE, HDPE, UHMWPE, PP and PMMA. The experimental results are then summarized and discussed. Moreover, in this thesis, the PEA method principle is further extended to nonuniform fields (i.e. needle-plane electrode configurations), where space charge effects are considered crucial.

ACKNOWLEDGMENTS

I wish to express sincere appreciation to my supervisor Professor M.M.A. Salama for his encouragement, support and insightful remarks during the entire course of this research.

I wish to thank Prof. P. Castle, Prof. R. Bartnikas, Prof. Y.L.Chow, Prof. J.D. Cross, Prof. A.K. Khandani, Prof. G. Tzoganakis, and Prof. S. Jayaram for the time and efforts that they spent reviewing my thesis. I also wish to thank Prof. A.K. Khandani for some important discussions regarding to the signal processing.

I am grateful to R.G. van Heeswijk for his support and encouragement during my first year study in Canada, and to Mr. Terry Weldon for providing technical assistance in the High Voltage Insulation laboratory.

I am indebted to Prof. Ziyu Liu who introduced me to the area of Electrical Insulation. I am also indebted to his family for helping me to come abroad to pursue my studies.

I am particularly grateful to my parents. Without their continuous encouragement and selfless support, I may not have been able to complete this work.

Finally, my deepest appreciation goes to my husband Rong for his understanding and support, and to our son Kevin, for his lovely smiles.

Dedication

To my parents, my husband Rong, and our son Kevin

CONTENTS

1 INTRODUCTION	1
1.1 PROBLEM STATEMENT AND RESEARCH OBJECTIVES	1
1.2 RESEARCH PROGRAM AND THESIS ORGANIZATION	3
2 LITERATURE REVIEWS	5
2.1 INTRODUCTION	5
2.2 OVERVIEW OF POLYMERS SELECTED IN RESEARCH	5
2.3 OVERVIEW OF SOLID BREAKDOWN MECHANISMS AND SPACE CHARGE EFFECTS..	8
2.3.1 <i>Basic Space Charge Effects</i>	8
2.3.2 <i>Solid Breakdown Mechanisms and Space Charges Effects</i>	10
2.3.3 <i>Discussions</i>	17
2.4 SPACE CHARGE DISTRIBUTION MEASURING TECHNIQUES	18
2.4.1 <i>Destructive Methods</i>	18
2.4.2 <i>Non-destructive Methods</i>	21
2.4.3 <i>Comparing Advantages and Disadvantages</i>	23
2.5 THE PEA METHOD UNDER UNIFORM FIELD	24
2.5.1 <i>Introduction</i>	24
2.5.2 <i>Basic Principle for Uniform Field PEA Method</i>	25
2.5.3 <i>The Deconvolution Procedure</i>	29
2.5.4 <i>The Direct Method</i>	31
2.5.5 <i>Discussions</i>	32
2.5.6 <i>Summary of Experiments Using the PEA Method</i>	34

3 SIMULATION MODEL	36
3.1 INTRODUCTION	36
3.2 RE-ANALYZING THE PEA SYSTEM.....	37
3.2.1 Introduction	37
3.2.2 System Representation.....	38
3.2.3 Re-analyzing the Deconvolution Procedure(DCON).....	41
3.2.4 Re-analyzing the Direct Method(DM).....	44
3.3 UNIFORM FIELD SIMULATION MODELS	46
3.3.1 Introduction	46
3.3.2 Step 1: Setting up Simulation models.....	47
3.3.3 Step 2: Obtaining σ Sequence.....	52
3.3.4 Reconstructing Space Charge Distribution $\rho(x)$	54
3.3.5 Discussions	57
3.4 NONUNIFORM FIELD SIMULATION MODELS	59
3.4.1 Introduction	59
3.4.2 Principle	59
3.4.3 Nonuniform Simulation Model.....	65
3.4.4 Discussions	67
4 SIMULATION MODEL CRITIQUE.....	68
4.1 INTRODUCTION	68
4.2 COMPARISON OF DM, DCON AND PMSM METHODS FROM ANALYTIC POINT OF VIEW.....	69
4.2.1 Introduction	69
4.2.2 The 1st Set of Signals	74
4.2.3 The 2nd Set of Signals	79
4.2.4 The 3rd Set of Signals	93
4.2.5 The 4th Set Signals.....	106
4.3 PMSM CRITIQUE FROM AN EXPERIMENTAL POINT OF VIEW	114
4.3.1 Introduction	114
4.3.2 Experimental Signal Processing Procedures.....	116

4.3.3 <i>Experimental Signals and Processing Results</i>	119
4.4 DISCUSSION	126
5. CHARGE DYNAMICS	130
5.1 INTRODUCTION	130
5.2 EXPERIMENTAL ARRANGEMENT	133
5.2.1 <i>Experimental Set-up</i>	133
5.2.2 <i>General Test Procedure</i>	139
5.3 STEP INCREASED VOLTAGE EXPERIMENTS	144
5.3.1 <i>Procedures</i>	144
5.3.2 <i>Results</i>	144
5.3.3 <i>Discussion</i>	149
5.4 CONSTANT VOLTAGE APPLICATION EXPERIMENTS	151
5.4.1 <i>Procedures</i>	151
5.4.2 <i>Results</i>	151
5.4.3 <i>Discussion</i>	154
5.5 SHORT CIRCUIT EXPERIMENTAL RESULTS	157
5.5.1 <i>Procedures</i>	157
5.5.2 <i>Results</i>	157
5.5.3 <i>Discussion</i>	166
5.6 SUMMARIES AND DISCUSSIONS	167
6 CONCLUSIONS AND FURTHER WORK	171
6.1 CONCLUSIONS AND CONTRIBUTIONS	171
6.2 FURTHER WORK.....	174
REFERENCES	176
A RELEVANT CONCEPTS	185
A-1 ELECTRIC PULSE FIELDS	185
A-2 CONVOLUTION[88].....	186

A-3 TRANSFER FUNCTION.....	187
A-4 DISCRETE-TIME SIGNALS	190
B FORMULAS FOR TRANSDUCER AT AN ARBITRARY POSITION ON THE PLANE ELECTRODE.....	193
C OTHER SIMULATION MODEL APPROACHES	200
C-1 MINIMUM VARIANCE DECONVOLUTION(MVD) SIMULATION MODEL	200
C-2 MAXIMUM LIKELIHOOD DECONVOLUTION(MLD) SIMULATION MODEL	203
D NONLINEAR DETECTION AND OPTIMIZATION PROCESS (NDOP): PROCEDURES AND SOME APPLICATION RESULTS.....	207
D-1 PROCEDURES OF A NONLINEAR DETECTION AND OPTIMIZATION PROCESS	207
D-2 NODP FOR THE 2ND SET OF SIGNALS.....	210
D-3 NODP FOR THE 3RD SET OF SIGNALS	213
D-4 NODP FOR THE 4TH SET OF SIGNALS	215

LIST OF TABLES

2.1 Chemical Structures of Polyethylene, Polypropylene, and Polymethylmethacrylate.....	6
2.2 A Survey of Solid Breakdown and Electric Treeing Mechanisms.....	11
2.3 Summary of Space Charge Distribution Measuring Techniques.....	19
2.4 Advantages and Disadvantages of Space Charge Distribution Measuring Techniques.....	20
4.1 Block Diagram of Experimental Signal Processing Procedures.....	115
4.2 A Routine Used for Data Pre-processing.....	116
4.3 Comparison of the DM, the DCON and the PMSM Methods.....	127
5.1 Information of Each Specimen.....	135

LIST OF FIGURES

2.1 The influence of space charges on electric field distributions[8].....	8
2.2 Diagram for the principle of the PEA method.....	26
2.3 Methods used to obtain a sheet of charge.....	30
3.1 System representation of the PEA principle system.....	40
3.2 System representation of deconvolution through direct inverse of system IR	42
3.3 Resolution Function.....	43
3.4 System representation of the PEA measuring system.....	43
3.5 Comparing direct method results for the ideal and practical cases.....	45
3.6 System representation of the PEA system in discrete-time domain.....	48
3.7 Processing scheme of anti-causal, zero-phase filter implementation.....	52
3.8 The algorithm of the point matching simulation model (PMSM).....	58
3.9 Principle of the PEA method for needle-plane electrode configuration.....	60
3.10 Refraction of a spherical wave at a plane interface.....	61
4.1 Assumed charge distribution SPD1.....	70
4.2 Assumed charge distribution SPD2.....	70
4.3 Assumed system IR, $g^f(k)$	71
4.4 Assumed system IR, $g^w(k)$	71
4.5 The first set output signal $v_{sm}^1(k)$	72
4.6 The second set output signal $v_{sm}^2(k)$	73
4.7 The noise-corrupted measured IR ($g_m^2(k)$ and $g_m^3(k)$).....	73
4.8 The third set output signal $v_{sm}^3(k)$	73
4.9 The fourth set output signal $v_{sm}^4(k)$	73
4.10 The noise-corrupted measured IR ($g_m^4(k)$).....	74

4.11	Charge distribution obtained by the DM method for the 1st set of signals.....	75
4.12	Comparison between $v_{sm}^1(k)$ and SV (using Figure 4.11 charge distribution.....	75
4.13	Difference between $v_{sm}^1(k)$ and SV of Figure 4.12.....	75
4.14	Amplitude of the Fourier transform of $g_m^1(k)$	76
4.15	Amplitude of the Fourier transform of $v_{sm}^1(k)$	76
4.16	Charge distribution obtained by DCON for the 1st set signals.....	76
4.17	Comparison between $v_{sm}^1(k)$ and SV (using Figure 4.16 charge distribution).....	77
4.18	σ sequence obtained by PMSM at $\Delta=2$ for the 1st set signals.....	78
4.19	σ sequence obtained by PMSM at $\Delta=4$ for the 1st set signals.....	78
4.20	Charge distribution after reconstruction mainly based on $\Delta=2$	78
4.21	Difference between $SV(k)$ and $v_{sm}^1(k)$ for Figure 4.19 charge distribution.....	78
4.22	Charge distribution after optimization process[accuracy: $\sigma(0.01)$, $F(0.01)$].....	79
4.23	Difference between $v_{sm}^1(k)$ and $SV(k)$ for Figure 4.21 charge distribution.....	79
4.24	Charge distribution obtained by the DM method for the 2nd set signals.....	80
4.25	Filtered charge distribution obtained by the DM method for the 2nd set signals.....	80
4.26	Comparison between $v_{sm}^2(k)$ and $SV(k)$ for Figure 4.24 charge distribution.....	80
4.27	Difference between $SV(k)$ and $v_{sm}^2(k)$ of Figure 4.26.....	80
4.28	Comparison between $v_{sm}^2(k)$ and $SV(k)$ for Figure 4.25 charge distribution.....	81
4.29	Difference between $SV(k)$ and $v_{sm}^2(k)$ of Figure 4.28.....	81
4.30	Amplitude of Fourier transform of system IR ($g_m^2(k)$)	82
4.31	Amplitude of Fourier transform of output signal ($v_{sm}^2(k)$).....	82
4.32	Charge distribution results by the DCON method for the 2nd set.....	82
4.33	Comparison between $v_{sm}^2(k)$ and $SV(k)$ (Figure 4.32 charge distribution).....	83
4.34	Difference between $v_{sm}^2(k)$ and $SV(k)$ of Figure 4.33.....	83
4.35	Filtered charge distribution by the DCON method.....	83
4.36	Comparison between $v_{sm}^2(k)$ and $SV(k)$ (Figure 4.35 charge distribution).....	83
4.37	Difference between $v_{sm}^2(k)$ and $SV(k)$ of Figure 4.36.....	83
4.38	Filtered system IR ($g_m^{2'}(k)$).....	85
4.39	Filtered output signal ($v_{sm}^{2'}(k)$).....	85
4.40	Amplitude of Fourier transform of filtered IR($g_m^{2'}(k)$).....	85
4.41	Amplitude of Fourier transform of filtered output ($v_{sm}^{2'}(k)$).....	85
4.42	Charge distribution obtained by the DCON procedure.....	86

4.43 Comparison between $v_{sm}^{2'}(k)$ and $SV(k)$ (Figure 4.42 charge distribution).....	86
4.44 Difference between $v_{sm}^{2'}(k)$ and $SV(k)$ of Figure 4.43.....	86
4.45 Filtered charge distribution.....	86
4.46 Comparison between $v_{sm}^{2'}(k)$ and $SV(k)$ (Figure 4.45 charge distribution).....	86
4.47 Difference between $v_{sm}^{2'}(k)$ and $SV(k)$ of Figure 4.46.....	87
4.48 σ sequence when $\Delta=2$ and $m_0=47$	87
4.49 σ sequence when $\Delta'=4$ and $m_0=47$	87
4.50 Charge distribution obtained by the PMSM method(Filterd).....	88
4.51 Comparison between $v_{sm}^{2'}(k)$ and $SV(k)$ (Figure 4.50 charge distribution).....	88
4.52 Difference between $v_{sm}^{2'}(k)$ and $SV(k)$ of Figure 4.51.....	88
4.53 Comparison between $v_{sm}^{2'}(k)$ and $SV(k)$ (Figure 4.50 charge distribution).....	88
4.54 Difference between $v_{sm}^{2'}(k)$ and $SV(k)$ of Figure 4.53.....	89
4.55 Charge distribution obtained by PMSM method(zero-order-hold).....	89
4.56 Comparison between $v_{sm}^{2'}(k)$ and $SV(k)$ (Figure 4.55 charge distribution).....	89
4.57 Difference between $v_{sm}^{2'}(k)$ and $SV(k)$ of Figure 4.56.....	90
4.58 Comparison between $v_{sm}^{2'}(k)$ and $SV(k)$ (Figure 4.55 charge distribution).....	90
4.59 Difference between $v_{sm}^{2'}(k)$ and $SV(k)$ of Figure 4.58.....	90
4.60 Comparison between $v_{sm}^{2'}(k)$ and $SV(k)$ (SPD1).....	91
4.61 Difference between $v_{sm}^{2'}(k)$ and $SV(k)$ of Figure 4.60.....	91
4.62 Comparison between $v_{sm}^{2'}(k)$ and $SV(k)$ (SPD1).....	91
4.63 Difference between $v_{sm}^{2'}(k)$ and $SV(k)$ of Figure 4.62.....	91
4.64 Charge distribution obtained by the DM method for the 3rd set signal.....	93
4.65 Comparison between $v_{sm}^3(k)$ and $SV(k)$ (Figure 4.64 charge distribution)	93
4.66 Difference between $v_{sm}^3(k)$ and $SV(k)$ of Figure 4.65.....	94
4.67 Filtered charge distribution obtained by the DM method.....	94
4.68 Comparison between $v_{sm}^3(k)$ and $SV(k)$ (Figure 4.67 charge distribution).....	94
4.69 Difference between $v_{sm}^3(k)$ and $SV(k)$ of Figure 4.68.....	94
4.70 Amplitude of Fourior transform of output $g_m^3(k)$	95
4.71 Amplitude of Fourior transform of output $v_{sm}^3(k)$	96
4.72 Charge distribution obtained by the DCON for the 3rd set.....	96
4.73 Comparison between $v_{sm}^3(k)$ and $SV(k)$ (Figure 4.72 charge distribution).....	96
4.74 Difference between $v_{sm}^3(k)$ and $SV(k)$ of Figure 4.73.....	96

4.75	Filtered charge distribution obtained by the deconvolution procedure.....	96
4.76	Comparison between $v_{sm}^3(k)$ and $SV(k)$ (Figure 4.75 charge distribution).....	97
4.77	Difference between $v_{sm}^3(k)$ and $SV(k)$ of Figure 4.76.....	97
4.78	Filtered system IR $g_m^3(k)$	98
4.79	Filtered output signal $v_{sm}^3(k)$	98
4.80	Amplitude of Fourier transform of filtered IR $g_m^3(k)$	98
4.81	Amplitude of Fourier transform of filtered output signal $v_{sm}^3(k)$	98
4.82	Charge distribution for filtered signals by the DCON.....	98
4.83	Comparison between $v_{sm}^3(k)$ and $SV(k)$ (Figure 4.82 charge distribution).....	99
4.84	Difference between $v_{sm}^3(k)$ and $SV(k)$ of Figure 4.83.....	99
4.85	Filtered charge distribution.....	99
4.86	Comparison between $v_{sm}^3(k)$ and $SV(k)$ (Figure 4.85 charge distribution).....	99
4.87	Difference between $v_{sm}^3(k)$ and $SV(k)$ of Figure 4.85.....	99
4.88	σ sequence obtained by the PMSM when $\Delta=2, m_0=47$	100
4.89	σ sequence obtained by the PMSM when $\Delta'=4, m_0=47$	100
4.90	Charge distribution obtained by the PMSM(Filtered).....	101
4.91	Comparison between $v_{sm}^3(k)$ and $SV(k)$ (using Figure 4.90 charge distribution).....	101
4.92	Difference between $v_{sm}^3(k)$ and $SV(k)$ of Figure 4.91.....	101
4.93	Adjusted charge distribution by the PMSM.....	101
4.94	Comparison between $v_{sm}^3(k)$ and $SV(k)$ (Figure 4.93 charge distribution).....	101
4.95	Difference between $v_{sm}^3(k)$ and $SV(k)$ of Figure 4.94.....	102
4.96	Comparison between $v_{sm}^3(k)$ and $SV(k)$ (Figure 4.93 charge distribution)	102
4.97	Difference between $v_{sm}^3(k)$ and $SV(k)$ of Figure 4.96.....	102
4.98	Charge distribution by PMSM(zero order hold)	102
4.99	Comparison between $v_{sm}^3(k)$ and $SV(k)$ (Figure 4.98 charge distribution).....	102
4.100	Difference between $v_{sm}^3(k)$ and $SV(k)$ of Figure 4.99.....	103
4.101	Adjusted distribution by PMSM(zero-order-hold).....	103
4.102	Comparison between $v_{sm}^3(k)$ and $SV(k)$ (Figure 4.101 charge distribution).....	103
4.103	Difference between $v_{sm}^3(k)$ and $SV(k)$ of Figure 4.102.....	103
4.104	Comparison between $v_{sm}^3(k)$ and $SV(k)$ (Figure 4.101 charge distribution).....	103
4.105	Difference between $v_{sm}^3(k)$ and $SV(k)$ of Figure 4.104.....	104
4.106	Compare Figure 4.93 and Figure 4.101 charge distributions with SPD2.....	104

4.107 Comparison between $v_{sm}^{3'}(k)$ and $SV(k)$ (SPD2).....	105
4.108 Difference between $v_{sm}^{3'}(k)$ and $SV(k)$ of Figure 4.107.....	105
4.109 Comparison between $v_{sm}^3(k)$ and $SV(k)$ (SPD2).....	106
4.110 Difference between $v_{sm}^3(k)$ and $SV(k)$ of Figure 4.109.....	106
4.111 Amplitude of Fourier transform of system IR ($g_m^4(k)$).....	107
4.112 Amplitude of Fourier transform of the output $v_{sm}^4(k)$	107
4.113 Charge distribution obtained by the DCON procedure for the 4th set.....	107
4.114 Comparison between $v_{sm}^4(k)$ with $SV(k)$ (Figure 4.113 charge distribution).....	108
4.115 Difference between $v_{sm}^4(k)$ with $SV(k)$ of Figure 4.114.....	108
4.116 Filtered charge distribution by the DCON.....	108
4.117 Comparison between $v_{sm}^4(k)$ with $SV(k)$ (Figure 4.116 charge distribution).....	108
4.118 Difference between $v_{sm}^4(k)$ with $SV(k)$ of Figure 4.117.....	108
4.119 Filtered system IR ($g_m^{4'}(k)$).....	109
4.120 Filtered output signal ($v_{sm}^{4'}(k)$).....	109
4.121 σ sequences using PMSM when $m_0=162$ and $\Delta=2$	109
4.122 σ sequences using PMSM when $m_0=162$ and $\Delta'=4$	110
4.123 Charge distribution obtained by the PMSM(Filtered).....	110
4.124 Comparison between $v_{sm}^{4'}(k)$ with $SV(k)$ (Figure 4.122 charge distribution).....	110
4.125 Difference between $v_{sm}^{4'}(k)$ and $SV(k)$ of Figure 4.124.....	110
4.126 Charge distribution by the PMSM after adjustment.....	110
4.127 Comparison between $v_{sm}^{4'}(k)$ with $SV(k)$ (Figure 4.126 charge distribution).....	111
4.128 Difference between $v_{sm}^{4'}(k)$ with $SV(k)$ of Figure 4.127.....	111
4.129 Comparison between $v_{sm}^4(k)$ with $SV(k)$ (Figure 4.126 charge distribution).....	111
4.130 Difference between $v_{sm}^4(k)$ and $SV(k)$ of Figure 4.129.....	111
4.131 Comparison between $v_{sm}^{4'}(k)$ and $SV(k)$ (SPD2).....	112
4.132 Difference between $v_{sm}^4(k)$ and $SV(k)$ of Figure 4.131.....	113
4.133 Comparison between $v_{sm}^4(k)$ and $SV(k)$ (SPD2).....	113
4.134 Difference between $v_{sm}^4(k)$ and $SV(k)$ of Figure 4.133.....	113
4.135 Original measured output signals.....	120
4.136 The (-35kV and -60kV) signals after the Data selection and organization process.....	120
4.137 Signals after minimizing their dc trends.....	121
4.138 The obtained $v_{gm}'(k)$ and $v_{sm}'(k)$	121

4.139	Obtained system transfer function $g_m'(k)$	122
4.140	Impulse results of the -35kV signal used to generate the transfer function.....	123
4.141	Impulse results for the -60kV signal.....	123
4.142	Charge distribution after adjustment for transfer function signal.....	124
4.143	Charge distribution after adjustment(-60kV signal).....	124
4.144	Electric field distribution.....	124
4.145	Potential distribution.....	124
4.146	Space charge distribution by simulation model.....	125
4.147	Comparison among three methods.....	126
5.1	Experimental setup.....	133
5.2	Dimension of the three electrode system.....	134
5.3	Calibration chart of the transducer.....	135
5.4	Circuit diagram of the electric pulse generator.....	136
5.5	Waveshapes of the electric pulse.....	137
5.6	Dc voltage applications for LDPE, Thin&Thick HDPE, and UHMWPE specimen.....	139
5.7	Dc voltage applications for HDPE, HDPE-Cu, PP, and PMMA specimen.....	140
5.8	Dc voltage applications for four Al evaporated electrode specimens.....	140
5.9	Block diagram of the voltage application procedures.....	142
5.10	The changes of surface charges vs the applied voltage.....	144
5.11	Space charge distributions vs applied voltage for LDPE, Thin/Thick HDPE, and UHMWPE under the <i>first step increased voltages</i>	144
5.12	The changes of surface charges vs the applied voltage.....	145
5.13	Space charge distribution vs applied voltage (<i>the second step increased voltage</i>).....	145
5.14	The changes of surface charges vs applied voltage.....	145
5.15	Space charge distribution vs applied voltage for PMMA, HDPE-Cu, HDPE and PP under the <i>first step increased voltages</i>	146
5.16	The changes of surface charges vs the applied voltage.....	146
5.17	Space charge distribution vs applied voltage (<i>the 2nd step increased voltages</i>).....	146
5.18	The changes of surface charges vs applied voltage (Al-evaporated specimens).....	147
5.19	Space charge distribution vs applied voltage for specimens with Al-evaporated electrode under the <i>1st step increased voltages</i>	147

5.20	Space charge dynamics (same polarity as step increased voltage tests).....	152
5.21	Space charge dynamics (same polarity as step increased voltage tests).....	152
5.22	Space charge dynamics (same polarity as step increased voltage tests).....	152
5.23	Space charge dynamics under reversed dc voltage for LDPE Thin HDPE Thick HDPE and UHMWPE.....	153
5.24	Space charge dynamics under reversed dc voltage for PMMA, HDPE-Cu, LDPE-E, and higher voltage for UHMWPE-E.....	153
5.25	Space charge dynamics for LDPE&UHMWPE under the 2nd & 3rd reversals.....	153
5.26	Space charge dynamics for LDPE&UHMWPE under the 4th & 5th reversals.....	154
5.27	Short-circuit experiments for Thin HDPE.....	158
5.28	Short-circuit experimental results for LDPE.....	159
5.29	Short-circuit experimental results for Thick HDPE.....	159
5.30	Short-circuit experimental results for UHMWPE.....	160
5.31	Short-circuit results for PMMA.....	161
5.32	Short circuit results for HDPE-Cu.....	162
5.33	Short circuit results for HDPE.....	163
5.34	Short circuit results for PP.....	163
5.35	Short-circuit results for UHMWPE-E.....	164
5.36	Short-circuit results for PMMA-E and HDPE-E.....	164
5.37	Short-circuit results for LDPE-E.....	165
5.38	Charge dynamics after short circuit in Thick HDPE and PP.....	165
5.39	Charge decay dynamics in UHMWPE-E and LDPE.....	166
5.40	The decay of total amount of space charges in LDPE.....	167
A-3-1	Input-output form for CTLTI system.....	187
A-4-1	Development of sampled-data signal using ideal impulse sampling.....	191
B-1	Principle set-up <i>Case 1</i> for transducer at an arbitrary position.....	194
B-2	Principle set-up <i>Case 2</i> for transducer at an arbitrary position.....	194
B-3	The inner limits $R_1, R_2, \theta_1, \theta_2$	197
B-4	Diagram used for setting up $\mu(x)$ for <i>Case 1</i>	198
B-5	Diagram used for setting up $\mu(x)$ for <i>Case 2</i>	199

C-1-1 Interconnection of the four computational subsystems that comprise the recursive MVD algorithm[82].....	202
C-2-1 A simple maximum likelihood deconvolution algorithm.....	204
D-1-1 Single most likely replacement detector search algorithm.....	209
D-2-1 The 1st application of the SMLR detector.....	210
D-2-2 The 10th application of the SMLR detector.....	211
D-2-3 The σ' obtained after one run of NDOP for the 2nd set of signals.....	211
D-2-4 Charge distribution obtained after one run of the NDOP for the 2nd set of signals.....	212
D-2-5 Comparison between $v_{sm}^{2'}(k)$ and $SV(k)$ (using Figure D-2-4 charge distribution).....	212
D-2-6 Difference between $v_{sm}^{2'}(k)$ and $SV(k)$ of Figure D-2-5.....	212
D-3-1 The 1st application of the SMLR detector.....	213
D-3-2 The 7th application of the SMLR detector.....	214
D-3-3 The σ' obtained after one run of NDOP for the 3rd set of signals.....	214
D-3-4 Charge distribution obtained after one run of the NDOP for the 3rd set of signals.....	214
D-3-5 Comparison between $v_{sm}^{3'}(k)$ and $SV(k)$ (using Figure D-3-4 charge distribution)	214
D-3-6 Difference between $v_{sm}^{3'}(k)$ and $SV(k)$ of Figure D-3-5.....	215
D-4-1 The 1st application of the SMLR detector.....	216
D-4-2 The 10th application of the SMLR detector.....	216
D-4-3 The σ' obtained after one run of NDOP for the 4th set of signals.....	216
D-4-4 Charge distribution obtained after one run of the NDOP for the 4th set of signals.....	217
D-4-5 Comparison between $v_{sm}^{4'}(k)$ and $SV(k)$ (using Figure D-4-4 charge distribution)	217
D-4-6 Difference between $v_{sm}^{4'}(k)$ and $SV(k)$ of Figure D-4-4.....	217

GLOSSARY

CCM	Charge Compensation Method
DCON	Deconvolution Procedure
DM	Direct Method
FLSC	Field Limited Space Charge
FPT	Field Probe Technique
IR	Impulse Response
HDPE	High Density Polyethylene
LDPE	Low Density Polyethylene
LIMM	Laser Intensity Modulation Method
MDPE	Medium Density Polyethylene
MLD	Maximum Likelihood Deconvolution
MVD	Minimum Variance Deconvolution
NDOP	Nonlinear Detection and Optimization Process
PE	Polyethylene
PEA	Pulsed Electro-Acoustic Method
PD	Partial Discharge
PMMA	Polymethymethacrylate
PMSM	Point Matching Simulation Model
PP	Polypropylene
PWP	Pressure Wave Propagation Method
REA	Rural Electrification Administration
TP	Thermal Pulse Method
UHMWPE	Ultra High Molecular Weight Polyethylene
XLPE	Crosslinked Polyethylene

CHAPTER 1

INTRODUCTION

1.1 PROBLEM STATEMENT AND RESEARCH OBJECTIVES

Polymer technology has experienced steady and strong growth since the early 1930s. Today, it would be difficult to imagine life without polymers; in fact, they are fundamental to virtually every phase of our daily lives. The principal reasons for their widespread application can easily be understood: they are readily shaped, inexpensive dielectric materials with easily controlled physical, mechanical and electrical properties. Dielectric materials (i.e. the electrical and electronic insulating materials), are essential to the proper operation of all electrical and electronic equipment, having applications in a wide variety of components[1]: in integrated circuits, transistors, and diodes; in wires and cables; in connectors; in hybrids; in transformers, coils, and bushings; etc. It is believed that much of the driving force behind the development of many modern polymers came from the electrical and electronics industries. Most principal polymers for typical electrical insulation, according to their broad product group classification, are well outlined in reference [2].

For high voltage insulation systems such as high voltage cables, capacitors, insulators, transformers, and bushings, polymers have been extensively used. However, in high voltage power transmission cables, for example, the oil-impregnated-paper insulation has traditionally been regarded as the most reliable composite insulation system[3].

The main disadvantages with polymers are that they are highly susceptible to degradation by corona discharges and may undergo additional degradation due to treeing when exposed to high voltage stresses[3]. In 1979, there was an attempt to use PE (polyethylene) cable for dc transmission in Japan. This attempt was aborted because the cable broke down when the polarity

was changed[4]. After decades of research work on solid breakdown(including electric treeing), one thing has become very clear. The presence of space charge inside polymers plays an important role in the degradation, the treeing and the breakdown of polymers[3-30]. It is therefore essential to clarify space charge effects on polymers if the application of polymers in the high voltage insulation is to become more reliable.

The basic space charge effect is usually referred to as the distortion of the electric field pattern. This term underlines the vital importance of obtaining direct space charge distribution measurements to determine the actual internal electric field pattern under the electric stress. Several space charge distribution measuring techniques have already been proposed[31-71]. Much work has been done to improve these measuring techniques in order to clarify space charge dynamic behaviours inside polymers. However, it is still necessary to improve these techniques to provide space charge dynamics with higher accuracy and enough resolution. In addition, most of the reported space charge measurements in the literature are under uniform fields(i.e., plane-plane electrode setups)[31-76]. Recently, these measurements have been extended to the cylindrical field[77-79]. Electric treeing is an important phenomenon that occurs when a nonuniform field exists. Needle-plane electrode configuration is often adopted for treeing investigations. However, up to now, only a little work[19-24] has been done to measure the total space charge or average position inside a needle-plane electrode configuration. To the author's knowledge, there has been no approach proposed in the literature to measure space charge distributions under non-uniform fields where space charge effects are crucial, probably because of the difficulty of presenting the non-uniformity. Therefore, this study plans to choose one of the available space charge distribution techniques, improve the technique under uniform fields for higher resolution and accuracy and, in the addition, extend it to needle-plane electrode configurations.

The main purpose in developing space charge measuring methods is to investigate the space charge dynamic behaviour and thereby to help in understanding the breakdown and electric treeing processes. Recently, some researchers have used measurement methods for space charge dynamic investigation and tried to relate their results with the breakdown mechanisms. However, we are still far from a full understanding of space charge dynamic behaviours. Much more experimental

research is necessary to clarify space charge characteristics, especially its dynamic characteristics inside polymers (such as charge injection, accumulation and transportation).

The present research is aimed at further developing the space charge distribution measuring techniques in order to clarify the charge dynamics inside polymers. More specifically, it has the following objectives.

1. Choosing one space charge distribution measuring technique that is not only suitable for the space charge dynamic investigation but also easy to set up experimentally; improving the accuracy and the resolution of the technique under a uniform field through a signal processing approach and comparing the new approach with the old approaches.
2. Implementing a uniform field space charge distribution measuring system, setting up some experimental procedures and applying the improved space charge distribution signal processing method to investigate space charge dynamic behaviours in some selected polymers.
3. Discussing the space charge effect inside polymers based on the measurements and findings of the second part.
4. Extending uniform field space charge distribution measuring principles to a nonuniform field (i.e. needle-plane electrode configuration).

1.2 RESEARCH PROGRAM AND THESIS ORGANIZATION

To fulfil the above objectives, the following research program was undertaken and organized in the following order.

Chapter 2 contains the pertinent literature reviews. It presents an overview of typical properties of the selected polymers (PE, PP and PMMA); an overview of solid breakdown mechanism investigations and space charge effects; a survey on the existing space charge distribution measuring techniques among which the pulsed electro-acoustic (PEA) method was chosen for further development; and finally, a literature review of the PEA method.

Chapter 3 re-analyses the PEA system and describes the proposed simulation model which attempted to improve the available PEA signal processing methods so as to provide the space charge distribution with higher accuracy and enough resolution. This included the simulation models for uniform field and needle-plane field.

Chapter 4 compares, from an analytic point of view, the charge distribution results obtained under uniform field assumptions by the two previous data processing methods, the deconvolution procedure (DCON) and the direct method (DM), with the proposed point matching simulation model(PMSM). Four sets of synthetic signals are used. Then, from an experimental point of view, two sets of experimental signals are processed by the PMSM to demonstrate the procedures and pertinent points associated with the application of the PMSM to experimental signals.

Chapter 5 demonstrates the experimental arrangement for setting up PEA measuring systems for uniform field space charge distribution measurement and the measuring results obtained for the sheets of LDPE, HDPE, UHMWPE, PP and PMMA under *Step Increased Voltage*, *Constant Voltage*, and *Short Circuit* experimental conditions. The influence of material density, molecular weight and specific insulating material on the space charge dynamics is discussed.

Chapter 6 presents the conclusions of this research study and recommendations for future study.

Appendix A collects the relevant subjects and concepts used in the thesis.

Appendix B shows the detected pressure wave equations when the transducer is put in a arbitrary position on the plane side of the needle-plane electrode configuration.

Appendix C proposes a recursive minimum variance deconvolution simulation model and a maximum likelihood deconvolution simulation model.

Appendix D presents a nonlinear detection and optimization process (NDOP) used to further improve the obtained charge distribution results, and the application of the NDOP to three set of the synthetic signals.

CHAPTER 2

LITERATURE REVIEWS

2.1 INTRODUCTION

This Chapter presents the relevant literature reviews. Firstly, Section 2.2 presents an overview of the typical properties of the polymers selected in the experimental research. A brief literature overview on solid breakdown mechanisms and space charge effects is presented in Section 2.3. It illustrates the importance of space charge distribution measurements. Then, in Section 2.4, the developed space charge distribution techniques are summarized and compared. Among them, the pulsed electro-acoustic (PEA) method was chosen to be further developed in the research. Section 2.5 is a survey of the literature on the previous studies of the PEA method.

2.2 OVERVIEW OF POLYMERS SELECTED IN RESEARCH

The polymers adopted in this research to investigate space charge effects were polyethylene(PE), polypropylene (PP) and polymethymethacrylate(PMMA). Table 2.1 shows their chemical structures. The typical physical properties that are related to high voltage applications are presented in this section.

For wire and cable, polyethylene(PE) has become the most versatile insulation material, largely because of its relative low price, processability, resistance to chemicals and moisture, flexibility at low temperatures and excellent electrical properties[5]. Polyethylene is produced by polymerizing ethylene gas ($\text{CH}_2=\text{CH}_2$) into long polymer chains. Depending upon the

polymerization processes, polyethylene is produced in low (0.919-0.925 g/cm³), medium (0.926-0.940 g/cm³), and high (0.941-0.965 g/cm³) densities, called low density polyethylene (LDPE), medium density polyethylene (MDPE) and high density polyethylene (HDPE) respectively.

TABLE 2.1
CHEMICAL STRUCTURES OF POLYETHYLENE, POLYPROPYLENE, AND
POLYMETHYLMETHACRYLATE

Polyethylene (PE)	Polypropylene (PP)	Polymethylmethacrylate (PMMA)
$\left[\begin{array}{cc} \text{H} & \text{H} \\ & \\ \text{---C} & \text{---C---} \\ & \\ \text{H} & \text{H} \end{array} \right]_n$	$\left[\begin{array}{cc} \text{H} & \text{H} \\ & \\ \text{---C} & \text{---C---} \\ & \\ \text{H} & \text{CH}_3 \end{array} \right]_n$	$\left[\begin{array}{c} \text{H} & \text{CH}_3 \\ & \\ \text{---C} & \text{---C---} \\ & \\ \text{H} & \text{C}=\text{O} \\ & \\ & \text{O-CH}_3 \end{array} \right]_n$

Polyethylene is classified not only by density, but also by molecular weight. High density polyethylene, with molecular weights averaging in the 300,000 to 500,000 range, is called high-molecular-weight high density polyethylene (HMW-HDPE) and is used principally as primary insulation. Although the average molecular weight is from 300,000 to 500,000, the molecular weight distribution is broad, with a significant proportion of lower molecular weight molecules to facilitate processing[2]. A high density polyethylene with molecular weights in the range of 3 to 6 million is called ultrahigh-molecular-weight polyethylene (UHMWPE).

Important factors affecting the properties of PE are degree of crystallinity, molecular weight, and molecular weight distribution. Higher crystallinity can increase tensile strength, rigidity, chemical resistance, and opacity, while reducing permeability to liquids and gases.

The above mentioned PE polymers are thermoplastic, which means that they soften on heating below their decomposition temperature and that they harden to their original state on cooling. Polyethylene may be crosslinked (XLPE) to a thermoset material by the addition of one and a half to two percent dicumyl peroxide to formulations or by electron beam radiation [2].

Thermosets refer to rigid, infusible organic materials which lose their plasticity when fully cured. Since their appearance in the 1960s, XLPE cables have dominated the distribution cable field in North America, Japan and Northern Europe[5], largely because they may be operated at 90°C and intermittently at 130°C during fault conditions. They also have good low temperature properties, show increased resistance to ozone and corona(as compared to linear PE) and have good impact, abrasion and environmental stress cracking resistance characteristics. However, the XLPE cables are also subject to tree growth.

Among various kinds of polyethylene, LDPE, HDPE and UHMWPE were chosen to investigate the influence of density and molecular weight on space charge dynamics. XLPE was not selected because it is not commercially available in sheet form. To compare the difference of charge dynamics in different polymeric materials, polypropylene(PP) (nonpolar polymer as PE) and acrylic(PMMA) (polar polymer) were selected.

Polypropylene (PP), formed by polymerizing propylene($\text{CH}_3\text{CH}=\text{CH}_2$), is closely related to PE, both chemically and in end uses. It is the most rigid polyolefin, with high resistance to environmental stress cracking, even when it comes into contact with solvents and polar materials. Its dielectric properties and moisture resistance are among the best for all plastic polymers. Besides, it is one of the lightest plastics(0.90g/cm^3), making it more economical to mold than most other resins and more suitable for processing into molded insulation parts, extruded wire and cable insulation, and dielectric films. Also, PP is heat sealable and non-toxic. Due to these advantages, the Rural Electrification Administration (REA) and cable manufacturers recognize PP and HDPE as alternatable[2]. Some people have claimed that PP has significant manufacturing advantages. However, the brittleness (glass transition) temperature of PP (-15°C) is much higher than PE (-76°C), a fact which limits its applications in power cables.

Polymethylmethacrylates(acrylics) are noteworthy for superlative optical properties and weatherability. They are produced by polymerizing methyl methacrylate alone or combined with other unsaturated monomers. Acrylic resins exhibit outstanding arc resistance even after immersion in water or long-term outdoor exposure. Clarity is excellent. Major uses for

acrylics take advantage of their superior optical properties. They are being used increasingly in fiber optics. High arc resistance makes acrylics suitable for high voltage applications such as circuit breakers. A decreasing dielectric constant with increasing frequencies makes acrylics attractive candidates for high frequency applications.

2.3 OVERVIEW OF SOLID BREAKDOWN MECHANISMS AND SPACE CHARGE EFFECTS

2.3.1 Basic Space Charge Effects

Changing or distorting the electric field pattern is considered the basic effect of space charge.

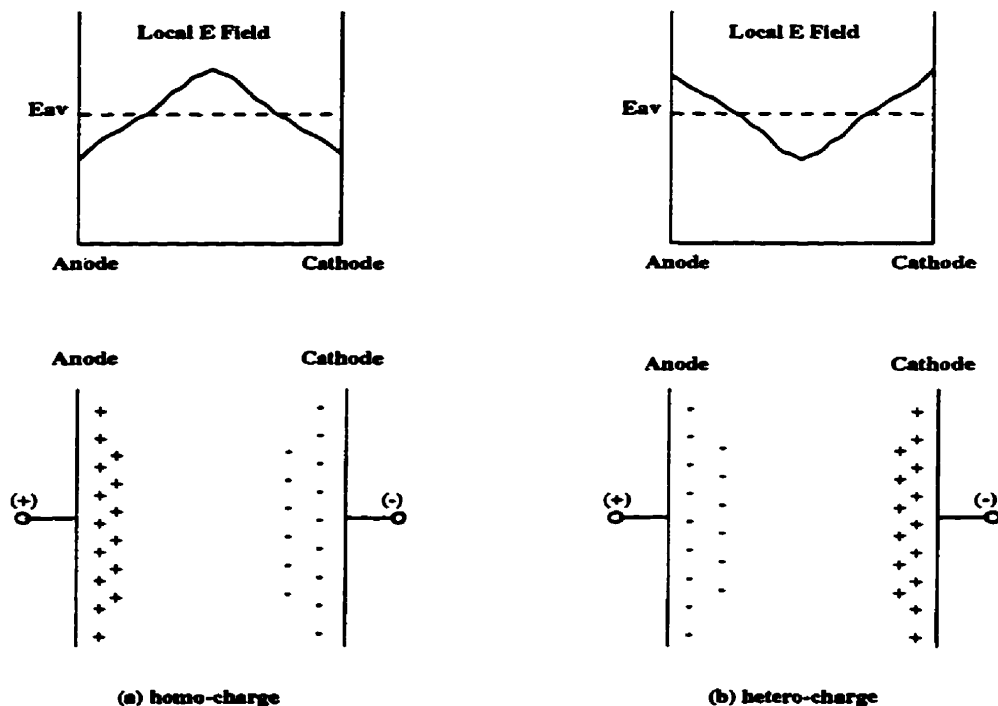


Figure 2.1 The influence of space charges on electric field distributions[8]

Experimentally, for uniform fields, it was found that after pre-stressing with dc, the same polarity impulse breakdown strengths were increased, while the opposite polarity impulse strengths were decreased[6]. This result suggests the formation of space charge causes the distortion in the effective internal electrical field.

Generally, according to whether space charge has the same polarity as its nearby electrode, the space charge distribution inside a sample is simply classified as a homo-charge distribution or a hetero-charge distribution. Figure 2.1 shows the influence of these distributions on the internal electric field profiles under uniform field set-ups. Qualitatively, the dc prestressing experiments can be explained by space charge effects.

Assume that space charges are built up during dc pre-stressing as a result of electrons injected from the cathode and/or holes being injected from the anode. A homo-charge distribution is formed in the sample as Figure 2.1(a) shows. As the electric fields near the interfaces of electrodes and insulating material are decreased, further charge injection tends to be weakened. If, after dc prestressing, a same polarity impulse voltage is applied, this voltage needs to be much higher in order to initiate further charge injection. Only when charge injection continues to take place can the electric field near the middle of the sample reach sufficient magnitude to lead to breakdown. If a reverse polarity impulse voltage is applied, the former homo-charge distribution becomes hetero-charge as shown in Figure 2.1 (b). The electric field intensity at interfaces can be much higher in a lower voltage application, causing a large amount of charge to release or inject suddenly, and initiating breakdown processes and/or degradation processes (like treeing) at the interface first, followed by the breakdown of the insulating sample[8].

For nonuniform field, usually, a partial breakdown is observed at the site of the high local electric field, which leads to a "tree", named after the characteristic feature of the breakdown paths. Trees are found to start at asperities, voids, or imbedded particles, all of which serve as local field enhancement sites[15]. There are electric trees, water trees, electro-chemical trees, etc., classified according to the condition leading to the tree[8]. The two stages of tree growth are initiation and propagation. Factors which stimulate initiation do not necessarily encourage propagation, and vice versa. Space charge effects have been found to play an important role directly or indirectly in all these treeing processes, especially their initiations[15-28]. Electric trees can be initiated by different kinds of voltage applications. Apart from polarity reversal effects, treeing has been observed when both electrodes were short-circuited after the application of dc voltage lower than the nonuniform field dc tree inception voltage[6].

Moreover, a well-known experiment showed that an electric tree could be formed spontaneously. By injecting 3MeV electrons from a Van de Graaff accelerator into a PMMA block, a tree pattern was formed when a grounded metal nail was pressed into the sample perpendicular to the radiation direction only after the accumulated space charge in the sample reached certain density[7]. This experiment showed how powerful the sudden charge release can be. Also it hints, when a grounded metal nail is connected to offer a path, the sudden movement of the accumulated space charges under their self-generated high field is enough to damage the sample materials[7].

From the above mentioned experimental results and discussion, it is obvious that the space charge effects, especially the dynamic characteristics of space charge formation (injection), accumulation and transportation etc., play important roles in electric treeing and breakdown in polymers. From tracing of the footprints of theoretical investigations on solid breakdown mechanisms in Section 2.3.2, it becomes even more apparent that space charge effects are essential to solid breakdown and treeing processes and have to be introduced into the solid breakdown (treeing) theories to shorten the distance between theoretical predications and experimental results.

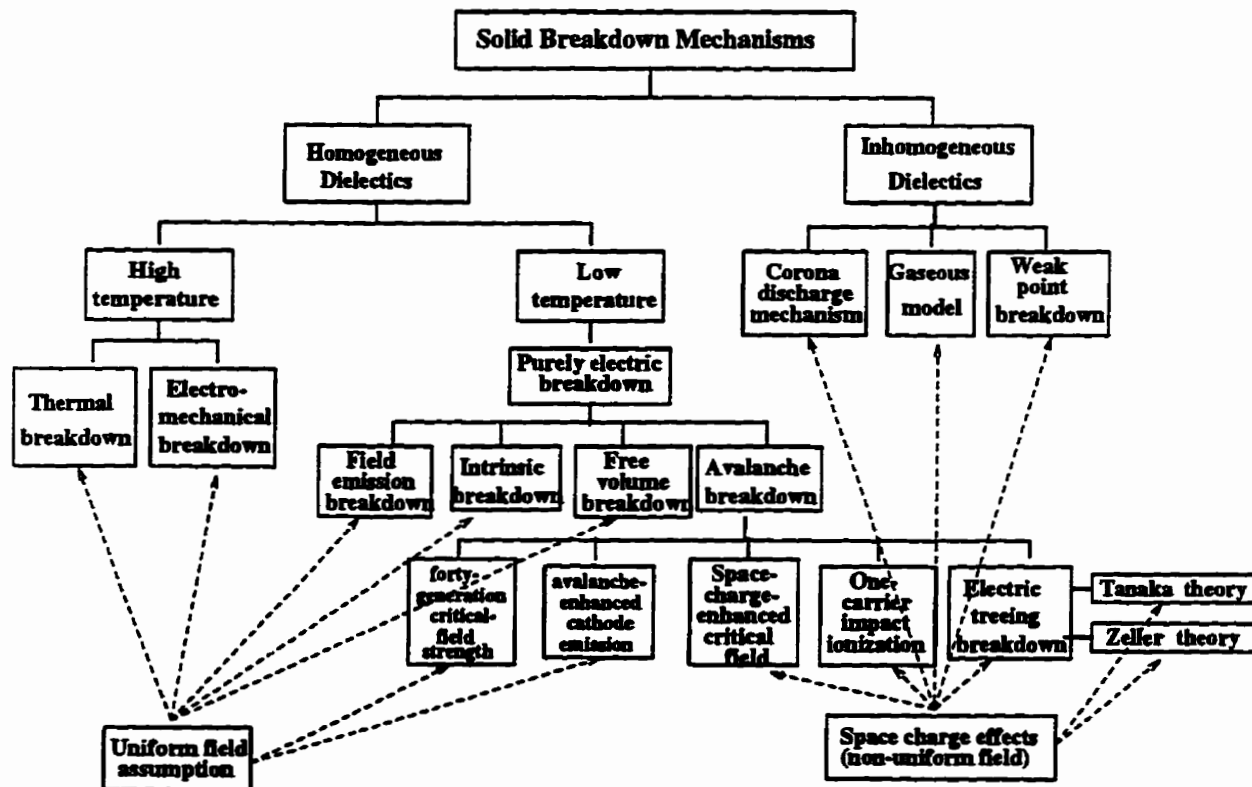
2.3.2 Solid Breakdown Mechanisms and Space Charges Effects

Table 2.2 summarizes most theories and models of electric breakdown and treeing mechanisms according to their basic assumptions and their application ranges. Only a brief overview of these theories is provided here. For detailed theories, one can refer to the corresponding references.

As shown in Table 2.2, theories developed under the homogeneous dielectric assumptions are classified into two groups. One is favoured at high temperature; the other is favoured at low temperature. The *thermal breakdown* presented by Wagner in 1922 [6] described the breakdown criterion in terms of the thermal conductivity of the dielectric and the pre-breakdown electrical conductivity. Under high electric field intensities, cumulative heating that developed in local paths within the materials could cause dielectric and ionic conduction losses which would generate heat more rapidly than it could be dissipated. Breakdown was proposed to occur because of the thermal instability [8,9]. *Thermal breakdown* is favoured at high temperature since, in general, the

electrical conductivity increases and the thermal conductivity decreases as the temperature increases[9]. The problem is that the theory could give the critical voltage ranges from about zero with bad electrode cooling to nearly infinity with efficient electrode cooling[10]. The *electromechanical breakdown* theory introduced by Stark and Garton in 1955[9] is also favoured at high temperature, and it is mainly for polymers since their Young's modules are low, especially at high temperature. It proposed that the compressive stress due to the electric stress could reduce the effective specimen thickness and result in a higher electric stress inside. The electromechanical critical condition was reached when electric field intensity reduced the specimen thickness to $\exp(-1/2)$ times the initial thickness[8,9].

TABLE 2.2
A SURVEY OF SOLID BREAKDOWN AND ELECTRIC TREEING MECHANISMS



In low temperature regions, thermal instability and electromechanical collapse usually do not result in failure. However, breakdown still occurs when the field intensity becomes sufficient to accelerate electrons through the insulation material. The electronic processes have been identified as playing

an important role in breakdown processes at low temperature. *Purely electrical breakdown* mechanisms are all based on the electronic processes. This research was intended to be conducted at low temperatures.

In the *field emission breakdown* theory, current multiplication is considered as the result of the quantum-mechanical tunnelling from the valence band to the conduction band in the presence of a strong electric field. The critical fields calculated by this theory are usually of an order of magnitude larger than experimental breakdown strengths[8,9] which indicate some other electronic processes might happen before the field emission critical field is reached. The *intrinsic breakdown* theories suggest that the critical field strength is reached when some instability occurs in the electronic conduction current. The intrinsic critical field strength is calculated from the conduction-electron energy balance equation. The balance state is reached when the rate of energy gained by conduction electrons from the field is equal to the rate of energy transferred to the lattice by these electrons. Compared with the experimental breakdown results as functions of temperature, the order of magnitude and temperature dependence of the breakdown strength are correct for some alkali halides[9]. This suggests that the onset of significant collision ionisation is an important factor in the onset of purely electrical breakdown. However, this theory is still not adequate to explain all experimental results; perhaps because it is based on a homogeneous infinite medium without considering the boundary conditions such as electrode separations, configurations, and material properties, etc.. The *free volume breakdown* theory is inherent to polymers. It explains the breakdown phenomena of polymers around the glass transition temperature (low temperature). The basic idea is that free volumes in polymers provide space for electrons to be accelerated under high fields. The electron mean free path is associated with the free volume, and is thus related to the energies that electrons can gain from the high field and the breakdown strength of the polymer[6,8].

In the *field emission*, *intrinsic* and *free volume breakdown* theories, the number of conduction electrons is viewed as increasing suddenly and following a situation in which breakdown has happened. *Avalanche critical-field* theories, on the other hand, consider that the conduction-electron multiplication is a process that gradually reaches intolerable proportions as the field strength enhanced[9].

There are several critical criteria formulated on the basis of the avalanche mechanism, such as the *forty-generation* theory, the *avalanche-enhanced cathode emission* theory, and *space-charge-enhanced critical fields*, etc.. They can explain the thickness dependence of breakdown strength that non-avalanche theories cannot.

The *forty-generation critical field strength* theory, originally developed by Fröhlich and by Seitz in 1949[9], is based on a single-electron collision-ionization. The *avalanche-enhanced cathode emission* theory was considered by Forlani and Minnaja in 1964[9]. Instead of taking account of the avalanche multiplication resulting from only one electron starting from the cathode, they considered the consequences of avalanche multiplication of emission current from the cathode. However, both theories are bounded on the assumption of uniform fields. When collision ionisation is considered as an important element in a theory, the uniform field assumption encounters severe difficulties, especially when there are many generations of collision ionisation. The reason is that space charges (both electrons and holes) caused by the build-up of an electron avalanche should result in a nonuniform field strength distribution[9]. Therefore, some other theories developed within the avalanche breakdown category have attempted to drop the assumption of uniform fields.

Space-charge-enhanced cathode emission theories, as proposed by O'Dwyer [9,11], consider the space charge effect and treat the hole current and electron current by assuming the continuity of current. The breakdown is described to occur when the space charge immediately in front of the cathode (due to relatively immobile holes) reaches such proportions that the electron current injected from the cathode is sufficient to destroy the material. From *space-charge-enhanced cathode emission* theories, a universal characteristic for the critical field strength as a function of thickness has been derived; a small negative resistance and, consequently, an unstable conduction characteristic is proposed (the negative differential resistance had been observed experimentally [12]); and the steady-state conduction characteristics for a dielectric between plane-plane electrode and spherical electrode geometry are calculated with the onset of negative resistance as the breakdown criterion[11].

One-carrier impact ionisation theories, proposed by Klein[13,14], consider not only electron injection and collision ionisation, but also the effects of recombination and trapping of electrons and holes. An important conclusion is that the critical breakdown field and breakdown time are affected by the trapped electron charge density. They will both increase when the charge density increases, which indicates a protective effect of electron charge from breakdown[14].

When a nonuniform field exists inside a solid, the partial breakdown will have a greater tendency to happen before the bulk breakdown. This is actually the case in practical situations. The electric treeing is generally accepted as the process of partial breakdown in very high electric field regions. Experimentally, needle-plane or needle-needle geometry is often used to investigate the treeing processes. From the previous reviews on breakdown mechanisms, it is obvious that the theories concerning electrode effects, and ionisation processes offer closer explanations of experimental results. These effects and processes introduce space charge effects into breakdown mechanisms and suggest the non-uniformity of internal field and the importance of local field intensity to breakdown initiation. Needle-plane or needle-needle electrode configuration can concentrate the electric field on the needle point, and thus may facilitate the research of breakdown initiation, i.e. tree initiation.

Several theories have been put forward to illuminate the electric treeing processes, such as the *charge injection and extraction* theory proposed by Tanaka and Greenwood[18], the *electrofracture mechanics (field limited space charge model)* [25], and the *fractal model* proposed by Zeller et al[23].

The *charge injection and extraction theory (Tanaka theory)* emphasised the initiation by charge injection and extraction among several other explanations for the initiation of an electric tree, such as a tree initiated by mechanical fatigue, or by partial discharge, etc. This theory explains the incubation period of initiation during which there are no apparent visual changes and no detectable partial discharges[18]. It proposes that electrons, when they are injected from an electrode and extracted backward, might gain energy high enough to attack polymer chains, initiate chemical reaction and cause polymer degradation. The degradation might result in the formation of a very narrow channel. A tree starts to grow when the narrow channel becomes large enough to allow

gaseous discharge[18]. This theory proposes that the logarithm of the tree initiation time is related to the electric field and the effective work function. Experiments have confirmed the injection and extraction of charge under a high field. This theory concerns the influence of a needle electrode work function on the tree initiation voltage, and proposes the importance of interface properties between electrode and dielectric materials. However, work functions are usually measured in ultra-high vacuum; the justification of the correlation between the work function and tree initiation is, therefore, only qualitative.

The work done by Zeller and his co-workers is regarded as the first attempt to predict the amount of charge that can accumulate, or the volume it can occupy in dielectrics[15, 22-26].

Electrofracture mechanics assumes that the formation of a partial discharge (PD) channel requires a formation energy, the initiation or growth of a PD channel leads to a release of electrostatic energy, and the growth is energetically possible only if the derivative of formation energy is less than or equal to the derivative of electrostatic energy to the growth co-ordinate[25]. They proposed that this relation is a "unifying" one for it is independent of whatever mechanism is predominant in the channel formation energy or the electrostatic energy for channel propagation. Thus, it might be possible to introduce any or any combined effects into the relation and set up a specific model. It has been found that the breakdown field is much higher than the space charge injection field requirement if the presence of space charge is excluded in a model; therefore, this result proves that space charge must be taken into account in a breakdown model. With the ***field limiting space charge(FLSC) model***, the calculation of the complicated space charge density is simplified without any parameters(such as mobility and trap densities) except the critical field, E_c . It assumes that electrons will move into the insulation if the electric field is greater than E_c . Since in a needle-plane set-up the field will decrease apart from the needle tip, at some distance the field will be too low to support the movement of electrons; thus the electrons will stop moving and form the edge of space charges. Within the space charge edge, the electric field is asserted to have a magnitude fixed at E_c since electrons will continue to move rapidly away from the cathode if $E > E_c$ and will maintain a sufficient volume of space charge to keep the field at E_c . This space charge region is called ***the field limiting space charge***. The model predicts that there will be no relation between the PD level and

useful service life because the crucial quantity for damage is the energy density which depends on the length and radius of the channel, not the change in the total electrostatic energy caused by the discharge[25].

Compared with the *FLSC model*, the *fractal model* provides an even more unifying picture covering homogeneous space charge injection, treelike structures, and filamentary breakdown. A qualitative relation is set up between the global form of the pattern and two simple physical parameters E_c and E_s . The tree growth probability is assumed to be proportional to the local field E_{loc} when $E_{loc} \geq E_c$ and zero when $E_{loc} < E_c$. The potential in a developed tree structure is defined to be equal to $V_0 + E_s s$, where V_0 is the potential of the connecting electrode, s is the length of the path along the structure which connects the point to the electrode. With different E_c and E_s , the tree pattern can be obtained by computer simulation. The space charge cloud was found to be homogeneous, leading to a self-limitation of local field enhancement as the *FLSC model* describes when $E_c = E_s$. Breakdown occurs only if the voltage exceeds the product $E_c d$ where d is the electrode spacing. The space charge cloud was found to consist of the non-symmetric charge distributions and filamentary or treelike structures, which might lead to an amplification, propagation, and branching of the local field enhancement, when $E_s < E_c$. Breakdown might occur at voltages below $E_c d$ in this case.

The *fractal model* illustrates the relation between local stochastic and global deterministic aspects of dielectric instabilities[23]. In reality, the materials are inhomogeneous on a microscopic scale, or even on a macroscopic scale, due to the dielectric structure, morphology, structural irregularity, the presence of additives, etc., Zeller et al believe it would be possible to absorb all unknown factors into an effective probability law for growth and to make deterministic predictions about the pattern of the pre-breakdown[23].

There have also been several theoretical solid breakdown models developed for inhomogeneous dielectrics. When a high electric field is applied, the typical phenomena are that some sites may concentrate higher field, and/or some sites may have a lower ability to sustain the electric field and act as weak points. Therefore, before the dielectric bulk breakdown, partial discharges may occur

in any internal voids or bubbles that are present or may develop. The *electric discharge or corona mechanism* is considered predominant. Besides, the *gaseous model* proposed by Budenstein[29] and the *weak point breakdown* theory[8] presents two typical ways to deal with the inhomogenous. In the *gaseous model*, a clear identification of various physical processes which have been observed in many experiments are included. A large number of material parameters and a number of assumptions would be necessary to proceed with the computation. The *weak point breakdown* theory, on the other hand, uses a statistical approach instead of considering detailed breakdown processes[8]. The probability of breakdown is assumed to have a Weibull distribution which reflects the weak point distributions inside dielectrics. Weibull distribution is also accepted in insulation ageing studies.

2.3.3 Discussions

The processes leading to breakdown are complicated because breakdown is influenced by many factors, such as the waveform of the applied voltage, the electrode configuration, the properties of the conductor and the insulator materials, the quality of the interface between the electrode and the insulating material, etc.. If all the experimental details are to be considered in a theoretical model or a different model for every different dielectric under every different circumstance is to be proposed, the model will be either too complicated or offer little insight into the physical processes involved and each has no practical value[10].

The further development of breakdown mechanisms is complicated owing to the material properties and the properties changing with temperature, electric field application, and other environmental conditions. A link seems to be necessary to account for the influence from all the factors and to relate them with the breakdown. From the above survey of breakdown mechanisms, space charge characteristics seem to be a basic clue for the breakdown developed under high field and thus seem to be the suitable link. No matter how one describes the behaviour of breakdown, thermally, electromechanically, or purely electrically, the actual breakdown or partial breakdown happens due to the local field strength. The low breakdown voltage doesn't mean the local field strength inside the dielectric or at the interface between the electrode and the dielectric is low. Rather, it suggests

the importance of evaluating the actual field distribution inside the dielectric under the high field, and suggests the importance of space charge distribution which distorts the local field. If the space charge distribution can be found, it may provide more detailed information about what happens inside the dielectric and may help to construct some simple breakdown criteria.

2.4 SPACE CHARGE DISTRIBUTION MEASURING TECHNIQUES

When an electric field is applied to a dielectric material, several processes can take place. The dipoles are oriented by the field, ions can migrate, and charges may be injected and/or extracted at the interfaces under some circumstances. These effects could be considered as useful effects as for electrets. However, they are very undesirable when the dielectric material is used as an insulator (HV cables or capacitors etc.) as discussed in Section 2.3. In these two very different situations, it is highly desirable to understand the physical processes involved in order to control them, for instance, to obtain long-lifetime electrets or, in contrast, to prevent the formation of breakdown conditions. Therefore, various experimental techniques, such as electrostatic measurements, current measurements, electron paramagnetic resonance, and determination of charge, field or potential distributions etc., have been put forward to fulfil this goal. Among them, the charge distribution measurements are most significant and attract the most attention. This section reviews several main techniques that have been developed for the charge distribution measurements. Table 2.3 summarizes these methods and puts them into two categories: destructive methods and non-destructive methods. Table 2.4 shows their principal set-ups, their advantages and their disadvantages.

2.4.1 Destructive Methods

Potential probe techniques, the classical procedures to measure charge distributions[31], have been applied extensively on thick dielectrics and have yielded a wealth of information[31-33]. The *field probe technique* (FPT)[34] is a typical example of these group methods. Based on the principle for a capacitive field probe[35,36], it measures the charge distributions as the cut specimen moves with a mobile table. Because of the limitations of cutting, these group techniques are of little use for thin

films. Besides, the specimen is damaged after cutting. Also cutting may change the charge distribution; therefore, these techniques are not very popular today.

The *charge compensation method* (CCM) comes from the method of virtual electrodes worked out by Sessler et al[31,37] in 1977. Also a destructive method, it is based on the generation of a conductive region within a two-sided metallized and short-circuited sample by means of a scanning electron microscope providing a mono-energetic, diffuse beam whose energy could be adjusted in the range of 5-55keV. When the front of the conductive region, which forms a virtual electrode, is swept through the sample by increasing the beam energy, all the charges originally stored within the material are progressively compensated for, resulting in a release of the induction charges residing on the rear electrode. The front electrode of the sample is connected to an electrometer to monitor the irradiation current while the rear electrode is connected to a high capacitance charge measuring set-up to determine the measuring Δq values needed to calculate $\rho(x)$ in the sample with a simple set of equations[31,37]. CCM can measure the charge distribution with a resolution of $1\mu\text{m}$.

TABLE 2.3
SUMMARY OF SPACE CHARGE DISTRIBUTION MEASURING TECHNIQUES

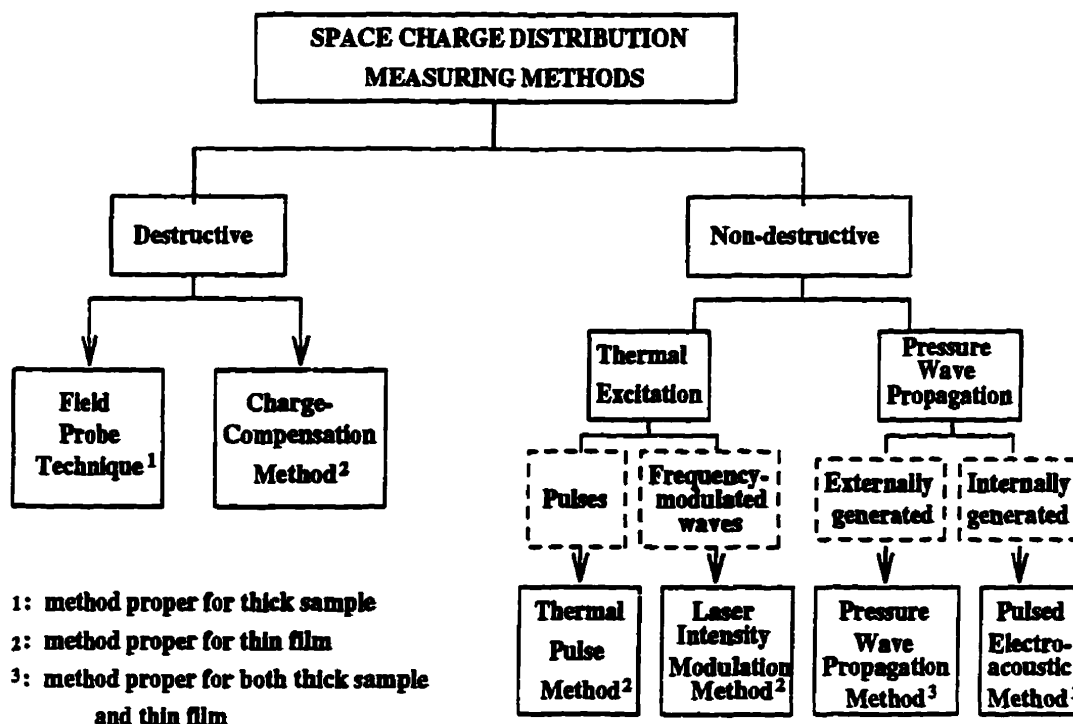
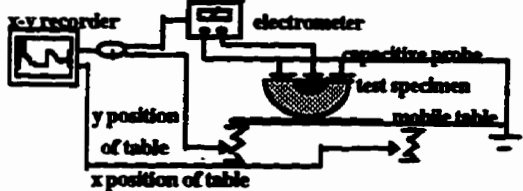
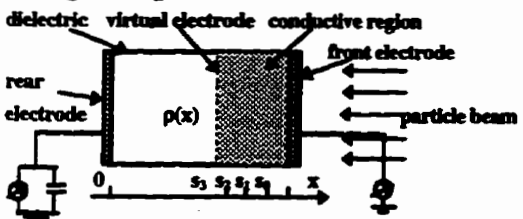
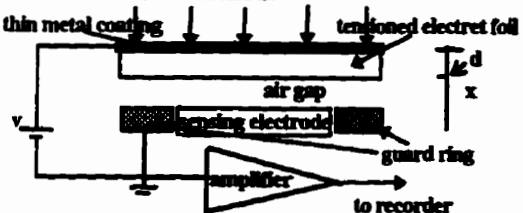
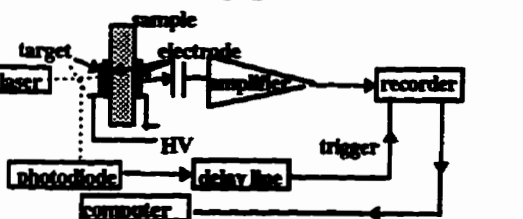
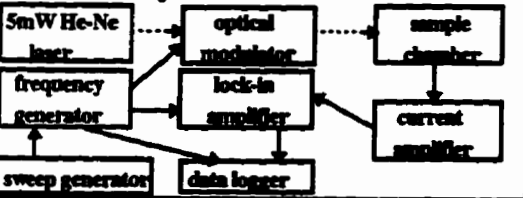
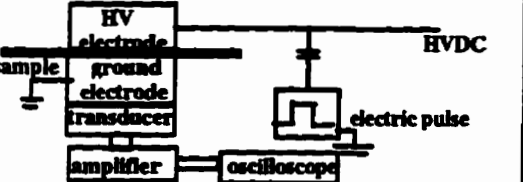


TABLE 2.4
ADVANTAGES AND DISADVANTAGES OF SPACE CHARGE DISTRIBUTION MEASURING TECHNIQUES

METHODS&PRINCIPLE SET-UPS	ADVANTAGES	DISADVANTAGES
<p>Field Probe Technique:</p> 	<ul style="list-style-type: none"> ◆ It provides space charge distribution in thick dielectrics. ◆ Measuring principle is simple. 	<ul style="list-style-type: none"> ◆ It is of little use for thin film. ◆ Cutting may change the charge distribution. ◆ Destructive.
<p>Charge Compensation Method:</p> 	<ul style="list-style-type: none"> ◆ It can measure distribution in thin film with a resolution of 1μm. ◆ It is easy to obtain charge distribution from experimental data. 	<ul style="list-style-type: none"> ◆ Destructive
<p>Thermal Pulse Method:</p> 	<ul style="list-style-type: none"> ◆ Nondestructive since thermal pulse results only in a minor temperature increase in the sample. ◆ It can measure the distribution in thin film. 	<ul style="list-style-type: none"> ◆ Solution is not unique. ◆ The accuracy depends on the accuracy of the deconvolution process. ◆ The resolution depends on the distribution profile.
<p>Pressure Wave Propagation Method:</p> 	<ul style="list-style-type: none"> ◆ Non-destructive. ◆ Charge distribution can be easily obtained since de-convolution is not needed. ◆ The maximum resolution is around 6μm now. 	<ul style="list-style-type: none"> ◆ A laser system capable of applying fast, high intensity, laser pulses(width 3ns) and an amplifier with bandwidth broader than 200 MHz. ◆ The set-up is expensive and sophisticated.
<p>Laser Intensity Modulation Method:</p> 	<ul style="list-style-type: none"> ◆ Non-destructive. ◆ It does not require any highly specialised equipment. 	<ul style="list-style-type: none"> ◆ A special numerical analysis is required to transform experimental data to space charge distribution. ◆ It is not straight forward.
<p>Pulsed Electro-acoustic Method:</p> 	<ul style="list-style-type: none"> ◆ Non-destructive. ◆ Set-up is cheap and applied outside a lab environment. ◆ Relationship between charge distribution and the measured signals is not complicated. 	<ul style="list-style-type: none"> ◆ Due to the limitation of electric pulse, transducer bandwidth, the resolution cannot be as high as the Pressure Wave Propagation method.

There are other destructive invasive probing methods, for example, diffusing chemical solvents [38] to liberate trapped charges. Because destructive methods cannot be repeated on the same sample, they are not suitable to measure the dynamic change of charges[39], and therefore were not chosen in the research.

2.4.2 Non-destructive Methods

In 1977, besides CCM, there were two other methods reported[32] which built-up two basic principles for non-destructive space charge distribution measurements. One was based on the thermal excitation, the method of short heat pulses, proposed by Collins[40], which was later developed as the *thermal pulse* method[41-44]. The other was based on the pressure wave propagation, the pressure pulse wave method, developed by Laurenceau et al[45], which was later called the *pressure wave propagation* Method[46,47] or the *laser-induced pressure pulse* method [48]. In the 1980s, another two methods were developed based on the two basic principles. One was called the *laser intensity modulation* method by Lang et al[49-51] in which frequency-modulated waves were used instead of thermal pulses. The other was called the *pulsed electro-acoustic* method by Takada et al[52-56] or the *electrically stimulated acoustic wave* method by Bernstein et al[39,57-59], in which the pressure waves were internally generated at locations of charges when an electric pulse was applied instead of externally generated by a laser.

The basic principle of *thermal pulse*(TP) method is to apply a step-like heat pulse to one side of a specimen by illumination. The time variations of the open-circuit potential difference across the specimen or the short-circuit current through the specimen can be analysed during the thermal equalization after the nonuniform heating by the pulse. The voltage or current response is due to the nonuniform thermal expansion and the local change in the dielectric constant. It appears possible to calculate $\rho(x)$ by deconvolution of an integral relation between temperature increase and voltage or current change corresponding to time[40-44].

In the *laser intensity modulation* (LIMM) method, each surface of a sample is exposed to a He-Ne laser beam whose intensity can be modulated in a sinusoidal fashion by an electro-mechanical

chopper or an acousto-optic modulator[60-63]. On the surface of the semi-transparent and vacuum deposited metallic electrode, there will be a sinusoidal fluctuation in temperature, which results in the propagation of temperature waves into the bulk of the polymer. As they progress through the sample, the temperature waves are attenuated and retarded in phase and provide a non-uniformly distributed thermal force. This force interacts with the spatially distributed charges to produce sinusoidal pyroelectric current. The real and imaginary part of this current are then measured with a lock-in amplifier which has the same reference phase as the frequency generator which derives the electromechanical (or acousto-optic) modulator. A special numerical analysis is required to transform the experimental current-frequency data into the desired spatial distributions[49-51,60-63].

Both these thermal excitation methods may be performed repeatedly on the same sample. They are non-destructive, but the numerical analysis is too complicated to originate space charge distributions from the measured signals for both methods. Therefore, they were not considered further.

The *pressure wave propagation* (PWP) method(45-48,64-71,77) applies a short rise time pressure wave propagating at the velocity of sound in a dielectric material. This mechanical perturbation compresses the atomic structure and results in three effects: the displacement of charges following the atomic lattice; the variation of the relative permittivity because of the variation of the local concentration of dipoles and charges; and the generation of charges by piezoelectric effects in the compressed region. These three effects will vary the charges on both electrodes. The open-circuit voltage or the short-circuit current will therefore contain information on the space charge distribution, the variation of piezoelectric activity in the sample, and the time dependence of the pressure wave[74]. The wave front of the pressure wave acts as a probe sensitive to charge or potential travelling at the velocity of sound through the sample. If the pressure profile is known, the electric field distribution can be obtained from the measurement of open-circuit voltage (or short-circuit current) by resolving an integral equation. The total charge distribution can be obtained through Poisson's equation, by derivation. When the pressure wave can be described by a short duration pulse, the open circuit voltage directly gives the spatial distributions of the electric field,

while the short-circuit current, directly provide the space charge density distribution, after the complete penetration of the pulse in the sample.

The basic principle of the *pulsed electro-acoustic* (PEA) method is to apply a short duration electric pulse to the sample. At locations where charges are present, the displacements of the charges due to electric forces caused by the electric pulse will generate pressure waves which transmit through the sample. A transducer can be used to detect the pressure waves and transfer them into a voltage signal which can be amplified, recorded and processed to obtain the charge distribution. The principles and experimental set-up of the PEA method are discussed in detail in Section 2.5.

The group of methods involving pressure wave propagation, PWP and PEA, may be performed repeatedly in the same sample while it is charging. Space charge accumulation can be monitored dynamically so as to identify the behaviour of microscopic charge motion[39]. Besides, the numerical analysis to obtain charge distribution from measurements is much simpler than those thermal excitation methods.

2.4.3 Comparing Advantages and Disadvantages

The purpose of the survey on the available space charge distribution measuring methods is to compare the advantages and disadvantages of these methods and select one among them that is suitable for the research objectives.

The objectives on space charge distribution measurement are to find out how space charges are generated, accumulated and transported to help in understanding the electric treeing and breakdown mechanisms in polymers. PWP and PEA methods have become the prime candidates. PWP is a well established method with high resolution. With the application of a high quality laser, the pressure wave can be as narrow as 3ns. However, the set-up is very expensive and sophisticated[39].

Due to the physical limitation of the duration of the electric pulse and the bandwidth of the transducer, the resolution of PEA cannot be as high as PWP. The highest resolution reported, until recently, is around 0.06mm, which corresponds to a pressure wave duration of about 30ns. However, the experimental set-up of PEA is much cheaper and simpler than the PWP. It can be applied outside laboratory environments. Since our investigation objects are not films, the resolution of PEA may be improved in this research to be high enough for the space charge distribution measurements. Based on these findings, the PEA method is chosen to be further developed and used as a tool to investigate the space charge distribution dynamics in this research.

2.5 THE PEA METHOD UNDER UNIFORM FIELD

2.5.1 Introduction

The idea of developing an electro-acoustic technique began in 1983[52]. It was called the electro-acoustic transducer technique and was used to measure electric field intensity at a dielectric/electrode interface. It provided information about the interfacial electric field that identified the polarity of charge carriers but not about the field distribution throughout the bulk of the dielectric. The acoustic wave was excited by an alternating electric source of 1MHz. Two piezoelectric transducers were used to pick up acoustic waves from both high voltage and ground electrodes, and transfer them into electric signals, which would be amplified and rectified. The rectified signal amplitudes were proposed proportional to the electric field intensities at the nearby electrodes.

In the middle 1980s, an improved version called Electric Stress Pulse Technique[53,54] was developed to measure the total charge quantity and the mean penetration depth of charges in a plastic plate irradiated by an electron beam. A HV up to 20kV electric pulse of 90ns was used to generate an acoustic wave. Only one piezoelectric transducer was used at the lower(ground) electrode. An oscilloscope was used to record the electric signal transferred from the transducer.

At the end of 1980s, a principle of processing the signals by the deconvolution procedure was put forward[55,56]. This made it possible to obtain a space charge distribution profile inside a material. This technique, called the Pulsed Electro-acoustic (PEA) method, is non-destructive, cheaper than the PWP method, and can be performed in situ with any space charge generating experiment. Therefore, research on improving the PEA method and using it for the investigation of space charge effects has proceeded ever since.

The first improvement on the method was to improve the transducer to obtain a nearly flat frequency response over the range of Fourier components averaged in the system pass band, such that the output signal from the transducer could be considered proportional to the detected pressure wave. Bernstein et al [39] used an acoustically matched PZT transducer in place of the resonant structure of previous work, while Takada et al [72] used a wider bandwidth PVDF transducer. The width of the electric pulse was reduced to 30ns for a higher resolution and the possibility of applying a direct method for charge distribution measurements [76]. The basic principle of the PEA method under a uniform field assumption, the two already developed signal processing methods (the deconvolution procedure and the direct method), along with a summary of the experimental research using the PEA method, are discussed in detail below.

2.5.2 Basic Principle for Uniform Field PEA Method

The PEA method for observing resident space charge in dielectric insulators involves applying a fast and relatively small voltage pulse across a sample containing space charge. The perturbation launches a stress wave which propagates at a velocity of sound and is received by a piezoelectric transducer mounted in the acoustic path[55]. The principle setup for the PEA method is shown in Figure 2.2.

Under uniform field assumption, the electric pulse field $e_p(t)$ generated by the electric pulse voltage $v_p(t)$ inside the sample is uniform, which indicates that any position inside the sample, the electric pulse field is given by:

$$e_p(t) = \frac{v_p(t)}{d} \quad (2-1)$$

where d is the sample thickness. Equation (2-1) is valid under the assumption that the application of the small short duration electric pulse would not result in any change of the space charge distribution (see Appendix A-1 for detail).

Assume there are surface charges with densities σ_1 and σ_2 distributed on the ground and the HV electrode-sample interfaces, and there are volume space charges with density $\rho(x)$ uniformly distributed at each layer x as shown in Figure 2.2. When the electric pulse voltage $v_p(t)$ is applied, these charges are subjected to additional electric forces due to the electric pulse fields $e_p(t)$. The short duration additional electric force acts on each small charge layer and creates an acoustic pressure wave[39,55,72-76]. If the generated pressure waves are considered to be plane waves with amplitude proportional to the electric forces, they will obey following relationships[55].

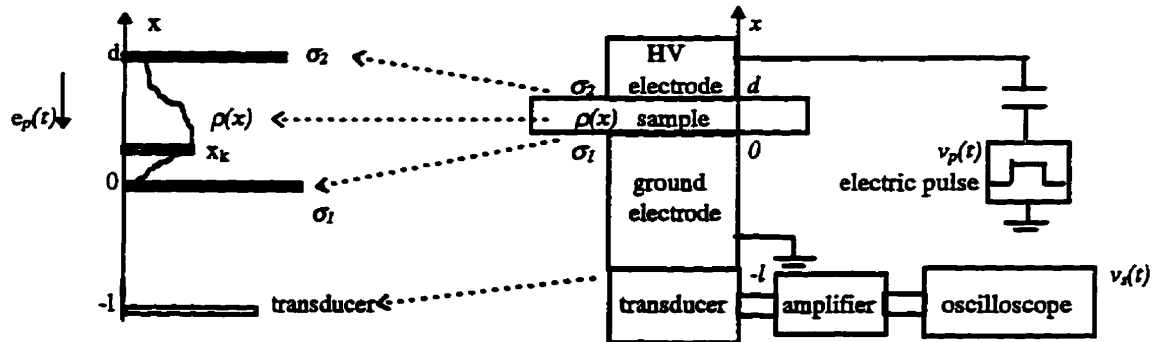


Figure 2.2 Diagram for the principle of the PEA method

At the ground electrode-sample interface, the pressure wave:

$$p(0, t) = K \left[\sigma_1 e_p(t) - \frac{1}{2} \epsilon_0 \epsilon_r e_p^2(t) \right], \quad (2-2)$$

at $x=x_k$ inside the sample,

$$p(x_k, t) = K \rho(x_k) \Delta x e_p(t), \quad (2-3)$$

and at the HV electrode-sample interface,

$$p(d, t) = K \left[\sigma_2 e_p(t) + \frac{1}{2} \epsilon_0 \epsilon_r e_p^2(t) \right]. \quad (2-4)$$

where K is a constant related to the transfer efficiency from the charge vibration to pressure wave, ϵ_0 stands for the free space permittivity and ϵ_r is the relative dielectric constant of the sample material.

When pressure waves are generated from their sources, they will be transmitted along $+x$ or $-x$ direction. The pressure waves along $-x$ direction are transmitted through the sample, through the ground electrode-sample interface, then reach the transducer and construct the first signal. The waves that are transmitted along $+x$ direction will reach the HV electrode-sample interface first; part of them will be reflected at the HV interface and will be transmitted back through the sample to the ground electrode-sample interface. The part of these waves that can be transmitted through the ground interface will get to the transducer and form the second signal. Whenever pressure waves reach the ground interface, part of them will be reflected back to $+x$ direction and thus there will be the third, the fourth, etc. signals which will eventually decay to zero since the reflection coefficients are less than 1.

Assume there is no attenuation and dispersion for the acoustic waves during their propagation, and the linear superposition principle can be used when two or more acoustic waves interact. The total pressure wave detected by the transducer could then be written as a sum of all signals from the first signal $n=1$ to $n=\text{infinity}$:

$$p(t) = \sum_{n=1}^{\text{infinity}} p_n(t) \quad (2-5)$$

and,

$$p_n(t) = K_1 K_2 p_{n-2}(t - \frac{2d}{c_2}) \quad (2-6)$$

where c_2 is the velocity of sound transmitted through the sample material, K_1 is the ground electrode-sample interface transmission coefficient, and K_2 is the HV electrode-sample interface reflection coefficient. If Z_g , Z_s , Z_h , and Z_t , stand for the acoustic impedance of the ground electrode, the sample, the HV electrode, and the transducer materials respectively,

$$\text{then, } K_1 = \frac{2Z_g}{Z_g + Z_s}, \text{ and } K_2 = \frac{Z_s - Z_h}{Z_s + Z_h}.$$

The acoustic impedance of a material is equal to the density of the material times the velocity of sound transmitted through the material[85,86].

The total signal is therefore based on the first and the second signals. It is proposed that half the signal after generation will be transmitted along $+x$ direction and half will be transmitted along $-x$ direction[79]. The sum of the first signal $p_1(t)$ and the second signal $p_2(t)$ has the following relationships.

$$p_1(t) + p_2(t) = p_0(t) + p_{\rho 1}(t) + p_d(t) + p_{\rho 2}(t), \quad (2-7)$$

where,

$$p_0(t) = k_1 \left[\sigma_1 e_p(t - t_{delay}) - \frac{1}{2} \epsilon_0 \epsilon_r e_p^2(t - t_{delay}) \right], \quad (2-8)$$

$$p_{\rho 1}(t) = k_2 \int_0^d \rho(x) e_p \left(t - \frac{x}{c_2} - t_{delay} \right) dx, \quad (2-9)$$

$$p_d(t) = k_3 \left[\sigma_2 e_p \left(t - \frac{d}{c_2} - t_{delay} \right) + \frac{1}{2} \epsilon_0 \epsilon_r e_p^2 \left(t - \frac{d}{c_2} - t_{delay} \right) \right], \quad (2-10)$$

$$p_{\rho 2}(t) = -k_2 K_2 \int_0^d \rho(d-x) e_p \left(t - \frac{d+x}{c_2} - t_{delay} \right) dx. \quad (2-11)$$

In equations (2-8)-(2-11), t_{delay} is equal to l/c_l , where l is the length of the ground electrode (acted as a delay line), c_l is the acoustic velocity of the ground electrode material. Aluminum is generally used as the ground electrode material. k_1 , k_2 , and k_3 are constants, $k_1 = \frac{1}{2} KK_1 K_3$,

$$k_2 = \frac{1}{2} KK_1 K_3 = k_1, \quad k_3 = \frac{1}{2} KK_2 K_3, \quad \text{and} \quad K_3 = \frac{2Z_1}{Z_1 + Z_2}.$$

Due to many other effects that may be present and influence the later signal, the space charge distributions have been obtained by recording and processing only $p_0(t) + p_{\rho 1}(t) + p_d(t)$, part of the whole pressure waves.

When pressure waves reach the transducer, the piezoelectric transducer will transfer the detected pressure waves into a voltage signal which can be amplified by an amplifier and then recorded by an oscilloscope.

The whole detecting system(transducer, amplifier & oscilloscope) is considered as a linear time-invariant system. If $h(t)$ is used to account for its system transfer function, $v_s(t)$ stands for the output signals recorded by the oscilloscope, then, from system point of view, $v_s(t)$ could be expressed as a convolution of $h(t)$ and $p(t)$.

$$v_s(t) = h(t) * p(t) \quad (2-12)$$

Obviously, $v_s(t)$ contains space charge distribution information.

2.5.2 The Deconvolution Procedure

To obtain space charge distribution from measurements, the deconvolution procedure was proposed in 1988[69], using frequency domain analysis to obtain space charge distributions. Although surface charge response was used to calibrate the space charge distribution density, only the signal corresponding to the internal space charge distribution $\rho(x)$ (i.e., related to pressure wave $p_{\rho 1}(t)$), was considered in the method. The presence of σ_1 and σ_2 was not mentioned in the developed procedure.

Define $\tau=x/c_2$, equation (2-9) can be written as:

$$p_{\rho 1}(t) = k_2 c_2 \int_0^{d/c_2} \rho(c_2 \tau) e_p(t - \tau - t_{delay}) d\tau. \quad (2-13)$$

Further, define $r(\tau)=\rho(c_2 \tau)$,

$$p_{\rho 1}(t) = k_2 c_2 \int_0^{d/c_2} r(\tau) e_p(t - \tau - t_{delay}) d\tau = k_2 c_2 r(t) * e_p(t - t_{delay}) \quad (2-14)$$

Combining equations (2-12) and (2-14), the effect of internal space charges on the first output signal $v_{s\rho 1}(t)$ can be written as:

$$v_{s\rho 1}(t) = h(t) * [k_2 c_2 r(t) * e_p(t - t_{delay})]. \quad (2-15)$$

If $V_{sp1}(f)$, $R(f)$, and $H(f)$ stand for the Fourier transforms of $v_{sp1}(t)$, $r(t)$, and $h(t)$ respectively, in the frequency domain,

$$V_{sp1}(f) = k_2 c_2 H(f) R(f) E_p(f) \exp(-j2\pi f t_{delay}) \quad (2-16)$$

It is proposed that the space charge distribution can be obtained from:

$$r(t) = \mathcal{F}^{-1}(R(f)) = \mathcal{F}^{-1}\left(\frac{V_{sp1}(f)}{k_2 c_2 H(f) E_p(f) \exp(-j2\pi f t_{delay})}\right) \quad (2-17)$$

Before applying equation (2-17), it is necessary to know the denominator $k_2 c_2 H(f) E_p(f) \exp(-j2\pi f t_{delay})$, which reflects the measuring system transfer function. This is obtained from a sheet of charge. Two ways were used to generate a sheet of charge. One was to use the ground electrode-sample interface surface charge σ_{10} as shown in Figure 2.3(a); the other was to generate a sheet of charge as shown in Figure 2.3(b)[57,58].

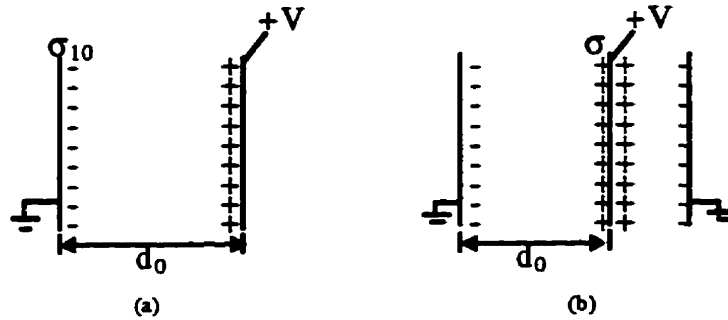


Figure 2.3 Methods used to obtain a sheet of charge

If the same materials and same contacting interface are used (i.e. all constants related to acoustic impedance of materials are the same), it can be deduced that under the same electric pulse voltage $v_p(t)$, the output voltage signal for Figure 2.3(a) case is,

$$v_{s10}(t) = h(t) * k_1 \left[\sigma_{10} \frac{v_p(t-t_{delay})}{d_0} - \frac{1}{2} \epsilon_0 \epsilon_r \left(\frac{v_p(t-t_{delay})}{d_0} \right)^2 \right] \quad (2-18)$$

while the voltage signal for Figure 2.3(b) case under the same electric pulse voltage $v_p(t)$ is,

$$v_{s0}(t) = h(t) * k_2 \left[\sigma_0 \frac{v_p(t-t_{delay} - d_0/c_2)}{d_0} - \frac{1}{2} \epsilon_0 \epsilon_r \left(\frac{v_p(t-t_{delay} - d_0/c_2)}{d_0} \right)^2 \right] \quad (2-19)$$

where, under uniform field assumption, σ_{10} and σ equal to $\epsilon_0 \epsilon_r V / d_0$.

Figure 2.3(a) case is usually used to calibrate the space charge density. Consider only Figure 2.3(a) case, specially, for $d_0=d$, then, $v_p(t)/d_0=e_p(t)$. When $v_p(t)$ is much smaller than the applied dc voltage V , the second term in equation (2-18) can be omitted directly (Let $v_{s10}^{(1)}(t)$ denote that the second term have been omitted in $v_{s10}(t)$). Alternatively, one can first apply no dc voltage ($V=0kV$) to get an output voltage $v_{s100}(t)$ only owing to the second term, then apply dc voltage V to get $v_{s10}(t)$, subtract $v_{s100}(t)$ from $v_{s10}(t)$, the second term can be taken out (Let $v_{s10}^{(2)}(t)=v_{s10}(t)-v_{s100}(t)$). The Fourier transforms of $v_{s10}^{(1)}(t)$ or $v_{s10}^{(2)}(t)$ can be readily written as:

$$\left. \begin{array}{l} V_{s10}^{(1)}(f) \\ \text{or} \\ V_{s10}^{(2)}(f) \end{array} \right\} = k_1 \sigma_{10} H(f) E_p(f) \exp(-j2\pi f t_{delay}) \quad (2-20)$$

Therefore, equation (2-17) can be simplified. Also, due to $k_1=k_2$,

$$r(t) = \mathcal{F}^{-1}(R(f)) = \mathcal{F}^{-1} \left\{ \begin{array}{l} \frac{\sigma_{10} V_{sp1}(f)}{c_2 V_{s10}^{(1)}(f)} \\ \text{or} \\ \frac{\sigma_{10} V_{sp1}(f)}{c_2 V_{s10}^{(2)}(f)} \end{array} \right. \quad (2-21)$$

When $r(t)$ is available, the space charge distribution $\rho(x)$ can be obtained correspondingly.

2.5.4 The Direct Method

To get rid of the deconvolution, a direct method was proposed in 1994[76] by applying a short-duration pulse and wide-bandwidth transducer with a nearly flat frequency response over the range of Fourier components averaged in the system pass band, such that the bandwidth of $V_{s10}^{(1)}(f)$ or $V_{s10}^{(2)}(f)$ is much wider than that of $R(f)$; $V_{s10}^{(1)}(f)$ or $V_{s10}^{(2)}(f)$ can then be considered as a constant to $R(f)$. Alternatively, from time domain point of view, $v_{s10}^{(1)}(t)$ or $v_{s10}^{(2)}(t)$ signal is much narrower than $r(t)$, such that $v_{s10}^{(1)}(t)$ or $v_{s10}^{(2)}(t)$ can be considered as an δ impulse to

$r(t)$. The measured signal $v_{sp1}(t)$ is then proportional to $r(t)$, which means that $v_{sp1}(t)$ directly gives the space charge distribution.

The first signal $v_{s1}(t)$ is considered but only the space charge distribution $v_{sp1}(t)$ is focused. It is supposed that the duration ΔT of the electric pulse $e_p(t)$ is much shorter, such that $e_p(t)$ in equations (2.8)-(2.10) can be considered as a delta function with an amplitude e_{po} . Thus, $v_{s1}(t)$ had the relationship as:

$$v_{s1}(t) = K_h [k_1 \sigma_1 + k_2 c_2 r(t) \Delta T + k_3 \sigma_2] e_{po} \quad (2-22)$$

where K_h was a constant related to $h(t)$.

To obtain space charge distribution, constants are calibrated by integrating the surface charge response $v_{s10}^{(1)}(t)$ or $v_{s10}^{(2)}(t)$ which can be obtained using the same method as described for the deconvolution procedure. Since $v_{s10}^{(1)}(t)$ or $v_{s10}^{(2)}(t)$ is linearly related to σ_{10} , the integration of $v_{s10}^{(1)}(t)$ or $v_{s10}^{(2)}(t)$ has the relationship as:

$$K_v = \begin{cases} \int_0^{\Delta T} v_{s10}^{(1)}(t) dt \\ 0 \\ \int_0^{\Delta T} v_{s10}^{(2)}(t) dt \\ 0 \end{cases} = K_h k_1 \sigma_{10} e_{po} \Delta T \quad (2-23)$$

As described before, $k_1 = k_2$, therefore,

$$r(t) = \frac{v_{sp1}(t)}{c_2 K_v} \sigma_{10} \quad (2-24)$$

2.5.5 Discussions

The principle of the deconvolution procedure is simple but the application of the procedure in practice confronts difficulty. First of all, it is not really possible to obtain $[V_{s10}^{(1)}(f)]^{-1}$ or $[V_{s10}^{(2)}(f)]^{-1}$ by simply “inverting” $V_{s10}^{(1)}(f)$ or $V_{s10}^{(2)}(f)$. As [81] cited, *the practical implementation of this principle is tricky*, since the system is not necessarily stable and strongly amplifies all the additional disturbances in the frequency ranges around the zeros of the function $V_{s10}(f)$. Additionally, the signals $v_{s10}(t)$ and $v_{sp1}(t)$ obtained from practical

measurements are contaminated with noises. Because we never know values for the noise, we can never compute exact $r(t)$ from equation (2.21). Finally, because we can never compute the exact inverse operation, it may be very difficult to obtain a high resolution version of the $r(t)$ instead of a blurred version[82]. As shown in Chapter 4, when $[V_{s10}^{(1)}(f)]^{-1}$ or $[V_{s10}^{(2)}(f)]^{-1}$ is stable and a perfect inverse operation of $V_{s10}^{(1)}(f)$ or $V_{s10}^{(2)}(f)$, no blurring occurs. However, when $[V_{s10}^{(1)}(f)]^{-1}$ or $[V_{s10}^{(2)}(f)]^{-1}$ is not stable and/or signals are corrupted by additive noises(which is mostly what happens in practice), the obtained results can be erroneous.

The signal processing in the direct method is much simpler than the deconvolution procedure. Of course, the cost lies in making a short duration electric pulse and a wide bandwidth transducer. When the electric pulse is shorter, the pressure wave has more high frequency contents, and the attenuation and the dispersion of the pressure wave, when transmitted through the polymeric sample material, become severe. The space charge distribution obtained by the direct method then needs a “recovery” which has to add a transfer function to account for the attenuation and dispersion effects and thus has to implement a deconvolution process in the end to accomplish the “recovery”[83]. Then, the “simple” direct method becomes complicated.

The deconvolution procedure disregards the surface charges at the electrode sample interfaces, while the direct method can only represent these surface charges as shapes of the electric pulse with a duration of ΔT which are like space charge distributions. This is due to the basic assumption that, for the direct method to apply, the bandwidth of charge distribution should be smaller than the bandwidth of the detecting system transfer function and that of the electric pulse. Since the surface charge is corresponding to a δ impulse in the space charge distribution, its bandwidth is from zero to infinity, there is no way practically to have a transducer or an electric pulse with such a wide bandwidth. Therefore, by the direct method, the surface charge can never be represented by a δ impulse in the charge distribution but blurred with a duration around ΔT . The resolution of the direct method is proposed to be $c_2\Delta T$. By electro-beam-irradiation, space charges may mainly distribute in the center of the dielectric with induced surface charges at electrode sample interfaces. For a thicker sample, a

short duration electric pulse, and a highly damped transducer, the signal response coming from the space charges may be discerned from the surface charge signals and processed independently. By applying a high electric field, space charges are generally distributed near the electrode polymer sample interfaces, where surface charges are usually present. The surface charges may be caused by the applied field or be induced by the inside space charges. Therefore, when the direct method is applied, it will be hard to distinguish from the output voltage signal whether the distribution is influenced by the surface charge or the space charge. The accuracy of the obtained space charge densities near the interfaces is then greatly decreased.

Above all, work still needs to be done to improve the signal processing methods for the PEA method. The work must focus on improving the resolution and the accuracy of the obtained space charge distribution, especially near the interfaces by trying to make surface charge distinguishable from the space charges. Section 3.2 will discuss the above comments further.

2.5.6 Summary of Experiments Using the PEA Method

The PEA method has successfully offered time-resolved space charge distribution profiles generated by two approaches. The first was space charge generated by applying HVDC voltage[57], and the second was generated by implanting an electron-beam at one boundary of the sample[55,56].

A few years ago, there were only a few studies using the PEA method to investigate bulk space charge behaviours and interface effects, such as studying the bulk space charge behaviours in PMMA under imposed virtual cathode condition[58], characterizing the charge behaviour of PMMA samples at temperature from 40 to 90°C with moderate applied fields[57] and comparing the space charge distributions under Oil-PE-Oil, Semiconducting-PE-Semiconducting interface conditions[73-75]. Recently, a lot of papers have presented their research on space charge dynamics in polymers using the PEA method. This is due to the fact that the PEA method, despite a lot of debate, has gradually been accepted as a powerful and simple tool to present space charge

distributions inside polymers; it is also due to the urgent demand to understand the space charge dynamics in polymers so that polymeric insulation, such as XLPE cables, can be applied with more reliability.

Under plane-plane and cylindrical electrode set-ups, polyethylene (mainly, LDPE, and XLPE) have been actively studied under dc voltage application. It has found that space charge distributions in polyethylene strongly depend upon additives, by-products of the crosslinking reaction, oxidation products, and the electrode materials [78-80]. The results are summarized as encouraging the formation of heterocharge for non-crosslinked LDPE. For XLPE, an additive such as antioxidant prohibited the formation of heterocharge, while the by-products encouraged the formation of heterocharge. Besides, heterocharge accumulation is found to take place mainly under a low field, and tends to saturate. Under a high field, heterocharges were formed soon after the application of a voltage, followed by the injection from the cathode. Following this, intermittent injections of charge packets from the anode are found to take place. The space charge distribution kept changing without becoming stabilised.

Besides the experiments under dc application, the PEA method has attempted to be applied to ac by using a voltage pulse generator with phase-resolving function [79]. The direct method has been used to get the space charge distributions from measurements. It seems that the PEA method is very promising, being easy to apply to various measurement conditions. If a better data processing method can be proposed and applied to provide higher resolution and higher accuracy of the space charge distributions, this method can be a mature and reliable tool for space charge dynamic investigations and on-line detection to help in the understanding of the solid breakdown mechanism and the accomplishment of reliable pre-fault detection of the insulation systems.

CHAPTER 3

SIMULATION MODEL

3.1 INTRODUCTION

The great need to investigate space charge accumulation inside solid dielectrics under high electric fields has stimulated the development of space charge distribution measuring techniques in solids in the high voltage insulation area. At present, the research goal is not just to obtain the charge distribution profile but also to represent the space charge distribution with higher accuracy and higher resolution. For all the distribution measuring techniques, it has been difficult to distinguish surface charges from the space charge distribution measurements. Under high electric fields, space charge distributions are mostly homocharges or heterocharges distributed near the electrode sample interfaces, where surface charges are usually present. These surface charges may be caused by the applied voltages and/or be induced by the inside space charges. Unless specially compensated, they cannot be treated as zeros even if the electrodes are short-circuited. Therefore, if surface charges can not be distinguished from the space charge distributions, treating the mixed distributions as the space charge distributions would definitely lead to the inaccurate representation of the space charge distributions.

Among the available measuring techniques, the Pulsed Electro-acoustic (PEA) method has its own advantages over the others due to its simple experimental setup and the simple relationship between charge distributions and output signals. Signals measured under uniform fields by the PEA method have been processed by the deconvolution procedure to obtain space charge distributions since 1988[55]. To simplify data processing, a direct method has been proposed [76] in which the deconvolution is eliminated. As discussed in Section 2.5.5, the practical implementation of the deconvolution procedure is difficult, and the direct method cannot represent surface charge well and loses its simplicity when the attenuation and the dispersion of the pressure wave have to be considered(because the deconvolution process is

necessary to account for the attenuation and dispersion factors when high frequency contents increase). The direct method limits the system resolution to the width of the electric pulse whereas the resolution for the deconvolution procedure depends upon whether the system is noise free (or with high signal-noise ratio) and invertible. The direct method can only represent a surface charge as a short duration distribution instead of a δ impulse whereas the deconvolution method attempts to evade the presence of surface charges. When surface charges cannot be distinguished from space charge distributions, the accuracy of the obtained space charge distribution decreases especially near the interfaces. Therefore, the proposed simulation model has been designed to improve the deconvolution procedure such that the measuring system need not to be noise free, and, in the meantime, to enable surface charges to be distinguished from space charge distributions, thereby improving the resolution and accuracy of the obtained space charge distribution.

This chapter re-analyzes the PEA measuring system in Section 3.2, then discusses how to apply the simulation model to obtain space charge distributions under uniform fields (plane-plane electrode configurations) in Section 3.3. The extension of the simulation model principle to nonuniform fields (needle-plane electrode configurations) is presented in Section 3.4.

3.2 RE-ANALYZING THE PEA SYSTEM

3.2.1 Introduction

From the literature reviews of space charge distribution measuring techniques (Section 2.4), the measuring principle of the PEA method (Section 2.5) has advantages over the others. From further literature reviews of the PEA method (Section 2.5), it seems that a novel signal processing method is necessary to overcome the difficulties of the deconvolution procedure and the direct method. In order to have a better appreciation of the new signal processing method (simulation model method), the PEA measuring system, the deconvolution procedure, and the direct method are re-analyzed from the dynamic system point of view in this section.

3.2.2 System Representation

Re-consider the typical uniform field PEA setup as shown in Figure 2.2. If $p_s(t)$ includes only the detected pressure wave $p_o(t)$, $p_{\rho_1}(t)$ and $p_d(t)$ among the total $p_1(t) + p_2(t)$, generated by σ_1 , $\rho(x)$, and σ_2 respectively, from equations (2-7)-(2-10), considering $k_2=k_1$, and let $k'=k_3/k_1$, one can obtain:

$$p_s(t) = p_o(t) + p_{\rho_1}(t) + p_d(t), \quad (3-1)$$

$$p_o(t) = k_1 [\sigma_1 e_p(t - t_{delay}) - \frac{1}{2} \epsilon_0 \epsilon_r e_p^2(t - t_{delay})], \quad (3-2)$$

$$p_{\rho_1}(t) = k_1 \int_0^d \rho(x) e_p(t - \frac{x}{c_2} - t_{delay}) dx, \quad (3-3)$$

$$p_d(t) = k_1 k' [\sigma_2 e_p(t - \frac{d}{c_2} - t_{delay}) + \frac{1}{2} \epsilon_0 \epsilon_r e_p^2(t - \frac{d}{c_2} - t_{delay})]. \quad (3-4)$$

where the symbols have the same meanings as described in Section 2.5.2. If the detecting system(transducer, amplifier, and oscilloscope) can be regarded as a linear time-invariant system, and $h(t)$ accounts for its system transfer function, the output voltage signal obtained from the oscilloscope corresponding to the $p_s(t)$ has this relationship (Appendix A-2 and A-3):

$$v_s(t) = h(t) * p_s(t). \quad (3-5)$$

Due to the presence of the second terms in equations (3-2) and (3-4), $p_o(t)$ and $p_d(t)$ are not linearly proportional to the surface charges σ_1 and σ_2 . Three approaches can be used to take the second terms out of the equations.

1. If $e_p(t)$ is very small compared to the electric fields $\sigma_1/\epsilon_0\epsilon_r$ and $\sigma_2/\epsilon_0\epsilon_r$ at the interfaces, the second term can be directly neglected, and denotes this $v_s(t)$ as $v_s^{(1)}(t)$.
2. If the sample starts with no space charge inside, one can obtain $v_{s0}(t)$, which is due to only the influence of the second terms, and hence we can get rid of the second term in $v_s^{(2)}(t) = v_s(t) - v_{s0}(t)$.

3. For general cases, one can apply a positive pulse first to obtain $v_{s+}(t)$, and then apply a negative pulse to obtain $v_{s-}(t)$, and then obtain $v_s^{(3)}(t) = 1/2[v_{s+}(t) - v_{s-}(t)]$ in which there are no second terms.

If we let $v_{s,t}(t)$ represent $v_s^{(1)}(t)$, $v_s^{(2)}(t)$, or $v_s^{(3)}(t)$, it can be shown that, after any one of these three approaches,

$$v_{ss}(t) = \left\{ \begin{array}{l} v_s^{(1)}(t) \\ or \\ v_s^{(2)}(t) \\ or \\ v_s^{(3)}(t) \end{array} \right\} = h(t) * p_s'(t) \quad (3-6)$$

where,

$$p_s'(t) = p_0'(t) + p_\rho'(t) + p_d'(t) \quad (3-7)$$

$$p_0'(t) = k_1 \sigma_1 e_p(t - t_{delay}) \quad (3-8)$$

$$p_\rho'(t) = k_1 \int_0^d \rho(x) e_p(t - \frac{x}{c_2} - t_{delay}) dx \quad (3-9)$$

$$p_d'(t) = k_1 k' \sigma_2 e_p(t - \frac{d}{c_2} - t_{delay}) \quad (3-10)$$

For a same thickness sample that contains no space charges, *i.e.*, $\rho(x)=0$, surface charges σ_{10} and σ_{20} are distributed on the ground, and HV electrode-sample interfaces when the sample is subjected to a dc voltage. Under the same setup and experimental conditions, the voltage signal responses for the three approaches respectively $v_{s10}^{(1)}(t)$, $v_{s10}^{(2)}(t)$, and $v_{s10}^{(3)}(t)$ to the surface charge σ_{10} has the relationship:

$$v_{ss10}(t) = \left\{ \begin{array}{l} v_{s10}^{(1)}(t) \\ or \\ v_{s10}^{(2)}(t) \\ or \\ v_{s10}^{(3)}(t) \end{array} \right\} = k_1 h(t) * \sigma_{10} e_p(t - t_{delay}). \quad (3-11)$$

Let $g(t)$ be the voltage response to a unit surface charge,

$$g(t) = \frac{v_{s10}(t)}{\sigma_{10}} = k_1 h(t) * e_p(t - t_{delay}). \quad (3-12)$$

Equations (3-6)-(3-10) can then be combined and simplified as:

$$v_{ss}(t) = \sigma_1 g(t) + \int_0^d \rho(x) g(t - \frac{x}{c_2}) dx + k' \sigma_2 g(t - \frac{d}{c_2}). \quad (3-13)$$

Let $x=c_2\tau$, so as the space domain signals are transferred into time domain signals, where the space charge distribution $\rho(x)$ is corresponding to $r(\tau)$, (3-13) can be written as:

$$v_{ss}(t) = \sigma_1 g(t) + c_2 \int_0^{d/c_2} r(\tau) g(t - \tau) d\tau + k' \sigma_2 g(t - d/c_2), \quad (3-14)$$

or in more compact form:

$$v_{ss}(t) = [\sigma_1 \delta(t) + c_2 r(t) + k' \sigma_2 \delta(t - d/c_2)] * g(t) \quad (3-15)$$

Equation (3-15) indicates that the PEA system can be described as a linear time invariant(LTI) system as shown in Figure 3.1. The output signal $v_{ss}(t)$ is the convolution of the charge distribution(surface charges and space charge distribution) and the system transfer function $g(t)$ (Appendix A-2 and A-3). Since a surface charge corresponds to a δ impulse in a space charge distribution, $g(t)$, the output response to a unit surface charge, actually corresponds to the system impulse response (IR).

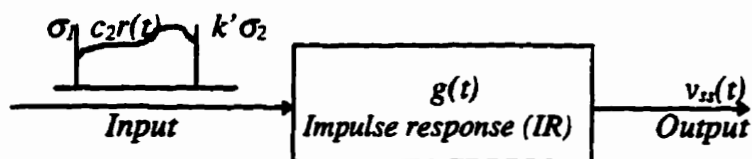


Figure 3.1 System representation of the PEA principle system

The LTI system satisfies:

$$\text{Output} = \text{Input} * \text{IR}, \quad (3-16)$$

where,

$$\begin{cases} \text{Output} = v_{ss}(t) \\ \text{Input} = \sigma_1 \delta(t) + c_2 r(t) + k' \sigma_2 \delta(t - \frac{d}{c_2}) \\ \text{IR} = g(t) \end{cases} \quad (3-17)$$

Therefore, to obtain the charge distribution, it is associated with the “inverse problem” of generating the *Input* to the LTI system from known values of its *Output* and *IR*. This is called deconvolution.

3.2.3 Re-analyzing the Deconvolution Procedure(DCON)

Since the Fourier transform of equation (3-15) has the form:

$$\mathcal{F}(\text{Output}) = \mathcal{F}(\text{Input})\mathcal{F}(\text{IR}) \quad (3-18)$$

Without considering σ_1 and σ_2 , the deconvolution procedure reviewed in Section 2.5.3 was actually attempted to obtain input from:

$$c_2 r(t) = \mathcal{F}^{-1}[\mathcal{F}(v_{s,\rho}(t))/\mathcal{F}(g(t))] \quad (3-19)$$

or in general,

$$\text{Input} = \mathcal{F}^{-1}[\mathcal{F}(\text{output})/\mathcal{F}(\text{IR})] \quad (3-20)$$

where $v_{s,\rho}(t)$ denotes the part of signals coming from the inside space charges. As it is known, when space charges are distributed near the surface charges, it is hard to obtain $v_{s,\rho}(t)$ from $v_{ss}(t)$. However, this is not the only difficulty of the deconvolution procedure(DCON).

If IR^{-1} denotes $\mathcal{F}^{-1}[1/\mathcal{F}(\text{IR})]$, it can be deduced that:

$$\mathbf{Input} = \mathbf{output} * \mathbf{IR}^{-1} \quad (3-21)$$

The procedure can be represented as shown in Figure 3.2, where $G(f)$ is the Fourier transform of $g(t)$.

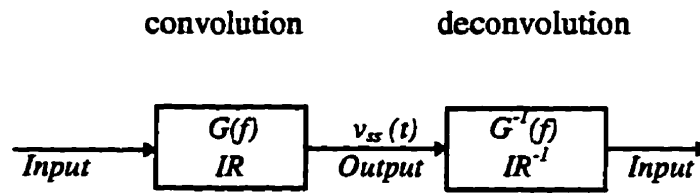


Figure 3.2 System representation of deconvolution through direct inverse of system IR

As discussed briefly in Section 2.5.5, the procedure to get the input is “tricky”[81], partly because it is not really possible to obtain the operation of \mathbf{IR}^{-1} by “inverting” a system’s IR. If, for example, some of the system’s zeros lie outside of the unit circle in the complex Z domain, then \mathbf{IR}^{-1} will be an unstable operation. Some of its poles will be unstable because they will lie outside of the unit circle; therefore, direct inversion of IR is never recommended[82].

Additionally, the measured output of a LTI system is often contaminated by additive noise, i.e.,

$$\mathbf{Measured\ Output} = \mathbf{Input} * \mathbf{IR} + \mathbf{Noise} \quad (3-22)$$

so that

$$\mathbf{Input} = \mathbf{Measured\ Output} * \mathbf{IR}^{-1} - \mathbf{Noise} * \mathbf{IR}^{-1} \quad (3-23)$$

Because we never know the values for the noise, we can never compute the input from (3-23). Even if we can compute \mathbf{IR}^{-1} , it is extremely difficult to compute $\mathbf{Noise} * \mathbf{IR}^{-1}$. Neglecting this term may lead to serious errors in reconstructing the *Input*.

Finally, because we cannot compute the exact inverse operation, it may be very difficult to obtain a high resolution version of the input instead of a blurred version because

$$\begin{aligned}
 \text{input} &= \text{measured output} * IR^{-1} - \text{noise} * IR^{-1} \\
 &= (\text{input} * IR + \text{noise}) * IR^{-1} - \text{noise} * IR^{-1} \\
 &= \text{input} * (IR * IR^{-1}) = \text{input} * \text{resolution function}
 \end{aligned} \tag{3-24}$$

where

$$\text{resolution function} = IR * IR^{-1} \tag{3-25}$$

If IR^{-1} is a perfect inverse operation of IR , then the resolution function is a δ function. No blurring occurs in this case because, when resolution function is a δ function, the convolution of input with a δ function is the input itself. If IR^{-1} is less than a perfect inverse operation, then $(IR * IR^{-1})$ does not equal a δ function. Instead, it equals a smeared delta function, where the amount of smearing depends on the bandwidth of the IR operation and signal-to-noise ratio. Figure 3.3 shows the profiles of the resolution functions[82].

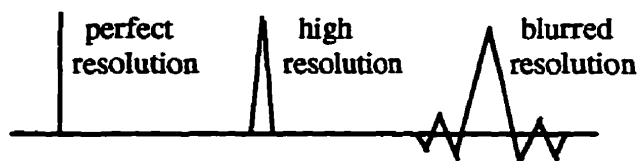


Figure 3.3 Resolution Function

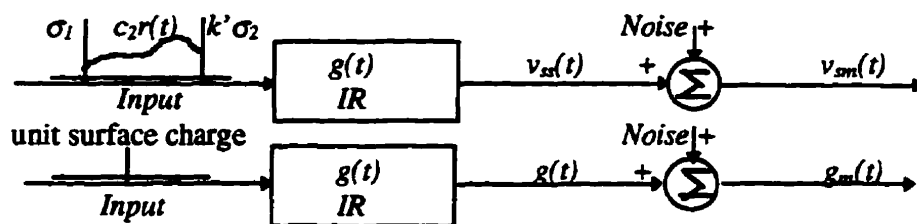


Figure 3.4 System representation of the PEA measuring system

The design of a deconvolution operator requires a careful balancing of bandwidth and signal-to-noise ratio effects. The more realistic measuring system representation is shown in Figure 3.4. The actually measured signals are denoted as $v_{sm}(t)$ and $g_m(t)$, which satisfy

$$\begin{cases} v_{sm}(t) = v_{ss}(t) + Noise = Input * IR + Noise \\ g_m(t) = g(t) + Noise = IR + Noise \end{cases} \quad (3-26)$$

The DCON is a design procedure based on deterministic principles. It is inadequate because it totally neglects the signal-to-noise-ratio effects.

3.2.4 Re-analyzing the Direct Method(DM)

If a system IR is a perfect δ impulse or an approximate one corresponding to a very wide bandwidth compared to the bandwidth of an input signal, i.e. one can write $IR = k\delta(t)$. When the signal-to-noise-ratio is very high (the noise is negligible), The *Output* signal is proportional to the actual *Input* as:

$$Output = input * k\delta(t) = k \times Input \quad (3-27)$$

Therefore,

$$Input = Output / k \quad (3-28)$$

which means only a linear calibration is necessary to obtain the *Input* from the *Output*.

The direct method(DM), as described in Section 2.5.4, is attempted to obtain the space charge distribution in this way.

$$r(t) = \frac{v_{ss}(t)}{\Delta T} \quad (3-29)$$

$$c_2 \int_0 g(t) dt$$

or more precisely,

$$r(t) = \frac{v_{sp1}(t)}{\Delta T} \quad (3-30)$$

$$c_2 \int_0 g(t) dt$$

where the denominator is a constant.

The DM overcomes part of the difficulties of the DCON as the deconvolution process is eliminated. However, as discussed already in Section 2.5.5, due to the presence of surface charges, the bandwidth of the input is from zero to infinite, the direct method still has difficulties unless one can get rid of surface charges or guarantee that space charges are not distributed near the surface charges. Only in these two special situations, the output signals $v_{sp}(t)$ due to space charges can be distinguished from those due to the surface charges contained in $v_{ss}(t)$.

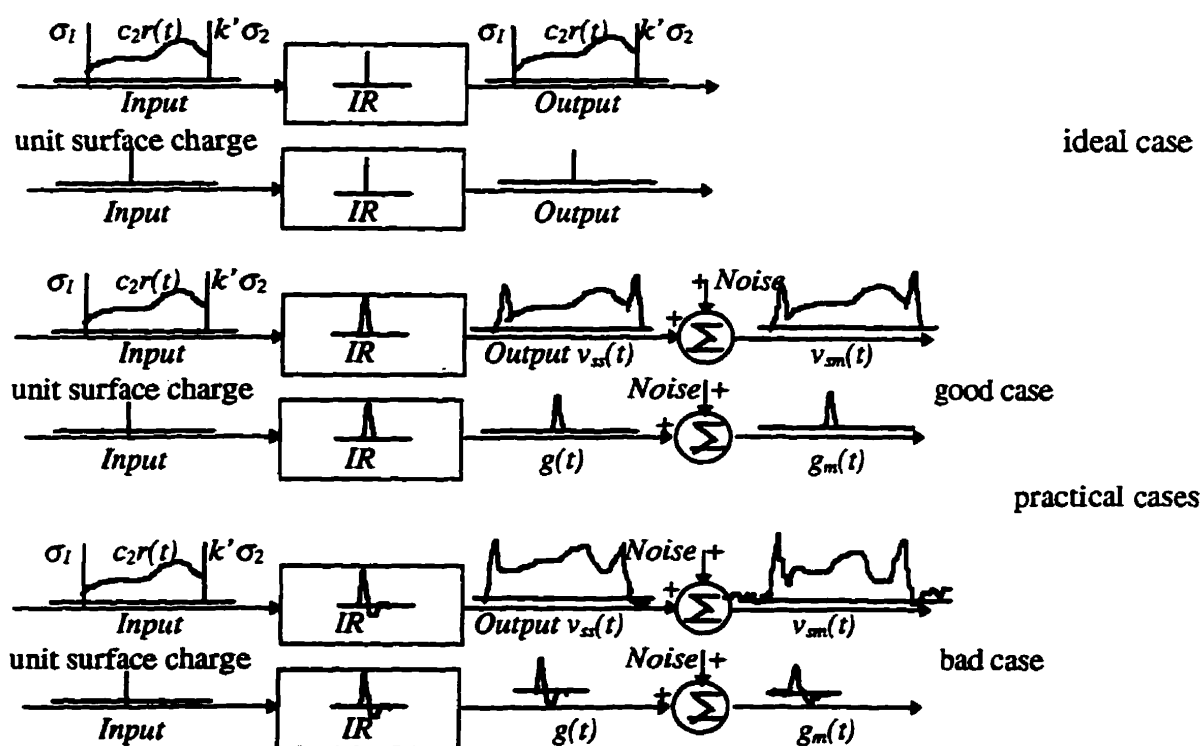


Figure 3.5 Comparing direct method results for the ideal and practical cases

First of all, it is impossible to have $IR = k\delta(t)$ due to the limitation of generating such a narrow electric pulse and the fact that attenuation and dispersion become severe in polymers for higher frequency contents. If one neglects the presence of the surface charges and assumes the bandwidth of the system IR can be considered as a constant corresponding to the space charge distribution, the obtained space charge distribution near the interfaces will be blurred with the

surface charge signals. The accuracy is decreased and the resolution is limited to the duration of the system IR . Therefore, the accuracy and the resolution of the DM do not seem worth the efforts made to increase the bandwidth of the system IR .

Additionally, for a practical PEA measuring system, additive noises and overshoots may not be totally ruled out. They may be disregarded as part of the space charge distributions. Figure 3.5 compares the DM results for the ideal case, and one good and one bad practical case. Since it is unrealistic to have the ideal case, it is not proper to blindly assume the system IR is ideal and disregard the actual waveshape of the system IR .

3.3 UNIFORM FIELD SIMULATION MODELS

3.3.1 Introduction

The simulation model is proposed to overcome the previously discussed difficulties of the DCON and the DM methods. Attempts are made to distinguish surface charges from the space charge distribution in the simulation model. The basic idea of the simulation model principle is to simulate the charge distribution in the discrete-time domain using the measured data from the PEA measurement [$v_m(t)$ and $g_m(t)$], and determine the charge distribution by minimizing the difference of the error between the measured data and the predicted results.

In the simulation model, the system IR needs to be a broad bandwidth but not like in the DM, in which it has to be at least approximately a δ impulse. The system IR will be fully considered in the simulation model in contrast to the DM, where only the integration of IR provides the denominator constant. The way to obtain the *input* (i.e. charge distribution) in the simulation model is also by deconvolution, but the design of the deconvolution is based on stochastic (i.e. random) principles instead of deterministic principles. The deterministic procedure totally neglects the signal-to-noise-ratio effects while the stochastic design procedure can handle both the bandwidth and the signal-to-noise-ratio effects.

Since the simulation model obtains the charge distribution in the discrete-time domain (Appendix A-4) through digital simulation, many algorithms in discrete-time signal processing, system identification and control theory can be applied. In this thesis, only one approach is attempted. It is called the point matching simulation model (PMSM) approach. Alternatively, other deconvolution approaches (such as the minimum-variance deconvolution approach, maximum-likelihood deconvolution approach, etc.) may be borrowed to construct other simulation model approaches (Appendix C). The differences among them will be their models set for the system and the methods used to determine the values of the model parameters. Whatever the approach, the simulation model has three main steps[91].

1. Setting up simulation models i.e., discretizing the PEA system and setting up discrete models such as *Input-model*(charge distribution), *IR-model*, and *Noise-model*;
2. Determining the values of the parameters of the models, mainly obtaining the discrete charge distribution;
3. Reconstructing the charge distribution from the discrete charge distribution results, which includes distinguishing surface charges from charge distribution and reconstructing the space charge distribution.

The three main steps for the point matching simulation model (PMSM) approach are detailed individually in Section 3.3.2, Section 3.3.3 and Section 3.3.4.

3.3.2 Step 1: Setting up Simulation models

“Models can be constructed for different purposes. For complex models, it is common that the equations are not explicitly expressed in closed form. The model might then only exist as a computer program that is used for simulation. Such models can be called simulation models.” [84]

The objectives in setting up the simulation model is to simulate the surface charges σ_1 and σ_2 , and the space charge distribution $\rho(x)$, such that the simulated output signal $SV(k)$ generated by

the simulated charge distribution is close to the measured signal with minimum error or a minimum statistical measure of $SV(k) - v_{sm}(k)$. The comparison between the simulated and the measured signals can easily be done in the discrete-time domain. Therefore, the first step is to discretize the measuring PEA system. This task is accomplished by discretizing space charge distribution $\rho(x)$, system IR and output signal. Figure 3.6 shows the PEA system in the discrete-time domain in contrast to the PEA system in continuous-time domain as shown in Figure 3.4.

Consider N points equally spaced within the sample. Replace space charge distribution $\rho(x)$ with $(N+2)$ pseudo surface charges $\sigma_p(x_i)$ to simulate the actual space charge distribution, let,

$$\sigma_p(x_i) = \rho(x_i) \Delta x, \quad (i=0-N+1), \quad (3-31)$$

where $x_0=0$, $x_{N+1}=d$ and $\Delta x = x_{i+1} - x_i = d/(N+1)$. Equation (3-13) can then be written as:

$$v_{ss}(t) = \sigma_1 g(t) + \sum_{i=0}^{N+1} \sigma_p(x_i) g(t - \frac{x_i}{c_2}) + k' \sigma_2 g(t - \frac{d}{c_2}). \quad (3-32)$$

If we define $\Delta \tau = \Delta x / c_2$, then $x_i = i c_2 \Delta \tau$. Equation(3-31) can be further simplified and written as:

$$v_{ss}(t) = \sum_{i=0}^{N+1} \sigma(i \Delta \tau) g(t - i \Delta \tau), \quad (3-33)$$

where $\sigma(0) = \sigma_1 + \sigma_p(0)$, $\sigma(i \Delta \tau) = \sigma_p(x_i)$, $(i=1-N)$, and $\sigma((N+1) \Delta \tau) = k' \sigma_2 + \sigma_p(d)$.

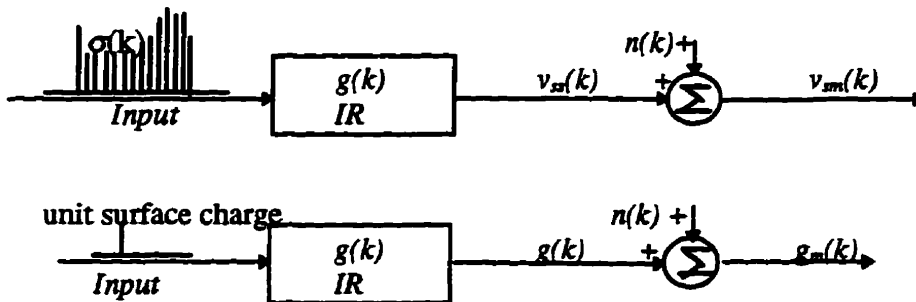


Figure 3.6 System representation of the PEA system in discrete-time domain

Discretizing $v_{ss}(t)$ and $g(t)$ also by the period $\Delta \tau$, equation(3-32) becomes:

$$v_{ss}(k\Delta\tau) = \sum_{i=0}^{N+1} \sigma(i\Delta\tau)g(k\Delta\tau - i\Delta\tau), \quad (3-34)$$

or in simpler form,

$$v_{ss}(k) = \sum_{i=0}^{N+1} \sigma(i)g(k-i). \quad (3-35)$$

Apply the Z transform to equation (3-35):

$$V_{ss}(z) = G(z)\sigma(z) \quad (3-36)$$

where $V_{ss}(z)$, $G(z)$ and $\sigma(z)$ are the Z transforms of $v_{ss}(t)$, $g(t)$ and σ sequence respectively.

Equation (3-22) gives the basic convolution model. It contains three components, i.e., *input*, *IR* and *noise*. The next step is to determine how to model the three components in the designated simulation model approach.

1) *Input-model:*

The information of charge distribution is contained in the *Input*. From equation(3-35), the *Input* is actually:

$$Input = \sigma(k) = \sum_{i=0}^{N+1} \sigma(i)\delta(k-i) \quad (3-37)$$

The PMSM approach uses equation (3-37)(i.e. the $\sigma(k)$ sequence directly as the input model). When a nonlinear detection and optimization process is used for “*More Improvement*” of the charge distribution results(as shown in Figure 3.8), the input σ sequence is modeled as an event sequence $q(k)$ times an amplitude sequence $d(k)$ as shown in equation (3-38).

$$\sigma(k) = d(k)q(k) \quad (3-38)$$

If other deconvolution simulation model approaches are set-up, for example, the minimum variance deconvolution approach, the equation (3.37) $\sigma(k)$ may be used and assumed to be a Gaussian white sequence with zero mean and a certain variance. If the maximum likelihood

deconvolution approach is used, the equation (3-38) is used and considered as a Bernoulli-Gaussian white sequence, which means that $q(k)$ denotes an element of the Bernoulli sequence, and $d(k)$ an element of the Gaussian sequence. It is necessary to investigate whether the actual charge distribution $\sigma(k)$ or $q(k)$ and $d(k)$ can be regarded as an Gaussian sequence or Bernoulli sequence before one can apply these two well-known deconvolution approaches. This is one of the main reasons that the minimum variance deconvolution and the maximum likelihood deconvolution approach are not attempted in this research.

2) *IR-model:*

Equation (3-18) gives the *IR* for continuous system, i.e. $IR=g(t)$. The sampled values of the *IR*(or $g(t)$) by $\Delta\tau$ are denoted $g(0), g(1), g(2), \dots$, as described in equation (3-34). One model for *IR* is to use its sample values directly. This is called a moving average(MA) model. Usually, *IR* is of finite length, i.e. $g(k)=0$ (or $\neq 0$) when $k \leq m_0$ or $k \geq m_0+M$, where m_0 acts as a delay. Then,

$$\begin{aligned} G(z) = Z(g(t)) &= \sum_{n=-\infty}^{\infty} g(n)z^{-n} \\ &= 0 + \frac{g(m_0+1)}{z^{m_0+1}} + \frac{g(m_0+2)}{z^{m_0+2}} + \dots + \frac{g(m_0+M)}{z^{m_0+M}}. \end{aligned} \quad (3-39)$$

The parameters of the moving average model are $g(m_0+1), g(m_0+2), \dots, g(m_0+M)$. Although they may not be exactly determined due to the presence of noise, the number M will be known as $g_m(m_0+1), g_m(m_0+2), \dots, g_m(m_0+M)$ are measured and known. The PMSM approach as presented in this thesis uses the MA model for the system *IR*. To build up MA model from the measured signal, one need to choose the proper delay m_0 , such that $g(m_0)=0$ while $g(m_0+1) \neq 0$. Due to the presence of noise, the chosen delay from the measured signal may not satisfy the above conditions. If the delay is chosen at an earlier point, $g(m_0+1)$ (which cannot be zero) is around zero, the simulation results can be very unstable. If the delay is chosen at a later point, $g(m_0)$ (which should be zero) is not zero, the information of the system before the chosen m_0 will be lost. Therefore, for the PMSM, the delay will be adjusted for better results.

There are many other ways to model IR , for example using the autoregressive-moving average (ARMA) model which models the Z -transform of IR as a ratio of two polynomials, i.e.,

$$G(z) = \frac{b_1 z^{n-1} + b_2 z^{n-2} + \dots + b_{n-1} z + b_n}{z^n + a_1 z^{n-1} + \dots + a_{n-1} z + a_n}. \quad (3-40)$$

An ARMA model is described by $2n$ parameters (a_1, a_2, \dots, a_n and b_1, b_2, \dots, b_n) which can be the smallest number of independent parameters. Generally, the number of parameters that describe the ARMA model, namely $2n$, is much smaller than the number M . For other deconvolution approaches, for example, the minimum variance deconvolution and the maximum likelihood deconvolution approaches, using the ARMA model may be better in order to reduce the dimension of the matrix involved and to speed up the computation. However, for PMSM approach, because the relationships used to obtain the σ sequence are simple and straightforward, the MA model is considered easier to apply.

3) *Noise-model:*

The *Noise* in the PMSM is assumed to be additive, zero mean, white, and Gaussian. The symbol $n(k)$ is used to denote an element of this sequence. For other deconvolution approaches, for example, the minimum variance deconvolution and the maximum likelihood deconvolution, the *Noise* is also modeled as an additive, zero mean, white, and Gaussian sequence.

It is necessary to mention that the simulation model presented above neglects many realistic and important effects that are often present in practical applications. These effects can be included in the simulation model, but at the expense of complexity. For example, the attenuation and dispersion effects, if they are not compensated for, will produce false values for the resulting σ impulse sequence. Compensation is usually achieved by applying a time-varying gain factor to the data[82,83]. The simulation model can be modified in a very straightforward manner to one that includes time-varying and/or nonstationary effects[82]. In addition, other effects may be involved, such as colored measurement noise, and recorded signals distorted by a bandpass filter, etc.. They can also be included in the simulation model if their characteristics are known.

3.3.3 Step 2: Obtaining σ Sequence

This step is the core of the simulation model methods. Every set-up simulation model approach may have its own way to determine its model parameters. However, the goal of each approach is to obtain the discrete input: σ sequence or called σ impulse train. The way in which the PMSM is used to obtain σ sequence is shown below.

According to the models that are set up for the PMSM, one can write the following relationships for the measured output signals:

$$\begin{cases} v_{sm}(k) = v_{ss}(k) + n(k) = \sigma(k) * g(k) + n(k) \\ g_m(k) = g(k) + n(k) \end{cases} \quad k=1, 2, 3, \dots, N+2 \quad (3-41)$$

If noise is very small and negligible, i.e., $n(k)=0$, one can directly have the relationship:

$$v_{sm}(k) = \sigma(k) * g_m(k) \quad (3-42)$$

due to:

$$\begin{cases} v_{sm}(k) = v_{ss}(k) = \sigma(k) * g(k) \\ g_m(k) = g(k) \end{cases} \quad (3-43)$$

If $n(k)$ is not negligible, a “Noise reduction process”, as shown in Figure 3.8, is necessary. Since the noise $n(k)$ is assumed to be additive with zero mean, white, and Gaussian sequence, it is proposed to apply an anti-causal, zero-phase filter such that the noise sequence can be minimized and neglected. The processing scheme is shown in Figure 3.7.

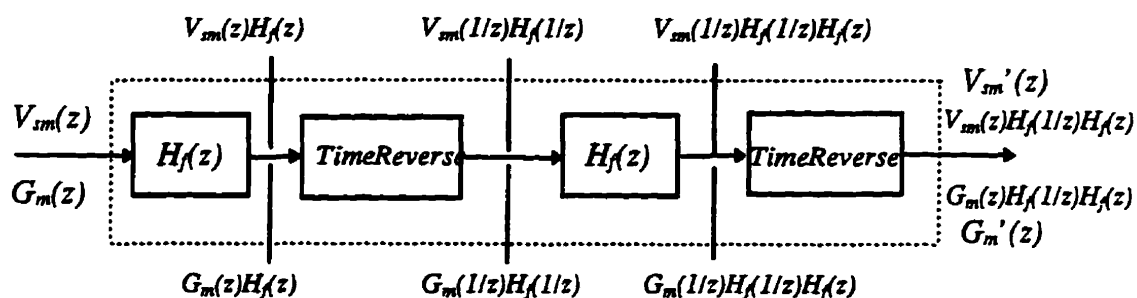


Figure 3.7 Processing scheme of anti-causal, zero-phase filter implementation

The relationship of the output after the filter implementation is:

$$\begin{cases} v_{sm}'(k) = \sigma(k) * g(k) * h_r(k) + n(k) * h_r(k) = \sigma(k) * g(k) * h_r(k) \\ g_m'(k) = g(k) * h_r(k) + n(k) * h_r(k) = g(k) * h_r(k) \end{cases} \quad (3-44)$$

where $H_r(z)$ stands for $H_f(1/z)H_f(z)$, the equation (3-44) is correct on the condition that $n(k) * h_r(k)$ is negligible comparing to $g(k) * h_r(k)$ and $\sigma(k) * g(k) * h_r(k)$. Since $n(k)$ is an additive, zero mean, white and Gaussian sequence, $H_f(z)$ is chosen to be a certain point averaging FIR filter. Best results are proposed to occur when the sequences $v_{sm}(k)$ and $g_m(k)$ have a length at least three times the filter order and when the sequences tapers to zero on both edges.

After the filtering, one can have the similar relationship as equation (3-42):

$$v_{sm}'(k) = \sigma(k) * g_m'(k) \quad (3-45)$$

Applying the Z transform to equation (3-44), one can obtain[91]:

$$V_{sm}'(z) = [0 + \frac{g_m'(m_0+1)}{z^{m_0+1}} + \frac{g_m'(m_0+2)}{z^{m_0+2}} + \dots + \frac{g_m'(m_0+M)}{z^{m_0+M}}] \sigma(z) \quad (3-46)$$

The difference equation that represents the system is:

$$v_{sm}'(m_0+k) = g_m'(m_0+1)\sigma(k-1) + g_m'(m_0+2)\sigma(k-2) + \dots + g_m'(m_0+M)\sigma(k-M) \quad (3-47)$$

From this difference equation, one can get the relationship:

$$\begin{cases} v_{sm}'(m_0+1) = g_m'(m_0+1)\sigma(0) \\ v_{sm}'(m_0+2) = g_m'(m_0+1)\sigma(1) + g_m'(m_0+2)\sigma(0) \\ v_{sm}'(m_0+3) = g_m'(m_0+1)\sigma(2) + g_m'(m_0+2)\sigma(1) + g_m'(m_0+3)\sigma(0) \\ \dots \\ v_{sm}'(m_0+N+2) = g_m'(m_0+1)\sigma(N+1) + g_m'(m_0+2)\sigma(N) + \dots + g_m'(m_0+N+2)\sigma(0) \end{cases} \quad (3-48)$$

Therefore,

$$\left\{ \begin{array}{l} \alpha(0) = \frac{v_{sm}'(m_0+1)}{g_m'(m_0+1)} \\ \alpha(1) = \frac{v_{sm}'(m_0+2) - \alpha(0)g_m'(m_0+2)}{g_m'(m_0+1)} \\ \alpha(2) = \frac{v_{sm}'(m_0+3) - \alpha(1)g_m'(m_0+2) - \alpha(0)g_m'(m_0+3)}{g_m'(m_0+1)} \\ \dots \\ \alpha(N+1) = \frac{v_{sm}'(m_0+N+2) - \alpha(N)g_m'(m_0+2) - \dots - \alpha(0)g_m'(m_0+N+2)}{g_m'(m_0+1)} \end{array} \right. \quad (3-49)$$

Similar equations can be obtained in terms of $v_{sm}(k)$ and $g_m(k)$ if the Z transform is applied to equation(3-42) for the case that noise is very small and negligible.

This method is called point matching because the obtained σ sequence in convolution with $g_m'(k)$ (or $g_m(k)$ when noises are negligible) matches all the discrete points of $v_{sm}'(k)$ (or $v_{sm}(k)$), $k=1, 2, \dots, N+2$. Although equations (3-46)-(3-49) follow the deterministic deconvolution procedure, the direct matching approach is not a deterministic deconvolution, not only because the noise reduction(pre-filtering) process minimizes the noise effect but mostly because one has the freedom to adjust delay m_0 such that $g_m'(m_0+1)$ (or $g_m(m_0+1)$) is significant for a stable and acceptable σ sequence. Therefore, it is acceptable if there is still some noise corrupted in $g_m'(k)$ and $v_{sm}'(k)$ (or $g_m(k)$ and $v_{sm}(k)$). Besides, the σ sequence obtained this way can be used as an initial sequence to start a nonlinear detection and optimization process(NDOP) for "More Improvement" of the charge distribution results. The NDOP is conducted in the 3rd simulation model step.

3.3.4 Reconstructing Space Charge Distribution $\rho(x)$

The signal outputs of $v_s'(t)$ and $g(t)$ from the digital oscilloscope are in discrete forms. If Δt stands for the signal sample duration from the oscilloscope, $\Delta \tau$ is equal to an integer number times Δt . This integer number is the step used in the simulation. If Δ denotes the step, the σ

sequence, $\sigma(j)(j=0-N+1)$, under step Δ can be obtained. If the simulation step is changed to another step, for example Δ' , one can obtain another σ sequence, $\sigma'(j')(j'=0-N'+1)$. The definition of the pseudo surface charges suggests that the densities $\sigma_\rho(x_i)$ are almost proportional to the step, while the real surface charges σ_1 and σ_2 will not change their values when the step is changed. The presence of surface charges can then be extracted from the two σ sequences.

The surface charges σ_1 , σ_2 , and pseudo surface charges $\sigma_\rho(0)$ and $\sigma_\rho(d)$ can be determined by solving:

$$\begin{cases} \sigma_1 + \sigma_\rho(0)\Delta = \sigma(0) \\ \sigma_1 + \sigma_\rho(0)\Delta' = \sigma'(0) \\ k' \sigma_2 + \sigma_\rho(d)\Delta = \sigma(N+1) \\ k' \sigma_2 + \sigma_\rho(d)\Delta' = \sigma'(N'+1) \end{cases} \quad (3-50)$$

When σ_1 , σ_2 , and the pseudo surface charges $\sigma_\rho(0)$ and $\sigma_\rho(d)$ are known, one can take σ_1 and σ_2 out and leave only the pseudo surface charge sequence $\sigma_\rho(0)$, $\sigma_\rho(1)$, ..., $\sigma_\rho(x_i)$, ..., and $\sigma_\rho(d)$. The space charge densities within the sample at each step point can be determined from:

$$\rho(x_i) = \frac{(N+1)\sigma_\rho(x_i)}{d} = \frac{\sigma(i)}{c_2\Delta\tau} = \frac{1}{\Delta} \cdot \frac{\sigma(i)}{c_2\Delta\tau}. \quad (3-51)$$

A data reconstructor such as a zero-order hold can then be applied to obtain the space charge density between x_i to x_{i+1} , where $i=0-N$. Thus, the continuous space charge distribution in the sample is obtained. Since the results after zero-order hold have some discontinuity, a waveshaper or smoother can be applied to make the space charge distribution smooth. This can be achieved using a zero-phase wavelet convoluted with the space charge distribution[87]. The anti-causal zero-phase filter described in Section 3.3.3 is used in the thesis. When space charge distribution is obtained, one can put σ_1 and σ_2 back in the position of 0 and d to get the total charge distribution, i.e. *"the Simulated Charge Distribution"* as called in Figure 3.8.

Since the simulated charge distribution is continuous, it is possible to discretize it in a very small step such as $\Delta=1$, the sampling rate. The obtained σ sequence is denoted as $\sigma^{(0)}$. Then, if the system IR-model sampled at $\Delta=1$ is applied, one can obtain the simulated output:

$$SV(k) = \sum_{i=1}^{N_m} \sigma^{(0)}(k) g_m'(k-i) \quad (3-52)$$

where, $\sigma^{(0)}(k)$ denotes the charge distribution sampled at $\Delta=1$, $g_m'(k)$ denotes the system impulse response sampled at $\Delta=1$, and N_m denotes the total sample points from 0-d when $\Delta=1$. Then, one can compare $v_{sm}'(k)$ with $SV(k)$ and see if the difference between the two is small and charge distribution is acceptable. If $F(k)$ is used to stand for $[SV(k)-v_{sm}'(k)]$, the best result is that $F(k)$ is small, compared to the noise level, and white, containing no more charge distribution information. If $F(k)$ is not small and the charge distribution based on common knowledge is not acceptable, one needs to adjust the delay m_0 and/or simulation step (Δ and/or Δ') and go back to Section 3.3.3 (the “*Point Matching Deconvolution*” as called in Figure 3.8) to obtain a new σ sequence. If $F(k)$ is small and the charge distribution is acceptable, “*the simulated charge that represents the actual charge in specimen within given tolerance*”, as called in Figure 3.8, is obtained.

As will be shown in Chapter 4, the results obtained from the above processes usually are already better than those obtained from the DM and the DCON, and can be output to generate “*the space charge distribution obtained by the simulation model*” by deducting the surface charges σ_1 and σ_2 from position 0 and d (from “*the simulated charge that represented the actual charge in specimen within given tolerance*”). Additionally, for the PMSM approach, the already mentioned nonlinear detection and optimization process (NDOP) can be applied if one wants “*More Improvement*” of the results. After the nonlinear detection and optimization process, the most significant σ sequence, $\sigma'(k)$, is obtained. The $\sigma'(k)$ sequence can be used to construct the “*simulated charge distribution*” and give the improved “*space charge distribution obtained by the simulation model*”. The described procedures of the point matching simulation model is summarized and shown in Figure 3.8.

The NDOP proposed in this research to obtain the most significant σ sequence contains three main steps, the threshold detection, the single most-likely replacement (SMLR) detection, and the nonlinear least-square optimization. Due to the fact that the NDOP is very time-consuming, the NDOP has only been applied to the four sets of synthetic signals instead of

experimental signals. The procedures of the NDOP and the results of applying one run of NDOP to the 2nd, the 3rd, and the 4th sets of synthetic signals are detailed in Appendix D. The results of applying one run of NDOP to the 1st set of synthetic signals are shown in Chapter 4.

3.3.5 Discussions

The application of the simulation model to the uniform field space charge distribution measurements improves the resolution of the obtained charge distribution up to the sampling interval (when $\Delta=1$) instead of the duration of system IR in the DM. Surface charges may be distinguished from the σ sequences when two simulation steps are used. The accuracy of the space charge distribution is improved especially near the electrode-sample interfaces. The improvement of resolution and accuracy is verified in Chapter 4. Comparing two simulation step results, one can have more confidence about the correctness of the obtained space charge distributions. However, the computation time is increased, especially for the application of NDOP. If the step is very small such that $\Delta\tau \ll d/c_2$, using the continuous nature of the space charge, one can approximately obtain:

$$\begin{cases} \sigma_{\rho}(0) = \sigma(1) \\ \sigma_1 = \sigma(0) - \sigma(1) \\ \sigma_{\rho}(d) = \sigma(N) \\ k' \sigma_2 = \sigma(N+1) - \sigma(N) \end{cases} \quad (3-53)$$

Therefore, one step is enough. Equations (3-51) and (3-53) are used to construct space charge distribution from the σ' sequence obtained from the NDOP.

Stochastic design procedures can handle both the signal-noise ratio effects and the bandwidth effects better than the deterministic design procedures[82]. There are two types of stochastic deconvolution operations: linear or nonlinear. Generally, linear operations lead to more smeared out resolution functions than do nonlinear deconvolution operations. Hence, the nonlinear processes inside the PMSM such as taking surface charge out before smoothing and adding a detection process before the least square optimization process is attempted in order to obtain high resolution charge distribution results from the detected signals.

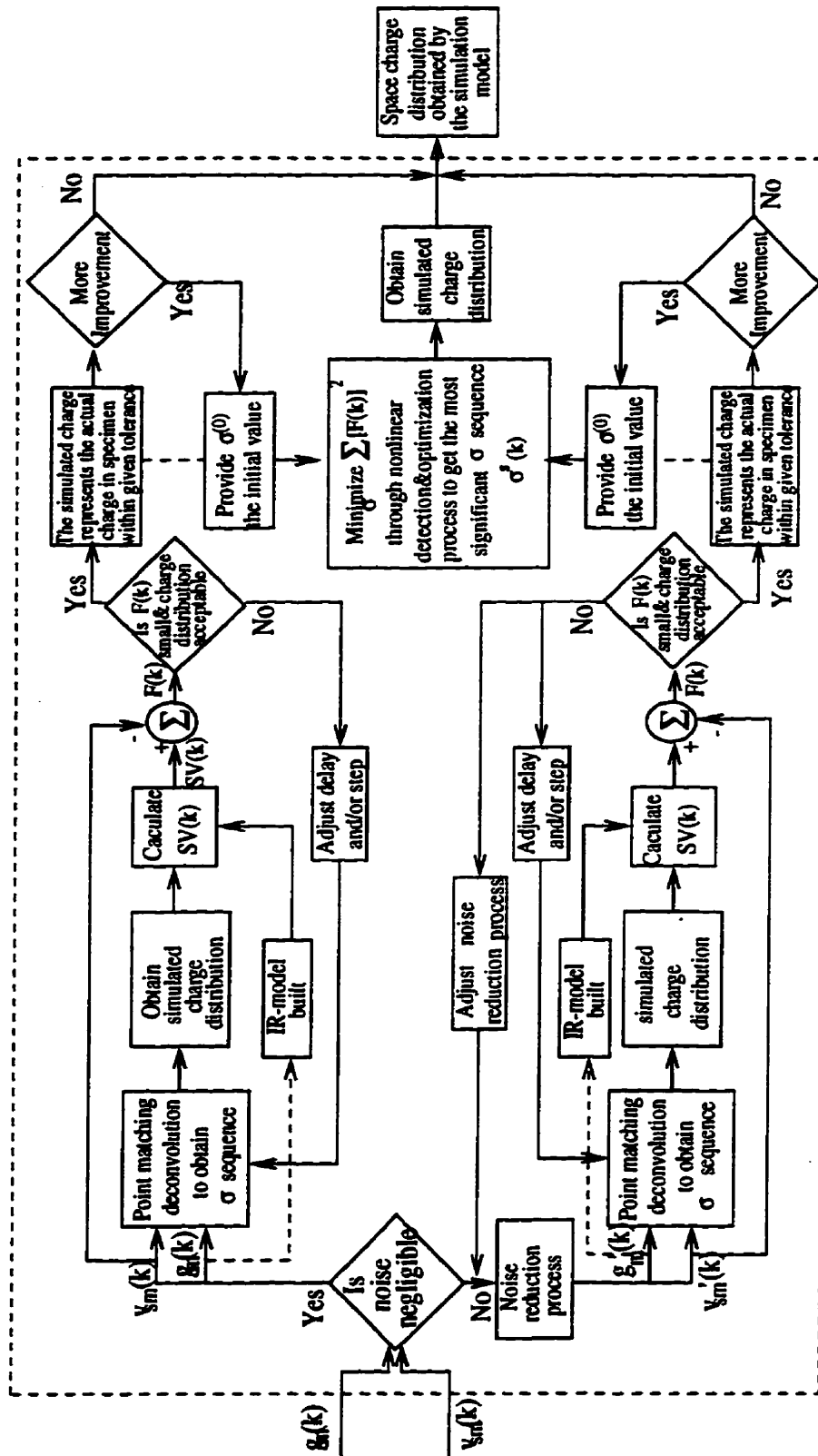


Figure 3.8 The algorithm of the point matching simulation model (PMSM)

3.4 NONUNIFORM FIELD SIMULATION MODELS

3.4.1 Introduction

Space charges have important effects upon treeing, aging and breakdown processes in solid dielectrics[6-7]. Many efforts have been made to develop measuring techniques for charge distributions in solids, especially in polymers. The pulsed electro-acoustic method(PEA) and pressure wave propagation method(PWP) have been used to measure charge distributions under plane-plane and coaxial electrode configurations[72-79]. To the author's best knowledge, there is almost no approach in the literature that measures dynamic changes of space charge distributions in solids under needle-plane electrode configurations except to measure the total injected space charge and its relative position[20,21,24]. In practice, treeing, aging and breakdown start at the point of local field enhancement. Needle-plane electrode configuration is usually adopted to simulate this extreme field situation. This section shows the attempt to further develop the PEA method to measure charge distributions under needle-plane electrode configurations. This measurement is important but difficult due to the nonuniformity of the electric field. Based on the generation and propagation properties of the pressure wave, along with the electric field calculation, a measuring principle is proposed in Section 3.4.2. With the application of the simulation model to process the obtained signals discussed briefly in Section 3.4.3, it seems possible to measure space charge distribution in a nonuniform field.

3.4.2 Principle

A principle PEA setup for a needle-plane electrode configuration is shown in Figure 3.9[93]. Assume there are space charges $\rho(x,r,\theta)$ distributed inside the dielectric, surface charges $\sigma_1(0,r,\theta)$ on the lower interface and surface charges $\sigma_2(d,0,0)$ concentrated at the needle tip. When a short duration electric pulse $v_p(t)$ is applied, an electric field due to the pulse $e_p(x,r,\theta,t)$ will be established. Each charge is then subjected to the electric stress, causing a displacement from its original position and generating a pressure wave. It is assumed that the dielectric is a

homogenous, isotropic and elastic solid. When the wavelength of the pressure wave is much greater than the dimension of the charge location and the acoustic pressures are measured at distances far from the source, each charge location acts as a simple source. The generated pressure wave is non-directional and transmits in all directions as a spherical acoustic wave[85].

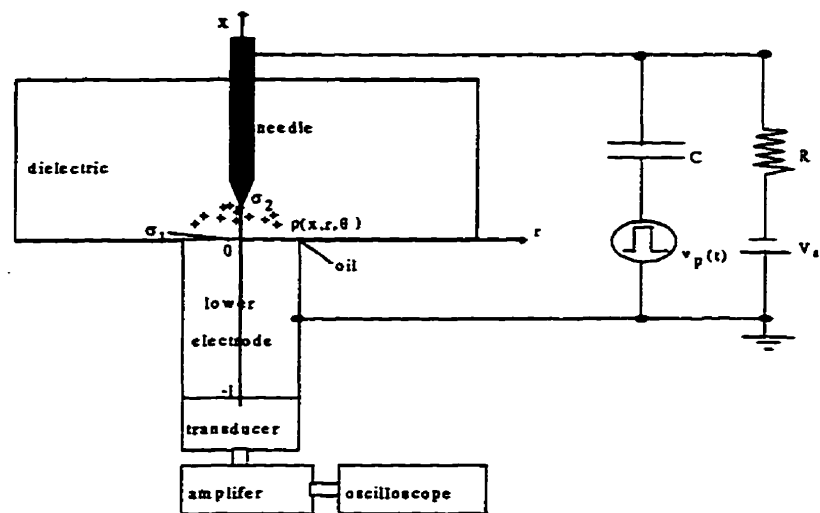


Figure 3.9 Principle of the PEA method for needle-plane electrode configuration

The amplitude of the pressure is then proportional to the source strength and reduces inversely in proportion to the distance from the source when the wave propagates from it[85].

$$p = p_1 \frac{1}{a} \quad (3-54)$$

where p is the acoustic pressure at a distance a from the source, p_1 is the acoustic pressure at $a=1$. According to (3-54), the acoustic pressure in the source itself would become infinite, which is just as unreal as a point source. Real sources always have finite dimensions and, in proximity to them, the acoustic wave is usually not strictly spherical. Equation (3-54) therefore applies only to very large distances compared with the dimensions of the source. When this condition is not yet fulfilled at a distance 1, as mentioned in [86], p_1 can refer merely to a quantity specified purely for determining the strength of the source.

Figure 3.10 shows refraction of a spherical wave at a plane interface for the longitudinal wave. Only rays which are almost perpendicular still intersect each other after refraction at a virtual center O' . The refracted wave can be regarded as a spherical wave only in this particular zone[86]. The relationships are:

$$\frac{d_2}{d_1} = \frac{\delta_1}{\delta_2} = \frac{c_2}{c_1} \quad (3-55)$$

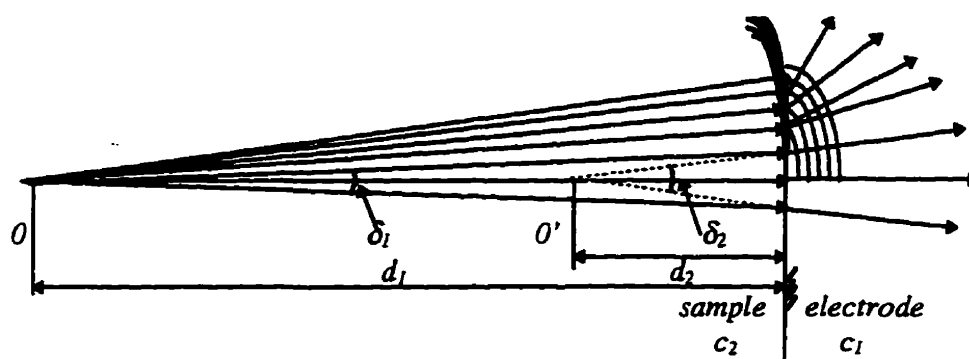


Figure 3.10 Refraction of a spherical wave at a plane interface

The angles of divergence of narrow beams incident at right angles are in the ratio of the acoustic velocities. The pattern of the acoustic pressure in the second material is determined by the virtual center O' from which the distance a in Equation (3-54) must be calculated. For Figure 3.9, if the source is at x , the virtual center will be at $c_2 x / c_1$. The distance from this virtual source to the transducer will be $l + c_2 x / c_1$.

Based on the above mentioned properties of spherical waves, a transducer with small active area is chosen. When the diameter of the transducer active area is much smaller than the length of lower electrode, according to Equation (3-55), it is reasonable to assume that only the pressure wave transmitted perpendicular to the lower dielectric-electrode interface can reach the transducer and be detected. If a 20mm in length 5mm in diameter aluminum electrode with a sound velocity above 5000m/s, for example, is placed on a dielectric polymer with a sound velocity around 2000m/s, then the maximum detectable injection angle is less than

5.6°. Besides, with a small active area transducer, one can assume that the space charges are distributed uniformly within an area equal to the transducer active area at arbitrary x from 0 to d . Thus, waves with the same x coordinates will reach the transducer at the same time. The three dimension charge distributions can be simplified to one dimension $\rho(x)$, $\sigma_1(0)$, and $\sigma_2(d)$ within the transducer active area[93].

Since the source strength for a simple acoustic source is equal to the surface integral of the scalar product of the vector velocity amplitude and its corresponding surface element[85], it can be deduced that the amplitude of pressure wave $p_x(t)$, due to $\rho(x)$ detected by the transducer, is proportional to the surface integral of the x component of the electric stress due to the pulse that space charges are subjected to.

$$p_x(t) = \frac{k}{l + \frac{c_2}{c_1}x} \left[\int_0^{r_a} \frac{2r}{r_a^2} e_{px}(x, r, t - \frac{x}{c_2} - \frac{l}{c_1}) dr \right] \rho(x) dx \quad (3-56)$$

where k is a constant, r_a is the radius of transducer active area, l is the length of the lower electrode, c_1 , c_2 are the sound velocity of the lower electrode and the dielectric respectively, and $e_{px}(x, r, t)$ is the x component of the electric pulse field at an arbitrary (x, r) point (variable θ is omitted due to the axial symmetry of the electric pulse field).

For surface charges $\sigma_2(d)$, its pressure wave $p_d(t)$ is:

$$p_d(t) = \frac{k k'}{l + \frac{c_2}{c_1}d} \left[\int_0^{r_a} \frac{2r}{r_a^2} e_{px}(d, r, t - \frac{d}{c_2} - \frac{l}{c_1}) \sigma_2(d) + \frac{1}{2} \epsilon_0 \epsilon_r [e_{px}(d, r, t - \frac{d}{c_2} - \frac{l}{c_1})]^2 \right] \quad (3-57)$$

where r , is the radius of the needle tip, k' is a constant.

For surface charges $\sigma_1(0)$, its pressure wave $p_0(t)$ is:

$$p_0(t) = \frac{k}{l} \left[\int_0^{r_a} \frac{2r}{r_a^2} e_{px}(0, r, t - \frac{l}{c_1}) dr \sigma_1(0) - \frac{1}{2} \epsilon_0 \epsilon_r \int_0^{r_a} \frac{2r}{r_a^2} e_{px}^2(0, r, t - \frac{l}{c_1}) dr \right] \quad (3-58)$$

Applying the superposition principle, the total pressure wave $p(t)$ detected by the transducer is:

$$p(t) = p_0(t) + p_p(t) + p_d(t) \quad (3-59)$$

where,

$$p_p(t) = \int_0^d \frac{k}{l + \frac{c_2}{c_1}x} \left[\int_0^r \frac{2r}{r_a^2} e_{px}(x, r, t - \frac{x}{c_2} - \frac{l}{c_1}) dr \right] \rho(x) dx \quad (3-60)$$

At this stage, the electric pulse field $e_p(x, r, \theta, t)$ contains both space and time variables. It is more convenient to separate them. This can be done under the assumption that the application of the electric pulse voltage will not change the space charge distribution [Appendix A-1]. If $Ce(x, r, \theta)$ stands for the electric field at a general point (x, r, θ, t) due to the application of a unit voltage ($V_c = 1 \text{ Volt}$) in the needle-plane configuration, $e_p(x, r, \theta, t)$ can then be written as:

$$e_p(x, r, \theta, t) = \frac{v_p(t) Ce(x, r, \theta)}{V_c} = v_p(t) Ce(x, r, \theta) \quad (3-61)$$

In addition, equations (3-56)-(3-58) and (3-60) can be further simplified using the correction coefficient $C_f(x)$, which is defined as:

$$C_f(x) = \int_0^r \frac{2r}{r_a^2} Ce_x(x, r) dr, \quad (3-62)$$

where $Ce_x(x, r)$ stands for the x component of $Ce(x, r)$.

When the total pressure wave $p(t)$ reaches the transducer, the same as the uniform field case, the pressure wave will be changed by the transducer into a voltage signal. The voltage signal will be amplified and recorded as $v_s(t)$. Suppose the system that transfers $p(t)$ to $v_s(t)$ is linear time-invariant, in the time domain; then there is the convolution relationship:

$$v_s(t) = p(t) * h(t) \quad (3-67)$$

where $h(t)$ is the system transfer function (Appendix A-3).

It can also be processed using three approaches for the uniform field case to get rid of the second term in equations (3-57) and (3-58).

1. Omit the terms when they are negligible compared to the surface charges response and denote as $v_s^{(1)}(t)$.
2. subtract signals $v_s(t)$ by the signal $v_{s0}(t)$ which is obtained when no dc voltage is applied and no space charge is distributed inside the sample, and denote the subtraction as $v_s^{(2)}(t)$.
3. for general cases, apply a positive electric pulse first and get an output $v_{s+}(t)$; then we change pulse polarity to negative and get an output $v_{s-}(t)$, let $v_s^{(3)}(t) = 1/2[v_{s+}(t) - v_{s-}(t)]$.

It can be deduced that:

$$v_{ss}(t) = \left\{ \begin{array}{l} v_s^{(1)}(t) \approx v_s(t) \\ \text{or} \\ v_s^{(2)}(t) = v_s(t) - v_{s0}(t) \\ \text{or} \\ v_s^{(3)}(t) = \frac{1}{2}[v_{s+}(t) - v_{s-}(t)] \end{array} \right\} = p'(t) * h(t) \quad (3-64)$$

$$p'(t) = p_0'(t) + p_\rho'(t) + p_d'(t) \quad (3-65)$$

where,

$$p_0'(t) = \frac{k}{l} [\sigma_1(0) v_p(t - \frac{l}{c_1}) C_f(0)] \quad (3-66)$$

$$p_\rho'(t) = k \int_0^d \frac{1}{l + \frac{c_2}{c_1} x} \rho(x) C_f(x) v_p(t - \frac{l}{c_1} - \frac{x}{c_2}) dx \quad (3-67)$$

$$p_d'(t) = k' k \frac{1}{l + \frac{c_2}{c_1} d} \frac{r_s^2}{r_a^2} [\sigma_2(d) C_e(d) v_p(t - \frac{l}{c_1} - \frac{d}{c_2})] \quad (3-68)$$

The above equations are developed when both the center of the transducer and the center of the needle tip are on the x axis. More general equations are developed [Appendix B] for the transducer moved to an arbitrary position of the plane side of the sample. Principally, by moving the transducer, the three dimension charge distributions can be profiled.

3.4.3 Nonuniform Simulation Model

With equations (3-64-3.68), along with the field calculation, the space charge distribution can be originated by using the principal idea of the deconvolution procedure (DCON) or the direct method (DM). However, the disadvantages of the DCON and the DM still exist for the nonuniform case. Moreover, for the DM, it is known that the system resolution can be improved only by decreasing ΔT . However, when ΔT is decreased, the electric pulse contains more higher frequency components. Thus, the bandwidth of the transducer has to increase. A transducer with wide bandwidth not only is expensive, but also has a low transfer coefficient, which means that the transferred voltage signal is small for the same pressure. Besides, due to the higher attenuation of pressure wave in polymers at higher frequency, the amplitude of pressure waves reaching transducer diminishes too. As mentioned earlier, a transducer with a small active area is essential. Therefore, it is better to find a way to improve the resolution without decreasing ΔT , or in other words, to propose a data processing method whose resolution can be less than $c_2\Delta T$. Therefore, the simulation model is the best one to apply[93].

Suppose there are N points x_i ($i=1, 2, \dots, N$) with spacing Δx within $(0, d)$, $\Delta x = d/(N+1)$. Define $\sigma_\rho(x_i) = \rho(x_i)\Delta x$, $v_{ss}(t)$ has its discrete form:

$$v_{ss}(t) = kh(t) * \left[\frac{\sigma_1(0)}{l} C_f(0) v_p \left(t - \frac{l}{c_1} \right) + \sum_{i=0}^{N+1} \frac{\sigma_\rho(x_i) C_f(x_i)}{l + \frac{c_2}{c_1} x_i} v_p \left(t - \frac{x_i}{c_2} - \frac{l}{c_1} \right) \right. \\ \left. + \frac{k}{l + \frac{c_2}{c_1} d} \frac{r_f^2}{r_a^2} \sigma_2(d) C_{ex}(d) v_p \left(t - \frac{d}{c_2} - \frac{l}{c_1} \right) \right] \quad (3-69)$$

If applying a low DC voltage to a sample without space charge, the output processed signal $v_{ss}(t)_{DC}$ then contains only the information on the two surface charges $v_1(t)$ and $v_2(t)$.

$$v_{ss}(t)_{DC} = v_1(t) + v_2(t) \quad (3-70)$$

where,

$$v_1(t) = kh(t) * \left[\frac{\sigma_{1DC}(0)}{l} C_{DC}(0) v_p \left(t - \frac{l}{c_1} \right) \right] \quad (3-71)$$

$$v_2(t) = kh(t) * \left[\frac{k}{l + \frac{c_2}{d} \frac{r_a^2}{c_1}} \frac{r_t^2}{r_a^2} \sigma_{2DC}(d) C_{exDC}(d) v_p \left(t - \frac{d}{c_2} - \frac{l}{c_1} \right) \right] \quad (3-72)$$

The subscripts *DC* indicate values that are known and obtained from the calibrating sample.

Therefore, when $v_1(t)$ and $v_2(t)$ are separable, one can obtain $g(t)$ that is only due to σ_i :

$$g(t) = kh(t) * v_p \left(t - \frac{l}{c_1} \right) = \frac{lv_1(t)}{\sigma_{1DC}(0) C_{DC}(0)} \quad (3-73)$$

Equation (3-69) can then be written as:

$$\begin{aligned} v_{ss}(t) = & \left[\frac{\sigma_1(0)}{l} C_f(0) g \left(t - \frac{l}{c_1} \right) + \sum_{i=0}^{N+1} \frac{\sigma_\rho(x_i) C_f(x_i)}{l + \frac{c_2}{c_1} x_i} g \left(t - \frac{x_i}{c_2} - \frac{l}{c_1} \right) \right. \\ & \left. + \frac{k}{l + \frac{c_2}{d} \frac{r_a^2}{c_1}} \frac{r_t^2}{r_a^2} \sigma_2(d) C_{ex}(d) g \left(t - \frac{d}{c_2} - \frac{l}{c_1} \right) \right] \end{aligned} \quad (3-74)$$

If we define $\Delta\tau = \Delta x / c_2$, then $x_i = ic_2 \Delta\tau$. Equation(3-74) can be further simplified and written as:

$$v_{ss}(t) = \sum_{i=0}^{N+1} \sigma(i\Delta\tau) g(t - i\Delta\tau), \quad (3-75)$$

where

$$\begin{aligned} \sigma(0) &= \frac{\sigma_1(0) + \sigma_\rho(0)}{l} C_f(0) \\ \sigma(i\Delta\tau) &= \frac{\sigma_\rho(x_i) C_f(x_i)}{l + \frac{c_2}{c_1} x_i} \\ \sigma((N+1)\Delta\tau) &= \frac{k}{l + \frac{c_2}{d} \frac{r_a^2}{c_1}} \frac{r_t^2}{r_a^2} \sigma_2(d) C_{ex}(d) + \frac{\sigma_\rho(d) C_f(d)}{l + \frac{c_2}{c_1} d} \end{aligned} \quad (3-76)$$

Discretizing $v_{ss}(t)$ and $g(t)$ also by the period $\Delta\tau$, equation(3-76) becomes:

$$v_{ss}(k\Delta\tau) = \sum_{i=0}^{N+1} \sigma(i\Delta\tau) g(k\Delta\tau - i\Delta\tau), \quad (3-77)$$

or in simpler form,

$$v_{ss}(k) = \sum_{i=0}^{N+1} \sigma(i)g(k-i). \quad (3-78)$$

Obviously, equations (3-75), (3-77) and (3-78) have the same forms as equations (3-32)-(3-34) respectively. Therefore, the simulation model discussed in Section 3.3 to obtain the σ sequence can be used to obtain the nonuniform field σ sequence. The only difference is that, after the σ sequence is obtained, one needs to use equation (3-76) to originate the $\sigma_1(0)$, $\sigma_p(x_i)$ ($i=0-N+1$), and $\sigma_2(d)$. The same as in the uniform field case, surface charges $\sigma_1(0)$ and $\sigma_2(d)$ can be distinguished using two steps or one step when $\Delta\tau \ll d/c_2$; the space charge distribution can be reconstructed by a hold device; and a zero-phase filter can be applied to smooth the space charge distribution.

3.4.4 Discussions

The proposed nonuniform space charge distribution measuring technique enables the measurement of space charge distribution under needle-plane configurations. Since the technique is based on the generation, propagation and detection of the pressure wave, it can be applied to any type of electrode system as long as its electric field of the electrode system (free of space charges) at 1 V voltage application is known or can be calculated. The proposed simulation model makes it possible to obtain enough resolution with the application of a wider electric pulse.

The equations developed in Section 3.4.2 and Section 3.4.3 are for the special case that the center of the transducer is on the x axis. One can assume the charge distribution is in one dimension for the uniform field case. However, one cannot make the assumption for the nonuniform field case, and the charge distribution is in three dimensions. Therefore, equations must be extended for the general case that the transducer is put in an arbitrary position on the plane side of the needle-plane electrode configuration. For the continuity of the thesis, the equations developed for the transducer in an arbitrary position are presented in Appendix B. With the simulation model, along with space charge free electric field calculation, the three dimension charge distribution under needle-plane electrode configuration can be obtained.

CHAPTER 4

SIMULATION MODEL CRITIQUE

4.1 INTRODUCTION

The purpose of this research is to develop an improved measuring technique for space charge distribution measurement. However, to achieve this aim, it would not be practical to compare this technique with the other measuring techniques experimentally; and there is no standard space charge distribution and no analytical tool to calculate accurately the charge distribution inside the specimen. Therefore, two steps of verification are used and discussed in Section 4.2 and Section 4.3 respectively.

The first is a simulation verification to show, from an analytic point of view (using four sets of synthetic signals) that:

1. the proposed method, the point matching simulation model (PMSM), is working; and
2. the PMSM method has advantages over the existing methods, the direct method (DM) and the deconvolution procedure (DCON).

The second is an experimental verification to show, from an experimental point of view (using two sets of experimental signals under uniform fields) that:

1. the PMSM is working for experimental signals; and
2. the procedures proposed for the PMSM method as applied to experimental signals are working.

The two verifications suggest that the PMSM method improves both the resolution and the accuracy of the obtained space charge distribution. An overall discussion of the results of the two verifications is then provided in Section 4.4.

4.2 COMPARISON OF DM, DCON AND PMSM METHODS FROM ANALYTIC POINT OF VIEW

4.2.1 Introduction

Four sets of synthetic signals are used to compare the DM, the DCON, and the PMSM methods from an analytic point of view. There are two reasons to use synthetic signals, as briefly mentioned in Section 4.1. Firstly, the DM requires a wide-bandwidth transducer and a short duration pulse. The transducer used in the present experiments has a bandwidth from 0.25MHz to 6MHz and has some pulse ringing. Therefore, the DM cannot be used to process the experimental signals. To compare the DM with the DCON and the PMSM, synthetic signals are necessary. Secondly, there is practically no standard space charge distribution available, and there is no analytical tool to provide the charge distribution accurately. One cannot test the accuracy of space charge measuring techniques experimentally. The synthetic signals can be generated corresponding to an assumed charge distribution and an assumed system IR ; therefore, after processing the synthetic signals with different methods, one can assess the accuracy and the resolution of these methods by comparing the space charge distribution obtained by these methods with the assumed charge distributions.

The purpose of using four sets of signals is to illustrate the effect of noise, the effect of the charge distribution, and the effect of the bandwidth of the system transfer function on the obtained space charge distributions by the three methods (the DM, the DCON, and the PMSM) methods. It is necessary to mention a small change in notation. In Chapter 3, σ sequence was denoted as $\sigma(k)$, $k=0-N+1$. For the easy application in Matlab code, σ sequence is denoted as $\sigma(k)$, but $k=1-N+2$.

Basically, two space charge distributions are assumed and used to build up the four sets of signals. One has sharp changes in charge distribution, denoted as SPD1; the other has slow changes in space charge distribution, denoted as SPD2. Figure 4.1 shows the waveshape of

SPD1. Only surface charges are distributed at the ground electrode sample interface $\sigma(1)=\sigma_1+\sigma_p(1)=\sigma_1=2C/m^2$. There are space charges $[\sigma(i)=\sigma_p(x_i)=\rho(x_i)c_2\Delta t, (i=1-300)]$ distributed inside the sample, but they existed mainly from points 180 to 240 and from points 280 to 300. Also, there are surface charges presented at the HV electrode sample interface ($\sigma_2=0.6C/m^2$). And $\sigma(300)=\sigma_2+\sigma_p(d)=\sigma_2+\rho(d)c_2\Delta t=1C/m^2$. Figure 4.2 shows the waveshape of SPD2, in which space charges are distributed all over the sample from points 1 to 261, $\sigma(1)=\sigma_1+\sigma_p(1)=-0.5C/m^2$, and $\sigma(261)=\sigma_2+\sigma_p(d)=0.44C/m^2$. The total charge, $\sum_{k=1}^{261} \sigma(k)$, is equal to zero to meet the experimental charge distribution condition for bound charges.

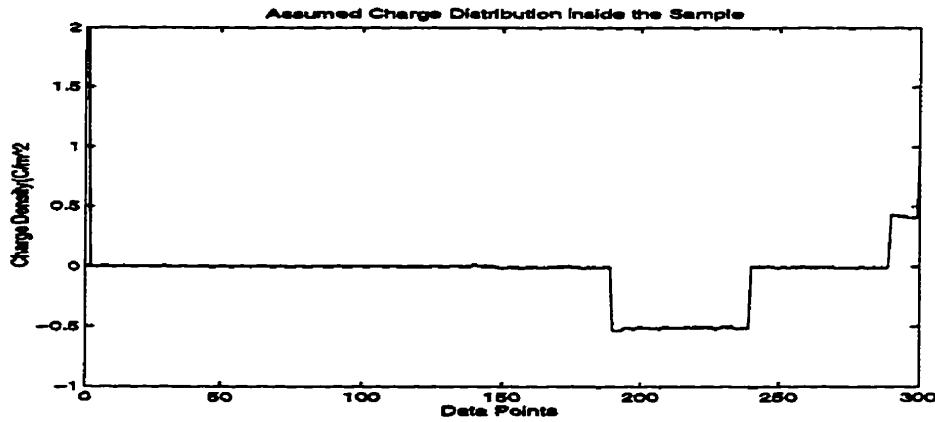


Figure 4.1 Assumed charge distribution SPD1

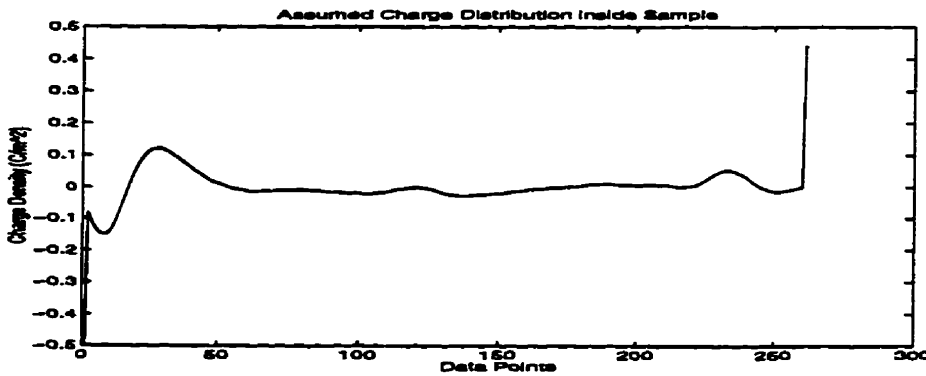
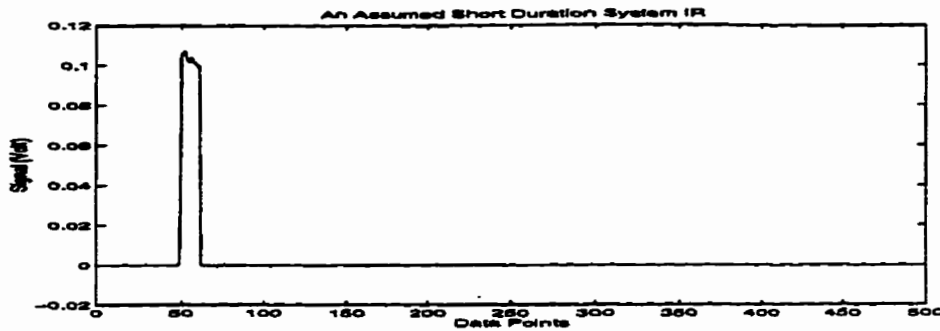
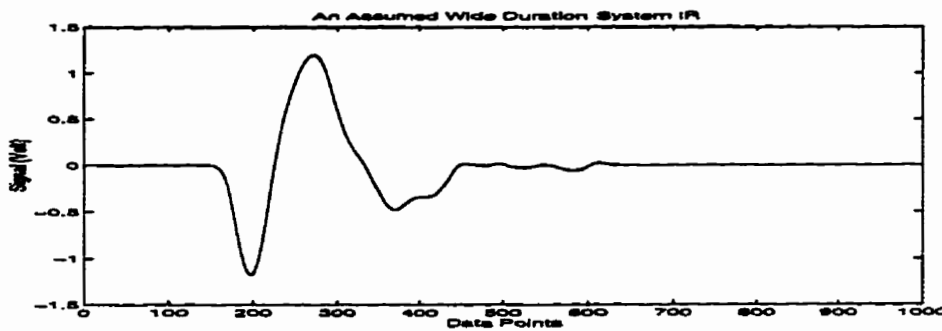


Figure 4.2 Assumed charge distribution SPD2

Two types of system $IR(g(k))$ are assumed. One has short duration, $g'(k)$, as shown in Figure 4.3; the other has wide duration, $g''(k)$, as shown in Figure 4.4. In fact, $g''(k)$ is actually the detected system IR from our PEA experimental system for the Thick HDPE specimen.

Figure 4.3 Assumed system IR, $g^s(k)$ Figure 4.4 Assumed system IR, $g^w(k)$

The noise sequence $n(k)$ is assumed to be additive, zero mean, white, and Gaussian. Its variance, Var_n , is chosen to be 5% of the maximum value of the signal without noise.

The first set of signals differs from the other three sets in that the first set is noise-free while the others are corrupted with noise. Therefore, the effect of noise can be studied. The first and the second sets of signals differ from the third and the fourth sets in that the first and the second sets use SPD1 while the third and the fourth sets use SPD2 to build up the synthetic output signals; thus the effect of space charge distribution can be observed. Finally, the fourth set of signals differs from the other three sets in that the wide duration system IR is used; thus, the effect of system IR can be compared. More specific descriptions of the four sets are listed below.

- The first (1st) set of signals uses SPD1 and $g^s(k)$ to built up noise-free synthetic output signals $v_{sm}^1(k)$ and $g_m^1(k)$:

$$\begin{cases} v_{sm}^1(k) = SPD1 * g^s(k) + 0 \times n(k) \\ g_m^1(k) = g^s(k) + 0 \times n(k) = g^s(k) \end{cases} \quad (4-1)$$

The waveshape of $v_{sm}^1(k)$ is shown in Figure 4.5. The waveshape of $g_m^1(k)$ is the same as that is shown in Figure 4.3.

- The second (2nd) set of signals uses SPD1 and $g^s(k)$ to build up the noise-corrupted synthetic output signal $v_{sm}^2(k)$ and $g_m^2(k)$:

$$\begin{cases} v_{sm}^2(k) = SPD1 * g^s(k) + n(k) \\ g_m^2(k) = g^s(k) + n(k) \end{cases} \quad (4-2)$$

The waveshapes of $v_{sm}^2(k)$ and $g_m^2(k)$ are shown in Figure 4.6 and Figure 4.7 respectively.

- The third (3rd) set uses SPD2 and $g^s(k)$ to build up a noise-corrupted synthetic signal $v_{sm}^3(k)$ and $g_m^3(k)$:

$$\begin{cases} v_{sm}^3(k) = SPD2 * g^s(k) + n(k) \\ g_m^3(k) = g^s(k) + n(k) \end{cases} \quad (4-3)$$

The waveshape of $v_{sm}^3(k)$ is shown in Figure 4.8. To reduce the work of computation, the waveshape of $g_m^3(k)$ is considered the same as $g_m^2(k)$, as shown in Figure 4.7.

- And finally, the fourth (4th) set uses SPD2 and $g^w(k)$ for the noise-corrupted synthetic signal $v_{sm}^4(k)$ and $g_m^4(k)$:

$$\begin{cases} v_{sm}^4(k) = SPD2 * g^w(k) + n(k) \\ g_m^4(k) = g^w(k) + n(k) \end{cases} \quad (4-4)$$

The waveshapes of $v_{sm}^4(k)$ and $g_m^4(k)$ are shown in Figure 4.9 and Figure 4.10, respectively.

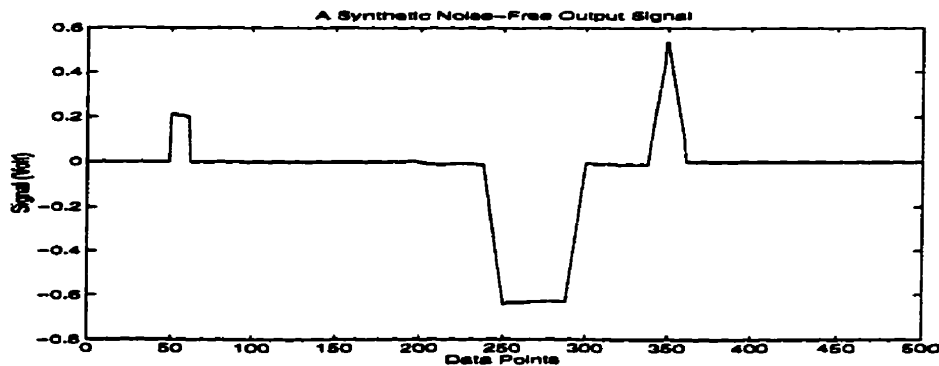


Figure 4.5 The first set output signal $v_{sm}^1(k)$

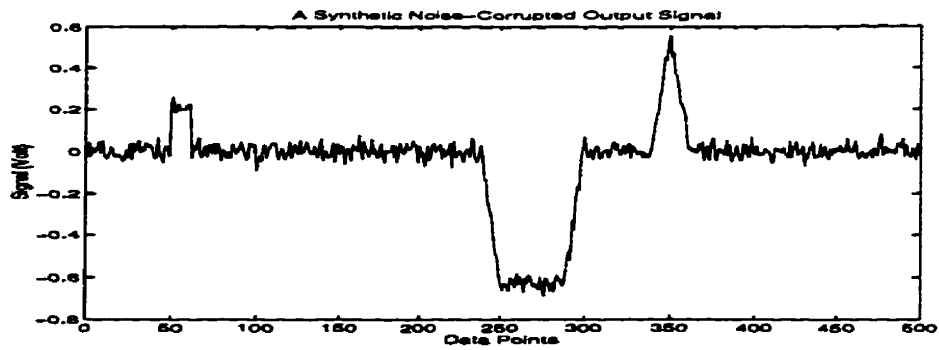


Figure 4.6 The second set output signal $v_{sm}^2(k)$

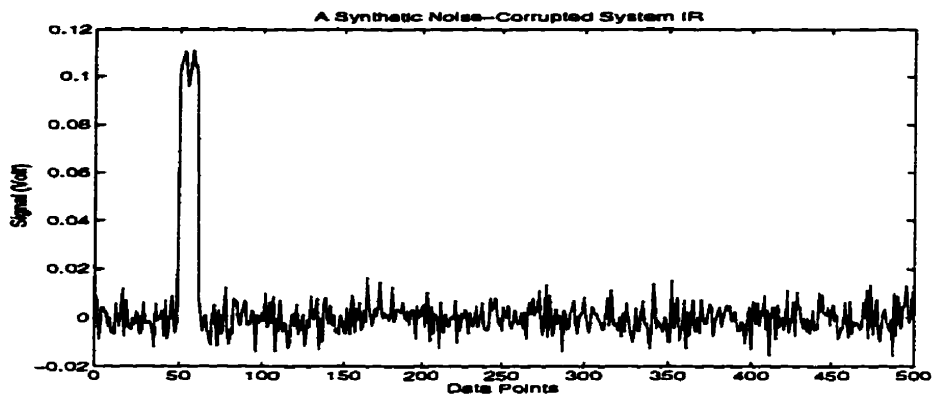


Figure 4.7 The noise-corrupted measured IR ($g_m^2(k)$ and $g_m^3(k)$)

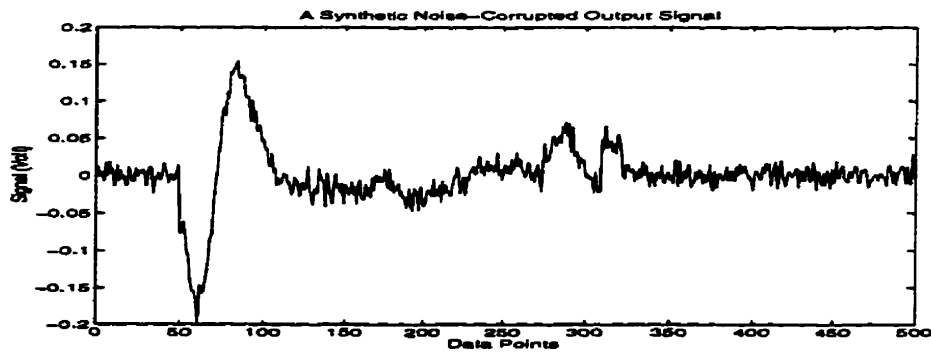


Figure 4.8 The third set output signal $v_{sm}^3(k)$

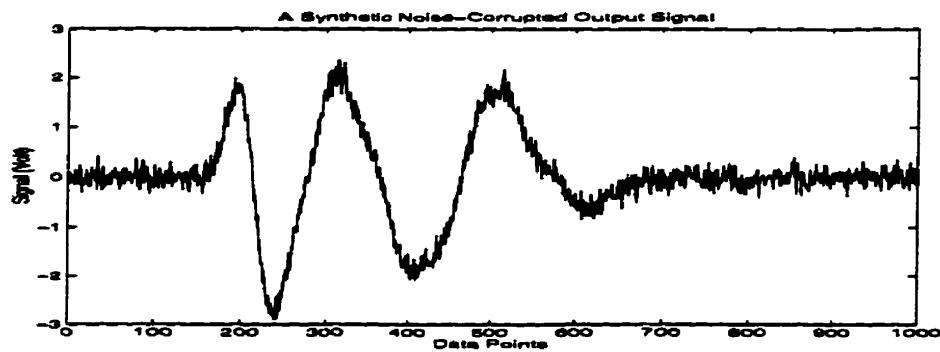


Figure 4.9 The fourth set output signal $v_{sm}^4(k)$

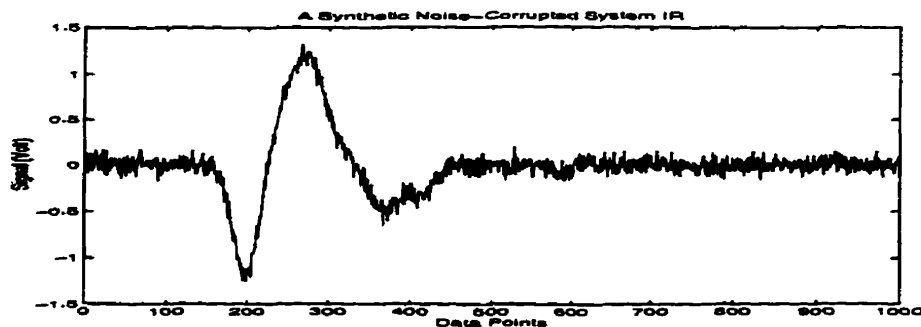


Figure 4.10 The noise-corrupted measured $IR (g_m^4(k))$

The processing results for the four sets of signals by the three methods are discussed individually in Section 4.2.2, Section 4.2.3, Section 4.2.4, and Section 4.2.5, respectively.

4.2.2 The 1st Set of Signals

The output measured signals for the 1st set are shown in Figure 4.3 ($g_m^1(k)$) and Figure 4.5 ($v_{sm}^1(k)$). No noise is added which indicates that $g_m^1(k)=g(k)$ and $v_{sm}^1(k)=v_{st}(k)$. The charge distribution results of this set of signals obtained by the DM, the DCON and the PMSM methods are shown below.

1) *The direct method(DM)*

As known in Section 2.5.4 and Section 3.2.3, the DM method believes that the measured output signal is proportional to the space charge distribution. The proportional constant is equal to 1 over the integration of system $IR(g(t))$. Figure 4.11 shows the charge distribution results obtained by the DM when m_0 is chosen at point 49. As described in Section 3.3.2, m_0 is related to the delay and refers to the point at which $g(m_0)=0$ while $g(m_0+1)\neq 0$. The difference between Figure 4.11 and 4.5 is only a linear calibration and a waveshifting. A comparison of Figure 4.11 with Figure 4.1 (the assumed charge distribution SPD1) shows that surface charges, the rapid change of space charges and the space charges distributed near the surface charges are obviously not represented well. When there is only surface charge present, the surface charge is represented as a distribution having the waveshape of the system IR. When there are space charges near surface charges, the resulting distribution is the mix of the two.

If one uses Figure 4.11 charge distribution to obtain a simulated output signal $SV(k)$, as compared in Figure 4.12, the difference between the simulated output signal $SV(k)$ and the actual measured signal $v_{sm}^I(k)$ is quite large. The difference is shown in Figure 4.13 around $\pm 0.3V$. Since the choice of m_0 is quite subjective, m_0 was adjusted around point 49. It was found that, if m_0 is chosen at points other than 49, the difference can be even larger.

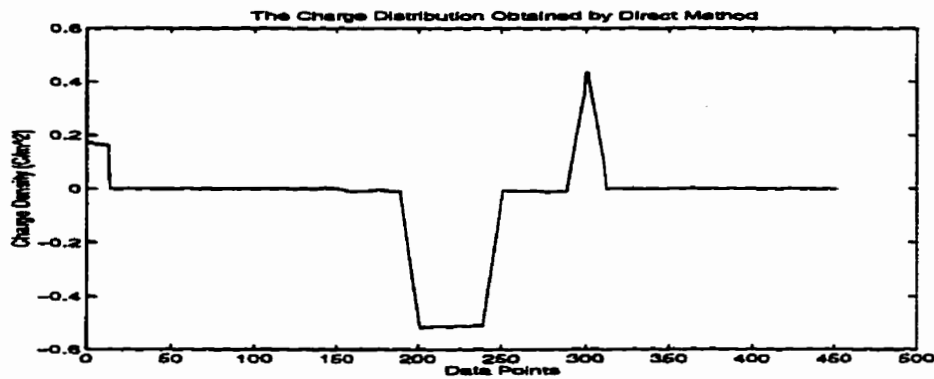


Figure 4.11 Charge distribution obtained by the DM method for the 1st set of signals

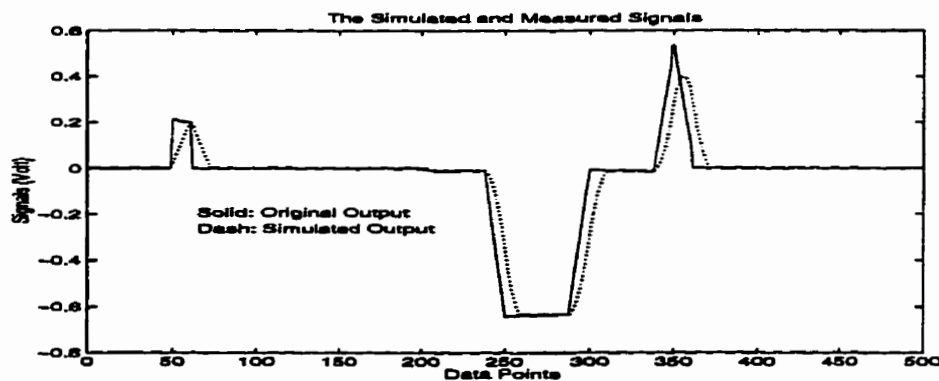


Figure 4.12 Comparison between $v_{sm}^I(k)$ and SV (using Figure 4.11 charge distribution)

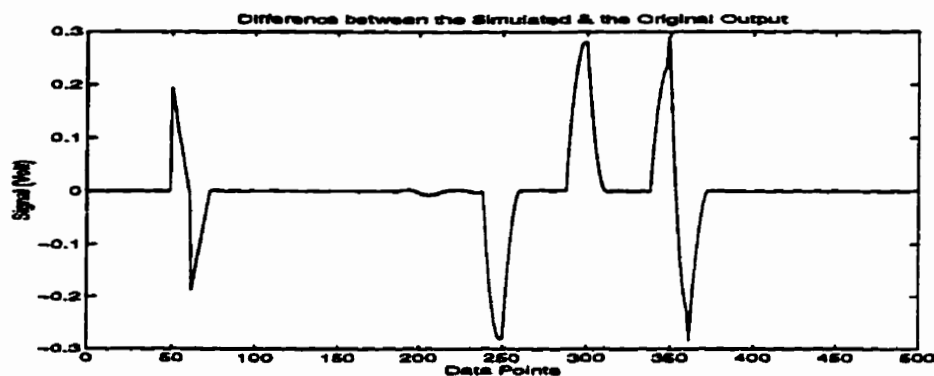


Figure 4.13 Difference between $v_{sm}^I(k)$ and SV of Figure 4.12

2) The deconvolution procedure(DCON)

Figure 4.14 gives the amplitude of the Fourier transform of system IR, - i.e. system transfer function, $g_m^1(k)$. Figure 4.15 gives the amplitude of the Fourier transform of the measured signal $v_{sm}^1(k)$. Figure 4.16 shows the results of the deconvolution procedure. The charge distribution is designated as the real component of $\mathcal{F}^{-1}\{\mathcal{F}[v_{sm}^1(k)]/\mathcal{F}(g_m^1(k))\}$. The obtained charge distribution is almost exactly the same as the SPD1 (shown in Figure 4.1). Figure 4.17 shows the difference between the simulated $SV(k)$ (calculated using Figure 4.16 charge distribution) and the original $v_{sm}^1(k)$ (as shown in Figure 4.5). The difference is in the order of 10^{-16} V. The perfect result is owing to that the 1st set of signals are noise-free, and the assumed $g^1(k)$ is invertible.

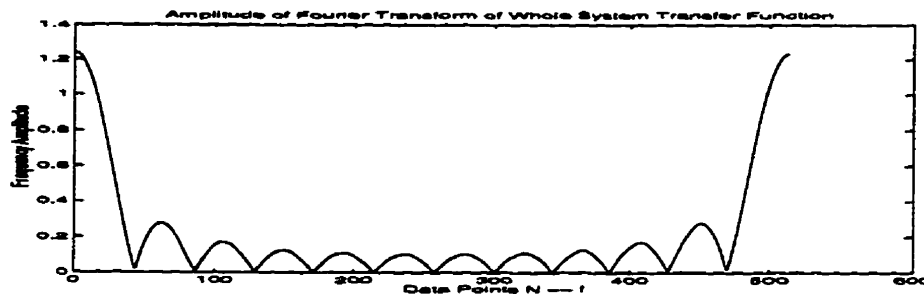


Figure 4.14 Amplitude of the Fourier transform of $g_m^1(k)$

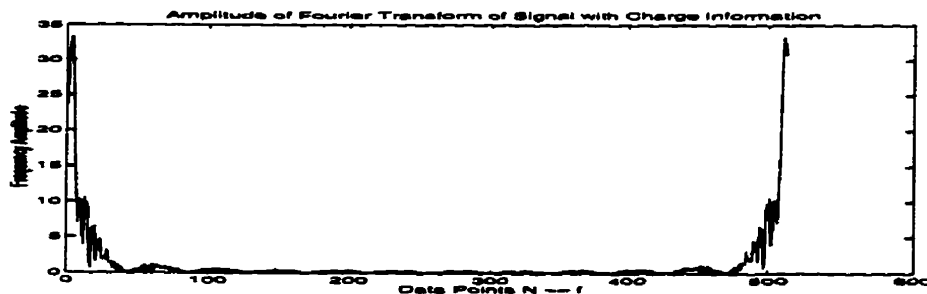


Figure 4.15 Amplitude of the Fourier transform of $v_{sm}^1(k)$

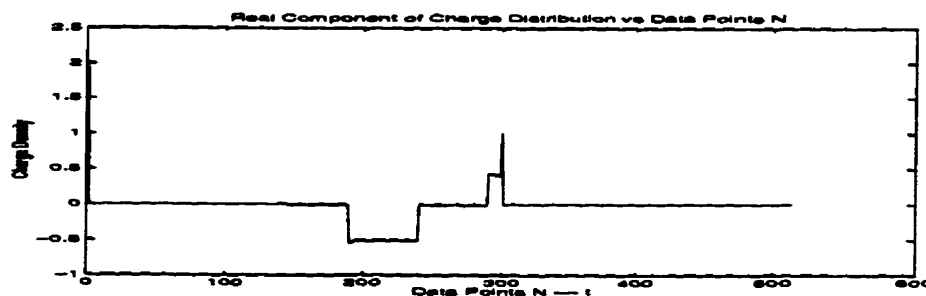


Figure 4.16 Charge distribution obtained by DCON for the 1st set signals

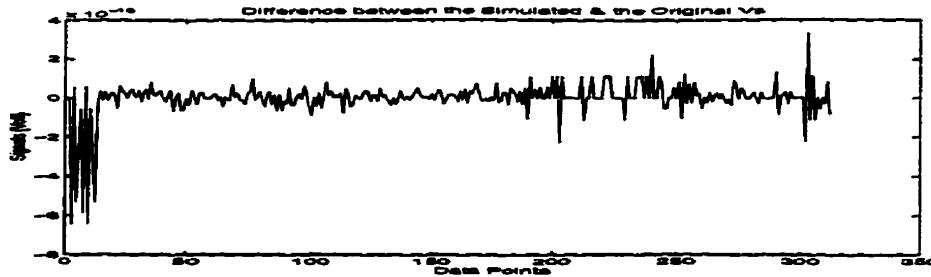


Figure 4.17 Comparison between $v_{sm}^I(k)$ and SV (using Figure 4.16 charge distribution)

3) The point matching simulation model(PMSM) approach

Since the noise is zero for the first set of signals, the noise reduction process is not necessary. In fact, $v_{sm}^I(k)$ and $g_m^I(k)$ can be processed directly. Figure 4.18 and Figure 4.19 show the results of σ sequence when the simulation step $\Delta=2$ and $\Delta=4$, respectively and where m_0 is set at point 49. Comparing these two figures, one sees that:

1. at $i=1$, $\sigma(1)=\sigma'(1)=2C/m^2$, which indicates that only the surface charge is present;
2. inside at points $i=1+4k(k=1-74)$, $\sigma(i) \approx \sigma'(i)/2$, which indicates that space charges are distributed within the sample; and
3. at $i=301$, $\sigma(301) \approx 1.4C/m^2$, $\sigma'(301) \approx 2.3C/m^2$, which indicates that surface charge and space charge may be present.

Solving Equation (3-50), one can obtain that $\sigma_2 \approx 0.5C/m^2$ and $\sigma_p(d) = \rho(d)c_2\Delta t = 0.45C/m^2$. Figure 4.20 shows the charge distribution after reconstruction using the results of Figures 4.18 and 4.19. Surface charges and volume charges are differently treated. The distributions inside the sample are mainly based on the $\Delta=2$ results. The distribution obtained is closed to the distribution in Figure 4.1. It is obvious that surface charges can be much better represented than they can in the DM. If Figure 4.20 charge distribution is used to construct the simulated output signal $SV(k)$, the difference between $SV(k)$ and $v_{sm}^I(k)$ is also much less than that obtained from the DM. The difference is less than $\pm 0.04V$ as shown in Figure 4.21. When Figure 4.20 charge distribution is used as the initial input to an optimization process to minimize the least square error between $SV(k)$ and $v_{sm}^I(k)$, good results can also be obtained. If F denotes the difference $(SV - v_{sm}^I)$, with the accuracy of σ setting at 0.01, the accuracy of F setting at 0.01, Figure 4.22 charge distribution is obtained after about 11 hour optimization

computation. The difference between $SV(k)$ and $v_{sm}^I(k)$ for Figure 4.22 charge distribution is in the order of 10^{-12} as shown in Figure 4.23.

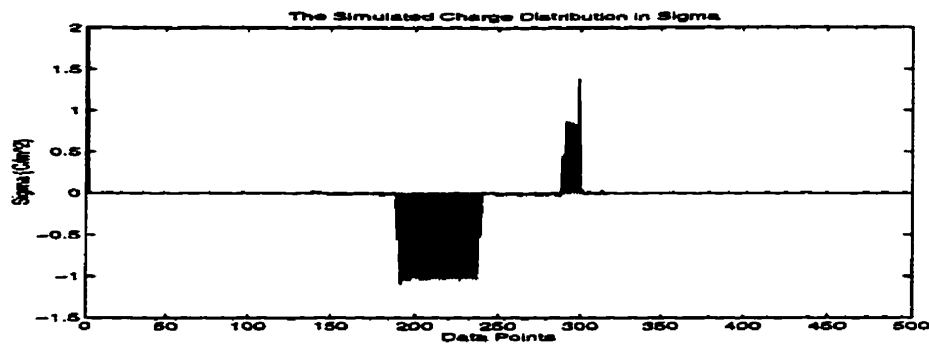


Figure 4.18 σ sequence obtained by PMSM at $\Delta=2$ for the 1st set signals

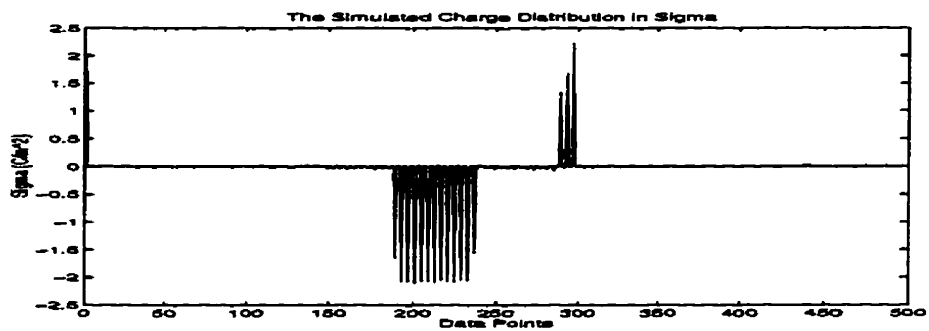


Figure 4.19 σ sequence obtained by PMSM at $\Delta=4$ for the 1st set signals

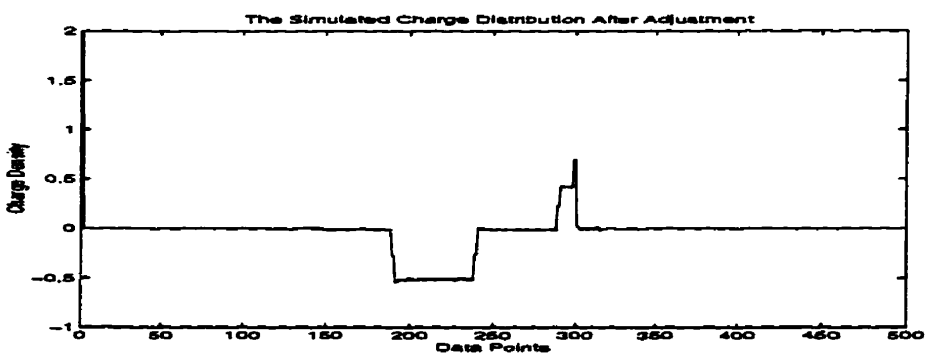


Figure 4.20 Charge distribution after reconstruction mainly based on $\Delta=2$

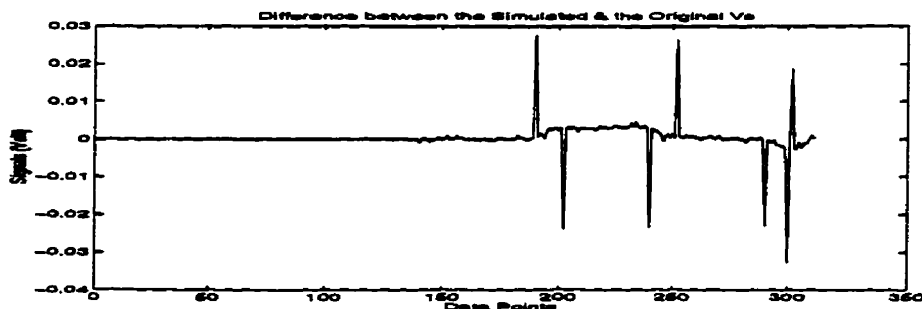


Figure 4.21 Difference between $SV(k)$ and $v_{sm}^I(k)$ for Figure 4.19 charge distribution

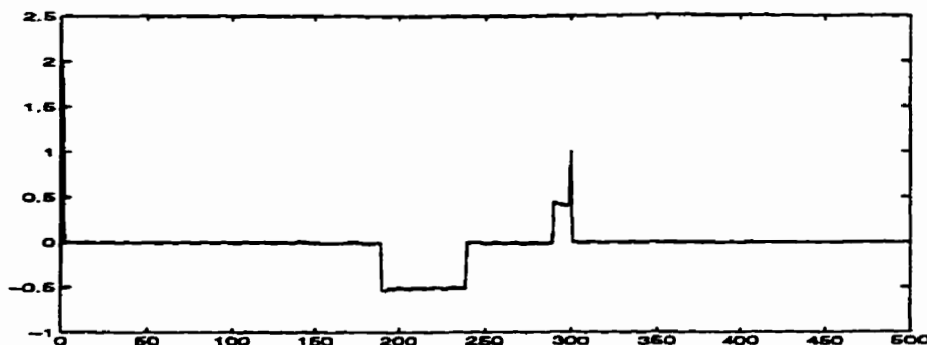


Figure 4.22 Charge distribution after optimization process[accuracy: $\sigma(0.01)$, $F(0.01)$]

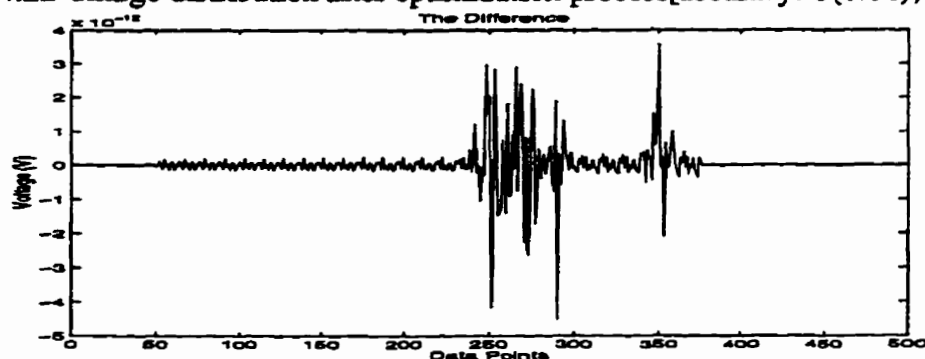


Figure 4.23 Difference between $v_{sm}^1(k)$ and $SV(k)$ for Figure 4.21 charge distribution

4.2.3 The 2nd Set of Signals

The second set of signals are $v_{sm}^2(k)$ and $g_m^2(k)$, as shown in Figure 4.6 and Figure 4.7 respectively. As noises are contaminated in this set signals, the charge distribution results obtained by the three methods will change.

1) *The direct method(DM):*

Figure 4.24 shows the charge distribution obtained using the DM method with $m_0=49$. A zero-phase waveshaper can be applied to make the distribution smooth. Figure 4.25 shows the charge distribution after a 10 point anti-causal zero-phase average filter is applied. Figure 4.26 compares the measured output $v_{sm}^2(k)$ with the simulated output $SV(k)$ (generated from Figure 4.24 charge distribution). The difference between the two is shown in Figure 4.27. Figure 4.28 then compares the measured output $v_{sm}^2(k)$ with the simulated output $SV(k)$ (generated from Figure 4.25 charge distribution). The difference between them is shown in Figure 4.29.

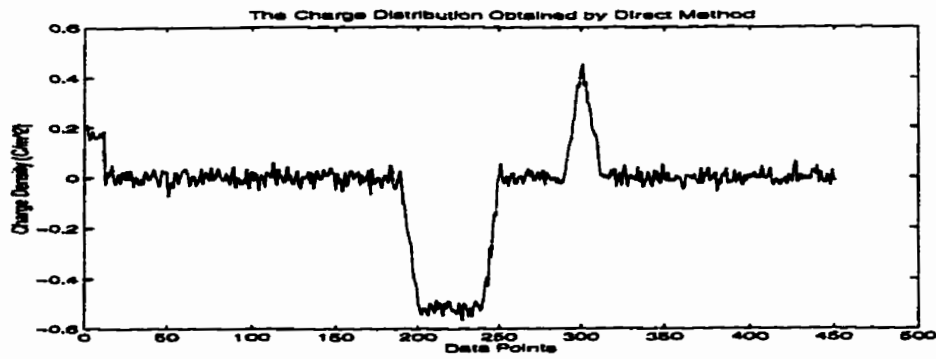


Figure 4.24 Charge distribution obtained by the DM method for the 2nd set signals

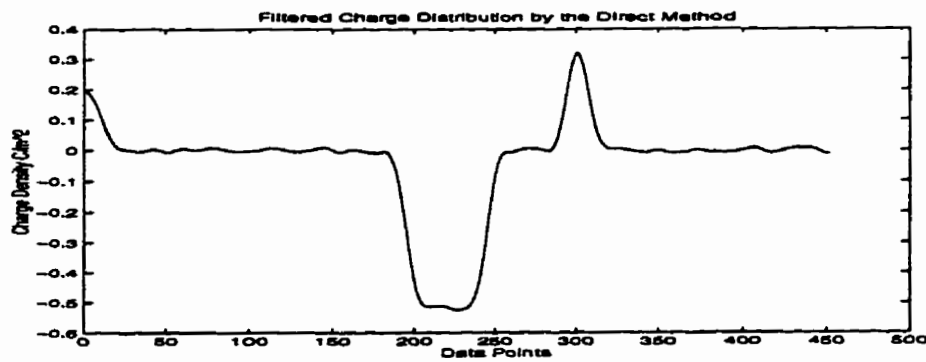


Figure 4.25 Filtered charge distribution obtained by the DM method for the 2nd set signals

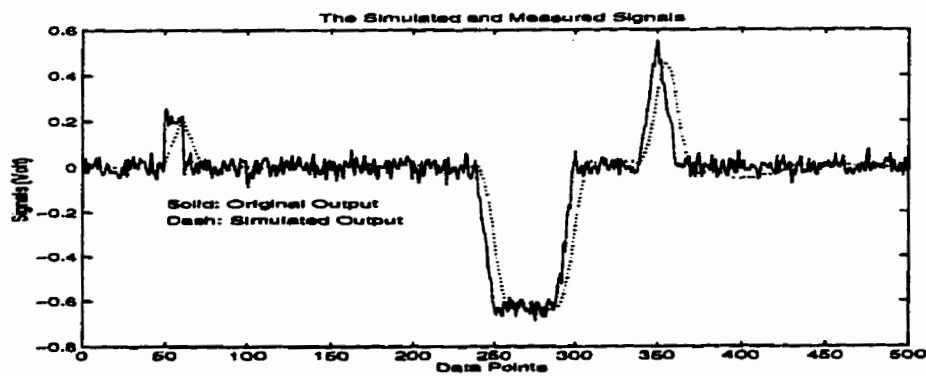


Figure 4.26 Comparison between $v_{sm}^2(k)$ and $SV(k)$ for Figure 4.24 charge distribution

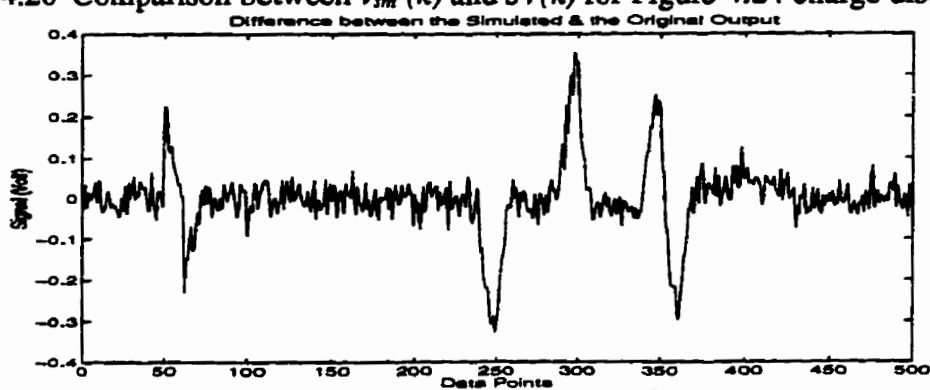


Figure 4.27 Difference between $SV(k)$ and $v_{sm}^2(k)$ of Figure 4.26

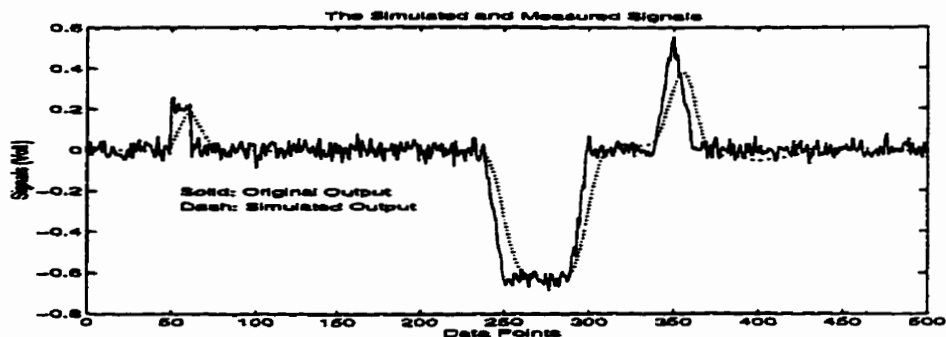


Figure 4.28 Comparison between $v_{sm}^2(k)$ and $SV(k)$ for Figure 4.25 charge distribution

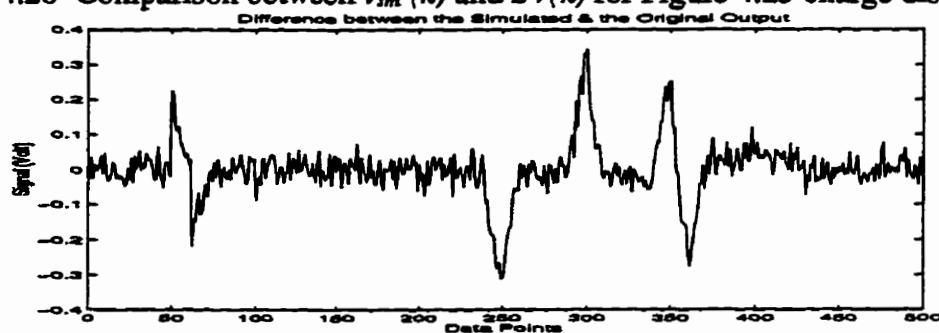


Figure 4.29 Difference between $SV(k)$ and $v_{sm}^2(k)$ of Figure 4.28

Comparing Figure 4.24 and Figure 4.25 with Figure 4.11 shows that the obtained charge distributions for the 2nd set signals are similar to the charge distribution obtained for the 1st set signals, except that Figure 4.24 is corrupted with noise and Figure 4.25 is not as sharp as Figure 4.11. This indicates that the DM method is not sensitive to noise. The presence of noise reduces the resolution and accuracy of the charge distribution, but the waveshape of the obtained charge distribution does not change very much due to the noise. Also, the difference between $SV(k)$ and $v_{sm}^2(k)$ does not change much compared to the difference between $SV(k)$ and $v_{sm}^1(k)$ as shown in Figure 4.13 mainly because the amplitude of the difference is even larger than the noise level.

2) The deconvolution procedure(DCON):

Figures 4.30 and 4.31 show the amplitude of Fourier transform of $g_m^2(k)$ and $v_{sm}^2(k)$, respectively. The charge distribution obtained by the DCON method is shown in Figure 4.32. Although, as demonstrated in Figure 4.33 and Figure 4.34, the difference between $v_{sm}^2(k)$ and the simulated $SV(k)$ (generated with Figure 4.32 charge distribution) is not as large as that

resulting from the DM method, the charge distribution is far from the SPD1 distribution. The charge distribution shown in Figure 4.32 is of no use unless the high frequency noise in the charge distribution can be eliminated using a properly designed filter. Figure 4.35 shows the charge distribution obtained by filtering Figure 4.32 with a 10 point anti-causal, zero-phase average filter. The resulting charge distribution is meaningful, and the resolution seems better than that of the DM. However, the comparison between $v_m^2(k)$ and $SV(k)$ as shown in Figure 4.36 and Figure 4.37 indicates that the difference is quite large from points 50 to 70, because surface charge $\sigma(l)$ is represented as a charge distribution with some duration.

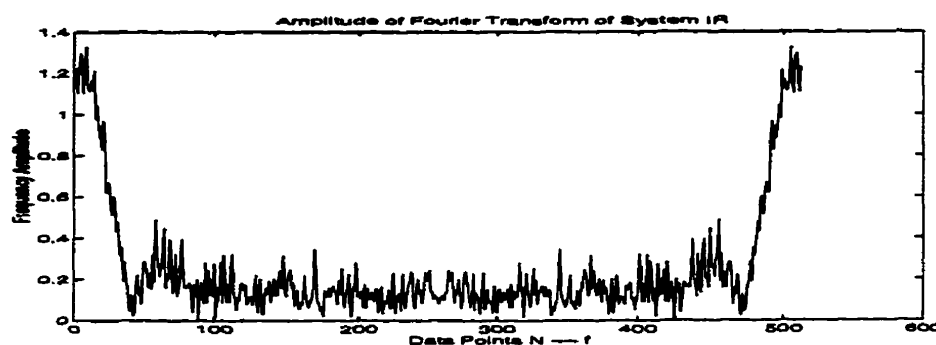


Figure 4.30 Amplitude of Fourier transform of system IR ($g_m^2(k)$)

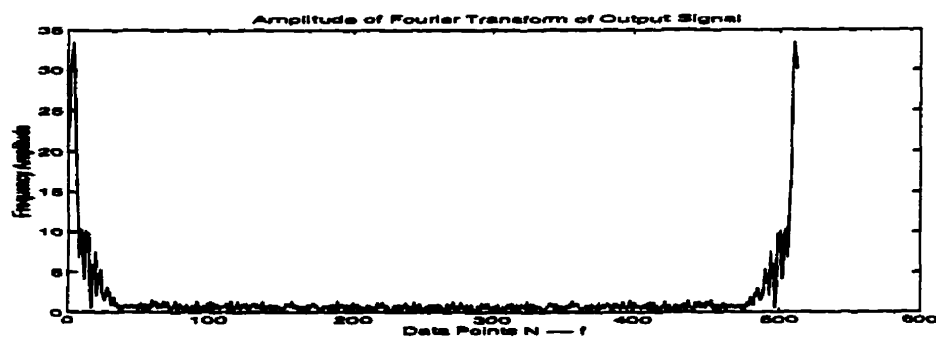


Figure 4.31 Amplitude of Fourier transform of output signal ($v_m^2(k)$)

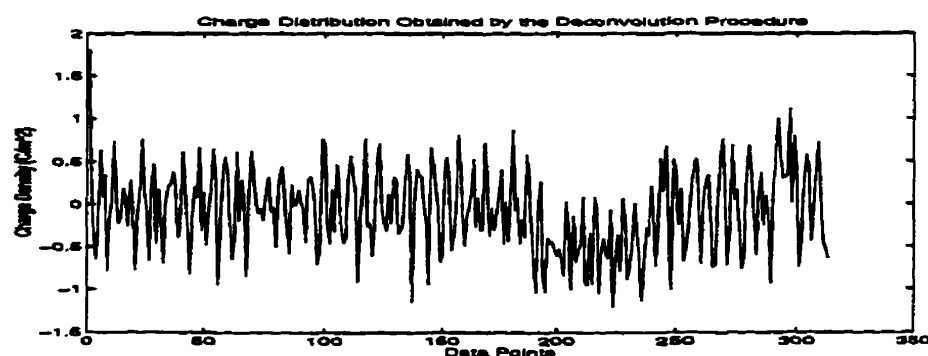


Figure 4.32 Charge distribution results by the DCON method for the 2nd set

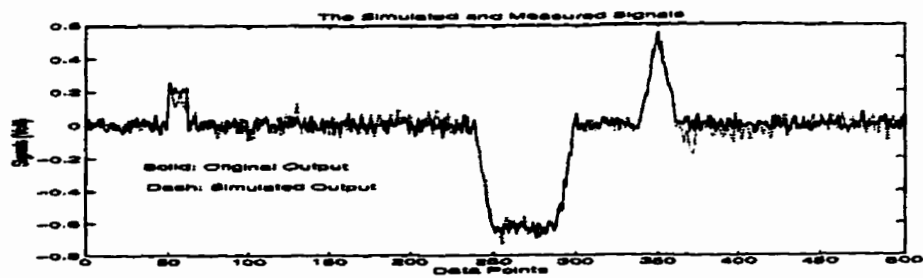


Figure 4.33 Comparison between $v_{sm}^2(k)$ and $SV(k)$ (Figure 4.32 charge distribution)

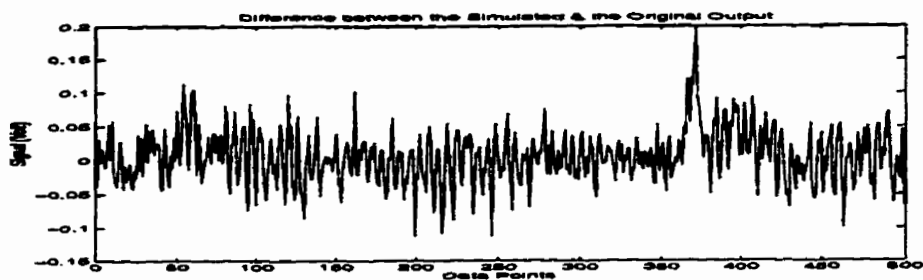


Figure 4.34 Difference between $v_{sm}^2(k)$ and $SV(k)$ of Figure 4.33

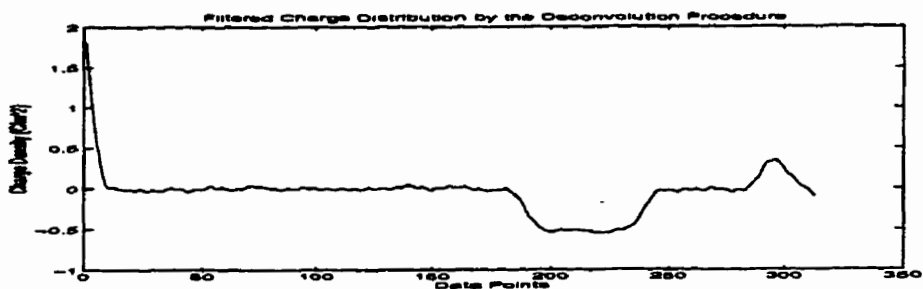


Figure 4.35 Filtered charge distribution by the DCON method

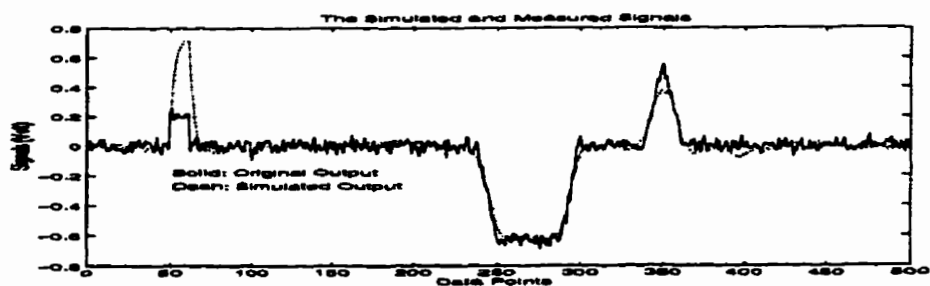


Figure 4.36 Comparison between $v_{sm}^2(k)$ and $SV(k)$ (Figure 4.35 charge distribution)

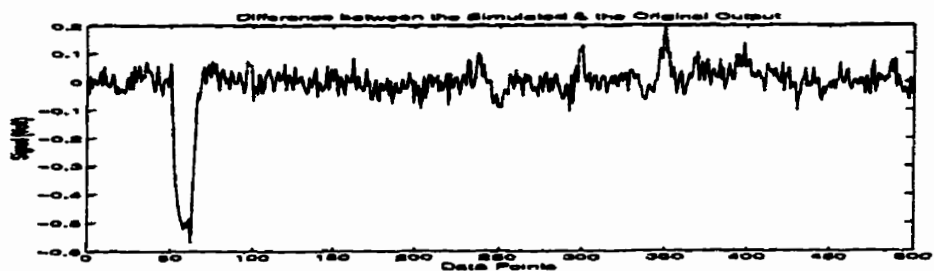


Figure 4.37 Difference between $v_{sm}^2(k)$ and $SV(k)$ of Figure 4.36

From these results, the following conclusions can be obtained:

1. when signals are noise-corrupted, the results obtained directly from the DCON method are very bad, indicating that the DCON is very sensitive to noise. A special filter, or so-called waveshaper, has to be designed to eliminate high frequency noise in the distribution. Hopefully, the filter will work efficiently and provide meaningful results.
2. When the low pass filter is applied, it will not cause significant problems to the representation of space charges; however, the presence of surface charges will be smeared in the charge distribution results, because the bandwidth of a surface charge is from zero to infinity. The low pass filter will make surface charges appear as a distribution with some duration as if some space charges are distributed. This can cause a large difference as shown in Figure 4.36 and Figure 4.37.
3. Better results can be obtained if one can:
 - identify the presence of surface charges, using the superposition theory, and subtract the surface charges from the total charge distribution;
 - apply a filter only to the subtraction, the space charge distribution; and then,
 - superimpose the surface charges upon the smoothed space charge distribution to construct the total charge distribution.

This is what the simulation model is intended to do.

As mentioned in Chapter 3, the PMSM approach will first apply a noise reduction process when the noise is not negligible in the output signals. Before presenting the results obtained from the PMSM approach, it is necessary to show what one can obtain from the DECON for the signals after the noise reduction process. Figure 3.38 and Figure 3.39 show the $g_m^2(k)$ and $v_{sm}^2(k)$ when a 10 point anti-causal zero-phase average filter is applied to $g_m^2(k)$ and $v_{sm}^2(k)$ respectively. Figure 4.40 and Figure 4.41 show the amplitude of the Fourier transform of Figure 4.38 and Figure 4.39 signals. Figure 4.42 is the charge distribution obtained directly by the DCON. Figures 4.43 and 4.44 compare the difference between $v_{sm}^2(k)$ and $SV(k)$ (generated using Figure 4.42 charge distribution). Figure 4.45 shows the charge distribution when the 10 point anti-causal zero phase average filter is applied. And Figures 4.45 and 4.46 compare the difference between $v_{sm}^2(k)$ and $SV(k)$ (using Figure 4.44 charge distribution).

It is obvious that $\alpha(I)$ is falsely represented because the DCON is very sensitive to noise. The above results indicate that, even if the true charge distribution is not known, the comparison between the measured output and the simulated output (using the charge distribution) can help determine whether the charge distribution is fine or has missed some important information and, therefore, whether the charge distribution needs improvement or correction.

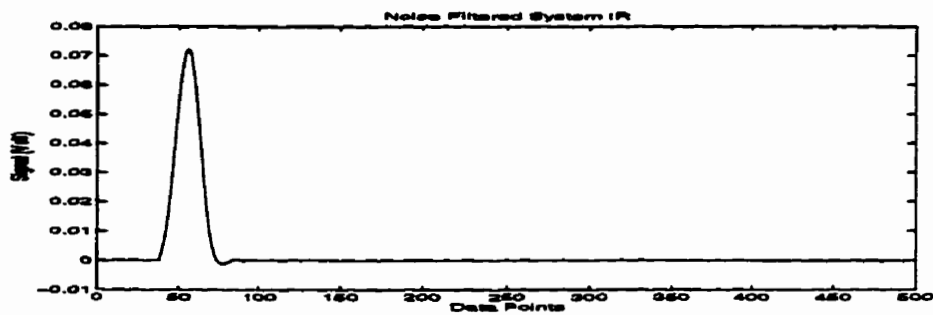


Figure 4.38 Filtered system IR ($g_m^{2'}(k)$)

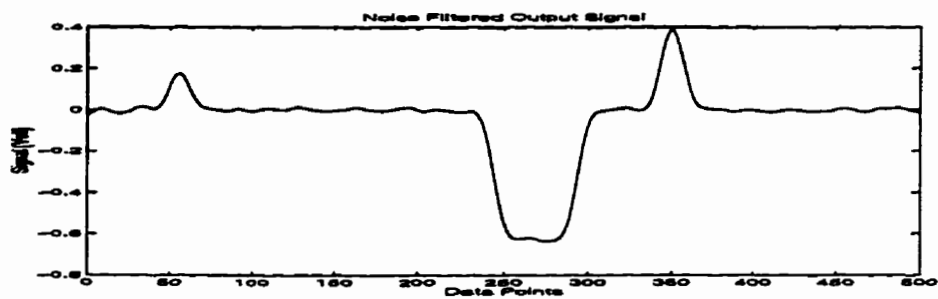


Figure 4.39 Filtered output signal ($v_{sm}^{2'}(k)$)

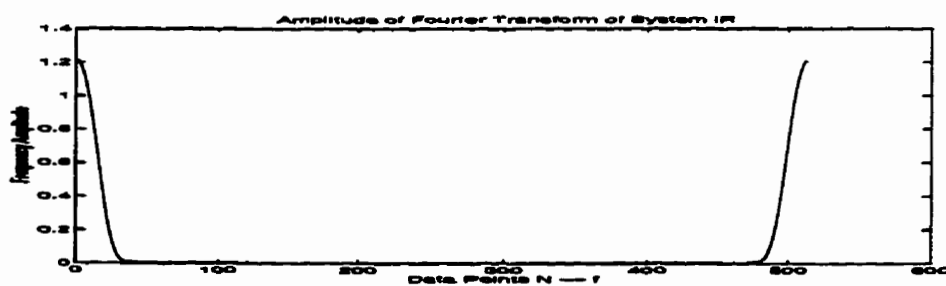


Figure 4.40 Amplitude of Fourier transform of filtered IR ($g_m^{2'}(k)$)



Figure 4.41 Amplitude of Fourier transform of filtered output ($v_{sm}^{2'}(k)$)

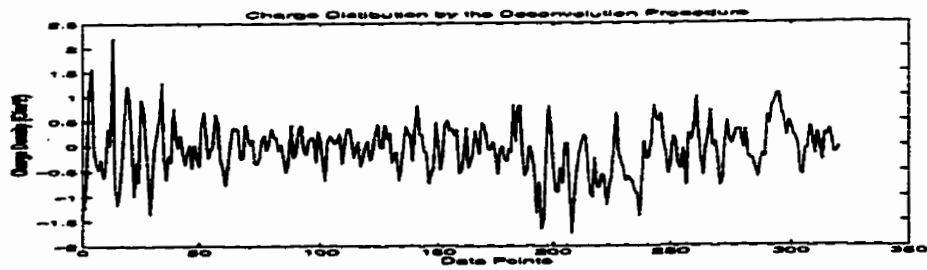


Figure 4.42 Charge distribution obtained by the DCON procedure

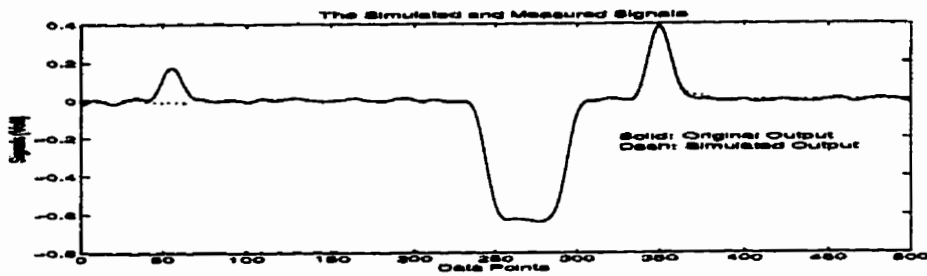


Figure 4.43 Comparison between $v_{sm}^{2'}(k)$ and $SV(k)$ (Figure 4.42 charge distribution)

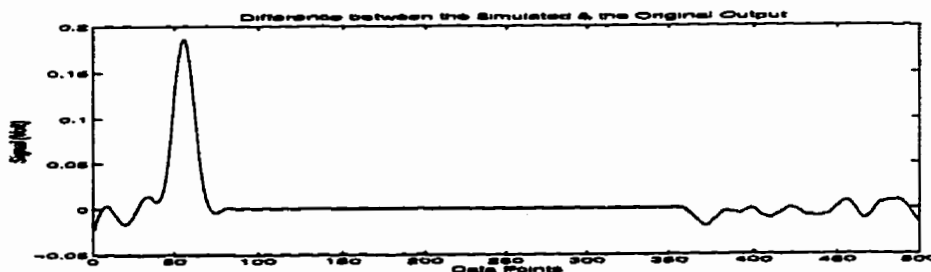


Figure 4.44 Difference between $v_{sm}^{2'}(k)$ and $SV(k)$ of Figure 4.43

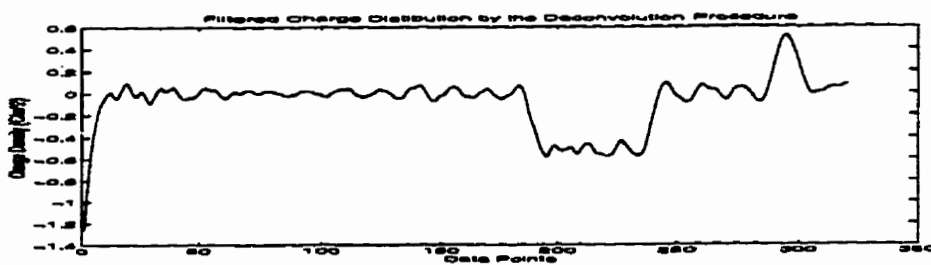


Figure 4.45 Filtered charge distribution

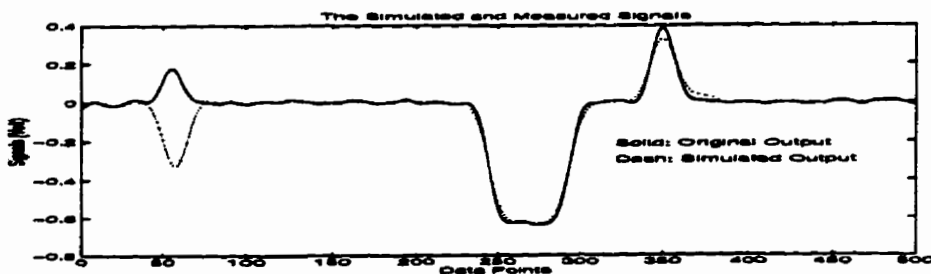


Figure 4.46 Comparison between $v_{sm}^{2'}(k)$ and $SV(k)$ (Figure 4.45 charge distribution)

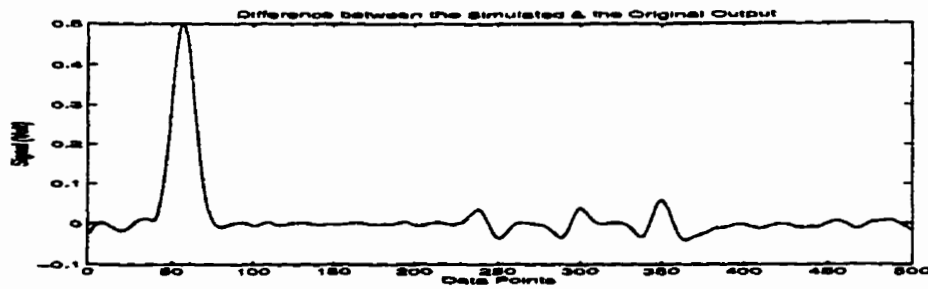


Figure 4.47 Difference between $v_{sm}^{2'}(k)$ and $SV(k)$ of Figure 4.46

3) The point matching simulation model(PMSM) approach

This section shows the charge distribution results obtained using the PMSM method for Figure 4.38 and Figure 4.39 $g_m^{2'}(k)$ and $v_{sm}^{2'}(k)$. Figures 4.48 and 4.49 present the σ sequences when m_0 is set at 47, step $\Delta=2$ and $\Delta'=4$, respectively.

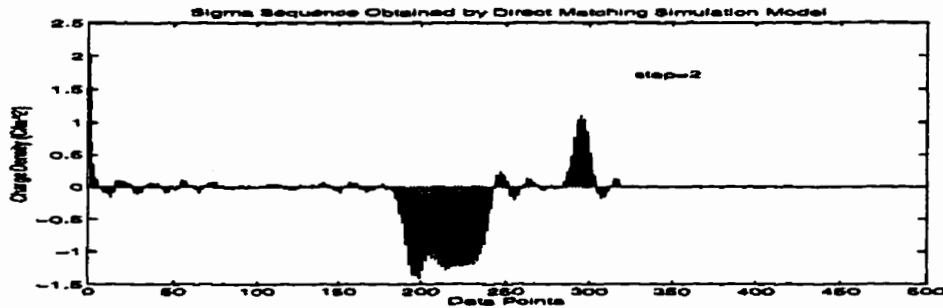


Figure 4.48 σ sequence when $\Delta=2$ and $m_0=47$

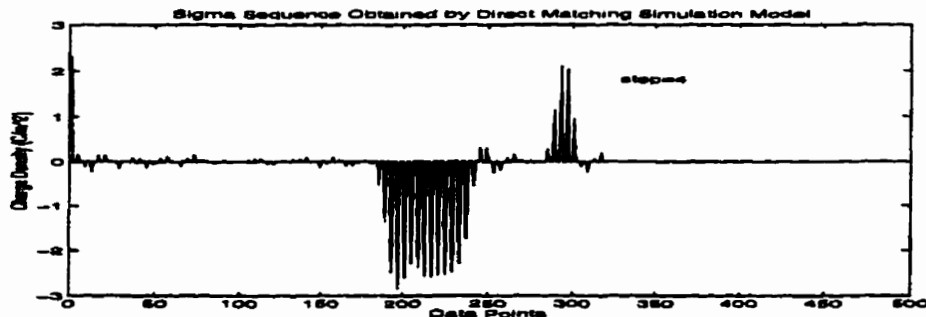


Figure 4.49 σ sequence when $\Delta'=4$ and $m_0=47$

From the obtained σ sequences, σ_1 , σ_2 , $\sigma_p(1)$, and $\sigma_p(N+2)$ can be calculated using equation (3-50). Let $\sigma^*(1) = \Delta \times \sigma_p(1)$, $\sigma^*(i) = \sigma(i)$, ($i=2$ to $N+1$), and $\sigma^*(N+2) = \Delta \times \sigma_p(N+2)$; one can apply zero-phase filter or zero-order hold to make the sequence continuous. A 10 point zero-

phase average filter is used to smooth the σ^* sequence. After smoothing, σ_1 and σ_2 are added to points 1 and $N+2$; thus charge distribution is built as shown in Figure 4.50. Figures 4.51 and 4.52 compare $v_{sm}^{2'}(k)$ and $SV(k)$ (using Figure 4.49 charge distribution). Figures 4.53 and 4.54 use the noise-corrupted $g_m^2(k)$ and compare noise-corrupted $v_{sm}^2(k)$ and $SV(k)$.

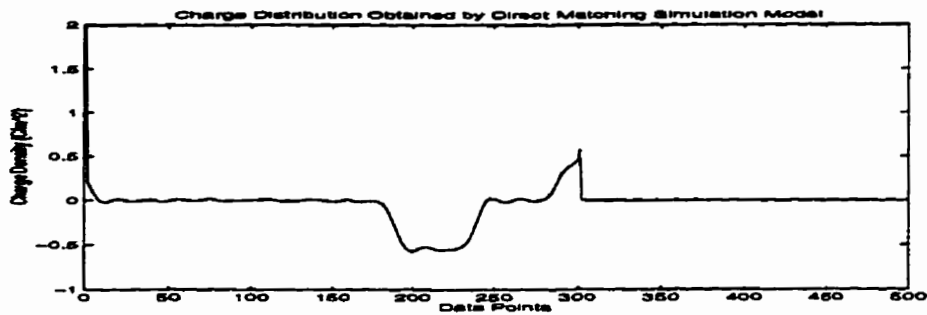


Figure 4.50 Charge distribution obtained by the PMSM method(Filtered)

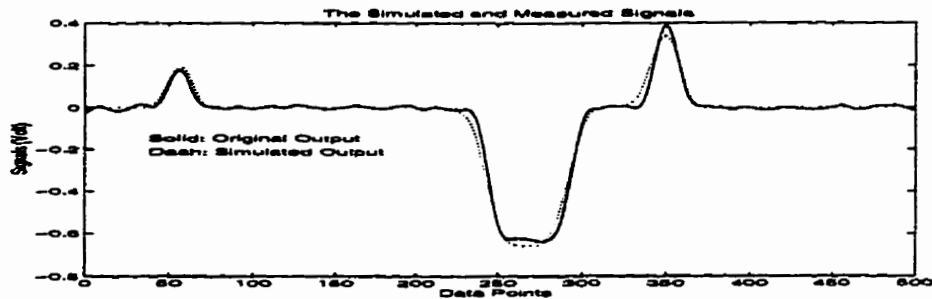


Figure 4.51 Comparison between $v_{sm}^{2'}(k)$ and $SV(k)$ (Figure 4.50 charge distribution)

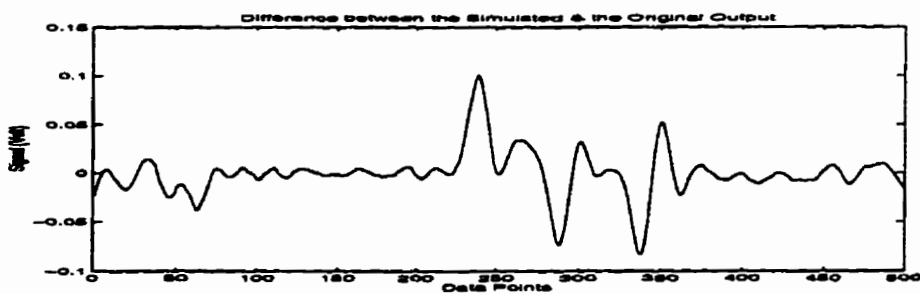


Figure 4.52 Difference between $v_{sm}^{2'}(k)$ and $SV(k)$ of Figure 4.51

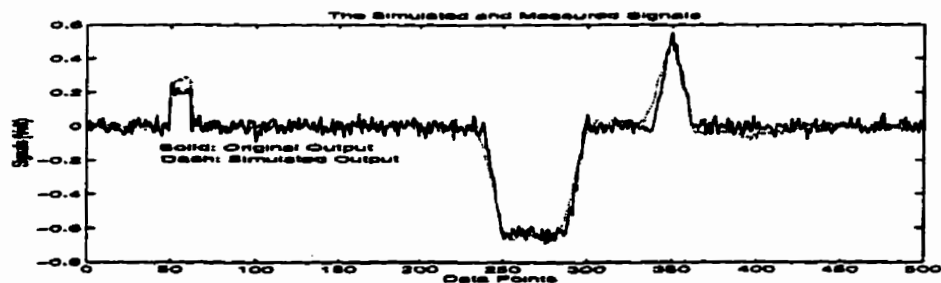


Figure 4.53 Comparison between $v_{sm}^2(k)$ and $SV(k)$ (Figure 4.50 charge distribution)

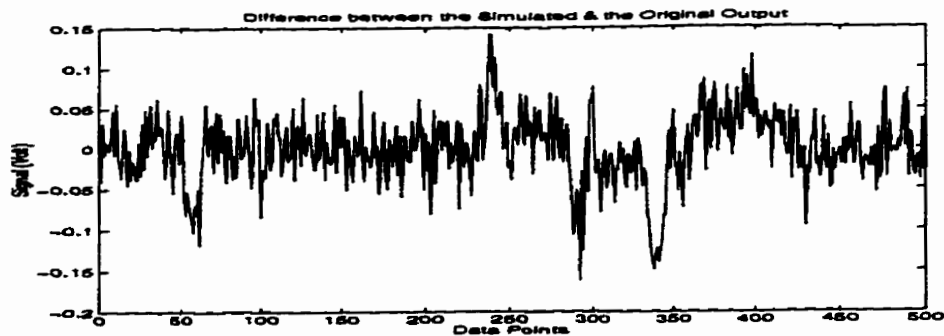


Figure 4.54 Difference between $v_{sm}^2(k)$ and $SV(k)$ of Figure 4.53

Figure 4.55 is built by first applying a zero-order hold to σ^*/Δ sequence and then superimposing σ_1 and σ_2 on the space charge distribution at points 1 and $N+2$. Figures 4.56 and 4.57 compare $v_{sm}^{2'}(k)$ and $SV(k)$ (using Figure 4.55 charge distribution). Figures 4.58 and 4.59 use the noise-corrupted $g_m^2(k)$ and Figure 4.55 charge distribution to obtain $SV(k)$ and compare noise corrupted $v_{sm}^2(k)$ with the $SV(k)$.

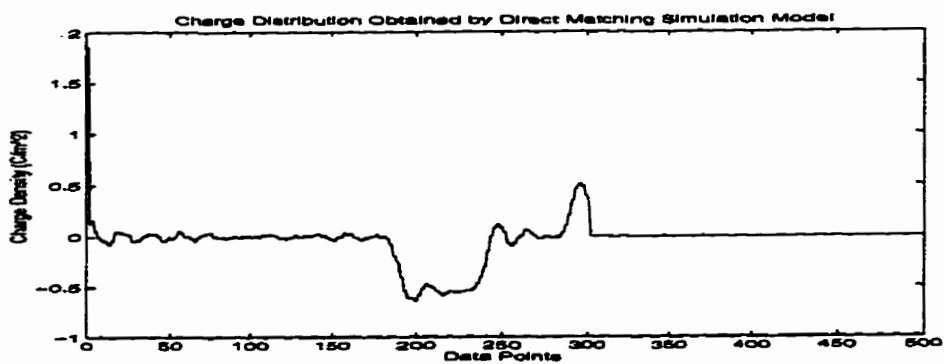


Figure 4.55 Charge distribution obtained by PMSM method(zero-order-hold)

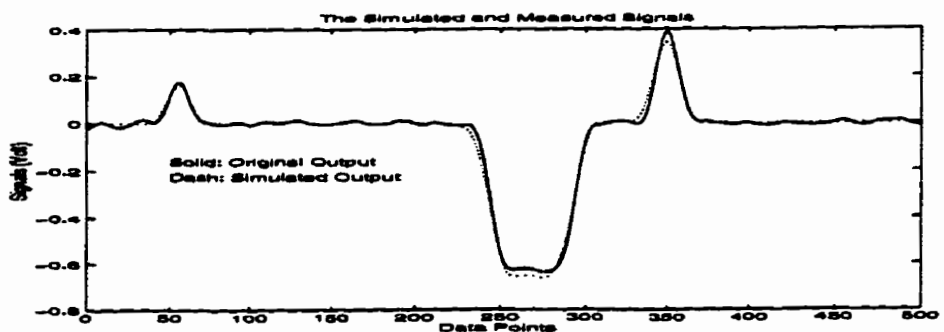


Figure 4.56 Comparison between $v_{sm}^{2'}(k)$ and $SV(k)$ (Figure 4.55 charge distribution)

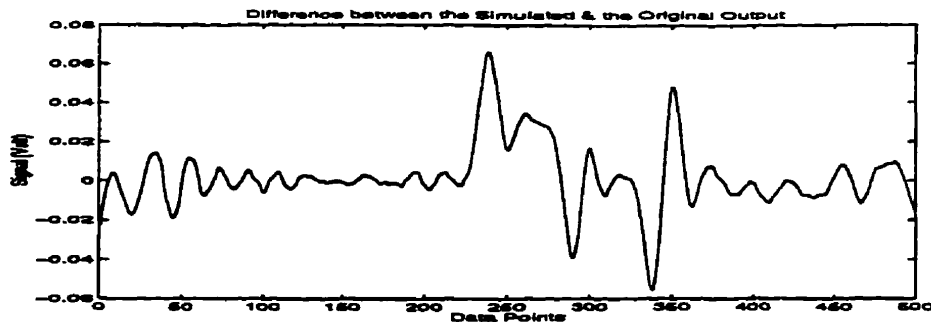


Figure 4.57 Difference between $v_{sm}^2(k)$ and $SV(k)$ of Figure 4.56

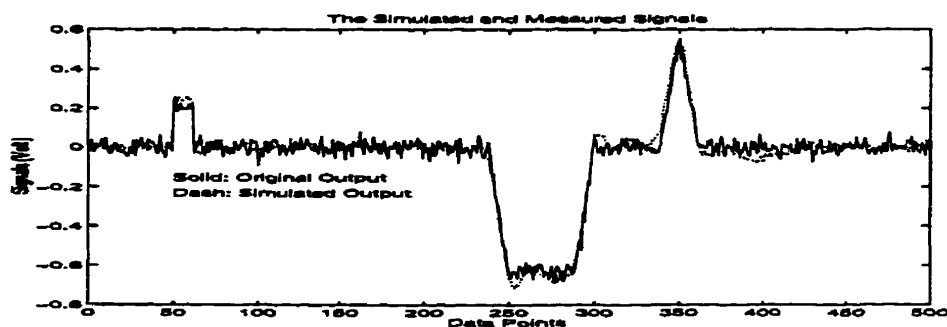


Figure 4.58 Comparison between $v_{sm}^2(k)$ and $SV(k)$ (Figure 4.55 charge distribution)

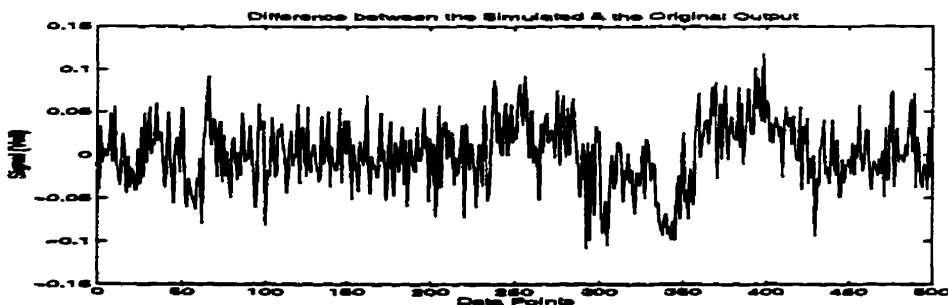


Figure 4.59 Difference between $v_{sm}^2(k)$ and $SV(k)$ of Figure 4.58

A comparison of the charge distribution obtained by the PMSM(Figure 4.50 or Figure 4.55) with those obtained by the DM(Figure 4.24 or Figure 4.25) and the DCON(Figures 4.32 & 4.35 or Figures 4.42 & 4.45) reveals that the resolution and the accuracy of the PMSM are obviously better than those of the DM and the DCON. The PMSM shows little sensitivity to noise as compared with the DCON and still provides high resolution as compared with the DM and DCON. Besides, the difference between $v_{sm}^2(k)$ and $SV(k)$ generated using the charge distribution obtained by the PMSM method is much smaller than the difference between $v_{sm}^2(k)$ and $SV(k)$ generated using the charge distribution obtained by the DM and DCON, indicating no misrepresentation of the actual charge distribution(SPD1).

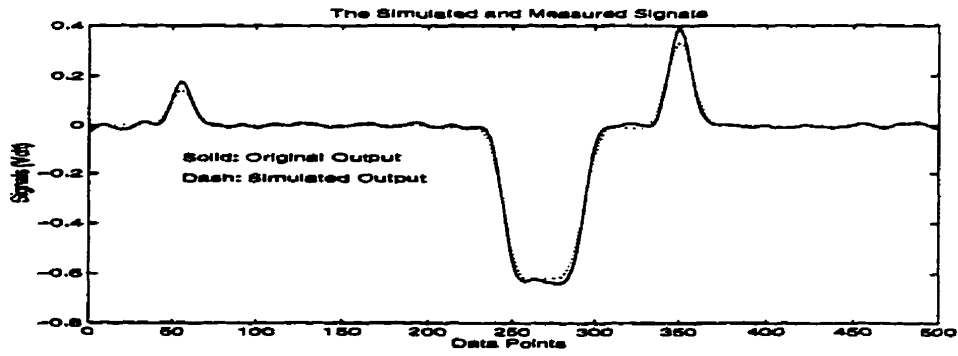


Figure 4.60 Comparison between $v_{sm}^2(k)$ and $SV(k)$ (SPD1)

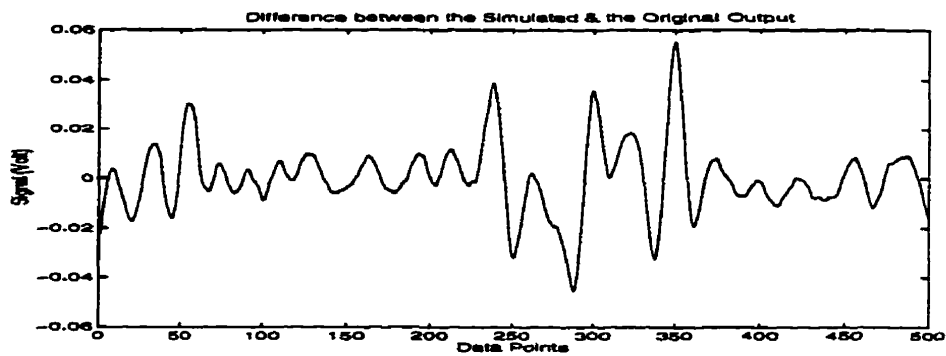


Figure 4.61 Difference between $v_{sm}^2(k)$ and $SV(k)$ of Figure 4.60

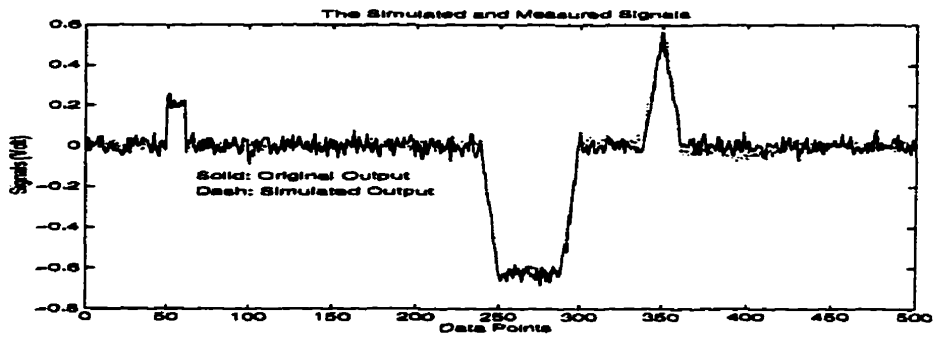


Figure 4.62 Comparison between $v_{sm}^2(k)$ and $SV(k)$ (SPD1)

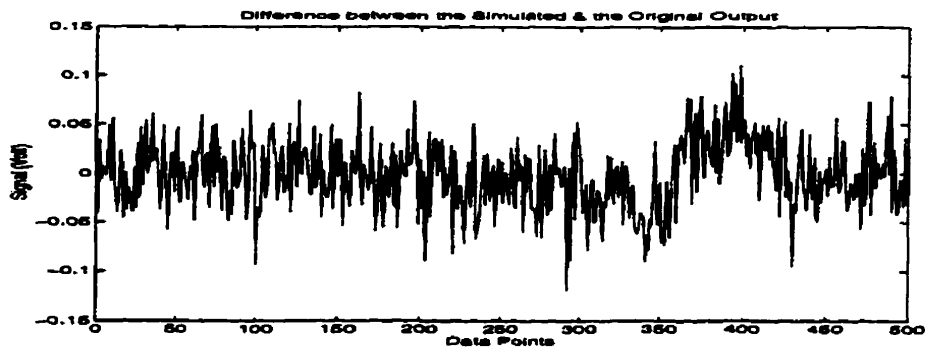


Figure 4.63 Difference between $v_{sm}^2(k)$ and $SV(k)$ of Figure 4.62

Owing to the presence of noise, one cannot expect the obtained charge distribution to be the same as SPD1 or the difference between $v_{sm}^{2'}(k)$ and $SV(k)$ or $v_{sm}^2(k)$ and $SV(k)$ to be very small, approaching zero, as for the noise-free signal set. Figures 4.60 and 4.61 compare $v_{sm}^{2'}(k)$ and $SV(k)$ generated using SPD1, and Figures 4.62 and 4.63 compare $v_{sm}^2(k)$ and $SV(k)$ generated using SPD1. Obviously, the difference between $v_{sm}^{2'}(k)$ and $SV(k)$ or $v_{sm}^2(k)$ and $SV(k)$ still exists even with charge distribution SPD1. Comparing the amplitude of the difference between $v_{sm}^{2'}(k)$ and $SV(k)$ or $v_{sm}^2(k)$ and $SV(k)$ using SPD1 and the amplitude of corresponding difference using the charge distribution obtained by the PMSM, one can see that the PMSM results are very good.

The accuracy and resolution of the obtained charge distribution depend upon the noise level, system bandwidth, and the sensitivity of the method (used to get the charge distribution) to the noise and bandwidth effects. As mentioned in Chapter 3, the linear process is more sensitive to the noise and bandwidth effects than the nonlinear process. To obtain Figure 4.50 and Figure 4.55 charge distribution, a nonlinear process already used at the interfaces, i.e., at points 1 and $N+2$. From comparisons, it is clear that this process produces better results than the DM and the DCON. However, near the place where rapid change of charge distribution occurs, the results seem to be a little bit smeared. Therefore, for even better results, the nonlinear detection and optimization process (NDOP) can be considered to further improve the resolution.

Since the nonlinear detection and optimization process is very time-consuming, it has not been applied to the experimental signals but only to the synthetic signals. For the continuity of the thesis, the application of the nonlinear detection and optimization process for the 2nd set of signals are presented in Appendix D-2. The function of the nonlinear detection and optimization process shows the potential of the PMSM for high resolution and accuracy in representing the charge distribution.

4.2.4 The 3rd Set of Signals

The 3rd set of signals are noise-corrupted $g_m^3(k)$ and $v_{sm}^3(k)$ as shown in Figures 4.7 and 4.8 respectively. The charge distribution results obtained using the DM, the DCON, and the PMSM methods for this set of signals are demonstrated in this section.

1) *The direct method(DM)*

Figure 4.64 shows the charge distribution obtained by the DM method when m_0 is set at point 53. Figure 4.65 and Figure 4.66 compare $v_{sm}^3(k)$ and $SV(k)$ (Figure 4.64 charge distribution). When the 10 point zero-phase average filter is applied to Figure 4.64, Figure 4.67 charge distribution is obtained. Figures 4.68 and 4.69 compare $v_{sm}^3(k)$ and $SV(k)$ using Figure 4.67 charge distribution.

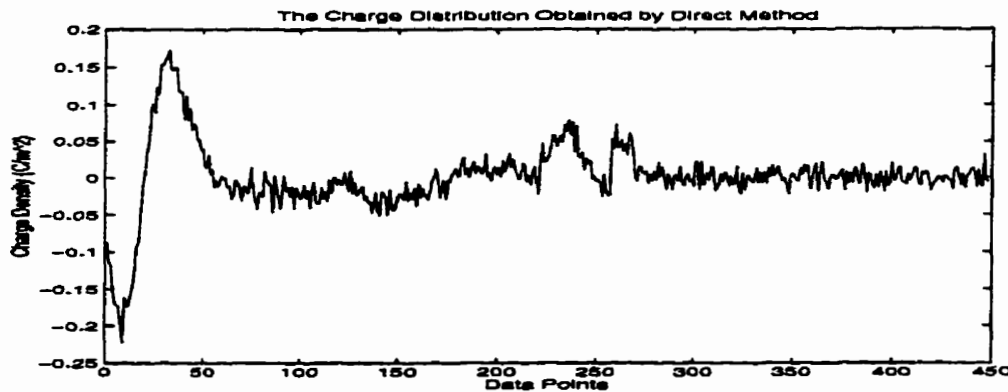


Figure 4.64 Charge distribution obtained by the DM method for the 3rd set signal

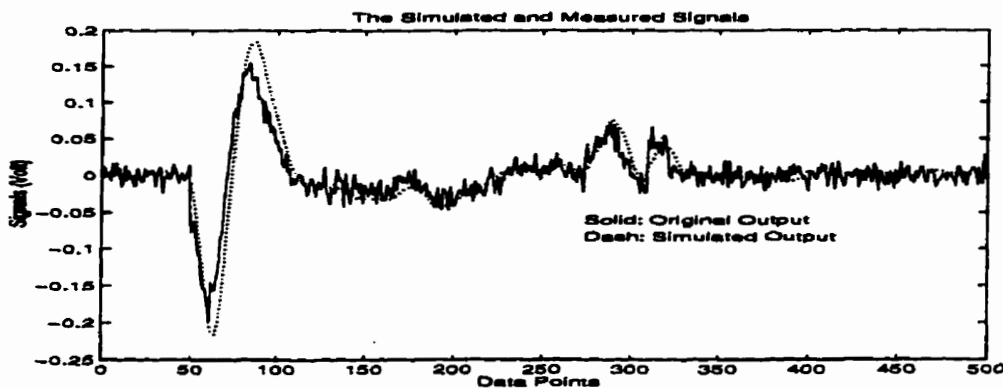


Figure 4.65 Comparison between $v_{sm}^3(k)$ and $SV(k)$ (Figure 4.64 charge distribution)

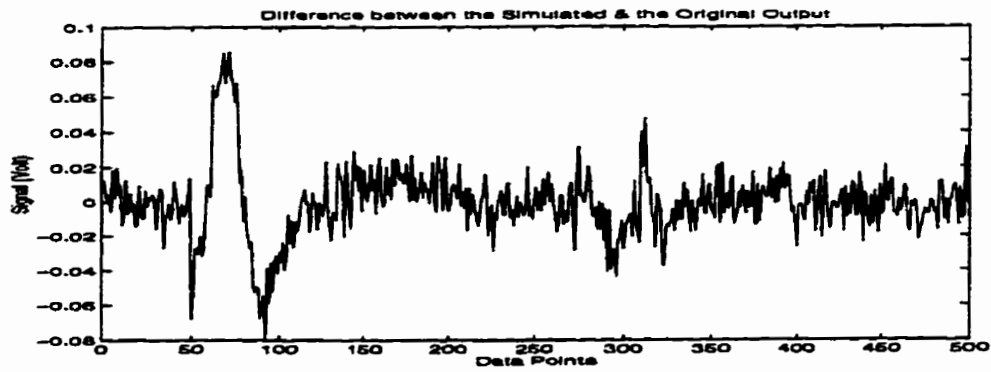


Figure 4.66 Difference between $v_{sm}^3(k)$ and $SV(k)$ of Figure 4.65

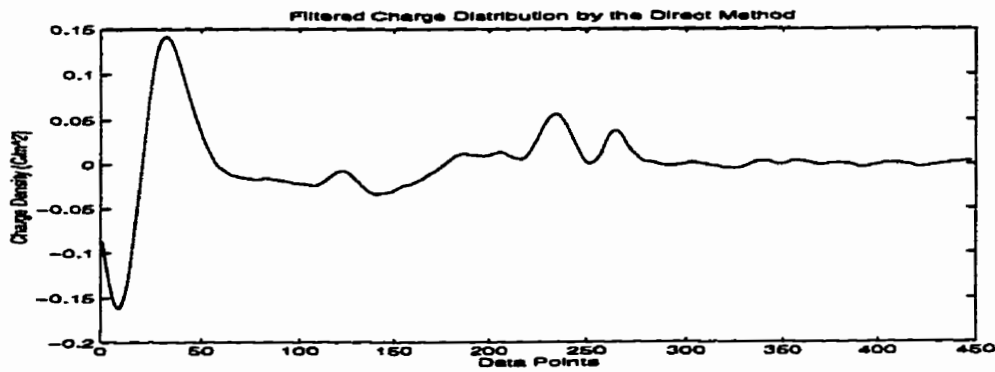


Figure 4.67 Filtered charge distribution obtained by the DM method

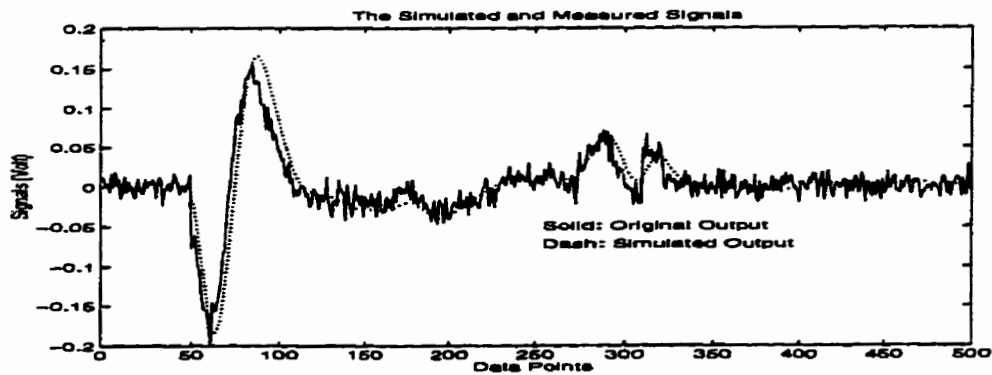


Figure 4.68 Comparison between $v_{sm}^3(k)$ and $SV(k)$ (Figure 4.67 charge distribution)

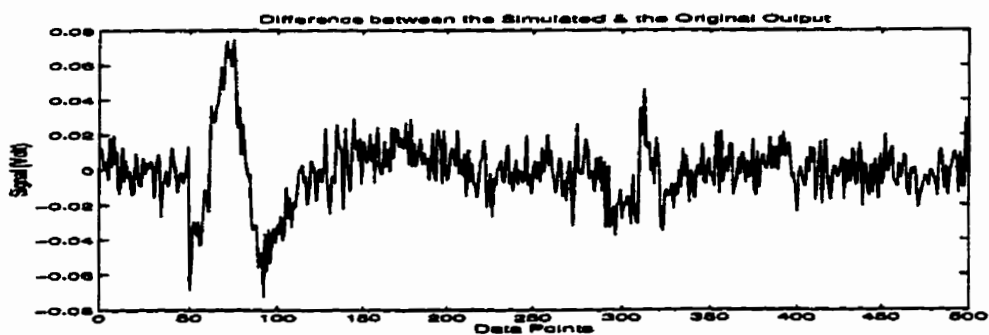


Figure 4.69 Difference between $v_{sm}^3(k)$ and $SV(k)$ of Figure 4.68

From these results and a comparison of the 2nd set of signals processed by the DM, the DM can clearly identify the slow change of charge distribution. The difference between $v_{sm}^3(k)$ and $SV(k)$ generated using the DM charge distribution result is comparable to the noise level. However, it is still difficult for the DM to identify the presence of surface charges. Comparing the charge distribution obtained by the DM (Figure 4.64 or 4.67) with SPD2 shows that σ_1 is missing while the presence of σ_2 is similar to a space charge distribution. Nevertheless, from these results, one can see that, if no surface charges exist in a distribution, if the space charges are distributed at a considerable distance from the surface charges, or if the space charges distributed near the surface charges are not important, the representation of space charge distribution from the DM is fine. The procedure to obtain the space charge distribution is quite simple and straightforward, as long as the system IR is narrow and with no rings.

2) *The deconvolution(DCON) procedure*

Figures 4.70 and 4.71 show the amplitudes of the Fourier transform of output $g_m^3(k)$ and $v_{sm}^3(k)$. Figure 4.72 shows the charge distribution obtained by the DCON, which is bad. Figure 4.73 and Figure 4.74 compare $v_{sm}^3(k)$ with $SV(k)$ using Figure 4.72 charge distribution. Figure 4.75 is the charge distribution obtained when Figure 4.72 is filtered by the 10 point anti-causal zero-phase average filter. Further, Figure 4.76 and Figure 4.77 compare $v_{sm}^3(k)$ with $SV(k)$ using Figure 4.75 charge distribution.

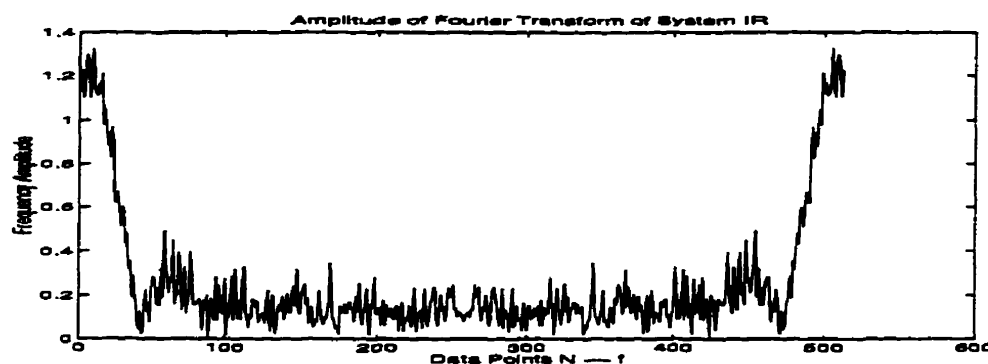


Figure 4.70 Amplitude of Fourier transform of output $g_m^3(k)$

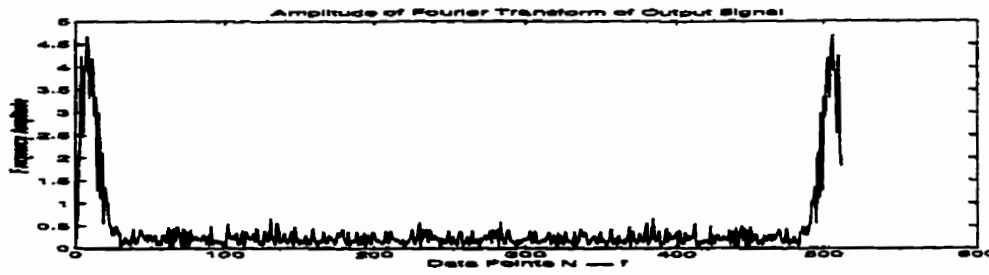


Figure 4.71 Amplitude of Fourier transform of output $v_{im}^3(k)$

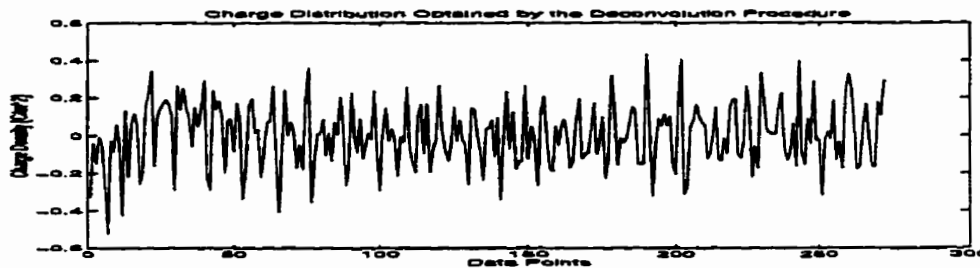


Figure 4.72 Charge distribution obtained by the DCON for the 3rd set

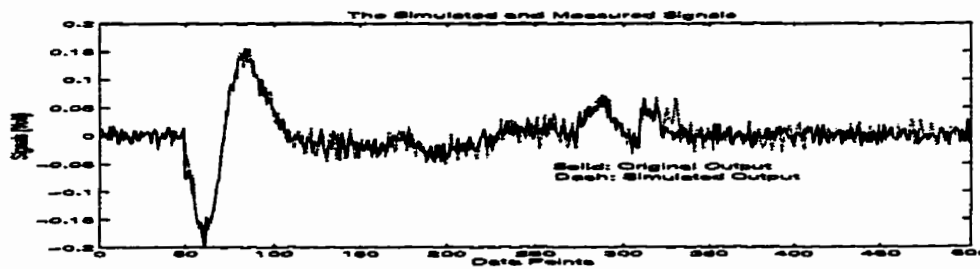


Figure 4.73 Comparison between $v_{im}^3(k)$ and $SV(k)$ (Figure 4.72 charge distribution)

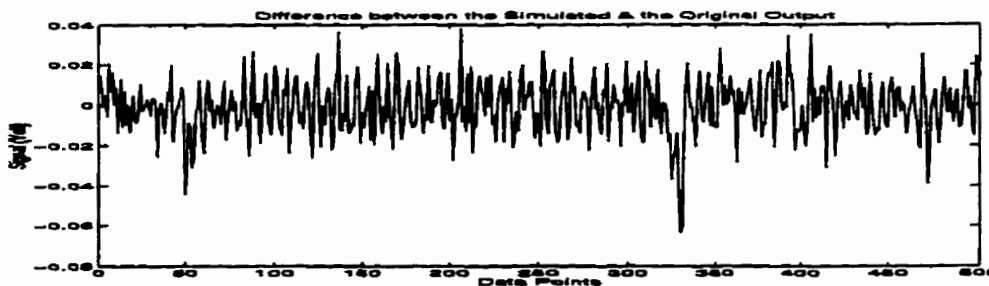


Figure 4.74 Difference between $v_{im}^3(k)$ and $SV(k)$ of Figure 4.73

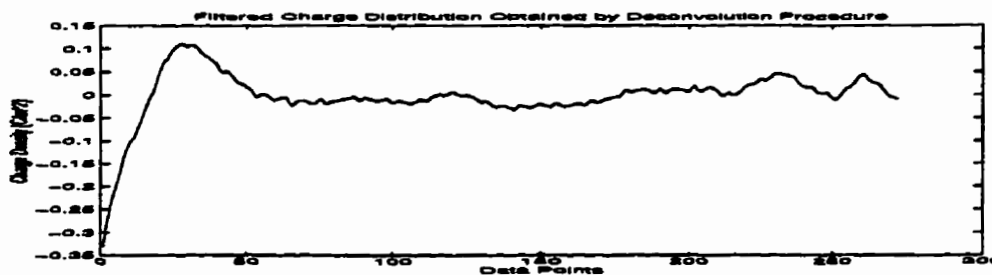


Figure 4.75 Filtered charge distribution obtained by the deconvolution procedure

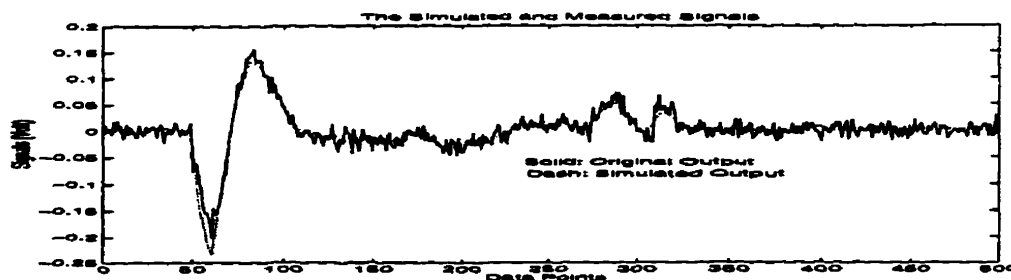


Figure 4.76 Comparison between $v_{sm}^3(k)$ and $SV(k)$ (Figure 4.75 charge distribution)

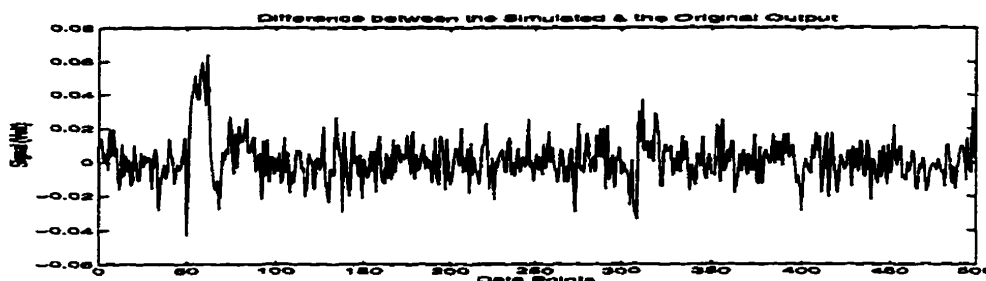


Figure 4.77 Difference between $v_{sm}^3(k)$ and $SV(k)$ of Figure 4.76

Although the filtered charge distribution is not the same as SPD2, especially near the interfaces, the representation of internal space charge distribution is not bad. This can also be seen from the results of applying the DCON to the filtered output $g_m^{3'}(k)$ and $v_{sm}^{3'}(k)$. Figure 4.78 and Figure 4.79 show $g_m^{3'}(k)$ and $v_{sm}^{3'}(k)$ which are obtained by applying the 10 point zero-phase average filter to Figure 4.7 and Figure 4.8 $g_m^3(k)$ and $v_{sm}^3(k)$, respectively. Figures 4.80 and 4.81 are the amplitudes of the Fourier transforms of $g_m^{3'}(k)$ and $v_{sm}^{3'}(k)$. Figure 4.82 shows the charge distribution obtained by the DCON. Figures 4.83 and 4.84 compare $v_{sm}^{3'}(k)$ with $SV(k)$ using Figure 4.82 charge distribution. Figure 4.85 shows the filtered charge distribution by the deconvolution procedure and Figures 4.86 and 4.87 compare $v_{sm}^{3'}(k)$ with $SV(k)$ generated using the filter charge distribution. The first surface charge is again falsely represented, resulting in a large difference between $v_{sm}^{3'}(k)$ with $SV(k)$ around that position. The internal space charge distribution is still acceptable, but surface charges and space charge near the interfaces are far from being represented well. Therefore, as compared with the DM at the conditions of noise-corrupted signals, short duration IR, and slow changes of space charge distribution, the DCON has no advantages over the DM; instead, the DM seems better than the DCON because of the simple way in which it obtains the space charge distribution.

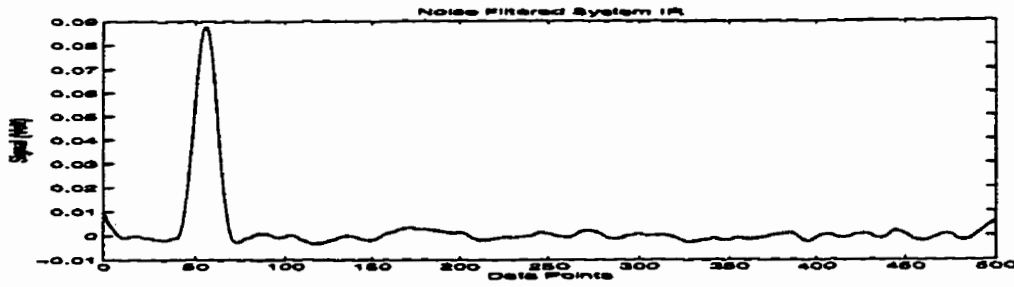


Figure 4.78 Filtered system IR $g_m^{3'}(k)$

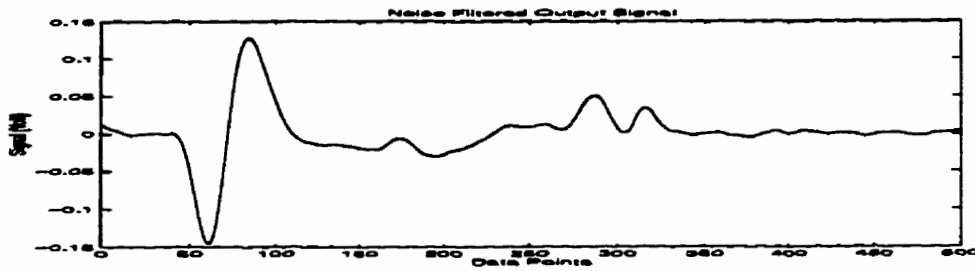


Figure 4.79 Filtered output signal $v_{sm}^{3'}(k)$

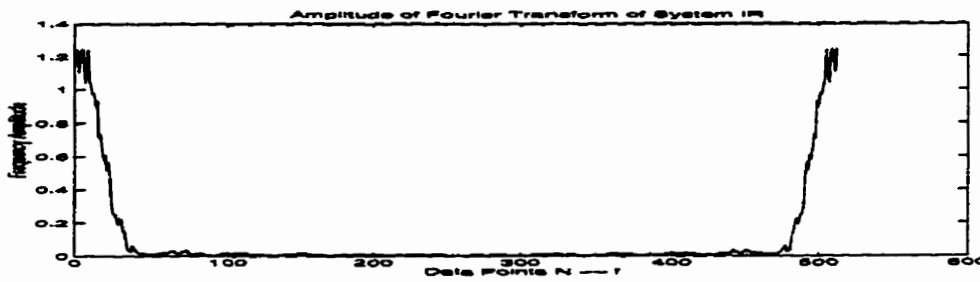


Figure 4.80 Amplitude of Fourier transform of filtered IR $g_m^{3'}(k)$



Figure 4.81 Amplitude of Fourier transform of filtered output signal $v_{sm}^{3'}(k)$

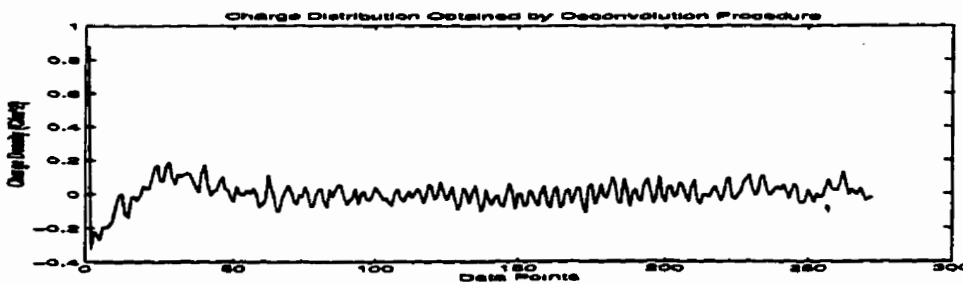


Figure 4.82 Charge distribution for filtered signals by the DCON

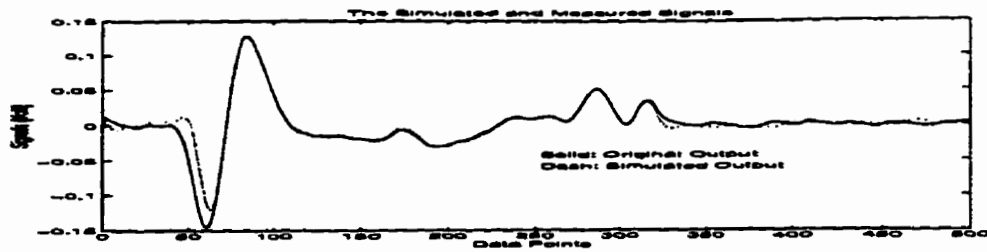


Figure 4.83 Comparison between $v_{sm}^3(k)$ and $SV(k)$ (Figure 4.82 charge distribution)

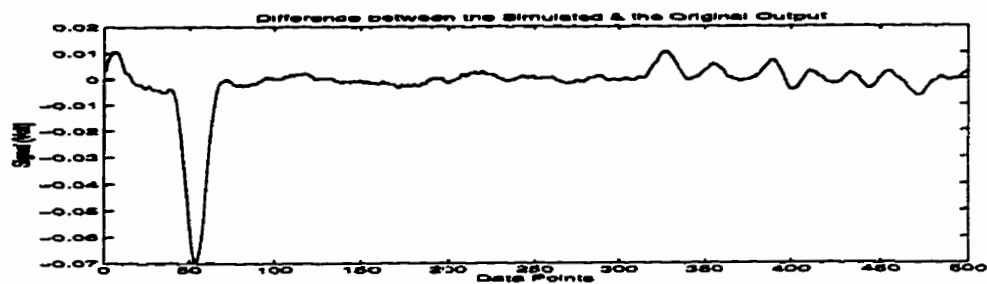


Figure 4.84 Difference between $v_{sm}^3(k)$ and $SV(k)$ of Figure 4.83

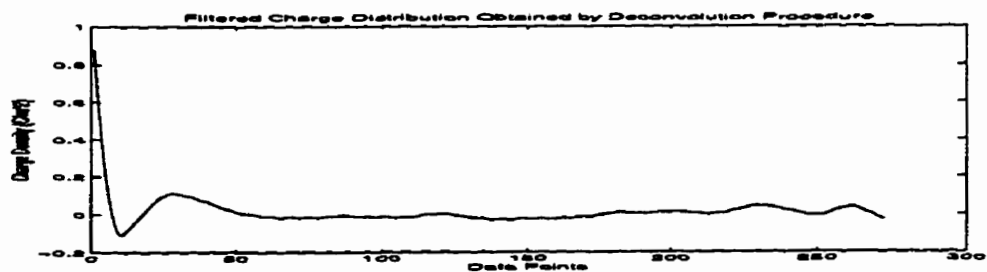


Figure 4.85 Filtered charge distribution

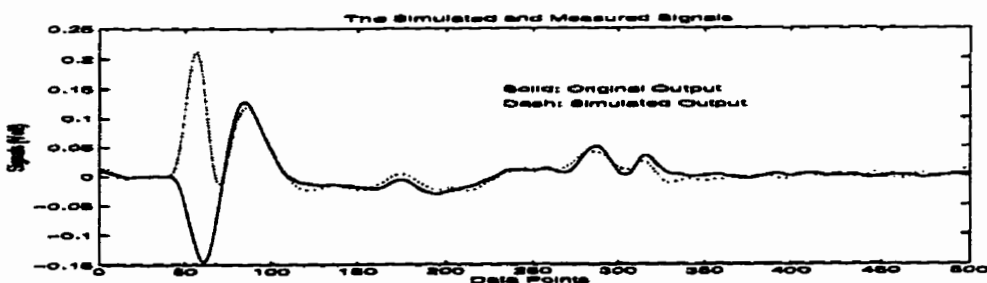


Figure 4.86 Comparison between $v_{sm}^3(k)$ and $SV(k)$ (Figure 4.85 charge distribution)

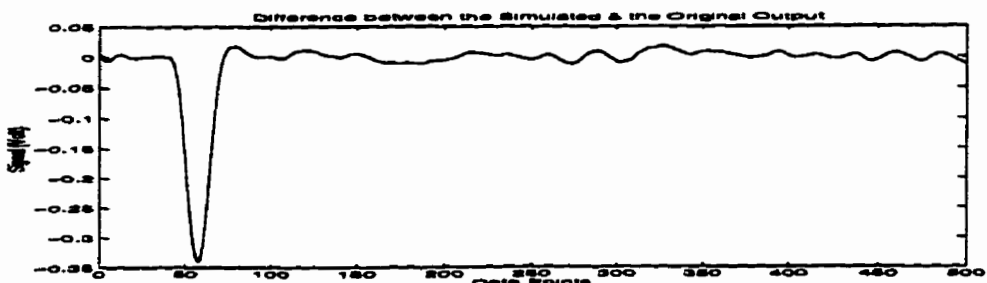


Figure 4.87 Difference between $v_{sm}^3(k)$ and $SV(k)$ of Figure 4.85

3) The point matching simulation model (PMSM) approach

Figures 4.88 and 4.89 show the σ sequence obtained by the PMSM using Figures 4.78 and 4.79 filtered output when m_0 is set at point 47, $\Delta=2$ and $\Delta'=4$, respectively. Figure 4.90 and Figure 4.98 show the charge distribution obtained using Figure 4.88 and Figure 4.89 sequences. The constructing procedures are the same as described in Section 4.2.4, 3) for the 2nd set of signals. The 10 point zero-phase filter is used to obtain Figure 4.90 charge distribution while the zero-order-hold is used to obtain Figure 4.98 charge distribution. Figures 4.91, 4.92, 4.99 and 4.100 compare $v_{sm}^3(k)$ and $SV(k)$ using Figures 4.90 and 4.98 charge distribution respectively. It is clear from the difference plot(Figures 4.92 and 4.100) that the difference near the interfaces is a bit larger than that inside the sample. As the total sum of the charge is zero for SPD2, one can adjust $\sigma(N+2)$ to equal the sum of the obtained charge distribution from $i=1$ to $N+1$. Figures 4.93 and 4.101 show the charge distributions after adjusting the value at $N+2$. Figures 4.94, 4.95, 4.102, and 4.103 compare $v_{sm}^3(k)$ and $SV(k)$ using Figure 4.93 and Figure 4.101 charge distribution correspondingly. One can see that the difference (Figure 4.95 and Figure 4.103) gets a bit smaller around the adjusted place. Figures 4.96, 4.97 and 4.104, 4.105 compare between $v_{sm}^3(k)$ and $SV(k)$ using Figures 4.93 and 4.101 charge distributions respectively.

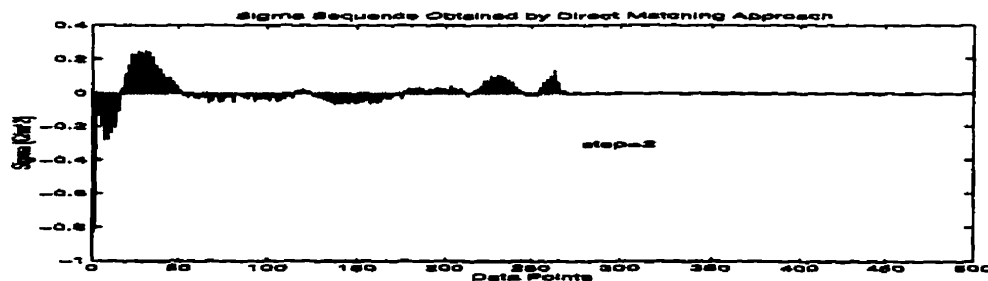


Figure 4.88 σ sequence obtained by the PMSM when $\Delta=2$, $m_0=47$

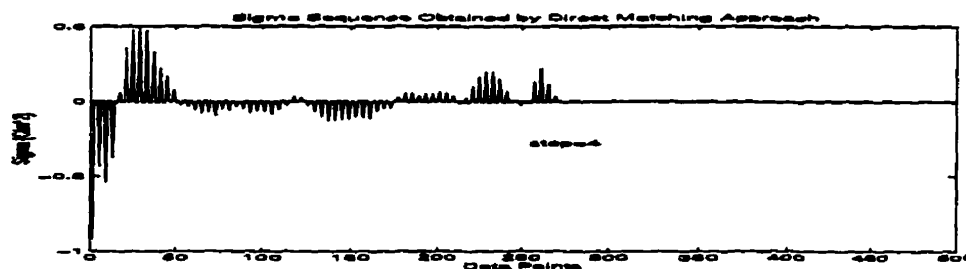


Figure 4.89 σ sequence obtained by the PMSM when $\Delta'=4$, $m_0=47$

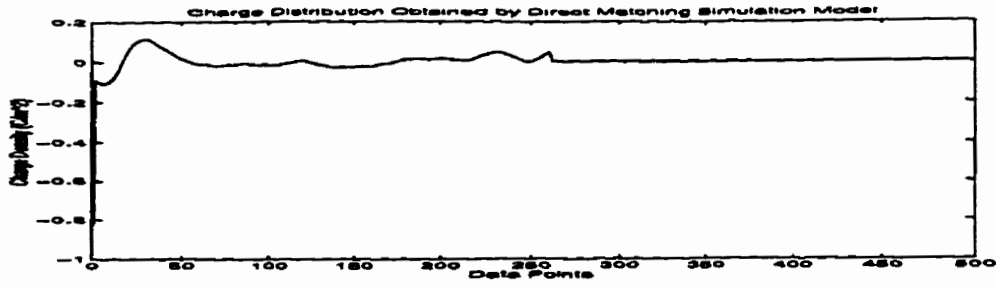


Figure 4.90 Charge distribution obtained by the PMSM(Filtered)

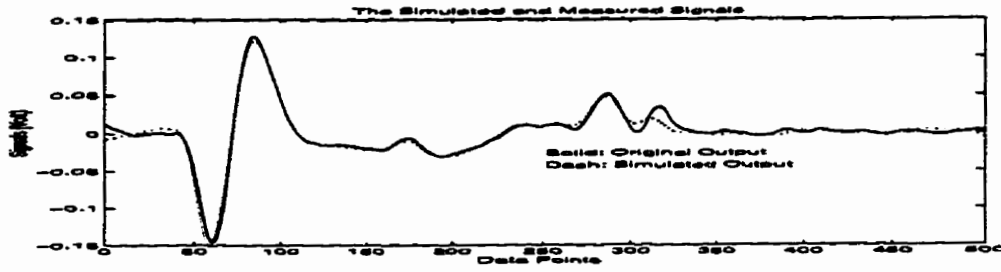


Figure 4.91 Comparison between $v_{sm}^{3'}(k)$ and $SV(k)$ (Figure 4.90 charge distribution)

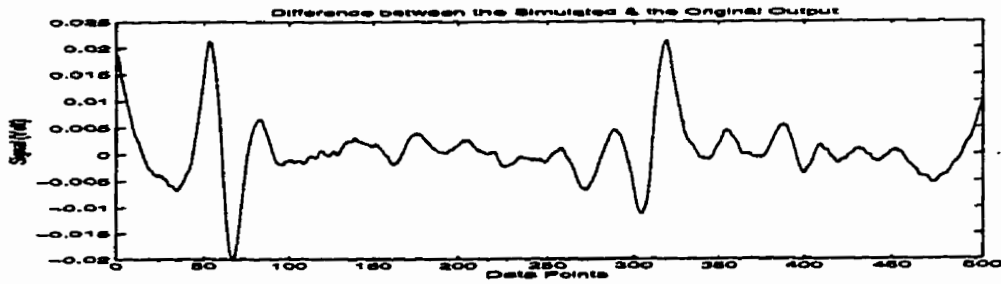


Figure 4.92 Difference between $v_{sm}^{3'}(k)$ and $SV(k)$ of Figure 4.91

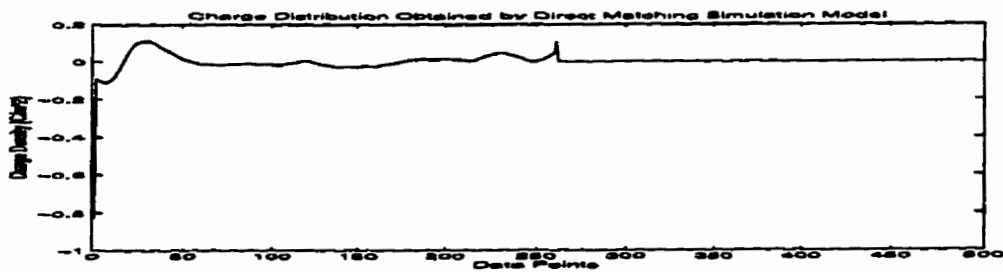


Figure 4.93 Adjusted charge distribution by the PMSM

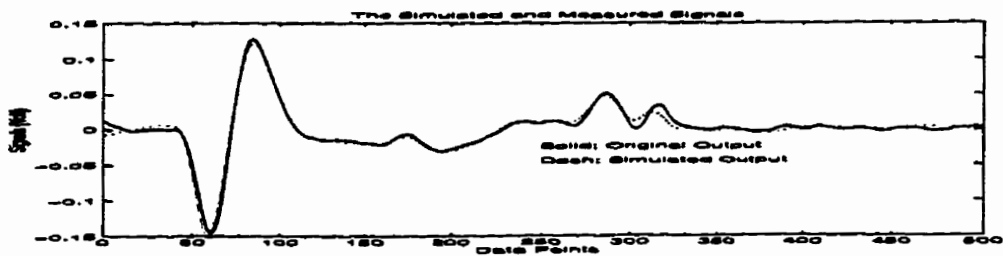


Figure 4.94 Comparison between $v_{sm}^{3'}(k)$ and $SV(k)$ (Figure 4.93 charge distribution)

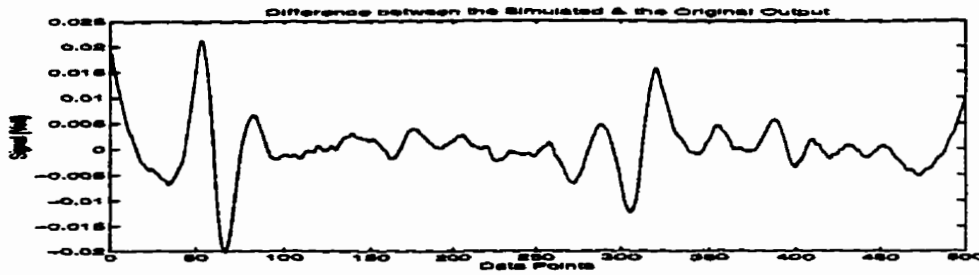


Figure 4.95 Difference between $v_{sm}^3(k)$ and $SV(k)$ of Figure 4.94

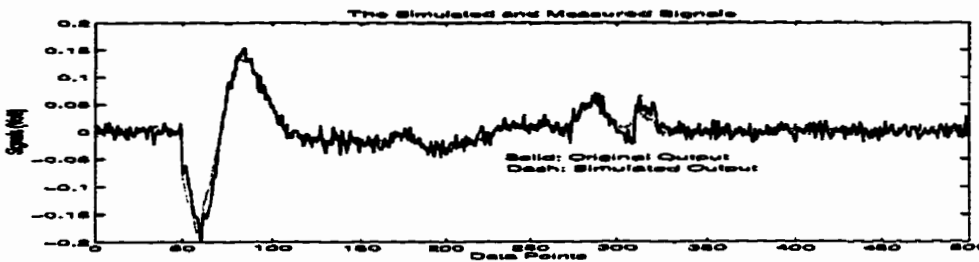


Figure 4.96 Comparison between $v_{sm}^3(k)$ and $SV(k)$ (Figure 4.93 charge distribution)

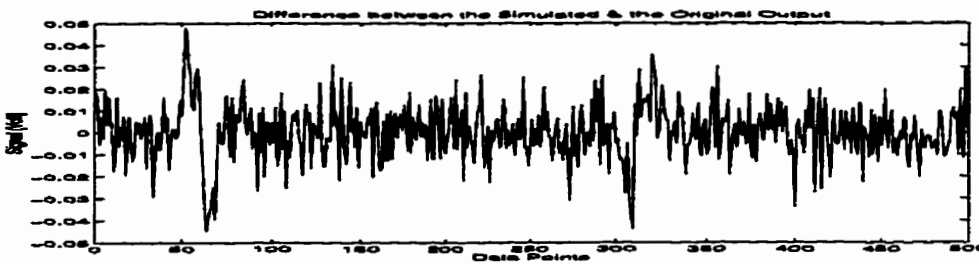


Figure 4.97 Difference between $v_{sm}^3(k)$ and $SV(k)$ of Figure 4.96



Figure 4.98 Charge distribution by PMSM(zero order hold)

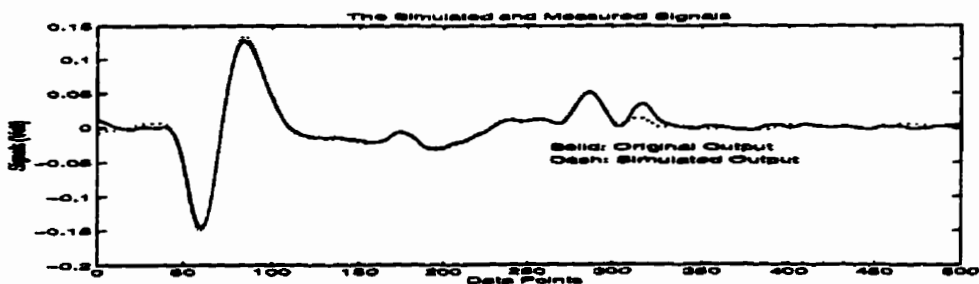


Figure 4.99 Comparison between $v_{sm}^3(k)$ and $SV(k)$ (Figure 4.98 charge distribution)

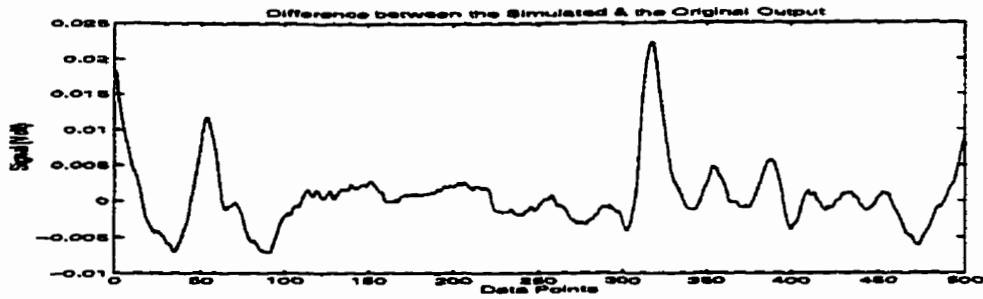


Figure 4.100 Difference between $v_{sm}^3(k)$ and $SV(k)$ of Figure 4.99

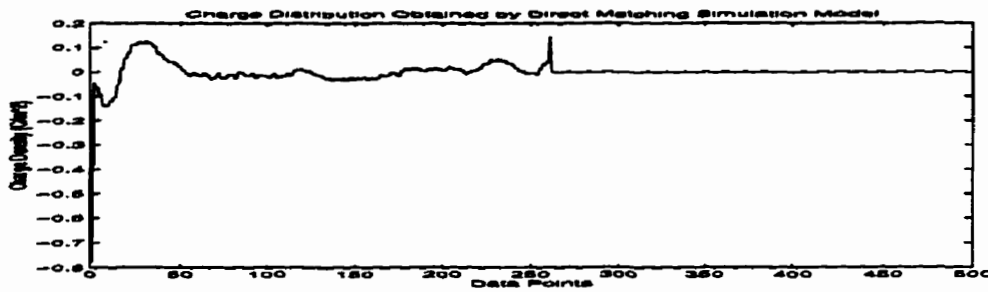


Figure 4.101 Adjusted distribution by PMSM(zero-order-hold)

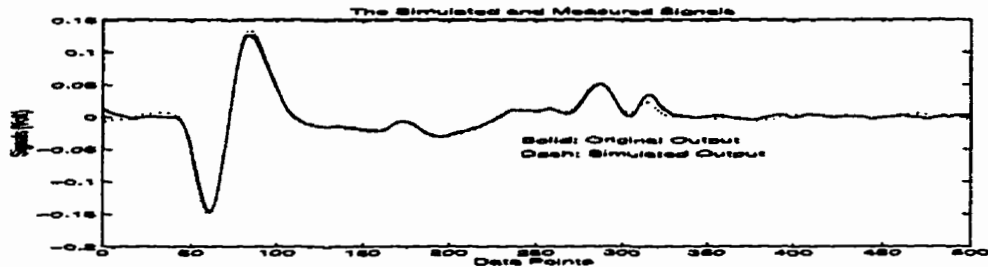


Figure 4.102 Comparison between $v_{sm}^3(k)$ and $SV(k)$ (Figure 4.101 charge distribution)

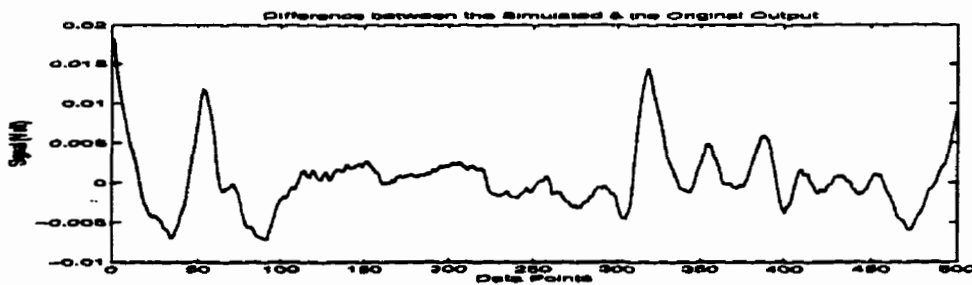


Figure 4.103 Difference between $v_{sm}^3(k)$ and $SV(k)$ of Figure 4.102

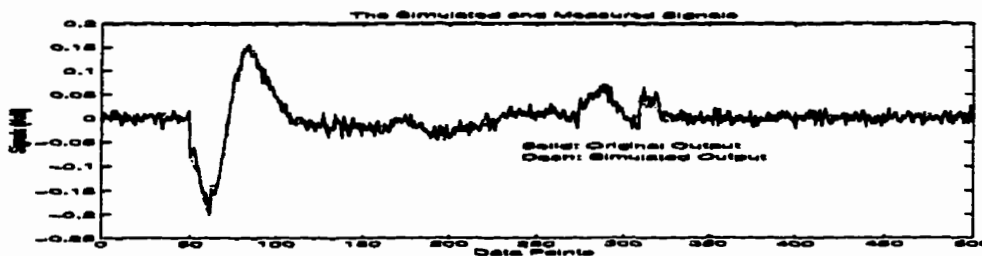


Figure 4.104 Comparison between $v_{sm}^3(k)$ and $SV(k)$ (Figure 4.101 charge distribution)

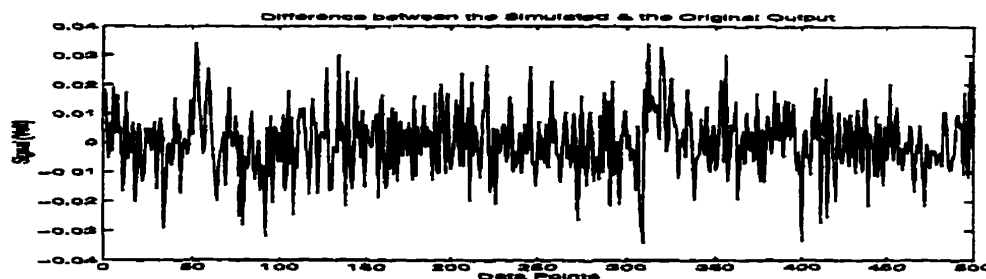


Figure 4.105 Difference between $v_{sm}^3(k)$ and $SV(k)$ of Figure 4.104

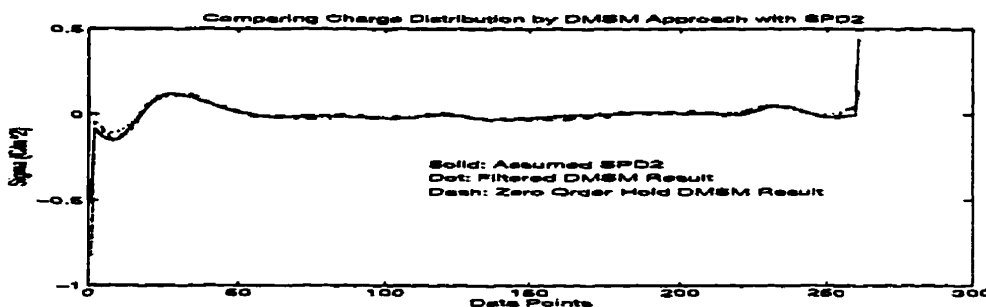


Figure 4.106 Compare Figure 4.93 and Figure 4.101 charge distributions with SPD2

It is obvious that the resolution and accuracy of the charge distribution obtained by the PMSM are also better than those obtained by the DM and the DCON methods for a slow change in charge distribution. Figure 4.106 further compares Figure 4.93 and Figure 4.101 charge distributions with the assumed SPD2. It is shown that the obtained charge distributions by the PMSM are nearly the same as SPD2. The difference only happens a bit more near the interfaces because m_0 is set at a slightly later point to obtain a more stable result. As discussed in Chapter 3, m_0 is defined as the beginning of the system IR signal at the point where the IR value $g(m_0)=0$. When the signal is contaminated with noise, m_0 may not be well chosen if one chooses the point that the signal is zero to determine the m_0 point. If m_0 is chosen earlier, $g(m_0+1)$, which should be nonzero, may actually be zero and if the noise contributes a large percentage of the value of $g(m_0+1)$, then the obtained results will be quite unstable. Section 4.3.3 will show the effect of delay on the resulting charge distribution with experimental signals. When m_0 is chosen at a later point, the obtained $\sigma(l)$ actually accounts for several points inside the sample. This is why the resulting $\sigma(l)$ is larger than what is actually at that point. On the other hand, the matching of the signal due to $\sigma(N+2)$ will start a bit earlier. As a result, $\sigma(N+2)$ is less

than what is actually at that point. In addition, a noise reduction process applied to the noise-corrupted signals before point matching process can also cause some smearing in the results.

The fact that the PMSM results are considered better than those of the DM and the DCON methods is also due to the fact that the difference between $v_{sm}^{3'}(k)$ and $SV(k)$ using charge distribution obtained by the PMSM is less than that using the charge distributions obtained by the DM and the DCON. The difference proves to be a little bit smaller for the charge distribution constructed using the zero-order-hold than for that obtained using the zero-phase filter. This small effect can also be observed from the corresponding figures for the 2nd set of signals. The reason is that the filter leads to slightly more smeared results than the zero-order-hold. More improvement can be achieved to obtain better results through the nonlinear detection and optimization process (NDOP) using Figure 4.93 or Figure 4.101 as the initial input. However, the PMSM results are considered good enough in the sense that, if the SPD2 is used to generate $SV(k)$, the difference between $v_{sm}^{3'}(k)$ and $SV(k)$ or between $v_{sm}^3(k)$ and $SV(k)$ is at the same level as that difference using the PMSM results. Figures 4.107 and 4.108 compare the difference between $v_{sm}^{3'}(k)$ and $SV(k)$ using SPD2. Figures 4.109 and 4.110 compare $v_{sm}^3(k)$ and $SV(k)$ using SPD2.

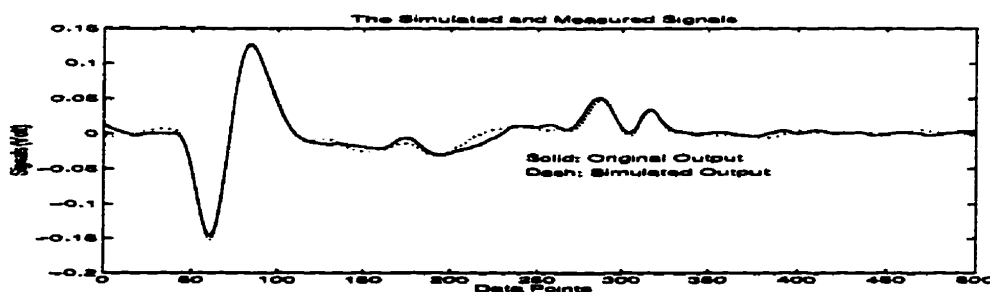


Figure 4.107 Comparison between $v_{sm}^{3'}(k)$ and $SV(k)$ (SPD2)

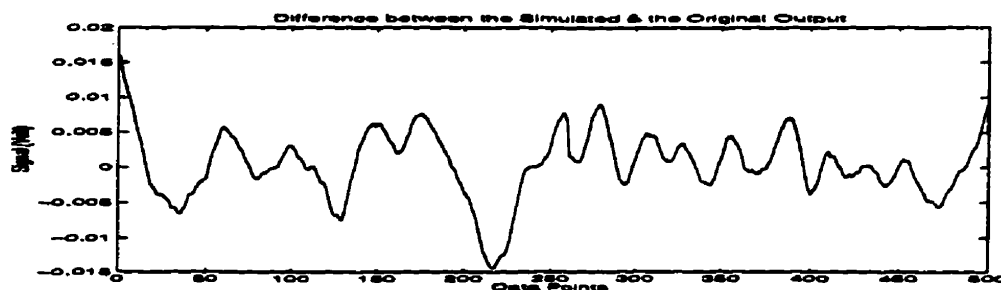


Figure 4.108 Difference between $v_{sm}^{3'}(k)$ and $SV(k)$ of Figure 4.107

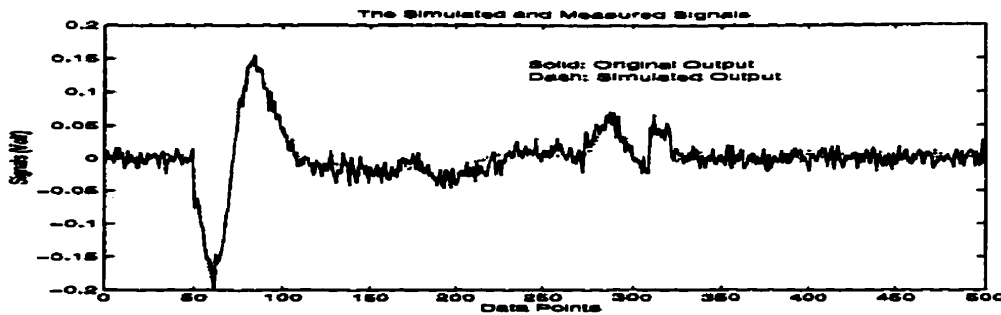


Figure 4.109 Comparison between $v_{sm}^3(k)$ and $SV(k)$ (SPD2)

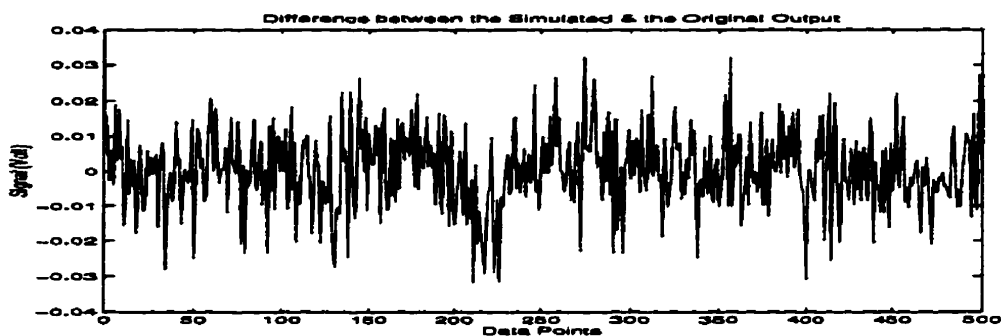


Figure 4.110 Difference between $v_{sm}^3(k)$ and $SV(k)$ of Figure 4.109

The attempt to apply NDOP to the PMSM results obtained for the 3rd set of signals is described in Appendix D-3. The representation of surface charge at point 261 can be recovered.

4.2.5 The 4th Set Signals

The 4th set of signals are $g_m^4(k)$ and $v_{sm}^4(k)$ as shown in Figure 4.10 and Figure 4.9, respectively. The charge distributions obtained by the DM, the DCON, and the PMSM methods for this set signals are presented in this section.

1) *The direct method(DM)*

The DM method cannot apply to this set of signals because the system IR has not only a wide duration but also significant rings in the signal.

2) The deconvolution procedure(DCON)

Figures 4.111 and 4.112 show the amplitude of the Fourier transform of $g_m^4(k)$ and $v_{sm}^4(k)$ respectively. Figure 4.113 gives the charge distribution obtained by the DCON procedure. Figures 4.114 and 4.115 compare $v_{sm}^4(k)$ with $SV(k)$ using Figure 4.113 charge distribution. Due to the bad distribution obtained, a 10 point zero-phase average filter is applied to Figure 4.113 to filter the charge distribution; however, the filtered charge distribution this time is not good either, as shown in Figure 4.116. Figures 4.117 and 4.118 compare $v_{sm}^4(k)$ with $SV(k)$ using Figure 4.114 charge distribution. Although the difference between $v_{sm}^4(k)$ and $SV(k)$ using the filter charge distribution, is not large compared with the noise level, the charge distribution result is obviously far from SPD2.

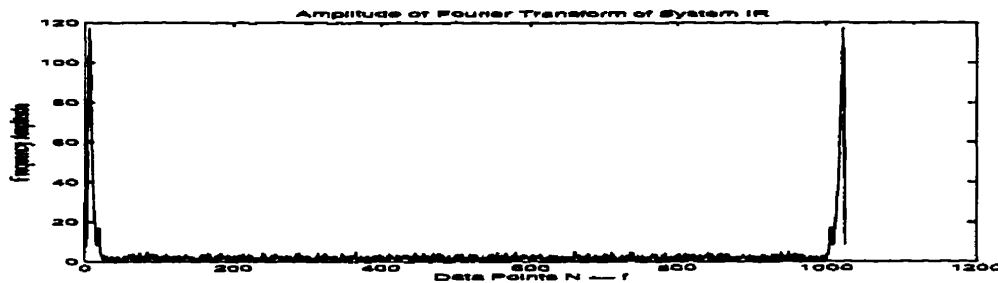


Figure 4.111 Amplitude of Fourier transform of system IR ($g_m^4(k)$)



Figure 4.112 Amplitude of Fourier transform of the output $v_{sm}^4(k)$

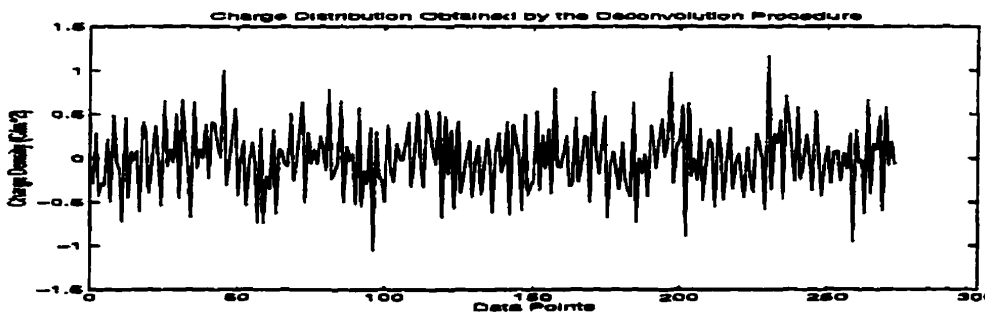


Figure 4.113 Charge distribution obtained by the DCON procedure for the 4th set

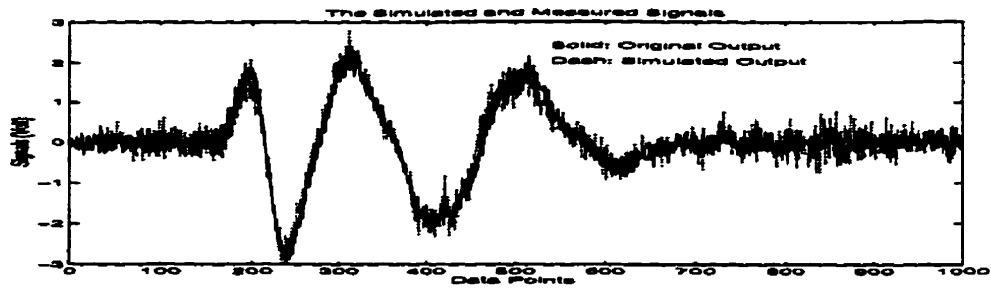


Figure 4.114 Comparison between $v_{sm}^4(k)$ with $SV(k)$ (Figure 4.113 charge distribution)

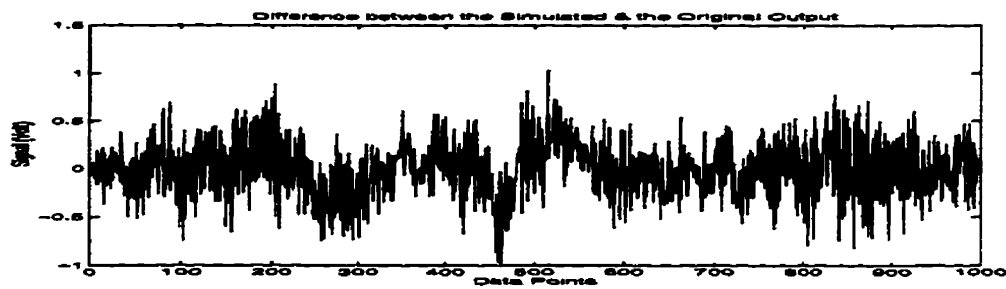


Figure 4.115 Difference between $v_{sm}^4(k)$ with $SV(k)$ of Figure 4.114

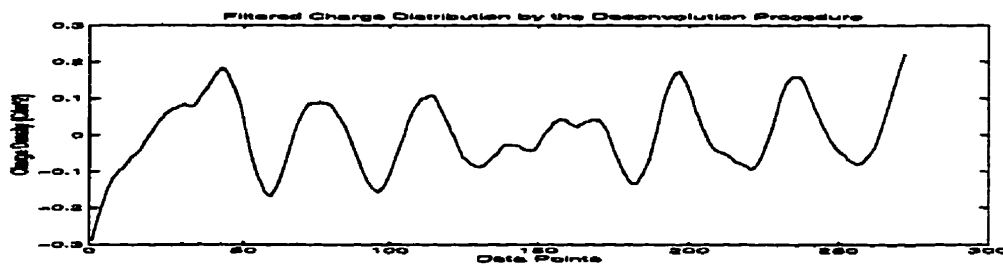


Figure 4.116 Filtered charge distribution by the DCON

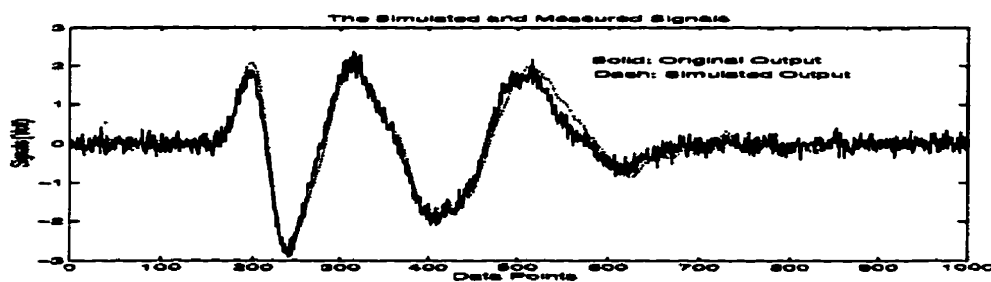


Figure 4.117 Comparison between $v_{sm}^4(k)$ with $SV(k)$ (Figure 4.116 charge distribution)

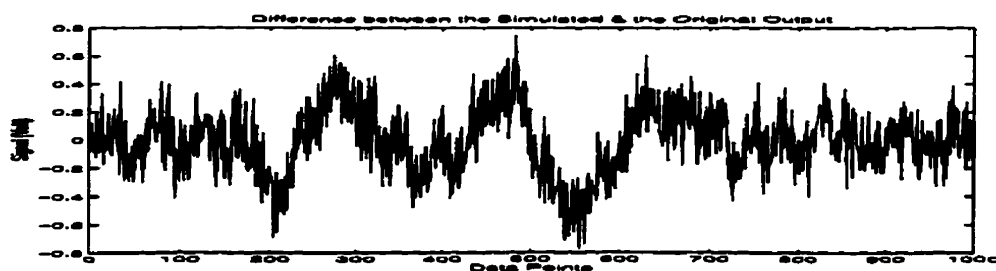


Figure 4.118 Difference between $v_{sm}^4(k)$ with $SV(k)$ of Figure 4.117

When the system IR has a wide duration and, more importantly, the rise time of the IR is slow, the bandwidth of the system is narrow. When the bandwidth of the system is narrow for the 4th set of signals as compared with the other sets, even the filtered charge distribution results cannot provide a good profile of the charge distribution. This demonstrates that the DCON is also sensitive to the bandwidth effects.

3) The proposed PMSM approach

Figures 4.119 and 4.120 show the signal output $g_m^{4'}(k)$ and $v_{sm}^{4'}(k)$ when a 10 point zero-phase average filter applied to $g_m^4(k)$ and $v_{sm}^4(k)$ as shown in Figure 4.10 and Figure 4.9. Figures 4.121 and 4.122 give the obtained σ sequences using the point matching approach when m_0 is set at point 162, $\Delta=2$ and $\Delta'=4$ respectively.

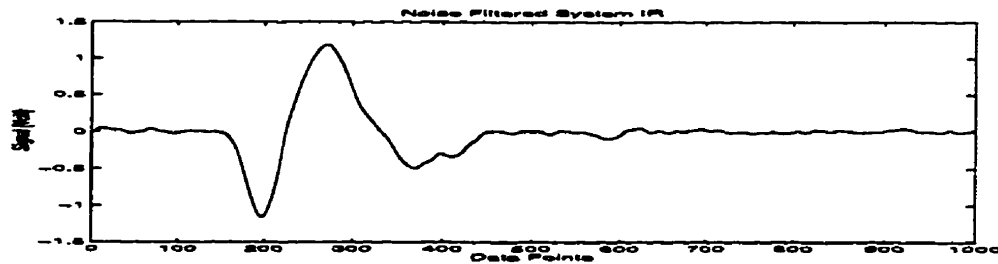


Figure 4.119 Filtered system IR ($g_m^{4'}(k)$)

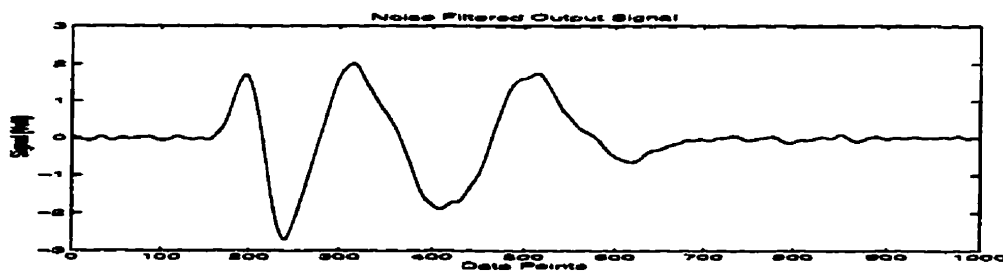


Figure 4.120 Filtered output signal ($v_{sm}^{4'}(k)$)

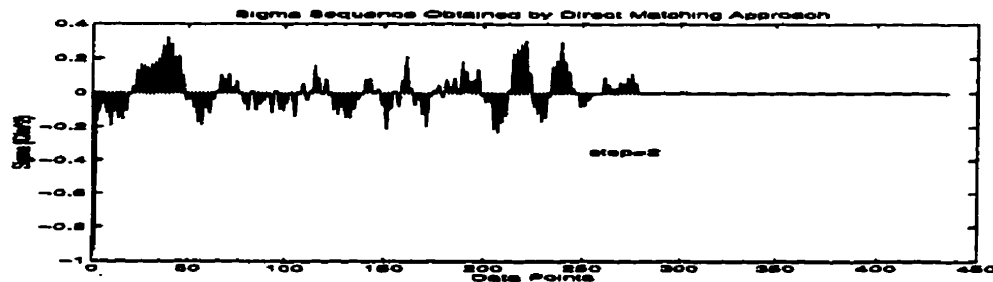


Figure 4.121 σ sequences using PMSM when $m_0=162$ and $\Delta=2$

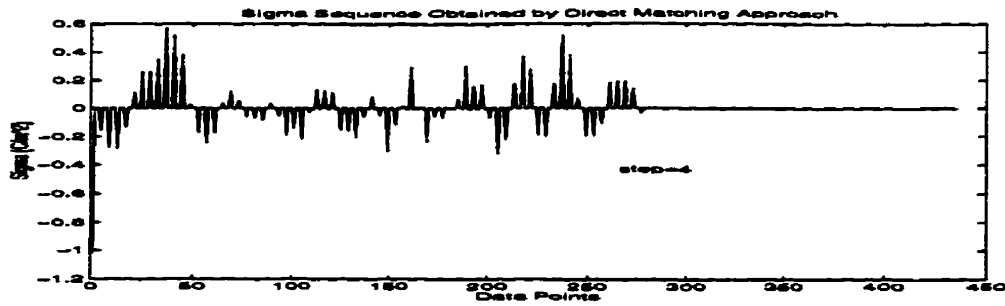


Figure 4.122 σ sequences using PMSM when $m_0=162$ and $\Delta'=4$

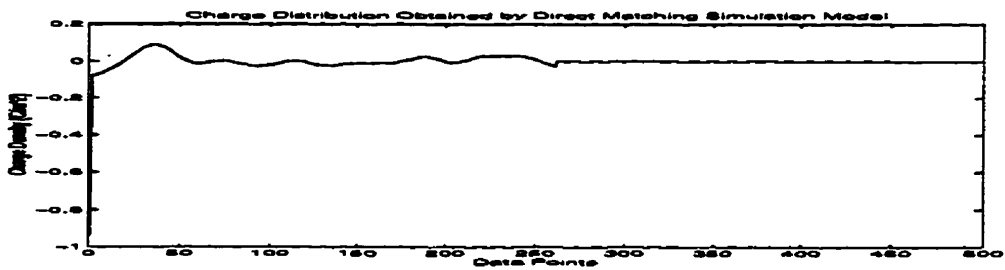


Figure 4.123 Charge distribution obtained by the PMSM(Filterd)

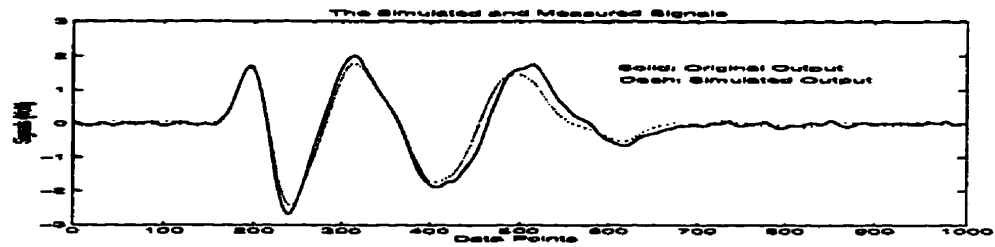


Figure 4.124 Comparison between $v_{im}^{*}(k)$ with $SV(k)$ (Figure 4.122 charge distribution)



Figure 4.125 Difference between $v_{im}^{*}(k)$ and $SV(k)$ of Figure 4.124

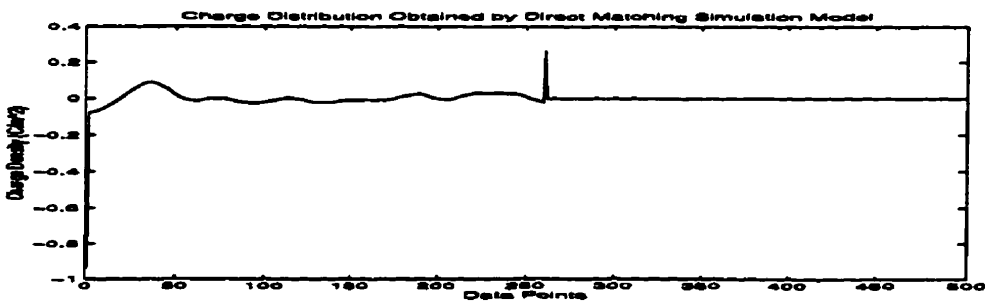


Figure 4.126 Charge distribution by the PMSM after adjustment

Figure 4.123 shows the filtered charge distribution obtained using the direct matching simulation model. A 20 point zero-phase average filter is applied at this time. Figures 4.124 and 4.125 compare $v_{sm}^4(k)$ with $SV(k)$ using Figure 4.123 charge distribution. Based on the total charge being zero, Figure 4.126, the adjusted charge distribution is obtained. Figures 4.127 and 4.128 compare $v_{sm}^4(k)$ with $SV(k)$ generated using Figure 4.126 charge distribution, and Figures 4.129 and 4.130 compare $v_{sm}^4(k)$ with the $SV(k)$.

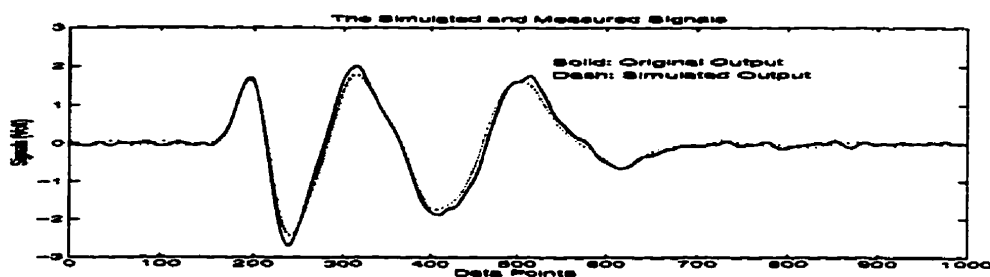


Figure 4.127 Comparison between $v_{sm}^4(k)$ with $SV(k)$ (Figure 4.126 charge distribution)

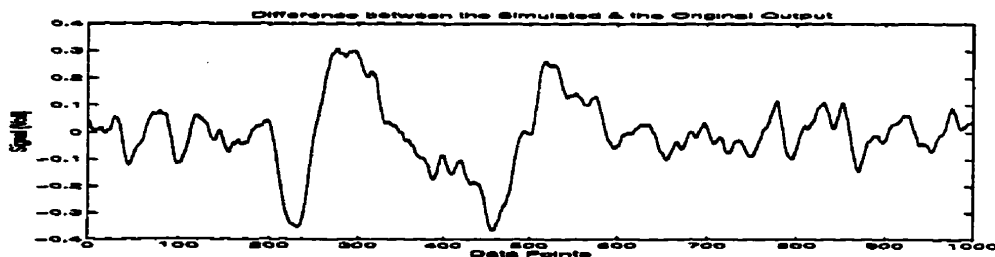


Figure 4.128 Difference between $v_{sm}^4(k)$ with $SV(k)$ of Figure 4.127

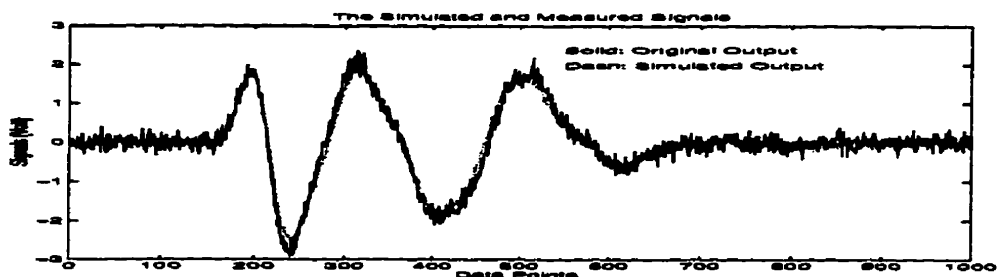


Figure 4.129 Comparison between $v_{sm}^4(k)$ with $SV(k)$ (Figure 4.126 charge distribution)

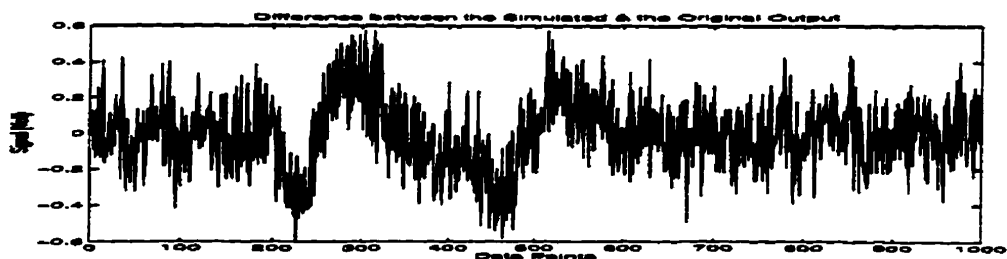


Figure 4.130 Difference between $v_{sm}^4(k)$ and $SV(k)$ of Figure 4.129

It is clear that the difference for the adjusted charge distribution in Figure 4.128 is less in magnitude than that for unadjusted charge distribution in Figure 4.125.

As the system bandwidth is decreased, the obtained charge distribution cannot be better than that obtained for the 3rd set of signals, which means that bandwidth effects exist in the PMSM approach. However, the PMSM is less sensitive to the bandwidth effects than the DCON. As compared to Figure 4.126, charge distribution with SPD2, the charge distribution profile is correct; therefore, it is still true that the resolution and accuracy of the PMSM is much better than those of the DM and the DCON.

In regards to what has been done to the 2nd and the 3rd sets of signals, Figures 4.131 and 4.132 compare $v_{sm}^{\wedge}(k)$ with $SV(k)$; while Figures 4.133 and 4.134 compare noise-corrupted $v_{sm}^{\wedge}(k)$ with $SV(k)$ using SPD2 charge distribution. Comparing the difference in Figure 4.128 and Figure 4.130 (using Figure 4.126 charge distribution) with that in Figure 4.132 and Figure 4.134 (using SPD2), one can observe that, although the difference using Figure 4.126 charge distribution is larger in amplitude than using SPD2, some information about the charge distribution does not seem to be represented well. This information can be recovered through the nonlinear detection and optimization process (NDOP). Because it is known that the nonlinear stochastic process can provide high resolution, Figure 4.126 charge distribution is used as an initial value for the NDOP. The results of the application of the NDOP for the 4th set of signals is shown in Appendix D-4, which proves that the nonlinear stochastic process can handle the noise effects and the bandwidth effects better than a linear stochastic process, but with much more computation time.

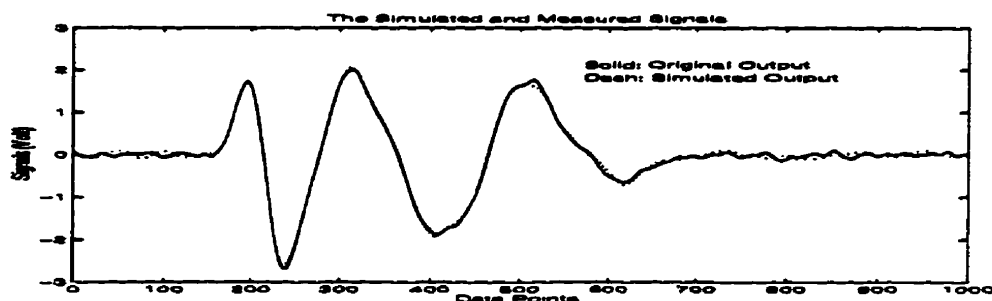


Figure 4.131 Comparison between $v_{sm}^{\wedge}(k)$ and $SV(k)$ (SPD2)

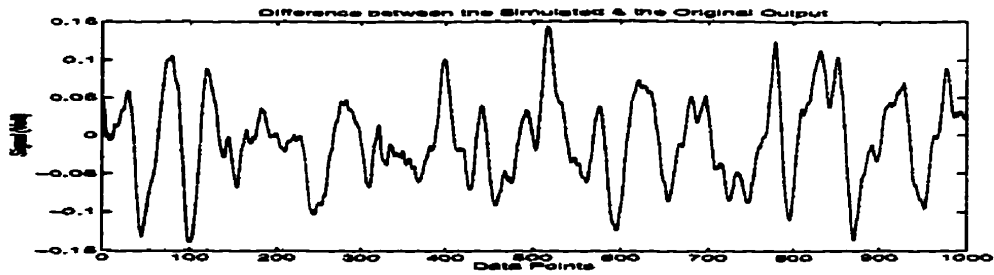


Figure 4.132 Difference between $v_{sm}^4(k)$ and $SV(k)$ of Figure 4.131

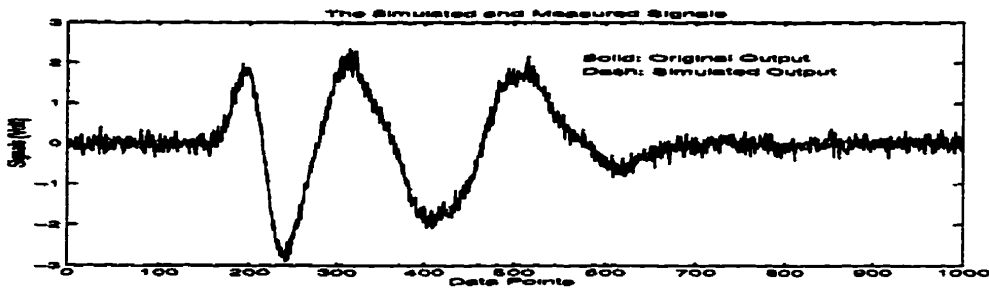


Figure 4.133 Comparison between $v_{sm}^4(k)$ and $SV(k)$ (SPD2)

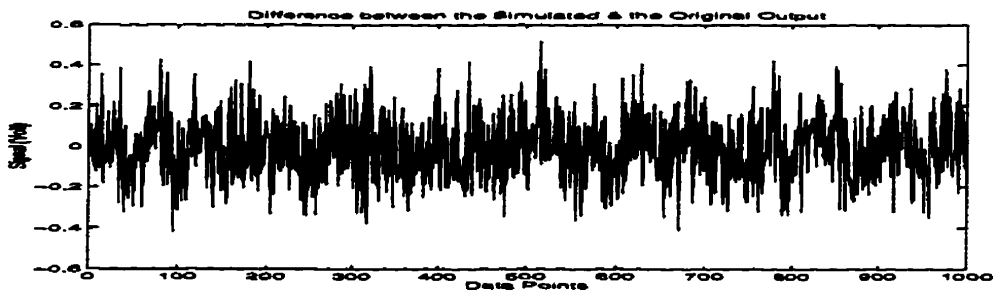


Figure 4.134 Difference between $v_{sm}^4(k)$ and $SV(k)$ of Figure 4.133

The charge distribution results using the three methods to process the four sets of synthetic signals are discussed and summarized in Section 4.4. The overall conclusion is that the PMSM method seems to be the best approach among the three methods. In the next section, Section 4.3, the PMSM method is verified from an experimental point of view with two sets of experimental signals: one contains only surface charges; the other contains both surface charges and the space charge distribution.

4.3 PMSM CRITIQUE FROM AN EXPERIMENTAL POINT OF VIEW

4.3.1 Introduction

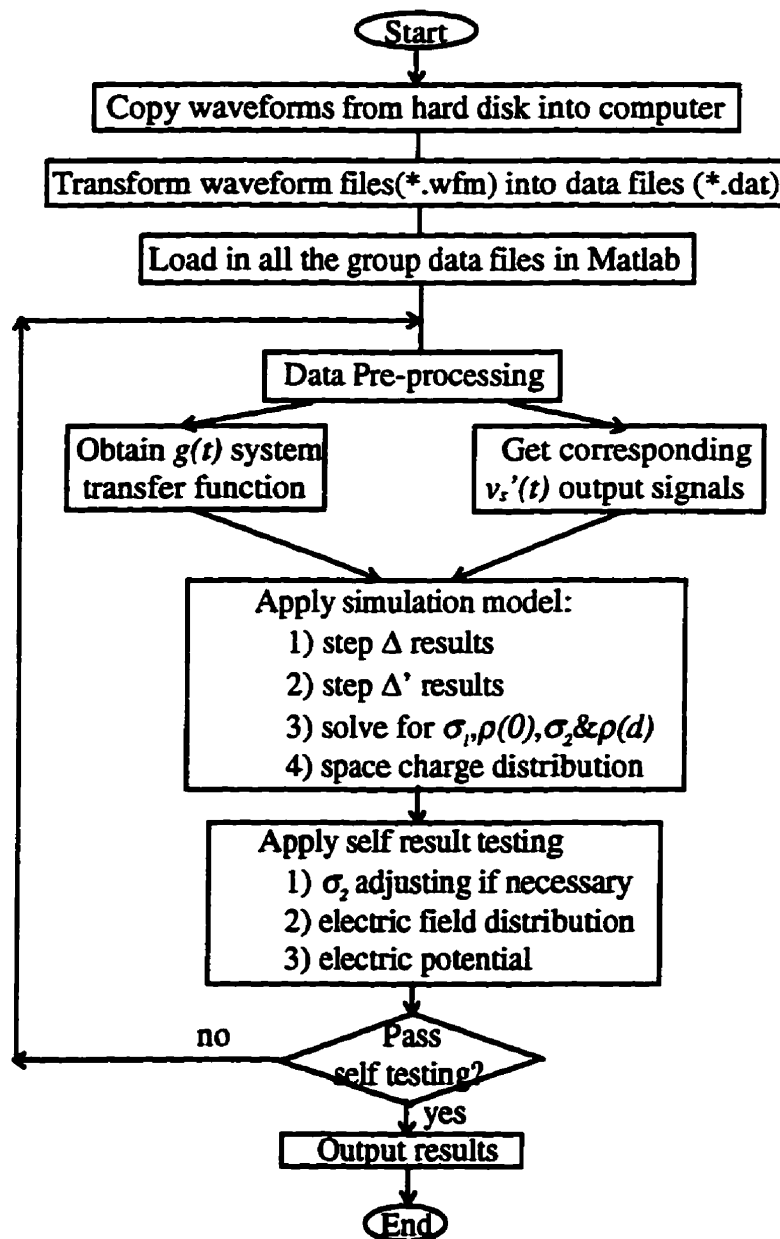
Synthetic signals can be used to verify whether a signal processing method is working or, more specifically, to illustrate the capability, the resolution and accuracy, and the advantages and disadvantages of the signal processing method. However, since the signal processing method is intended to be applied to the experimental signals(i.e. the real signals), it is necessary to further verify whether the signal processing method is working well with the experimental signals and to discover how to obtain good results from the experimental signals using the signal processing method.

In addition to the noise described in the noise model for synthetic signals (assumed to be a white Gaussian sequence with zero mean), many other disturbances can exist in the detected experimental signals, such as a dc trend (resulting in non-zero mean noises)[92] or even a low frequency trend (resulting in colored noise)[82]. Thus, the experimental signals may not approach the models that have been set up in order for the signal processing method to apply. Although one cannot get rid of these trends, it is necessary and possible to minimize the trends through some data pre-processing procedures. It is important not only to pre-process the measured output signals before applying signal processing methods to them, but also to test the obtained results from the signal processing method before regarding them as the correct results. Unlike synthetic signal processing, where one knows exactly the charge distribution used to build up the synthetic signals, there is no “standard” charge distribution available for one to test whether the obtained charge distribution correctly and accurately reflects the actual charge distribution. However, the experimental conditions are known, and therefore, it is important to test whether the obtained charge distribution satisfies the experimental conditions.

Table 4.1[94] shows the PMSM procedures that are set up for processing experimental signals. Section 4.3.2 discusses the procedures in detail. To demonstrate the procedures and verify the

results obtained by the PMSM, two experimental signals are used: one is used to generate the system transfer function(IR), which is considered to contain only surface charges in the charge distribution; the other is the arbitrary selected measured signal at -60kV dc voltage application. Section 4.3.3 shows how the two signals are processed and what results are obtained.

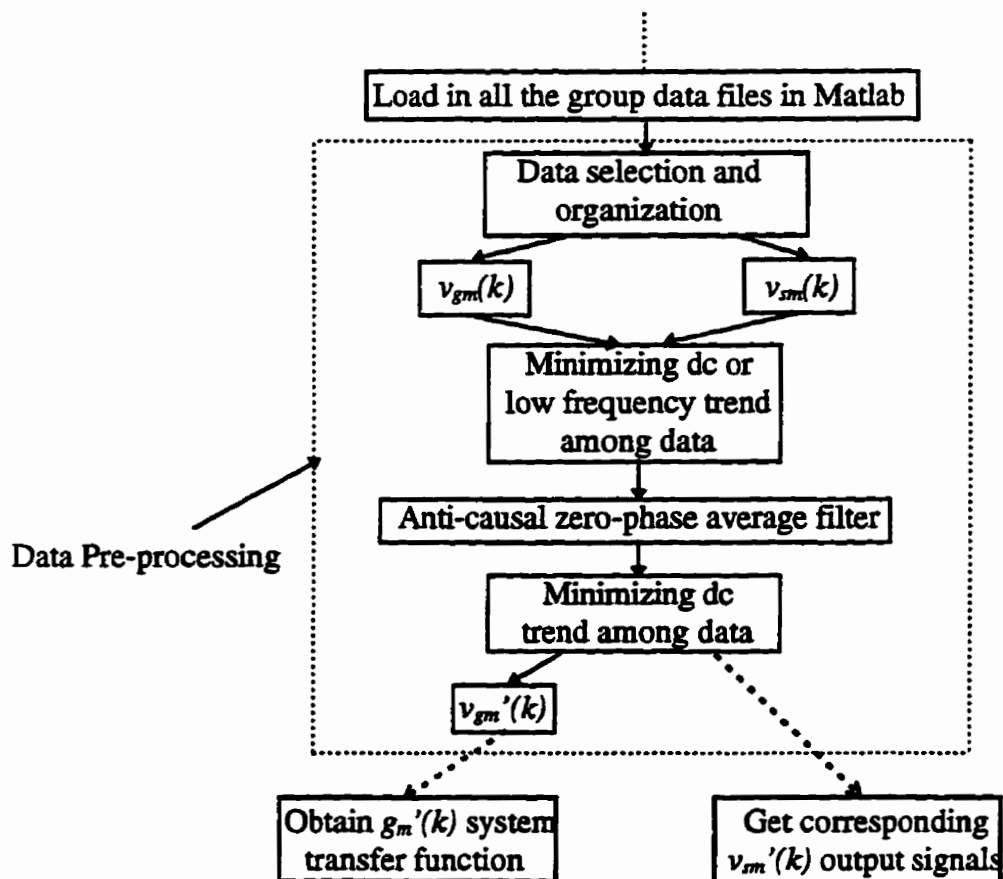
TABLE 4.1
BLOCK DIAGRAM OF EXPERIMENTAL SIGNAL PROCESSING PROCEDURES



4.3.2 Experimental Signal Processing Procedures

The principal set-up of the PEA method has been shown in Figure 2.1(Chapter 2). The experimental set-up of our PEA system can be found in Figure 5.1(Chapter 5). The procedures as shown in Table 4.1 are used to process each group of data obtained for each specimen. The TDS644A 500MHz digital oscilloscope is used in the experiments. It has a feature that allows one to save waveforms into a 3.5" disk with *.wfm files. Converting software is available which can transform *.wfm files into *.dat files. The *.dat file can be loaded in Matlab easily, and the data can be processed using Matlab code.

TABLE 4.2
A ROUTINE USED FOR DATA PRE-PROCESSING



When all the group data files are loaded in Matlab as shown in Table 4.1, a data pre-processing programs will be applied to them. The data pre-processing is a prerequisite for all

experimental signals. The same processing routine must be applied to all the group signals. It was found the routine shown in Table 4.2 works well.

When all the group data are loaded in, the *data selection and organization procedure* will select signals that can be used as the system IR (transfer function); decide how to minimize the influence of the second term in equations (3-2) and (3-4) using either of the three approaches as described in Chapter 3; and process all signals accordingly. For our experimental situation, the sample has no or little previous space charge, the signal obtained when only the electric pulse voltage is applied to the specimen (dc voltage application is 0 kV) is selected as $v_{sm0}(k)$. After all the other signals detract this $v_{sm0}(k)$ signal, the influence of the second term is taken out, and their corresponding $v_{sm}(k)$ are obtained. The selected signal that is used to generate the system IR will be processed the same way as all the other signals. The selection of the system IR signal is made to one signal or the sum of several signals at a low dc voltage application (less than the charge injection voltage). Then, this selected signal subtracts $v_{s0}(k)$, and the output of the subtraction is denoted as $v_{gm}(k)$.

When $v_{gm}(k)$ and $v_{sm}(k)$ are obtained, the next step is to minimize the small different dc biases or low frequency trends among the group signals. This is the most significant function of data pre-processing. Several methods can be applied to get the trends, such as calculating the average value of the first 100 points of data of the signal; calculating the average value of all the data of the signal; and applying a very low frequency pass filter(for example, a 200 point zero-phase average filter for a total 500 point signal) to the signal many times until the difference between the filtered signal at this time and the filtered signal at the last time is within a small tolerance. When the trend is obtained, the trend is subtracted from the signal; the trend in the subtracted signal is then minimized.

When the measured output signals are noisy (i.e. corrupted with high frequency random noise), a noise reduction process is necessary. Then a 10 or 20 point(depending on the total points of the signal) anti-causal zero-phase average filter is used to minimize the high frequency noises. After that, the dc trend is minimized again; then the obtained signal can be denoted as $v_{gm}'(k)$ or $v_{sm}'(k)$.

The system transfer function $g_m'(k)$ is essential to the accuracy and resolution of the obtained space charge distribution. It is defined as the system response to IC/m^2 surface charge density[2]. When $v_{gm}'(k)$ is available, two more processing steps are used to get $g_m'(k)$. One is to divide $v_{gm}'(k)$ by the dc voltage difference between the two signals used to generate $v_{gm}(k)$ times $\epsilon_0\epsilon_r/d$, where d is the thickness of the specimen. The other is to choose three cutting points from the obtained signal: the starting point of the first interface signal $p1$, the starting point of the second interface signal $p2$ and the first peak point of the second interface signal $p3$. When $p1$, $p2$, and $p3$ are available, we retain signal voltage values within $p1$ and $p2$, and set values to zero for data points less than $p1$ and more than $p2$, the system IR ($g_m'(k)$) is thus obtained. The point $p3$ is chosen as the termination point for the PMSM. The simulation will stop when the $p3$ point is reached.

This method to obtain the system IR ($g_m'(k)$) is correct under the assumption that there is no or a negligible amount of space charge inside the specimen; and if the specimen already has space charges, the sudden increased voltage will not change the inside space charge profile significantly.

With $g_m'(k)$ and $v_{sm}'(k)$, one can apply PMSM as already discussed in Section 4.2 to obtain the surface charges σ_1 , σ_2 , and space charge distribution. For experimental signal processing, it is better to apply self-testing[94] to see whether the obtained charge distribution results are acceptable. For the experimental conditions, it is known that, when the potential of the ground electrode is zero, the potential of the HV electrode equals the dc voltage applied. It is known,

$$V(x) = V(0) + \int_0^x E(x)dx \quad (4-5)$$

where, V denotes potential, E denotes the electric field,

$$V(d) = V(0) + \int_0^d E(x)dx \quad (4-6)$$

The electric field at the first interface is:

$$E_1 = -\frac{\sigma(0)}{\epsilon_0\epsilon_r} = -\frac{\sigma_1 + \sigma_p(0)}{\epsilon_0\epsilon_r}. \quad (4-7)$$

According to Poisson's law,

$$\nabla E = \frac{\rho}{\epsilon_0 \epsilon_r}, \quad (4-8)$$

the internal electric field can be calculated as:

$$E(x) = \frac{1}{\epsilon_0 \epsilon_r} \int_0^x \rho(x) dx = E_1 + \frac{1}{\epsilon_0 \epsilon_r} \sum_{i=1}^k \sigma(i). \quad (4-9)$$

where k is from 1 to $N+1$ corresponding to x from Δx to d . Therefore, the potential $V(d)$ can be calculated using the obtained charge distribution. The calculated $V(d)$ can then be compared with the applied voltage. If the two are close with an acceptable difference, self-testing is passed and the results are considered acceptable. If the two are far from each other for all the group data, one has to check the reason and go back to the pre-processing. By suitable adjustment of data pre-processing, one can usually obtain the charge distributions that can pass self-testing.

In addition, the experimental condition requires that the electric field at the second interface satisfies:

$$E_2 = \frac{\sigma(N+1)}{\epsilon_0 \epsilon_r} = \frac{\sigma_2 + \sigma_\rho(d)}{\epsilon_0 \epsilon_r} = E_1 + \frac{1}{\epsilon_0 \epsilon_r} \sum_{i=1}^{N+1} \sigma(i). \quad (4-10)$$

Therefore, σ_2 can be adjusted.

Two experimental signals measured for the Thick HDPE specimen are used to demonstrate the presented procedures in the next section. Detailed information about the Thick HDPE specimen and the experimental set-up is presented in Chapter 5.

4.3.3 Experimental Signals and Processing Results

Figure 4.135 shows three measured signals for a Thick HDPE specimen using the Figure 5.1 experimental set-up. One signal is obtained when only the electric pulse voltage(-2.3kV) is applied (no dc voltage application, i.e. dc voltage at 0 kV) to the specimen, which has not been subjected to any electric stress before and has virtually no space charge inside. Another is the

sum of the signals when -15kV and -20kV are applied to the specimen denoted as -35kV signal. The thickness of the Thick HDPE sample is 2.35mm. It is assumed that no space charge is injected when -15kV and -20kV are applied. This signal is selected to generate the system transfer function. The third is the signal measured when the sample is subjected to *Step Increased Voltage* and when the voltage reaches -60kV. This signal is denoted as the -60kV signal in this section. Detailed voltage applications for the Thick HDPE specimen can be found in Figure 5.2 in Chapter 5.

Figure 4.136 shows two signals: one is the subtraction of the total -35kV signal by the 0kV signal; the other is the subtraction of the -60kV signal by the 0kV signal. After the subtraction, the two signals can be denoted as $v_{sm}(k)$. Since the first signal is also used to generate the system transfer function, it can also be denoted as $v_{gm}(k)$. The *data selection and organization process* is complete for the two signals.

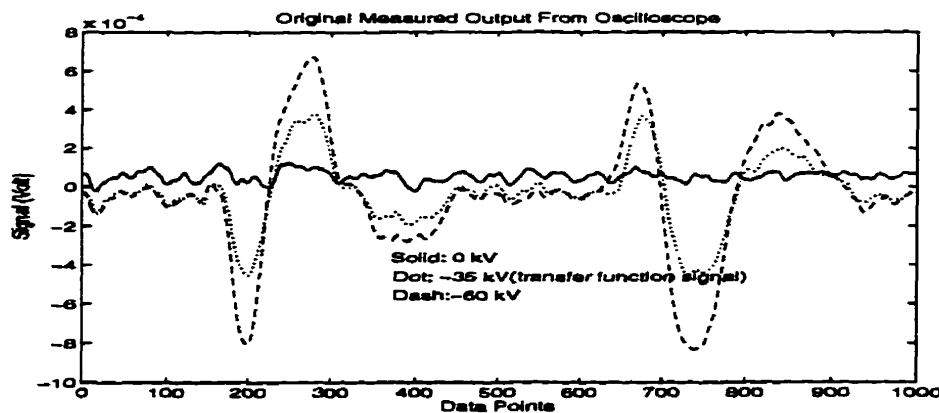


Figure 4.135 Original measured output signals

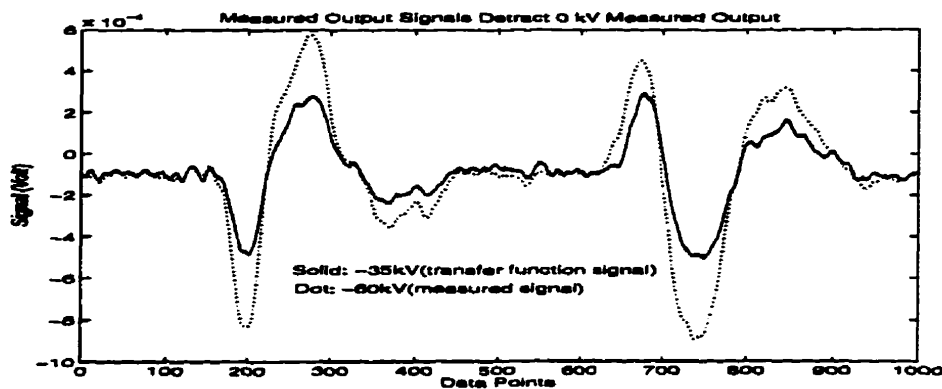


Figure 4.136 The (-35kV and -60kV) signals after the Data selection and organization process

One purpose in choosing the transfer function signal is to show how to obtain the system IR from the measurements. Besides, since it is known that the transfer function signal is regarded as containing only surface charges σ_1 and σ_2 , and $\sigma_1 = \sigma_2$, if the charge distribution obtained by the PMSM for the transfer function signal cannot reflect this fact, the PMSM method cannot be considered to be working well. Therefore, the transfer function signal is used as a verification of the PMSM method for experimental signals. The reason for choosing the -60kV signal is to demonstrate how to apply the PMSM signal processing procedures to an experimental signal, and to determine whether the PMSM signal processing procedures are working fine for an experimental signal.

Figure 4.137 shows the two signals after a dc trend minimization process. The trend was obtained by calculating the total average of the signal. Figure 4.138 shows the two signals after being filtered by a 20 point zero-phase average filter and a dc trend minimized by the total signal average again. Both signals can be denoted as $v_{sm}'(k)$. The -35kV signal can also be denoted as $v_{gm}'(k)$. Figure 4.139 shows the system transfer function $g_m'(k)$ obtained after processing $v_{gm}'(k)$ as described earlier in this section.

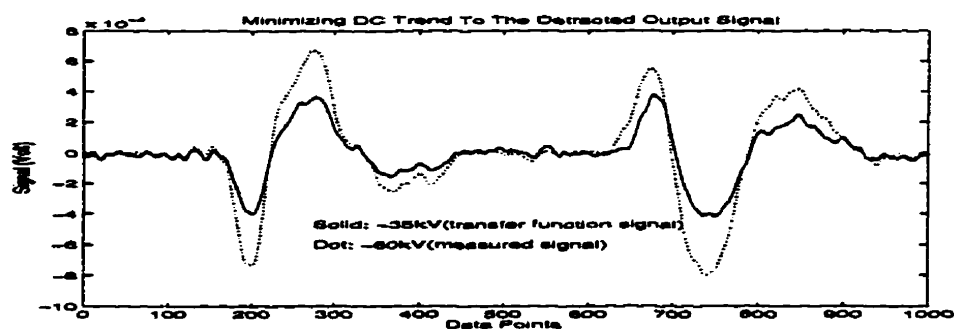


Figure 4.137 Signals after minimizing their dc trends

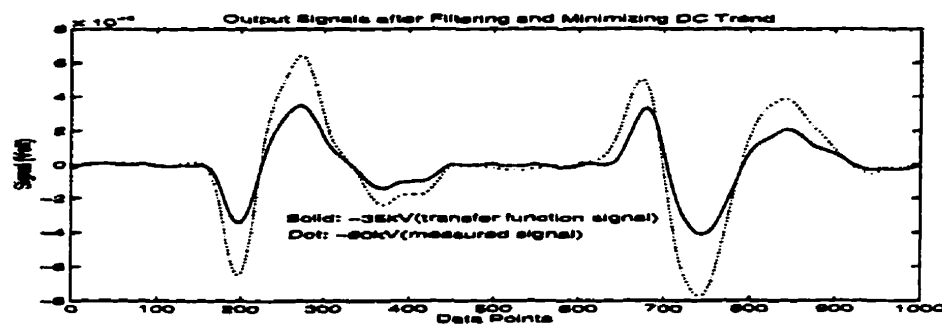


Figure 4.138 The obtained $v_{gm}'(k)$ and $v_{sm}'(k)$

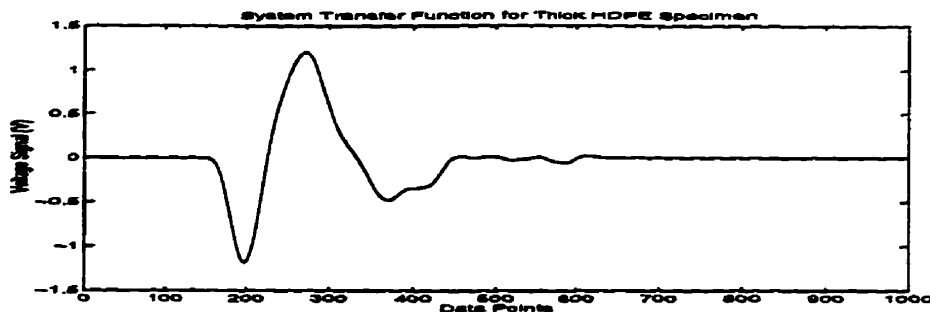


Figure 4.139 Obtained system transfer function $g_m'(k)$

There are two important points to consider in the experimental signal processing. One is the fact that the experimental signals are usually contaminated with noise. Therefore, m_0 needs to be chosen properly for stable results as already discussed in Section 3.3 and Section 4.2. For our particular PEA system, it is found that $g(m_0+1)$ should be around 10% of the first peak voltage. For a sampling rate at 500MS/s, a sampling time interval $\Delta t=2ns$, this means roughly about 10-15 data points' delay. One way is to choose $m_0=p1$ with the simulation step above 10. Alternatively, it is found that the simulation step can reach 1 (*i.e.* the sampling rate) if $g_m'(k)$ and $v_{sm}'(k)$ are both delayed for 10-15 points. This means that the first 10 to 15 points of $g_m'(k)$ after $p1$ are set to zero, $m_0=p1+delay$. This may influence the accuracy to some extent, but the resolution can be improved. Figure 4.140 shows the results of applying the PMSM to the signal used to generate Figure 4.139 transfer function. Figure 4.141 shows the results of applying the PMSM to the -60kV signal. The simulation steps are set to 1 and 2 while three delays are used, 5, 10 and 15 points after $p1$ point. The first peak of $g_m'(k)$ is at $g_m'(p1+37)=-1.1767V$, while $g_m'(p1+5)=-0.0337V$, $g_m'(p1+10)=-0.0912V$, and $g_m'(p1+15)=-0.2028V$.

It can be seen that when the delay is 5 because the percentage of the noise contaminated in the $g_m'(p1+5)$ is high, the signal-noise-ratio at that point is low, and unstable results are obtained for the -60kV signal. This is not obviously observed from the -35kV signal used to generate the transfer function due to the fact that the values of the signal from $p1$ to $p2$ are exactly proportional to the transfer function from $p1$ to $p2$. After the $p2$ point, when the simulation continues from $p2$ to $p3$, one can observe that the results obtained with delay 5 are noisier than those with delay 10 and 15.

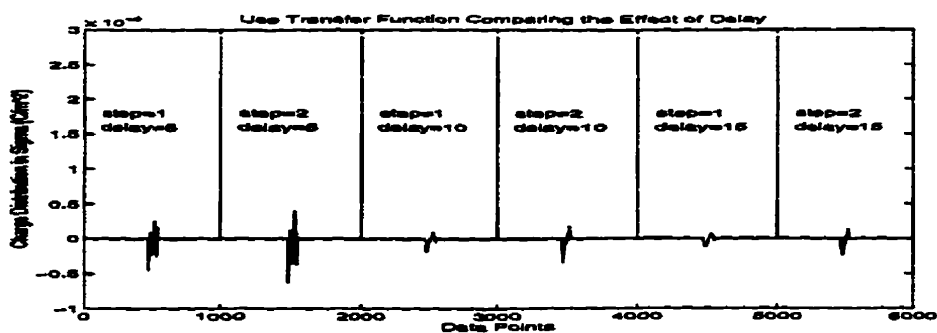


Figure 4.140 Impulse results of the -35kV signal used to generate the transfer function

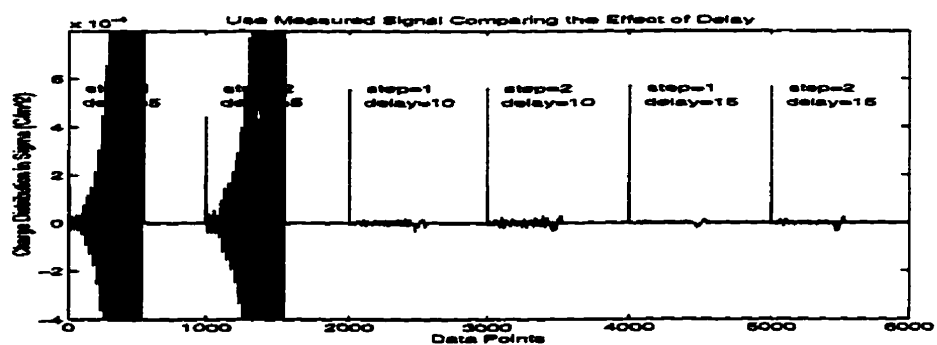


Figure 4.141 Impulse results for the -60kV signal

The addition of extra delay can mean that the surface charge σ_2 is not represented as sharply as σ_1 . This is the other important point that needs to be discussed for experimental signals. It is found that the second interface σ_2 (HV electrode) can sometimes be as sharp as the first interface (ground electrode) σ_1 , if p2 is picked considering the effect of delay. However, if p2 is not chosen that well, the second interface will tend to be a distribution as shown in Figures 4.140 and 4.141. Fortunately, the experimental condition provides a way to adjust σ_2 as discussed in Section 4.3.2. Comparing the impulse results at different steps can suggest whether the simulation itself is correct or not. Satisfying the experimental condition can verify whether the simulation results are correctly reflecting the experiments.

Figures 4.142 and 4.143 show the charge distribution after adjustment for the -35kV (transfer function) signal and the -60 kV signal respectively. An extra delay of 10 after p1 is used. Figure 4.144 shows the electric field distributions inside the sample calculated using the adjusted and unadjusted charge distributions for the two signals. Figure 4.145 gives the potential distribution based on the adjusted electric field distribution as a self testing to the

distribution results. And finally, Figure 4.146 shows the space charge distributions after taking out the surface charges for the -35kV and the -60kV signals.

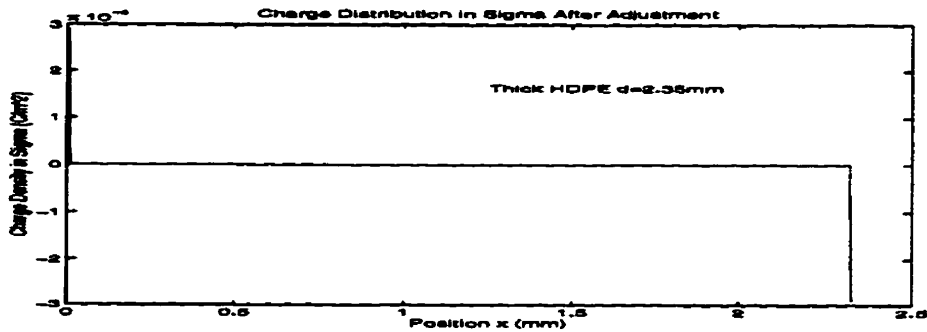


Figure 4.142 Charge distribution after adjustment for transfer function signal

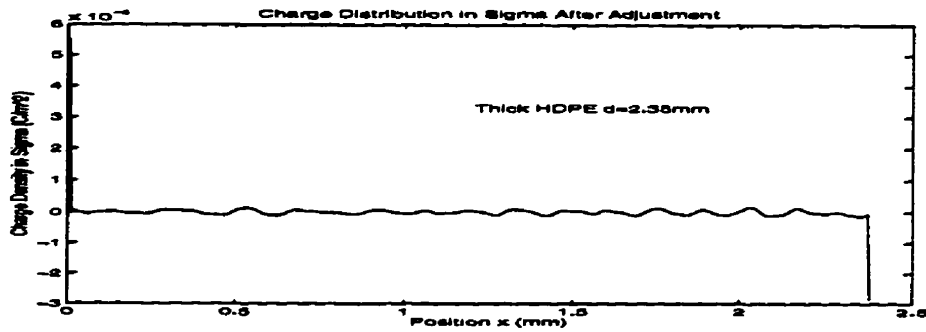


Figure 4.143 Charge distribution after adjustment(-60kV signal)

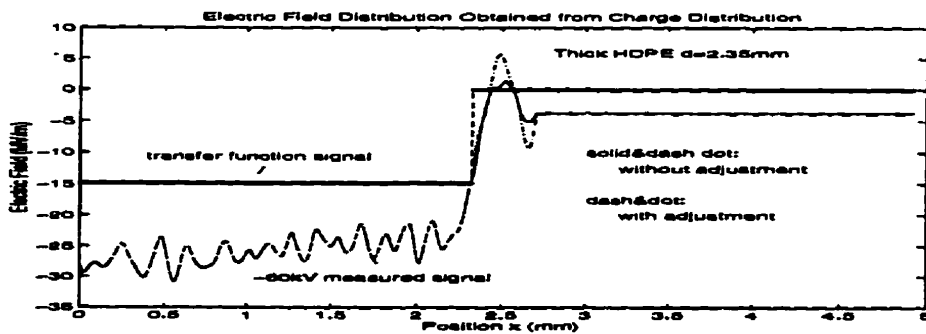


Figure 4.144 Electric field distribution

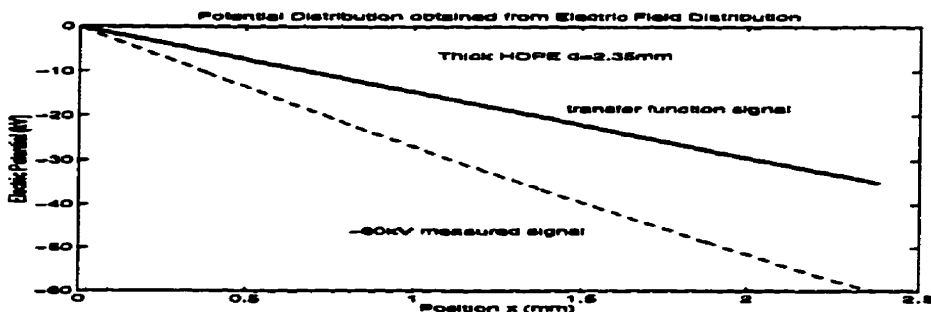


Figure 4.145 Potential distribution

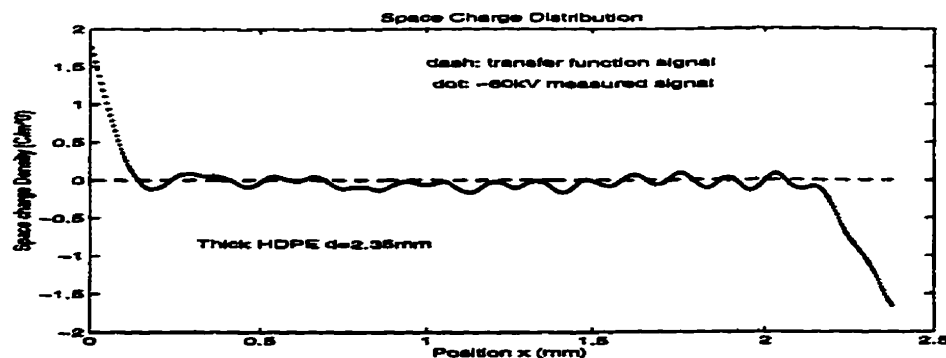


Figure 4.146 Space charge distribution by simulation model

It is obvious that the adjustments of σ_2 in Figure 4.142 and Figure 4.143 recover the smeared results in Figure 4.140 and Figure 4.141. From Figure 4.144 the electric field distribution, it can be observed that the σ_2 adjustment is actually forcing the field to reduce to zero immediately at the point corresponding to the HV electrode sample interface instead of gradually. Therefore, it is like using σ_2 at the point of HV electrode sample interface to account for all the gradually changed charge distribution after the point of σ_2 . This adjustment procedure appears to work quite well for the -35kV transfer function signal. As the results show in Figure 4.142 and Figure 4.146, surface charges are distributed only at the two interfaces, and no space charges are distributed inside the specimen. Furthermore, the potential distribution as shown in Figure 4.145 ends at -35kV; the electric field distribution in Figure 4.143 indicates a uniform field distribution. Besides, the results of the -60kV signal indicates that there are small amounts of homocharges distributed near the interfaces; the electric field distribution is almost uniform; and the potential distribution ends at around -60kV. All these results verify that the PMSM is working fine and the results obtained from the PMSM match the experimental conditions that are set for them.

The developed signal processing procedures described above have been applied to all obtained experimental signals to obtain their space charge distributions. The results of the experimental space charge distribution investigation are presented in Chapter 5.

4.4 DISCUSSION

Table 4.3 summarizes the characteristics of the DM, the DCON, and the PMSM methods from the charge distribution results for the four sets of signals obtained by the three methods individually. The effect of noise, the effect of charge distribution, and the effect of the bandwidth of the system *IR* on the three signal processing methods are discussed as advantages and disadvantages inside the Table. The procedures used for each method for each set of signals are summarized in the Table as well.

As one can see from Table 4.3, the DM method has the lowest capacity to present surface charges and the rapid change of charges, and the DCON has the lowest stability and highest sensitivity to noise. Both DM and DCON seem to be more sensitive to the bandwidth effects than the PMSM. When the bandwidth of system *IR* is narrow or the system *IR* has some ringing effects, the DM cannot be applied. Therefore, in this sense, the sensitivity of DM to the system bandwidth effects is even higher than the DCON. Figure 4.147 further shows the above comments on the three signal processing methods.

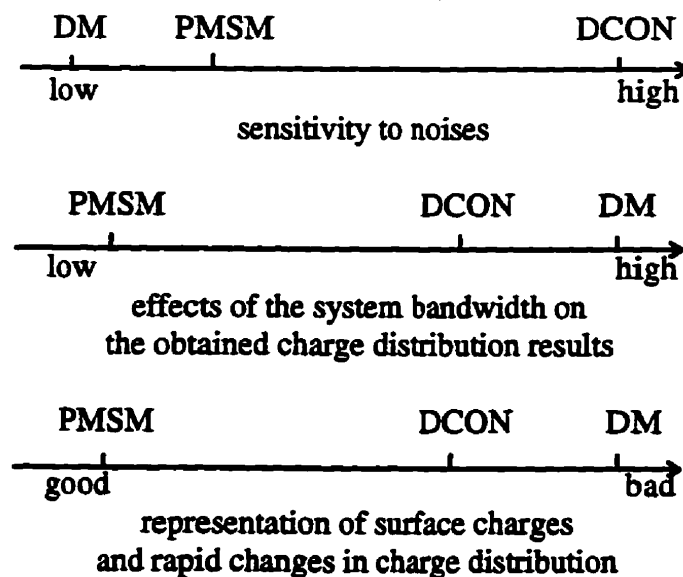


Figure 4.147 Comparison among three methods

TABLE 4.3
COMPARISON OF THE DM, THE DCON AND THE PMSM METHODS

The Used Signal Processing Method	Charge Distribution	SPD1	SPD1	SPD2	SPD2
	System IR	$g'(k)$	$g'(k)$	$g'(k)$	$g''(k)$
	Noise	$0 > n(k)$	$n(k)$	$n(k)$	$n(k)$
	Signals	1st set	2nd set	3rd set	4th set
DM	Procedures	1. Select m_0 2. Integrate $g_n'(k)$ 3. Divide $v_{m'}(k)$ by the constant 4. Waveshifting	1. Select m_0 2. Integrate $g_n^2(k)$ 3. Divide $v_{m'}(k)$ by the constant 4. Waveshifting 5. Filter noise	1. Select m_0 2. Integrate $g_n^3(k)$ 3. Divide $v_{m'}(k)$ by the constant 4. Waveshifting 5. Filter noise	N/A
	Advantages	1. Procedures to obtain charge distribution are very simple & straightforward	1. Procedures are simple 2. Not sensitive to the presence of noise	1. Simple 2. Not sensitive to noise 3. Slow changes in space charge distribution is well represented	N/A
	Disadvantages	Surface charges & rapid changes of space charge are not represented well	Surface charges & rapid changes of space charges are not represented well	Surface charges are not represented well	Cannot apply when the system IR is wide in duration and/or contains rings
DCON	Procedures	1. Apply FFT to $g_n'(k)$ & $v_{m'}(k)$ 2. Divide $\mathcal{F}[v_{m'}(k)]$ by $\mathcal{F}[g_n'(k)]$ 3. Apply IFFT to the division	1. Apply FFT to $g_n^{(2)}(k)$ & $v_{m'}^{(2)}(k)$ 2. Divide $\mathcal{F}[v_{m'}^{(2)}(k)]$ by $\mathcal{F}[g_n^{(2)}(k)]$ 3. Apply IFFT to the division 4. Filter noise	1. Apply FFT to $g_n^3(k)$ & $v_{m'}^3(k)$ 2. Divide $\mathcal{F}[v_{m'}^3(k)]$ by $\mathcal{F}[g_n^3(k)]$ 3. Apply IFFT to the division 4. Filter noise	1. Apply FFT to $g_n^4(k)$ & $v_{m'}^4(k)$ 2. Divide $\mathcal{F}[v_{m'}^4(k)]$ by $\mathcal{F}[g_n^4(k)]$ 3. Apply IFFT to the division 4. Filter noise
	Advantages	Distribution is the same as SPD1	Resolution of the filtered results is better than DM	N/A	N/A
	Disadvantages	N/A	1. Sensitive to the presence of noise 2. Result is bad without a well-designed filter	1. Sensitive to the presence of noise 2. Result is bad without a well-designed filter	1. Sensitive to noise and bandwidth 2. Result is bad even with a well-designed filter
PMSM	Procedures	1. Select m_0 2. Obtain σ & σ' 3. Get simulated charge distribution 4. $SV(k) \rightarrow v_{m'}(k)$ 5. Adjust m_0 & go back to step 2. 6. Improvement*	1. Noise reduction 2. Select m_0 3. Obtain σ & σ' 4. Get simulated charge distribution 5. $SV(k) \rightarrow v_{m'}(k)$ 6. Adjust m_0 & go back to step 3. 7. Improvement*	1. Noise reduction 2. Select m_0 3. Obtain σ & σ' 4. Get simulated charge distribution 5. $SV(k) \rightarrow v_{m'}(k)$ 6. Adjust m_0 & go back to step 3. 7. Improvement*	1. Noise reduction 2. Select m_0 3. Obtain σ & σ' 4. Get simulated charge distribution 5. $SV(k) \rightarrow v_{m'}(k)$ 6. Adjust m_0 & go back to step 3. 7. Improvement*
	Advantages	1. Better resolution/accuracy than DM 2. Comparable to DCON results can be obtained using step 6.	1. Better resolution/accuracy than DM & DCON 2. Less sensitive to noise than DCON 3. Further improvement using step 7.	1. Better resolution/accuracy than DM & DCON 2. Less sensitive to noise than DCON 3. Further improvement using step 7.	1. Better resolution/accuracy than DM & DCON 2. Less sensitive to noise & bandwidth 3. Further improvement using step 7.
	Disadvantages	1. Computation is more than DM & DCON 2. Step 6 is time-consuming	1. Computation is more than DM & DCON 2. Step 7 is time-consuming	1. Computation is more than DM & DCON 2. Step 7 is time-consuming	N/A

*: Alternatives (nonlinear detection and optimization process)

The resolution and the accuracy of the DCON depend on the resolution function $IR*IR^{-1}$, and therefore, depend on the bandwidth of the IR operation and signal-to-noise ratio. When there is no noise presented in the signals (1st set of signals) and the IR is invertible, the resolution and accuracy of the DCON are very good. However, if noise exists (the 2nd, 3rd and 4th sets), the resolution and the accuracy decrease greatly, especially when the bandwidth of the system IR is reduced (the 4th set). The resolution and the accuracy of the DM depend on the duration and the waveshape of the system IR . It has the strictest requirements for the system IR , in one sense: the sensitivity of DM to the system bandwidth effects is considered even higher than that of the DCON. However, the DM is not as sensitive to noise as the DCON. Overall, the PMSM is better than the DM and DCON concerning the resolution and accuracy.

The resolution and the accuracy of the PMSM depend upon the simulation step and the delay. Generally, the smaller the step used, the higher the resolution and the accuracy and, of course, the longer the computation time. Usually in the simulation, a larger step is used first, then the step is decreased, halved, for example. If the two results are about the same, this means the larger step can be used in the simulation and the simulation results are correct. Moreover, changing the simulation steps enables surface charges to be distinguished from space charge distributions. This can improve the accuracy of the obtained charge distribution, especially the space charge distribution near the ground electrode-sample interface.

The highest resolution for the PMSM can be up to the sampling interval, when the step $\Delta=1$, i.e., $\Delta\tau=\Delta t$. To obtain a stable σ sequence, the delay is adjusted to make $g(m_0+1)$ significant compared the noise level. As presented in Section 4.3 from experimental signals, $g(m_0+1)$ is better at around 10% of the first peak of the system IR . For no matter how sharply the system IR (wide bandwidth) is increased or how slowly system IR (narrow bandwidth) is increased, $g(m_0+1)$ will be less than the first peak, which indicates that the delay will never be more than the rise time of the system IR . The resolution of the PMSM method can then be guaranteed to at least correspond to the rise time of the system IR and can be up to the sampling interval, especially when a nonlinear detection and optimization process (NDOP) is applied.

For our typical PEA system, signals are sampled at 500MS/s (i.e. the sampling interval is 2ns) and the sound velocity of the specimen is around 2000m/s , the resolution of the obtained space charge distribution can be up to $4\mu\text{m}$.

The PMSM is better than the two previous methods in the sense that it is capable of providing more useful and more trustworthy information of unknown charge distributions from the measured or synthetic signals. With a nonlinear approach to identify the presence of surface charges or, furthermore, with a nonlinear detection and optimization process (NDOP), the resolution and the accuracy can be much better than the two previous methods.

The PMSM approach is just one way to apply the simulation model idea. Some other approaches can also be used, for example, the recursive minimum variance deconvolution approach and maximum likelihood deconvolution approach, as presented in Appendix C. With the maximum likelihood deconvolution approach, for example, one can apply the simulation model idea, update the system IR parameters and statistical parameters, until the maximum likelihood results are obtained. The resolution and accuracy can be expected to improve. However, the maximum likelihood deconvolution(MLD) requires the actual sequence being spike-like[87]. As for the charge distribution, the σ sequences are mainly pseudo σ sequences; therefore, the application of the MLD is still under investigation to determine whether it can be applied to obtain the space charge distribution.

CHAPTER 5

CHARGE DYNAMICS

5.1 INTRODUCTION

Chapter 4 demonstrated that the space charge distribution obtained by the PMSM method represents, with high resolution, the actual charge distribution inside the test specimens more closely than the DM and DCON methods. Chapter 5 extends the application of the improved PEA measuring technique presented in Chapter 4. The PMSM method is applied to some polymeric materials in order to investigate the charge dynamics inside these materials. In other words, the purpose of this chapter is to obtain useful information about the behavior of space charges under different testing conditions to establish a meaningful relationship between the space charge distribution inside the insulating material and the breakdown mechanisms.

As reviewed in Chapter 2 Section 2.3, the distortion to the electric field due to the space charge effect is considered one of the most important secondary effects on electric treeing, aging and breakdown phenomena in polymers. It is believed that space charges are injected into the insulating material under high voltage application. It is found experimentally(Section 2.3.1) that the polarity reversal or short circuit can cause an electric tree to occur at a voltage lower than the dc tree initiation voltage[6]. A sudden release of space charges in a PMMA block can damage the insulating material and lead to the electric treeing, and no voltage application is necessary. As discussed in Section 2.3, the dynamic changes of space charge distribution inside the insulating material play an important role in the initiation of electric treeing and breakdown, therefore, suggesting the great need to develop the space charge distribution techniques in order to clarify charge dynamics (*i.e.* charge injection, accumulation and transportation characteristics). With the improved PEA measuring technique using the proposed PMSM method, we plan to investigate the following phenomena in this research:

1. space charge *injection* under HVDC voltage application,
2. space charge *accumulation* and *transportation* under constant HVDC voltage application,
3. the effect of polarity reversal on the *dynamic changes of space charge distribution*,
4. the effect of short circuit on the *dynamic changes of space charge distribution*,
5. the *decay* of space charges under short circuit condition, and,
6. the *dynamic behaviors* of space charge distribution in different insulating materials.

To investigate the above aspects, experiments are designed and performed for the sheets of LDPE, Thin/Thick HDPE, UHMWPE, PP and PMMA, under these conditions:

1. step increased HVDC voltage applications--investigating the space charge *injection*, and *space charge dynamics* as HVDC voltage increases.
2. constant HVDC voltage application(including voltage reversal)--investigating the charge *accumulation* and *transportation* under constant HVDC voltage application and the effect of polarity reversal on the *dynamic changes of space charge distribution*.
3. short circuit condition--investigating the effect of short circuit on the *dynamic changes of space charge distribution*, and the *decay* of the space charges.

The *dynamic behaviors* of space charge distribution in different polymeric materials can be compared from the results of the above three types of experiments for the different specimens.

The Step Increased Voltage experiments: In this experiment, the PEA measurements are conducted at each step voltage as the dc voltages are first increased from 0 kV to positive or negative 10 kV. Then the voltage is increased with a step of positive or negative 5kV until the dc voltages get to positive or negative 85kV or 90kV.

The Constant Voltage Application experiments: This experiment is conducted at a constant positive or negative voltage not less than 60kV while the application time is increased. When the space charge distribution under the positive HVDC constant voltage application is compared with that under the negative HVDC, the effect of polarity reversal on dynamic changes of space charge distribution can be observed.

The Short Circuit experiments: There are two types of short circuit experiments.

- *Type#1:* Whenever a *Step Increase Voltage experiment* or a *Constant Voltage Application experiment* is finished, the HVDC voltage is reduced to zero. The specimen is short-circuited(both sides of the specimen are connected to ground). This is the connection for the short circuit experiment. Next we apply an electric pulse and measure the signal coming out of the transducer. After that, we allow the voltage to increase to a positive or negative polarity, depending on the test requirements.
- *Type#2:* The *Short Circuit experiments* can be conducted with the specimen continuously short-circuited for a long period without any further application of HVDC. The purpose of this procedure is to investigate the decay of the space charges inside the specimens as time increases.

The experimental setup and the voltage application to each specimen are detailed in Section 5.2. The three types of experimental results for all the investigated specimens are summarized in Section 5.3, Section 5.4, and Section 5.5 respectively. Finally, the space charge dynamic behavior inside LDPE, HDPE, UHMWPE, PP and PMMA are discussed overall in Section 5.6 based on the experimental results shown in Section 5.3-5.5.

5.2 EXPERIMENTAL ARRANGEMENT

5.2.1 Experimental Set-up

The experimental setup used in the experiments, shown in Figure 5.1, contains the insulating supporter, electrode holder, oil container, oil, specimen, electrodes, transducer, cable connection, preamplifier, oscilloscope, electric pulse generator, capacitor, and HVDC supply, etc.. The main components inside the set-up are discussed individually below.

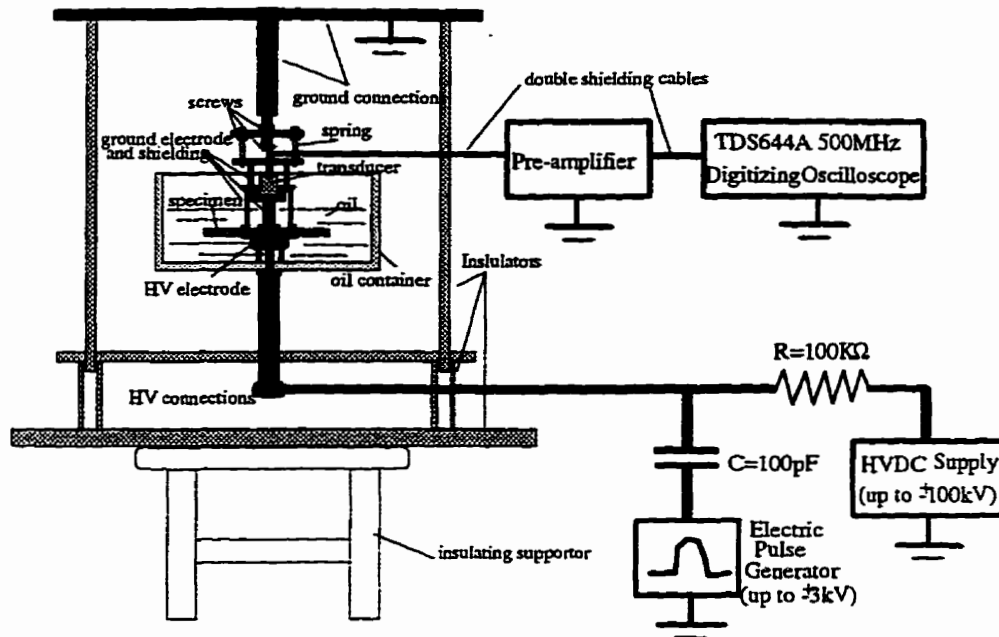


Figure 5.1 Experimental setup

1) Specimen and Electrodes

Totally, seven kinds of specimens were used in the experiments. Specimens were cut into $4\frac{1}{4}'' \times 4\frac{1}{4}''$ pieces from commercial sheets which had not been subjected to any electric stresses before. Each was cleansed using wash acetone (CH_3COCH_3) before preconditioning. According to ASTM 618, Procedure A, preconditioning at 40/23/50 was chosen because all the specimen thicknesses are less than 7mm. Condition 40/23/50 refers to the condition of the test specimen in the standard laboratory atmosphere (temperature at $23 \pm 2^\circ\text{C}$, relative humidity at $50\% \pm 5\%$) for 40 hours immediately prior to testing.

A three electrode system was adopted to guarantee that the electric field application was uniform in the center where the transducer picks up signals. To ensure electric connection between electrodes and the specimen, evaporated Al, conductive aluminum tape and conductive copper tape were used. The thickness of the evaporated Al was around $1\mu\text{m}$, the thickness of the Al tape was about 0.1mm, and the thickness of the copper tape was about 0.04mm. The overall results of 12 specimens are shown and discussed in this chapter. Each

specimen is given a name. Table 5.1 gives the name of each specimen along with its average thickness, its dielectric constant, and the connection electrode used. The dimensions of the three electrodes is shown in Figure 5.2. The Al and the Cu tape were cut into diameters $\phi 25\text{mm}$ and $\phi 50\text{mm}$ and $\phi 38/\phi 50\text{mm}$ ring, and pasted on the specimen. A roller was used to press the tape, eliminate gas bubbles, and ensure the connection.

TABLE 5.1
INFORMATION OF EACH SPECIMEN

specimen	LDPE	Thin HDPE	Thick HDPE	UHMWPE	PP	PMMA
d (mm)	3.20	1.46	2.35	3.04	3.15	3.00
ϵ_r	2.2					3.7
electrodes	Al tape					
specimen	HDPE	HDPE-Cu	HDPE-E	LDPE-E	UHMWPE-E	PMMA-E
d (mm)	3.20	3.28	3.28	3.25	3.06	3.00
ϵ_r	2.2					3.7
electrodes	Al tape	Cu tape	Evaporated		Al	

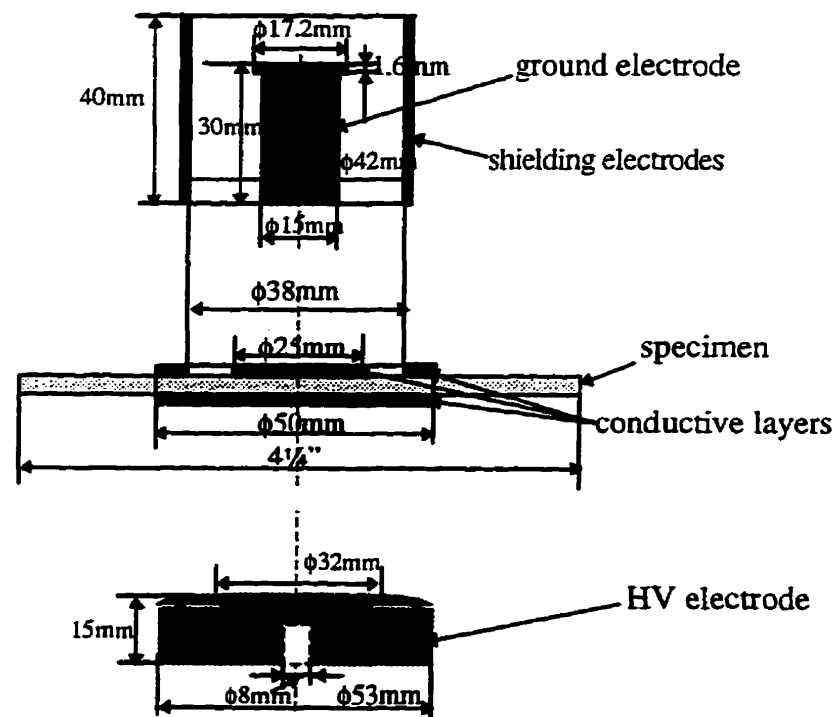


Figure 5.2 Dimension of the three electrode system

The ground electrode is a cylinder made of Al. The diameter of the cylinder is 15mm, and the total height is 30 mm. The shielding electrode is a Cu tube with an inner-diameter of 38mm and an outer diameter of 42mm. The HV electrode is made of stainless steel. The shape and dimension of the specimen, the HV electrode, the ground electrode, and the shielding electrode are shown in Figure 5.2.

2) Oil

The transformer oil Voltesso35 was chosen as the medium. Its physical properties and oil content (has inhibitor content 0.07 wt%) indicate that it is type I oil [ASTM 3487]. The viscosity of the oil at 40°C is 8.3 cst; therefore, conditions of 60°C and 40Pa (0.3 Torr) [ASTM 2413] are considered to apply for drying and degassing the liquid. The oil was preheated to 60°C and degassed for 45 minutes in a vessel connected to a ES250 pump which guarantees a vacuum much better than 0.5 Torr.

3) Transducer

The diameter of the active area of the transducer is $\frac{3}{8}$ inch. The bandwidth of the transducer was specially designed from 0.25-6MHz. The transducer was calibrated by the company (Etalon Inc.) in water using three transducers (1MHz, 2MHz, and 5MHz) as transmitters. The sound pressure was first calibrated by a calibrated hydrophone. The calibration chart is shown in Figure 5.3.

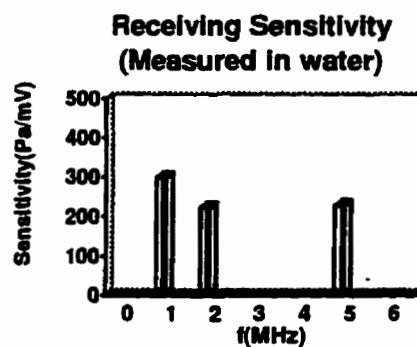


Figure 5.3 Calibration chart of the transducer

4) *Preamplifier*

The Tektronics type 1A1 dual trace plug-in unit was used as a preamplifier before the output of the transducer was connected to the oscilloscope. The bandwidth of the preamplifier is 30MHz with a gain up to 10.

5) *Oscilloscope*

TDS 644A 500 MHz digitizing oscilloscope was used to record the measured signals. The oscilloscope has a feature to let one record measured signals on a 3.5" floppy disk. Therefore, off-line signal processing can be easily performed. Another feature is that the oscilloscope can measure, for example, 100 signals, and output the average of these signals. In this way, the random noise can be decreased. In addition, the oscilloscope has two built-in low pass filters. The cut-off frequency of one is at 100MHz; that of the other is at 20MHz. Since the main frequency range of the useful signals is below 20MHz, the 20MHz filter was implemented to the signals.

6) *Electric Pulse Generator*

Figure 5.4 shows the circuit used to generate the electric pulse. The Fluke High Voltage Power Supply Model 408B was used since it can provide up to $\pm 6\text{kV}$ dc voltage. The electric pulse voltage, therefore, can be up to $\pm 3\text{kV}$. The electric pulse voltage of -2.3kV was used for all the measurements.

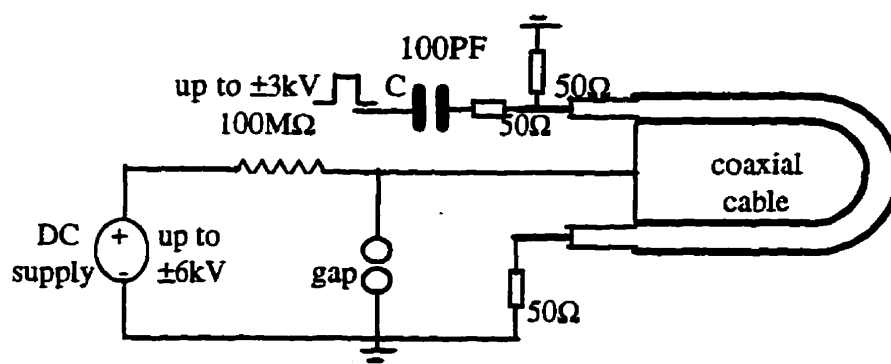


Figure 5.4 Circuit diagram of the electric pulse generator

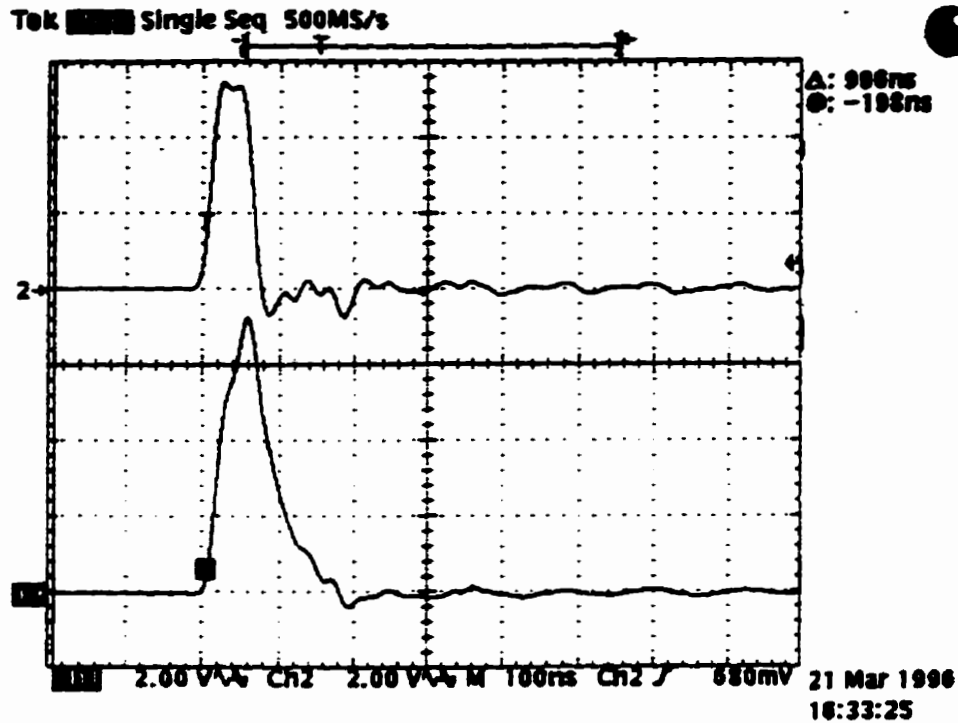


Figure 5.5 Waveshapes of the electric pulse

Figure 5.5 shows two waveshapes of the measured electric pulse. The Channel 1 signal was obtained by using a resistive voltage divider, and the Channel 2 signal was obtained using a capacitive voltage divider. As measured from the oscilloscope, the Channel 1 electric pulse has a width of 69.8ns and a rise time of 38.8 ns, while the Channel 2 has a width of 54.8ns and a rise time of 19.2ns.

7) HVDC Supply

Brandenberg Multiplier 100kV model 908R, along with Brandenberg Power Supply & Control Unit model 108, was used to provide HVDC up to ± 100 kV. The polarity was easily changed.

8) Others

The other parts are shown clearly in Figure 5.1. Double shielding cables were used to eliminate the interference. Springs were used in the electrode holder to ensure the electrodes were tightly attached to the specimen. Insulators and insulating supporters enable the HVDC to be safely supplied from the bottom of the specimen.

5.2.2 General Test Procedure

When each specimen was tested in the experimental setup, a -2.3kV electric pulse was applied to the specimen with no dc voltage applied (zero HVDC voltage). Measurements from the transducer were obtained and denoted as $v_{sm0}(t)$ for each specimen. The recorded $v_{sm0}(t)$ was used as mentioned in Section 4.3 to get rid of the influence of the second term in the pressure wave signals[equations (3-2) and (3-4)].

Then, a *Step Increased Voltage* was applied to each specimen. This is called *the first step increased voltage experiment*. Some of the specimens were subjected to a positive step increased dc voltage; others were subjected to a negative step increased dc voltage. When the absolute value of the dc voltage reached a certain level(such as 85kV or 90kV), the measurement was stopped. This voltage level was determined in this experiment by the maximum stable output voltage from the dc generator, which was 90kV in this case. After that, the applied voltage was set to zero quickly, and the specimen short-circuited; this is *the 1st short circuit* of all specimens. Then, four specimens (Thin HDPE, Thick HDPE, HDPE, and PP) were subjected to another *Step Increased Voltage* application, which is called *the second step increased voltage experiment*. After *the second step increased voltage experiment*, the specimens were again short-circuited. This is *the 2nd short circuit* for the four selected specimens.

After all the *Step Increased Voltage* applications were finished, a *Constant Voltage Application* of the same polarity as the step voltage was applied to the specimen for more than 1000 minutes. This is called *the first constant voltage application*.

After the *first constant voltage application*, the voltage was again turned to zero and the measurements taken during this period are called *the 3rd short circuit* for the four specimens, and the *2nd short circuit* for the other 8 specimens. Then, a reversed polarity HVDC was applied to the specimens, except UHMWPE-E, HDPE-E and PMMA-E. For UHMWPE-E, a higher same polarity HVDC was applied. For HDPE-E and PMMA-E, no more experiments were carried out. The reversed polarity HVDC is another *Constant Voltage Application*. It is denoted as *the second constant voltage application* and/or *the first reversal* for the rest of the specimens. After that, the specimen was short circuited again, these measurements are *the 4th short circuit* for the four specimens (Thin HDPE, Thick HDPE, HDPE, and PP), and *the 3rd short circuit* for the others.

Figure 5.6[94], Figure 5.7, and Figure 5.8 show in detail the voltage application procedures for each of the 12 specimens. Figure 5.9 shows in block diagram the voltage application procedures and the denotation for each experiments. Additional experiments for some specimens are as follows:

1. two specimens, LDPE and UHMWPE, were chosen for other 4 polarity reversals after *the first reversal* to investigate the effect of polarity reversal.
2. four specimens (Thick HDPE, PP, UHMWPE-E, and LDPE) were used to investigate the charge decay at the continuous short circuit condition.

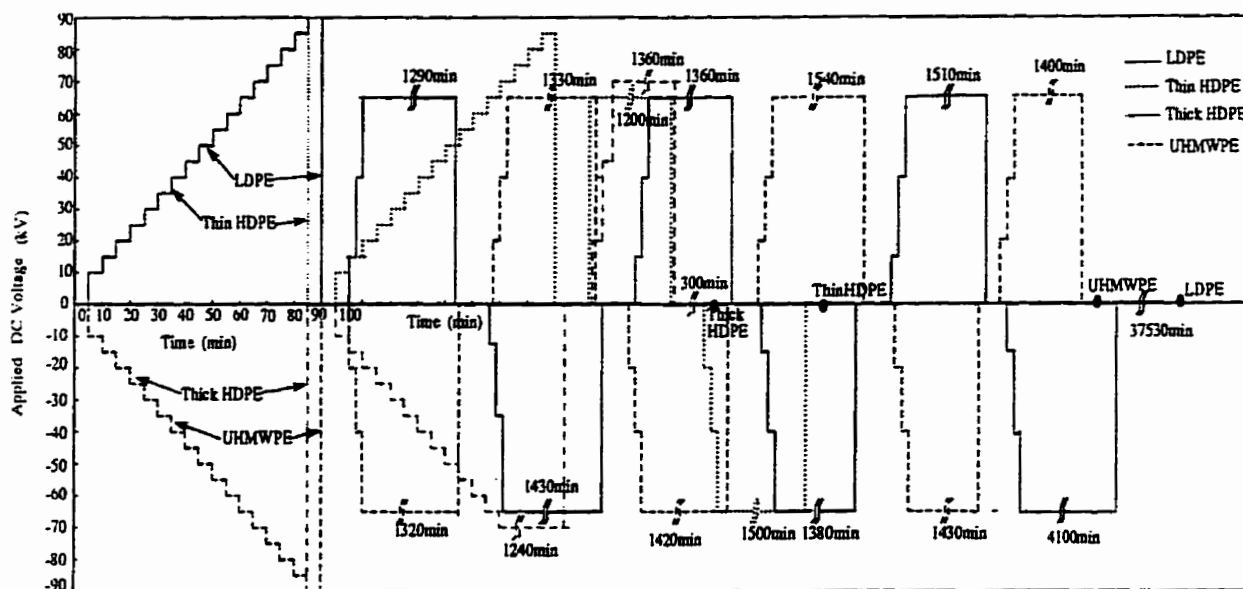


Figure 5.6 Dc voltage applications for LDPE, Thin&Thick HDPE, and UHMWPE specimen

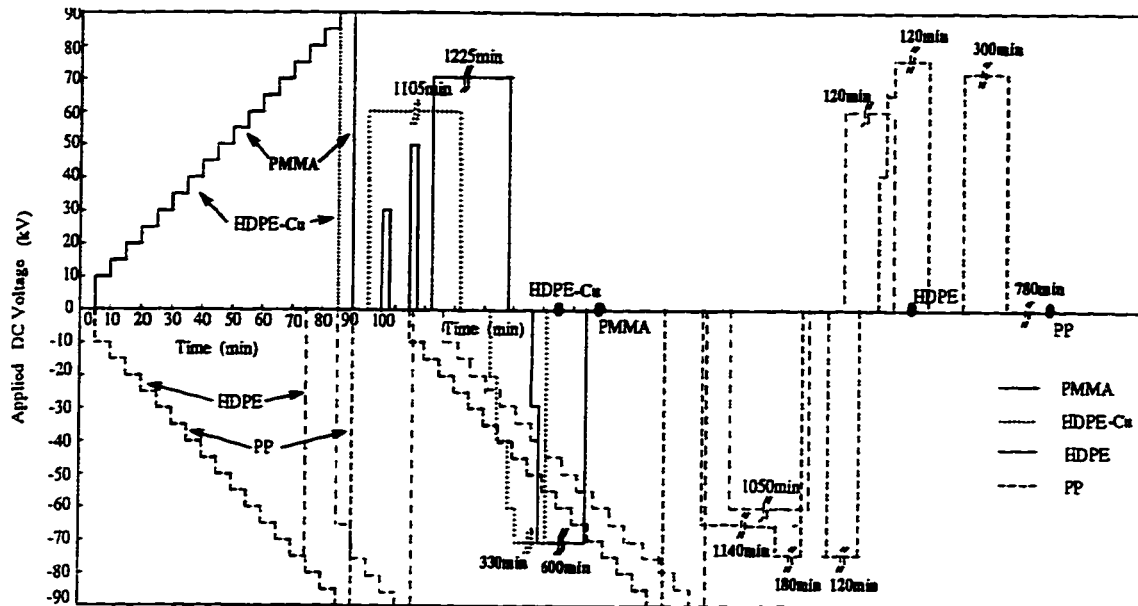


Figure 5.7 Dc voltage applications for HDPE, HDPE-Cu, PP, and PMMA specimen

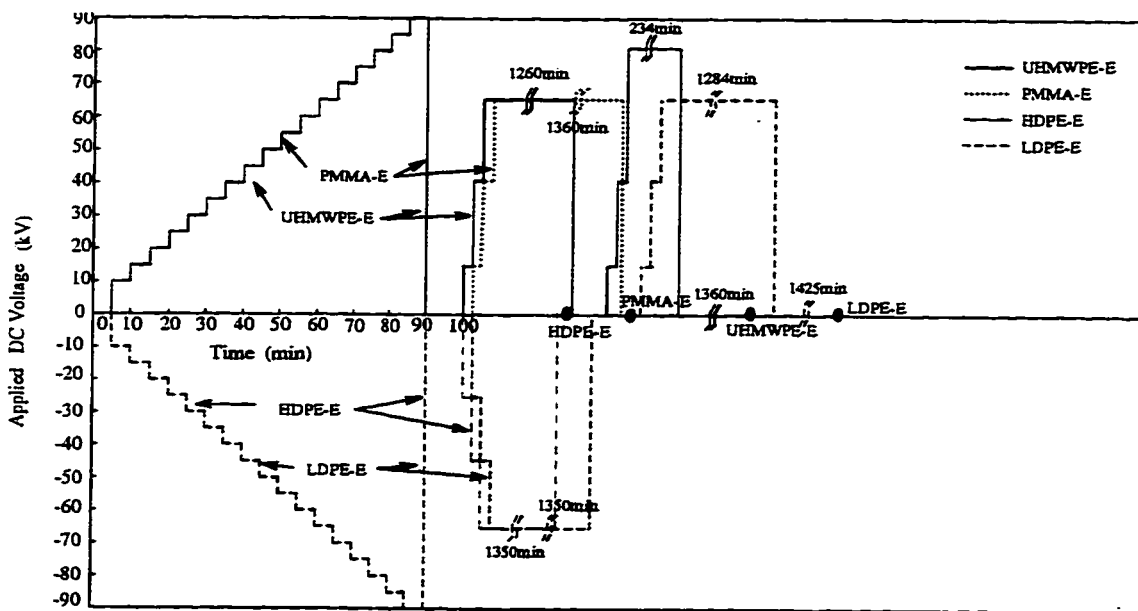
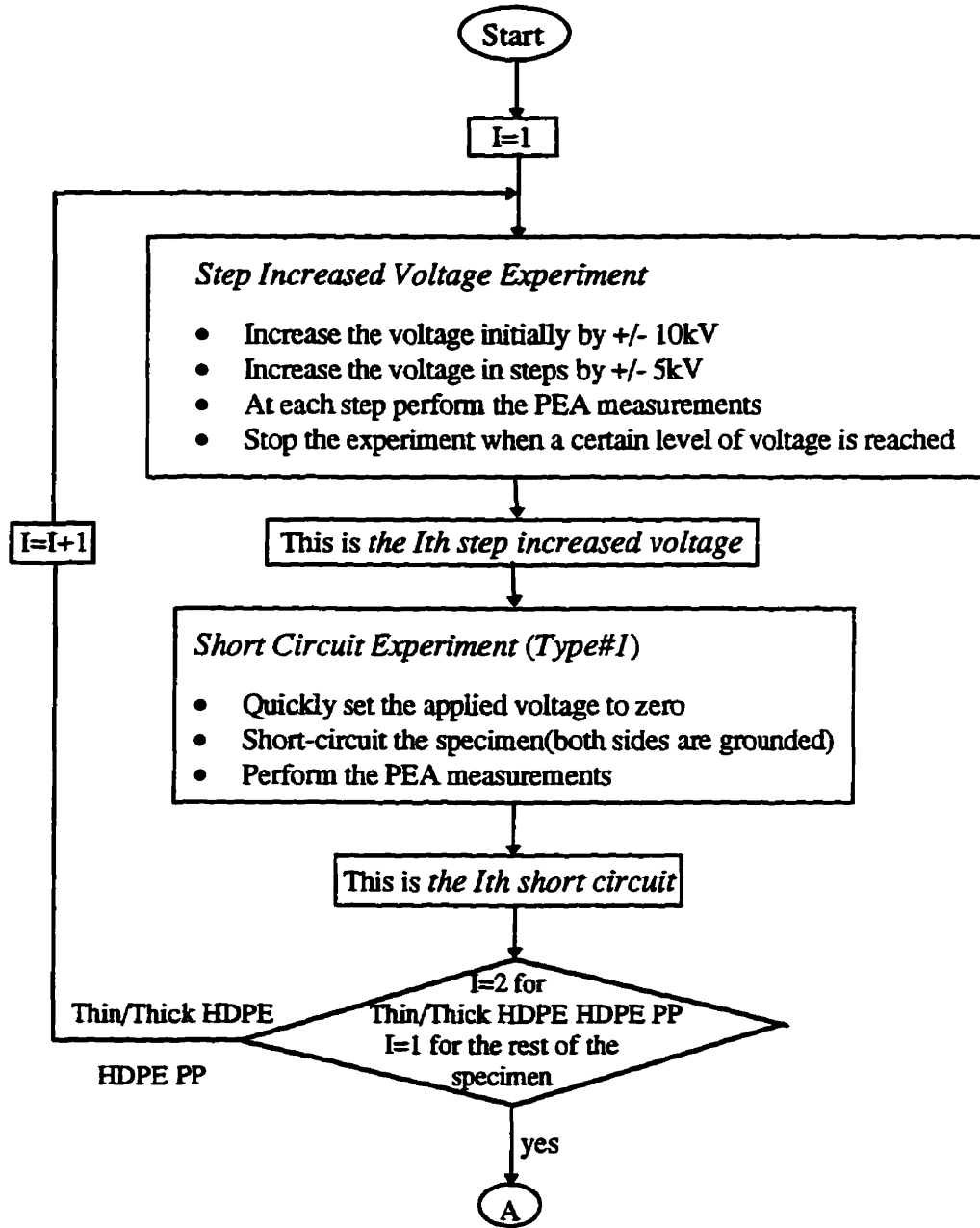


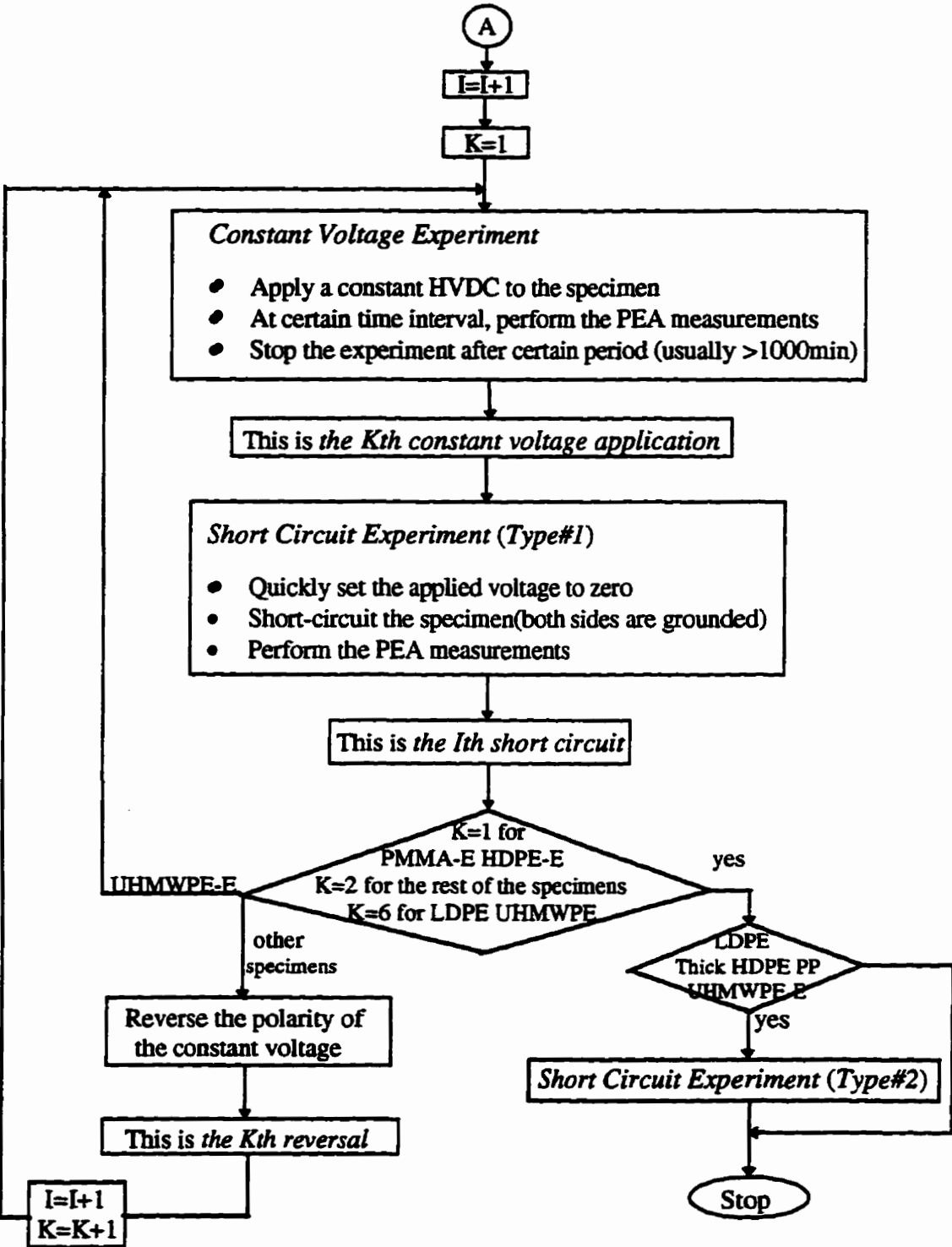
Figure 5.8 Dc voltage applications for four Al evaporated electrode specimens

The dc voltage application falls into three categories: the *Step Increased Voltage* application, the *Constant Voltage* application, and the *Short Circuit* application, the experimental results of the 12 specimens are presented in the next 3 sections according to these three categories respectively.



(a)

N.B. PEA measurements: apply an electric pulse to the specimen and pick up the signals from transducer



(b)

Figure 5.9 Block diagram of the voltage application procedures

5.3 STEP INCREASED VOLTAGE EXPERIMENTS

5.3.1 Procedures

As discussed in Section 5.2 and shown in Figure 5.6-5.8, the *first step increased voltage* experiments were conducted for all the 12 specimens. For six specimens, a positive polarity test was conducted. In this experiment, the dc voltage was first increased from zero to positive 10 kV. Then it was increased with a step of positive 5kV until dc voltage reached positive 85kV for Thin HDPE and HDPE-Cu, and positive 90kV for LDPE, PMMA, PMMA-E, and UHMWPE-E.

For the other six specimens, a negative polarity test was conducted. In this experiment, the dc voltage was first increased from zero to negative 10 kV. Then, it was increased with a step of negative 5kV until the dc voltages reached negative 75kV for HDPE, negative 85kV for Thick HDPE, and negative 90kV for UHMWPE, PP, HDPE-E, and LDPE-E.

The *second step increased voltage* was conducted (as shown in Figures 5.6, 5.7 and 5.9) for the Thin HDPE with voltage increased up to +85 kV; the Thick HDPE with voltage increased up to -70kV; HDPE and PP with voltage increased up to -90kV.

These experiments were intended to investigate the charge injection and space charge dynamics as HVDC voltage increases for different specimen materials.

5.3.2 Results

Figure 5.10 plots the surface charges σ_1 and σ_2 obtained using the PMSM as explained in Chapter 4 for the LDPE, Thick/Thin HDPE, and UHMWPE specimens when they were subjected to *the first step increased voltages*. The theoretical values of the surface charges for these specimens under uniform field assumption are calculated using equation $\sigma_1 = \sigma_2 = \epsilon_0 \epsilon_r V/d$ and plotted as dash dots in Figure 5.10 for all specimens. Figure 5.11 shows the dynamic changes of space charge distributions inside these specimens when the dc voltages were increased step by step. Figure 5.11 are in consistent with Figure 5.10 in the sense that the

amplitude of surface charge density is less than that of the uniform field surface charge density when homocharge injection is dominant while larger than that of the uniform field surface charge density when heterocharge collection is dominant.

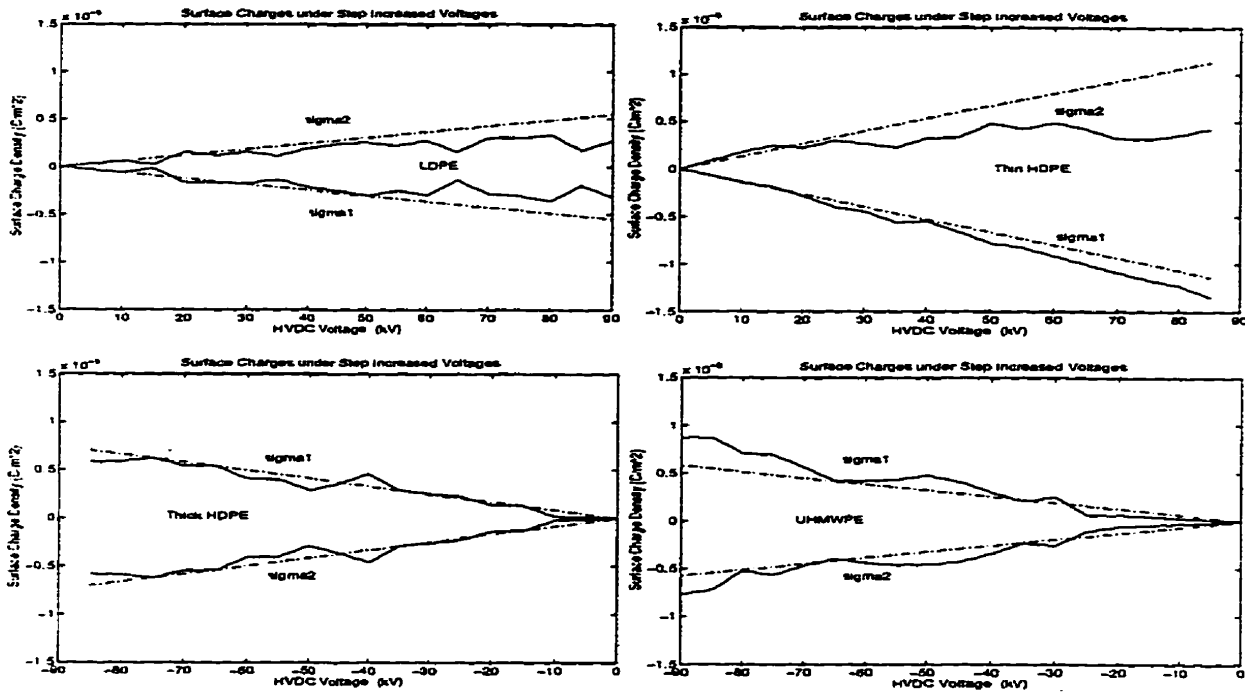


Figure 5.10 The changes of surface charges vs the applied voltage

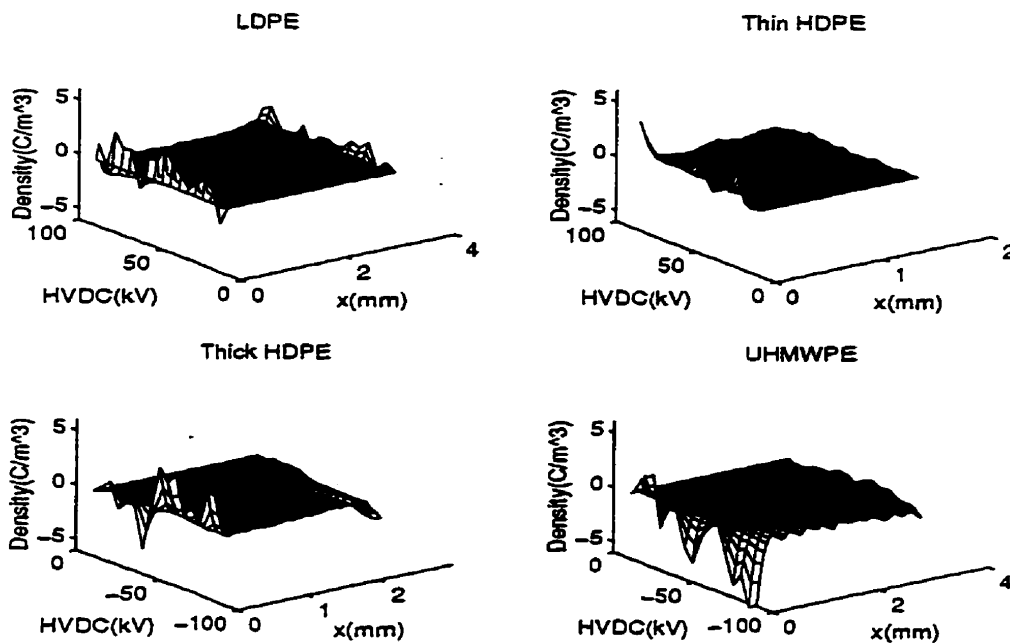


Figure 5.11 Space charge distributions vs applied voltage for LDPE, Thin/Thick HDPE, and UHMWPE under the first step increased voltages

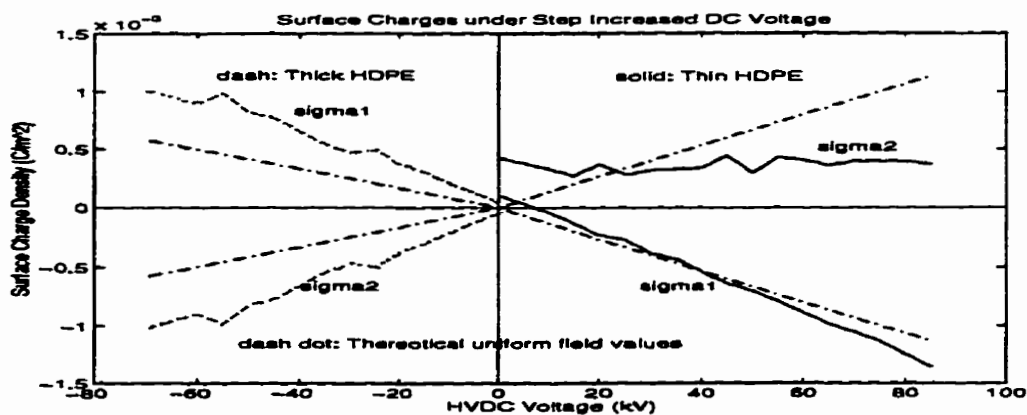


Figure 5.12 The changes of surface charges vs the applied voltage

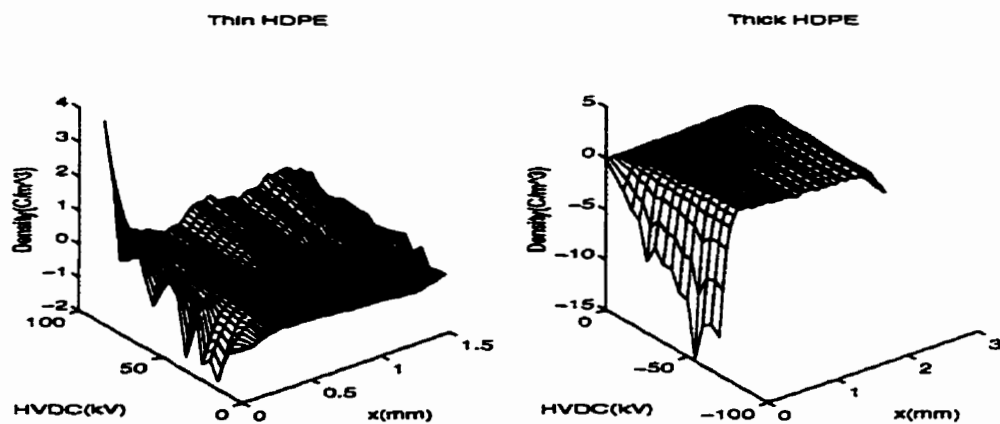


Figure 5.13 Space charge distribution vs applied voltage (the second step increased voltage)

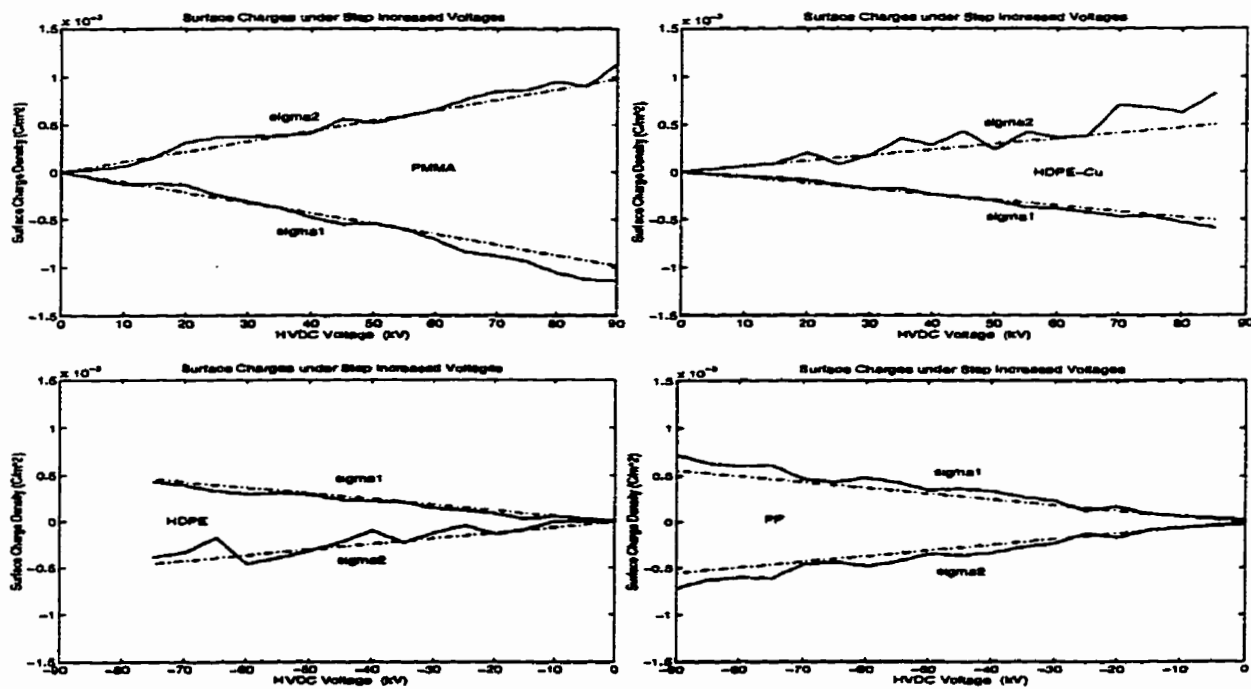


Figure 5.14 The changes of surface charges vs applied voltage

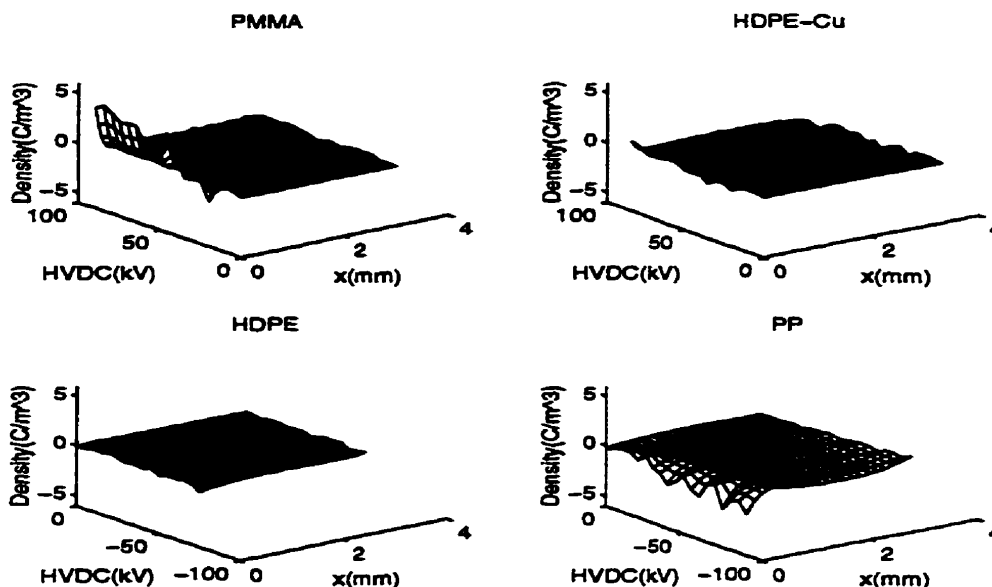


Figure 5.15 Space charge distribution vs applied voltage for PMMA, HDPE-Cu, HDPE and PP under the first step increased voltages

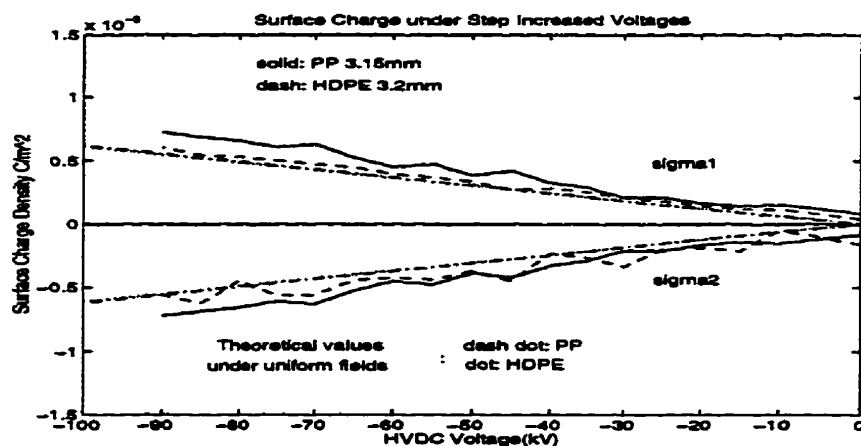


Figure 5.16 The changes of surface charges vs the applied voltage

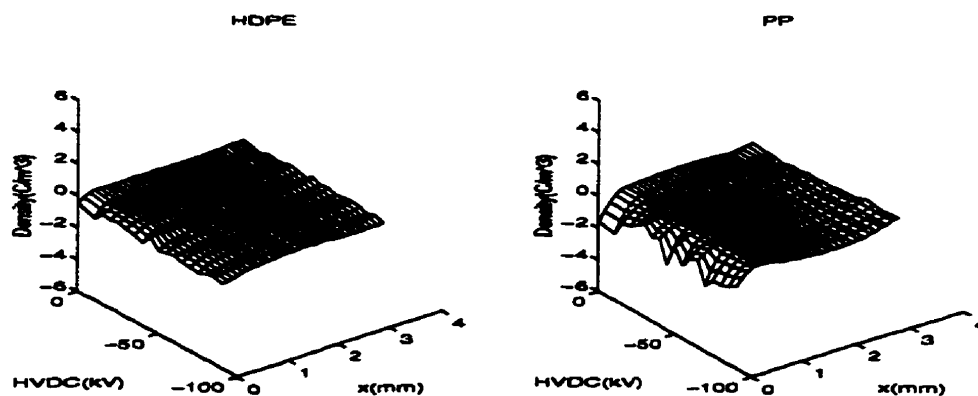


Figure 5.17 Space charge distribution vs applied voltage (the 2nd step increased voltages)

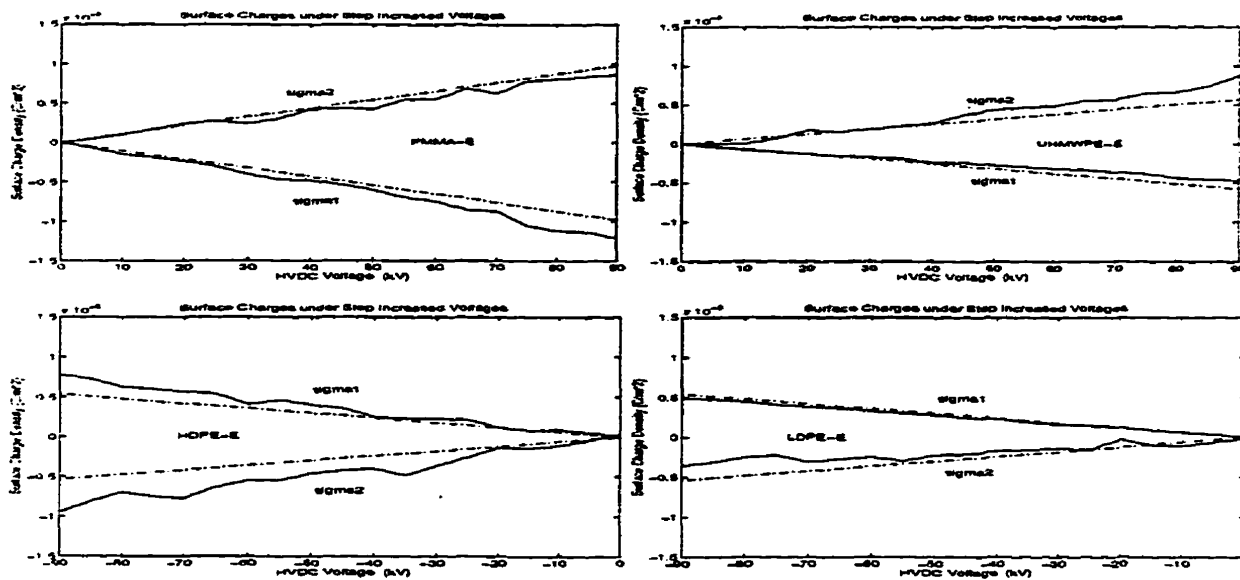


Figure 5.18 The changes of surface charges vs applied voltage (Al-evaporated specimens)

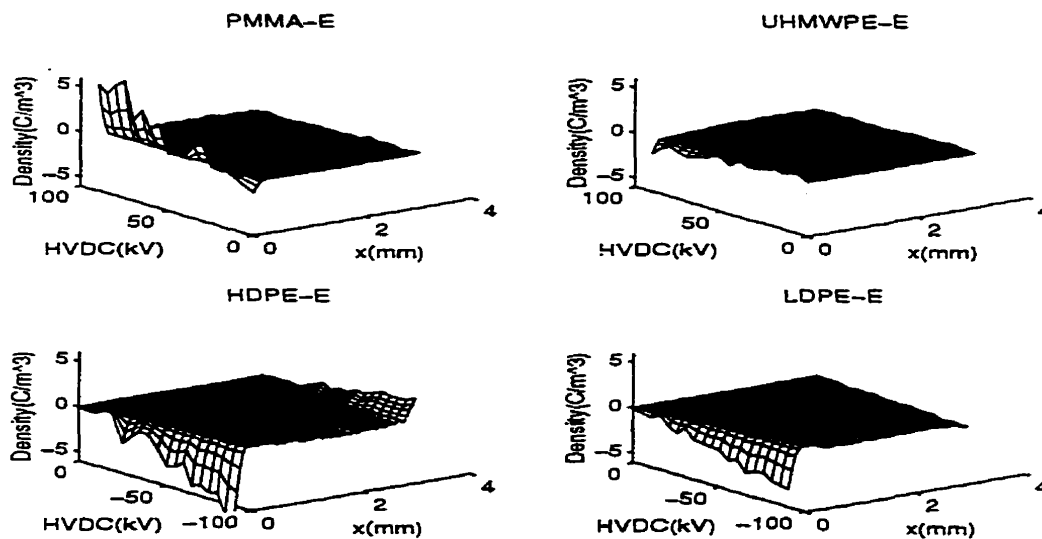


Figure 5.19 Space charge distribution vs applied voltage for specimens with Al-evaporated electrode under the 1st step increased voltages

Figure 5.12 shows the surface charge changes in Thin/Thick HDPE under the second step increased voltage. And Figure 5.13 gives the changes of space charge distribution in the two specimens. Figure 5.14 shows the changes of surface charges for PMMA, HDPE-Cu, HDPE and PP specimens under the first step increased voltage applications. Figure 5.15 shows the dynamic changes of their internal space charge distributions. The dash dot in Figure 5.14 indicates the calculated surface charge density (under uniform field assumption) verse the

applied voltage for each specimen. Figures 5.16 and 5.17 show the changes of surface charges and space charge distributions respectively, for the HDPE and PP specimens under *the 2nd step increased voltages*. Figures 5.18 and 5.19 show the changes of surface charges and space charge distributions respectively, for the HDPE-E, LDPE-E, PMMA-E, and UHMWPE-E specimens under the *1st step increased voltage* application. The dash dot in Figure 5.18 also indicates the calculated surface charge density (under uniform field assumption) verse the applied voltage for each specimen.

5.3.3 Discussion

The results of the above experimental results suggest that each specimen has a balance between charge injection and charge collection when it is subjected to a dc voltage. For specimens that have not been subjected to any electric stress before, at the start of the voltage application, a slight amount of the homocharge seems to form, perhaps due to homocharges being repelled from electrodes. As the application time and the voltage are increased, these charges seem to move to the other side of the electrode. This process is denoted as the heterocharge collection. At low dc voltage (less than the charge injection voltage), heterocharge distributions seem to form. As the HVDC voltage is further increased, the homocharge injection starts at both electrodes or mainly from the HV electrode depending on the interfacial properties of the specimen. If the charge injections from the HV electrode and ground electrode are almost at the same level (for example, Thick HDPE), the homocharge distribution tends to form. If the charge injection from the HV electrode is dominant (for example, Thin HDPE, UHMWPE and PMMA), a slight amount of charge with the same polarity of the HV electrode is distributed near the HV electrode sample interface; while a large amount of that polarity charge seems to be distributed near the ground electrode sample interface. The ground electrode acts like a heterocharge collector.

Comparing theoretical values (under uniform field assumption) with experimental results in Figure 5.10, it shows that for LDPE, injections happen at both electrodes when the voltage is larger than 20kV. For Thin HDPE, charge injection is mainly from HV electrode, and it

occurs around 25kV. For Thick HDPE, only a slight charge injection happens around -50kV. Furthermore, UHMWPE is like HDPE, but the heterocharge collection near the ground sample interface seems to be more dominant. The charge injection voltage is around -65kV for UHMWPE.

When we compare the results under *the 2nd step increased voltage* with those under *the first step increased voltage* application, we note that the charge distributions versus the applied voltages for Thin HDPE, HDPE, and PP do not change much, except for some negative charges at ground electrode sample interface, and a small amount of positive charges at the HV electrode sample interface under zero and low voltage application. However, for Thick HDPE, a large number of negative charges accumulate near the ground electrode sample interfaces and increase as the voltage increases.

The space charges of HDPE and HDPE-Cu are much less than those of Thin and Thick HDPE, perhaps because electric fields are less when the specimen thickness is increased. Therefore, there is only a small amount of charge injection and collection; the charge dynamic activity is obviously less. For PP, negative HVDC is applied. As voltage increases, negative charges are gradually increased near the ground electrode sample interface. Also, as the voltage increases, the positive charges gradually accumulate near the HV electrode sample interface, and in the meantime, the internal part of the specimen gradually has a concave shape negative charge distribution. This internal concave shape phenomenon can also be observed from *the second step increased voltage* application.

Comparing the experimental results of PMMA-E with PMMA, we see that the changes of charge distribution versus the applied voltage seem to be the same. Also, it seems that a small number of negative charges already exist before the voltage application for PMMA-E, possibly because of the evaporation process using an electron beam to evaporate Al. The small amount of electron injection during the evaporation process seems possibly to explain the different charge distribution behavior vs applied voltage between HDPE-E and HDPE or HDPE-Cu. As seen from *the second step increased voltage* application for Thick HDPE, the

space charges accumulate more substantially than for *the first step increased voltage* application; the possible explanation for the phenomenon is that the charge injection during *the first step increased voltage* application and *the 1st short circuit* may cause some degradation of the specimen near the interfaces and create more traps for the space charges to accumulate. For HDPE, there is not much charge accumulation even during *the second step increased voltage* application, perhaps because the smaller charge activity happens before the *second step increased voltage* application. For HDPE-E, probably the evaporation process introduces charge injections and causes some degradation of the specimen material near the interfaces, and therefore, the charge accumulation near interfaces becomes much more than the almost same thickness HDPE and HDPE-Cu specimens.

Comparing the results of the positive HVDC voltage application with negative HVDC voltage application [LDPE(+) with LDPE-E(-); UHMWPE-E(+) with UHMWPE(-); Thin HDPE(+) with Thick HDPE(-)], we see that negative HVDC has more tendency to lead to larger amount of (negative) charge accumulation than (positive) charge accumulation under positive HVDC.

More information about the dynamic changes of space charge distribution can be obtained from the *Constant Voltage* application experimental results, which will be discussed in the next section.

5.4 CONSTANT VOLTAGE APPLICATION EXPERIMENTS

5.4.1 Procedures

After the *Step Increased Voltage* applications, as described in Section 5.2 and shown in Figure 5.6-5.9, specimens were short circuited and constant voltages of the same polarity as the step increased voltages were applied to all the 12 specimens for more than 1000 minutes. After *the first constant voltage application*, polarity was reversed for most of the specimen except HDPE-E and PMMA-E, for which the voltage application was stopped; and UHMWPE-E, for which a higher magnitude of the same polarity voltage was applied. After *the first reversal*, the most significant *Constant Voltage Application* experiments were the 2nd, 3rd, 4th, and 5th reversals for LDPE and UHMWPE specimens. All these experiments were designed to study the charge dynamics under a constant voltage application and the effect of polarity reversal on the space charge distribution. The results are shown in Section 5.4.2 below.

5.4.2 Results

Figure 5.20 shows the dynamic changes of space charge distributions for LDPE and Thin HDPE under +65kV, and for Thick HDPE and UHMWPE under -65kV. Figure 5.21 shows the dynamic changes of space charge distributions for PMMA under +70kV, HDPE-Cu under +60kV, HDPE under -60kV, and PP under -65kV. And Figure 5.22 shows those for PMMA-E and UHMWPE-E under +65kV, and HDPE-E and LDPE-E under -65kV. After *the first constant voltage application*, the voltage is decreased to zero and the specimens are short circuited. HVDC polarity is changed and reverse polarity is applied except for UHMWPE-E. Figure 5.23 shows the space charge dynamics when this *first reversal* happens to LDPE, Thin HDPE, Thick HDPE and UHMWPE. Figure 5.24 shows those for PMMA, HDPE-Cu, and LDPE-E, and higher unreversed voltage for UHMWPE-E. To further investigate the charge dynamic behaviors when HVDC voltages are reversed, LDPE and UHMWPE have been chosen for more reversals.

Figure 5.25 shows the dynamic changes of charges in LDPE and UHMWPE when the second and the third reverses are applied. And Figure 5.26 shows those when the forth and fifth reverses are applied.

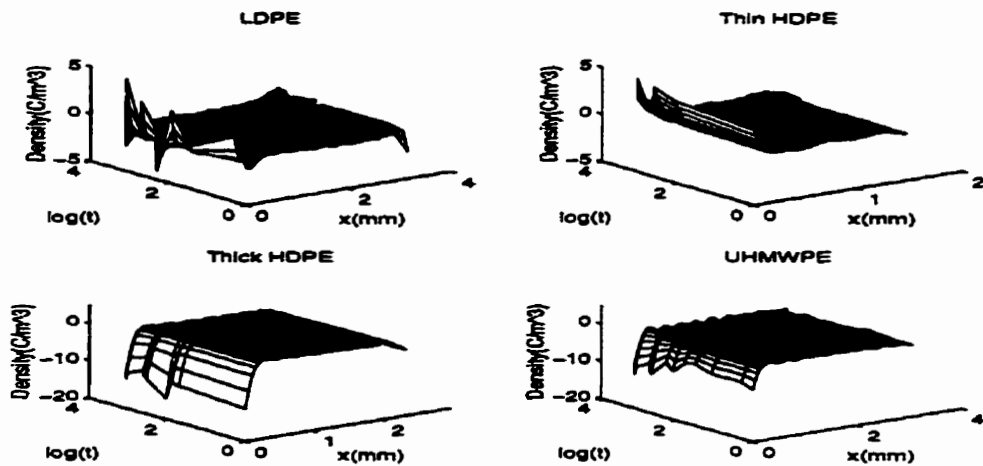


Figure 5.20 Space charge dynamics (same polarity as step increased voltage tests)

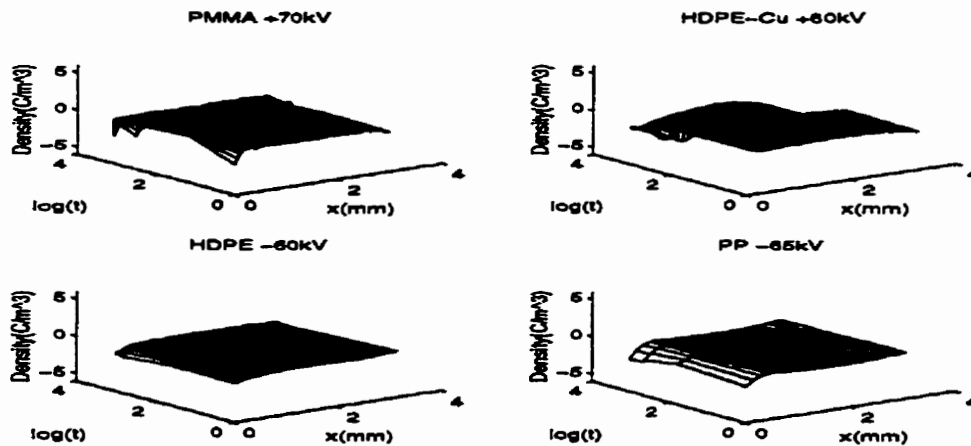


Figure 5.21 Space charge dynamics (same polarity as step increased voltage tests)

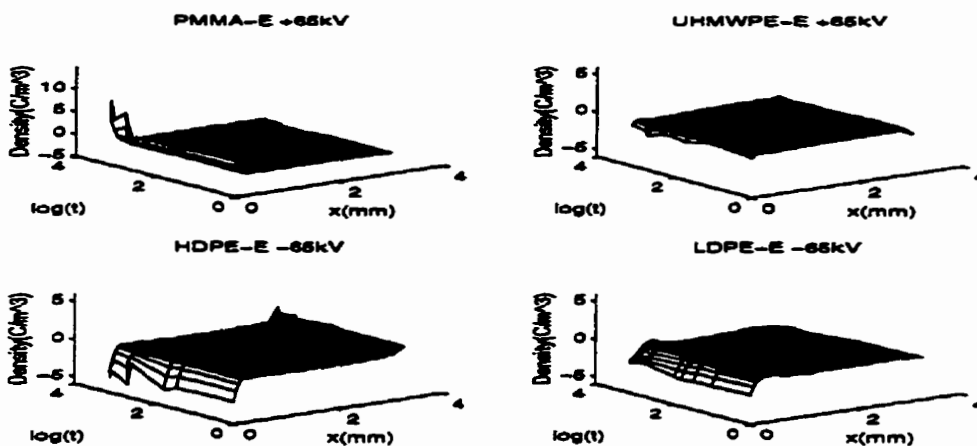


Figure 5.22 Space charge dynamics (same polarity as step increased voltage tests)

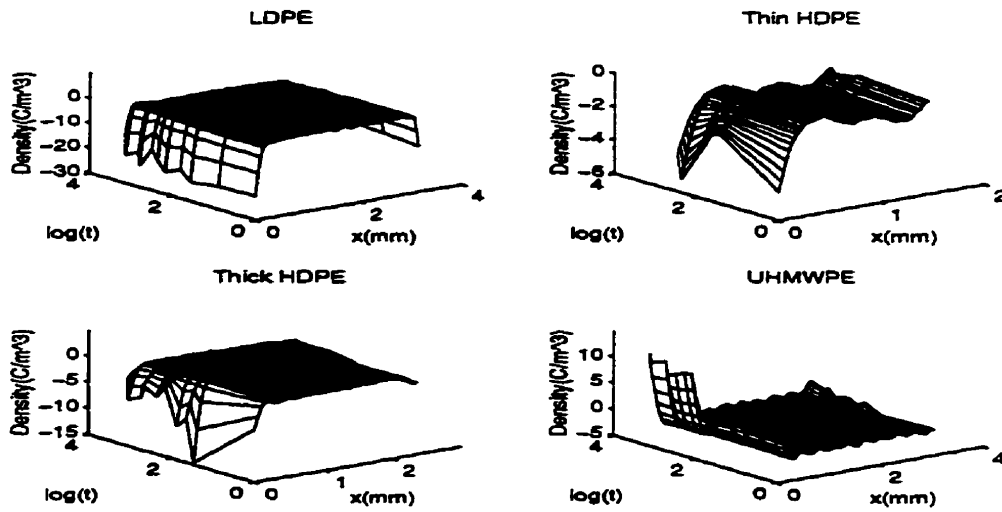


Figure 5.23 Space charge dynamics under reversed dc voltage for LDPE Thin HDPE Thick HDPE and UHMWPE

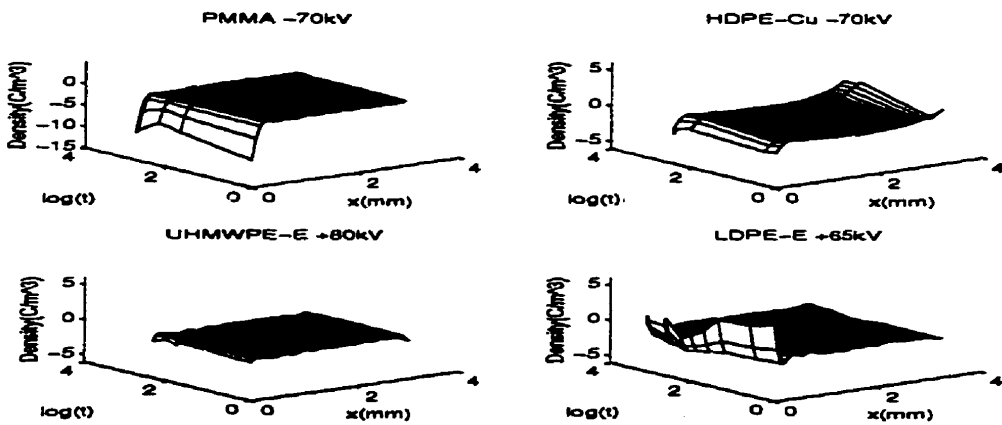


Figure 5.24 Space charge dynamics under reversed dc voltage for PMMA, HDPE-Cu, LDPE-E, and higher voltage for UHMWPE-E

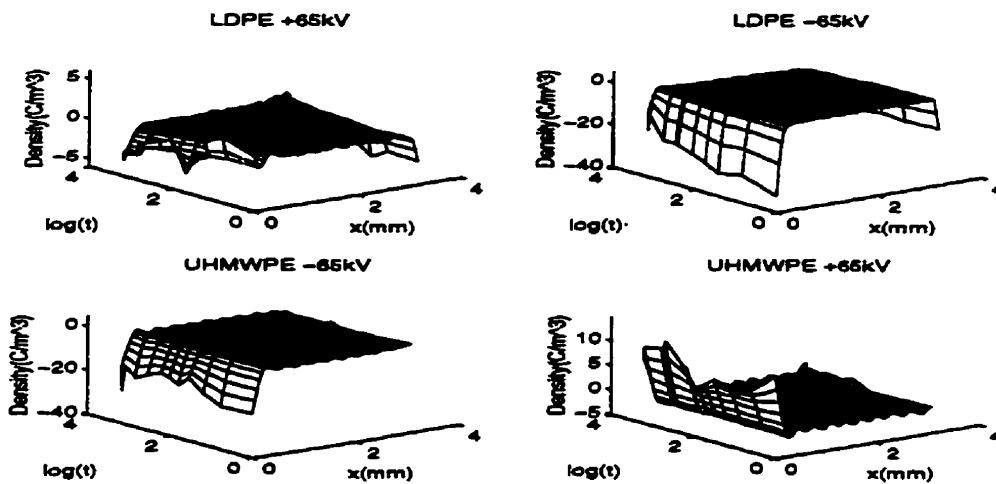


Figure 5.25 Space charge dynamics for LDPE&UHMWPE under the 2nd & 3rd reversals

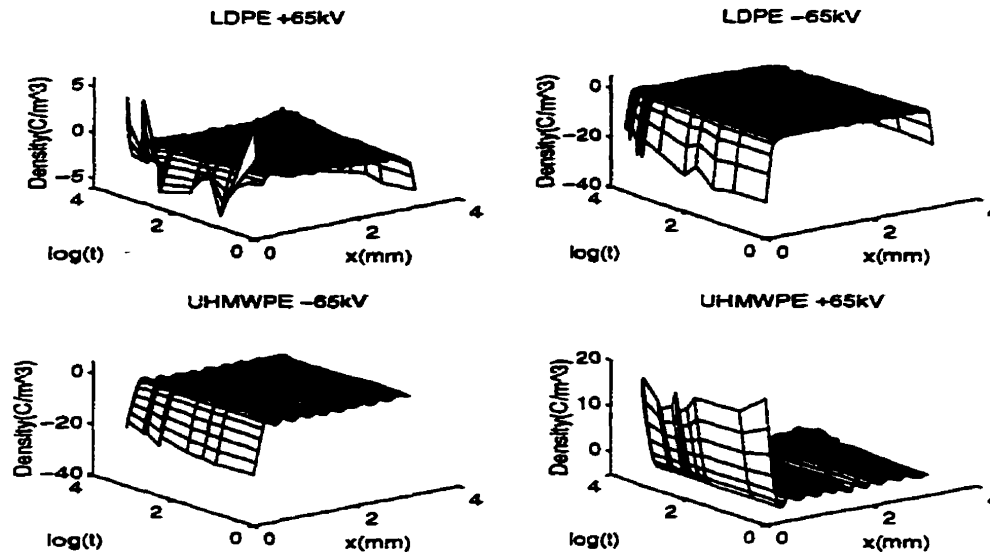


Figure 5.26 Space charge dynamics for LDPE&UHMWPE under the 4th and 5th reversals

5.4.3 Discussion

The results for *the first constant voltage application*(Figure 5.20-5.22) are summarized below:

1. When positive polarity is applied at HV electrodes, positive charges are distributed near the ground electrodes for Thin HDPE and PMMA-E, and for LDPE most of the time, however, small number of negative charges tend to distribute near ground electrodes for HDPE-Cu and UHMWPE-E, and for PMMA most of the time. Whatever positive or negative charges are distributed near the ground electrode, negative charges are present near the HV electrodes for all the specimens. For LDPE, there is obviously positive charge injection from the HV electrode side and negative charge injection from the ground electrode side. The negative charges injected from the ground electrodes and the positive charges from the HV electrodes seem to penetrate inside the specimen, away from the injected electrodes. As voltage application time increases, more charges are accumulated and the accumulation regions gradually tend to extend to the inner part of the specimen. These dynamic behaviors of space charge distribution are regarded as a space charge distribution

pattern and denoted as the *LDPE⁺ pattern*. For all the other specimens, this kind of tendency or pattern also exists, but to a much small degree. This finding indicates that space charges are much easier to be injected into LDPE materials than the other testing materials used (HDPE, UHMWPE, PP and PMMA).

2. When negative HVDC is applied at the HV electrode, negative charges are present at the ground electrode for all the testing specimens. A careful examination of the experimental results near the HV electrode side shows that negative charges are present there (Thick HDPE, UHMWPE, HDPE and LDPE-E), except PP and HDPE-E, for which positive charges are distributed near the HV electrode. As voltage application time increases, LDPE-E shows the increases of negative charges near the HV electrode. As the time increases, positive charges start to grow and penetrate deeper in the specimen near ground electrodes. This pattern is denoted as *LDPE-E pattern*.

It can be seen that there are remarkable changes in space charge distributions when the polarity is changed; however, the changes are quite small when the polarity is the same but the voltage is applied at a higher level. For UHMWPE-E, when higher voltage is applied, the charge pattern remains the same, and the amount of charges is slightly increased. For others, when reversed voltages are applied, the whole patterns seem to change. When polarity changes from positive to negative, for LDPE, large number of negative charges are distributed at both electrode sides, a pattern is denoted as *LDPE⁻ pattern*. For Thin HDPE, mainly positive charge distribution (*Thin HDPE⁺ pattern*) changes into all negative charges (*Thin HDPE⁻ pattern*). For PMMA, the pattern with a small amount of negative charge distributed near ground and HV electrode interfaces (*PMMA⁺ pattern*) changes into the pattern that a large amount of negative charge is distributed near ground electrode, while a small amount of positive charge is distributed near the HV electrode (*PMMA⁻ pattern* or heterocharge distribution). For HDPE-Cu, the pattern becomes a typical heterocharge distribution. The *heterocharge distribution pattern* is also held for PP and HDPE-E under negative voltage application.

When the HVDC voltage is changed from negative to positive, for Thick HDPE, negative charges decrease as the voltage application time increases. For UHMWPE, negative charges distributed near ground electrode sample interface (*UHMWPE⁻ pattern*) change to positive charges (*UHMWPE⁺ pattern*), and the number of charges increase to higher positive values as the application time increases. For LDPE-E, the pattern looks like the *LDPE⁺ pattern* but with less negative charge injection near the ground electrode.

The further reversal experiments for LDPE and UHMWPE (Figure 5.25 and Figure 5.26) show more clearly that a certain charge distribution pattern exists based on the charge injection voltage of the material and the polarity of HVDC voltage applied at the HV electrode. When negative voltages are applied, space charge distributions will tend to form the negative voltage application pattern, and vice versa. When the voltage is reversed, space charge distribution can change very fast towards the other pattern corresponding to the reversed voltage. Moreover, whenever the voltage is reversed back to the negative or positive, the number of charges inside the specimen are obviously increased compared to the previous negative or positive charge distribution pattern. In more simple words, frequent reverses of polarity seem to lead to more charge accumulation. It can be predicted that the breakdown of the specimen will happen earlier if the specimen is subject to more reversals.

Moreover, from the above experimental results, it is clear that negative polarity HVDC can lead to greater negative charge accumulation than positive polarity. This seems to prove that charge injection is easier for electrons than for holes, and may suggest that the density of the trap to catch electrons is higher than that of the trap to catch holes in the testing material.

5.5 SHORT CIRCUIT EXPERIMENTAL RESULTS

5.5.1 Procedures

After each cycle of step increased voltage application and each cycle of constant voltage application, the specimens were short-circuited as shown in Figures 5.6-5.9. It has been a well-known experimental phenomenon that a short-circuit can lead to earlier damage of the insulation materials[6]. Treeing and breakdown are found to happen when specimens are short-circuited (Section 3.3)[6-7]. Therefore, it has been an important part of this research to measure space charge distributions when specimens are short-circuited and to compare the space charge distributions before and after the short-circuits. In addition, for some specimens, for example, LDPE, continuous short-circuit experiments were conducted after space charges exist in the specimen to investigate the decay of space charges. Therefore, we can say that two types of short circuit experiments are conducted as mentioned in Section 5.1. The difference between the two types lies in that *Type#1* is performed immediately after a HVDC voltage application and that *Type#2* is performed while the specimen has been kept short-circuited for a long period. The results of the *Type#1* show the space charge distribution before and after the short-circuit. The results of the *Type#2* shows the decay of the space charges distributed inside the specimen as the short circuit time increases. The results of the *Type#1* for all specimens and the results of the *Type#2* for four specimens(Thick HDPE, PP, UHMWPE-E, and LDPE) are demonstrated in Section 5.5.2.

5.5.2 Results

Figures 5.27-5.37 show the first type short circuit experimental results of all the 12 specimens. Figure 5.38 shows the charge dynamics in Thick HDPE specimen for 300 minutes and in PP for 780 minutes after the last short-circuit. Figure 5.39 shows those results in UHMWPE for 1360 minutes and in LDPE for more than 37530 minutes(more than 20 days).

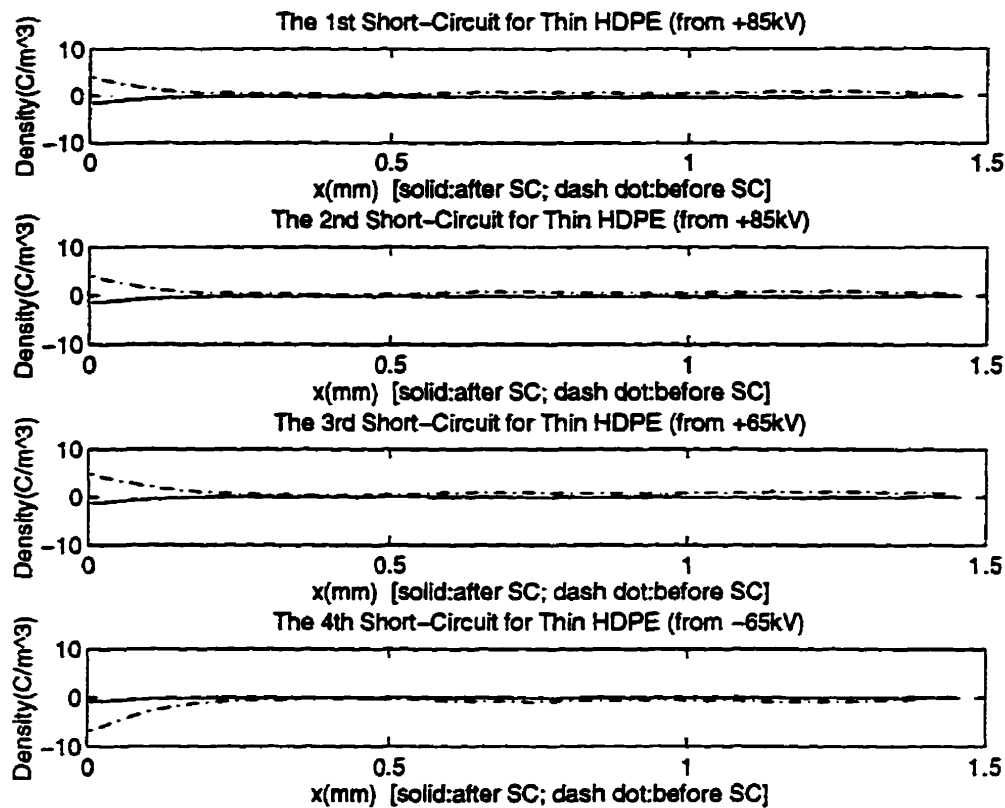
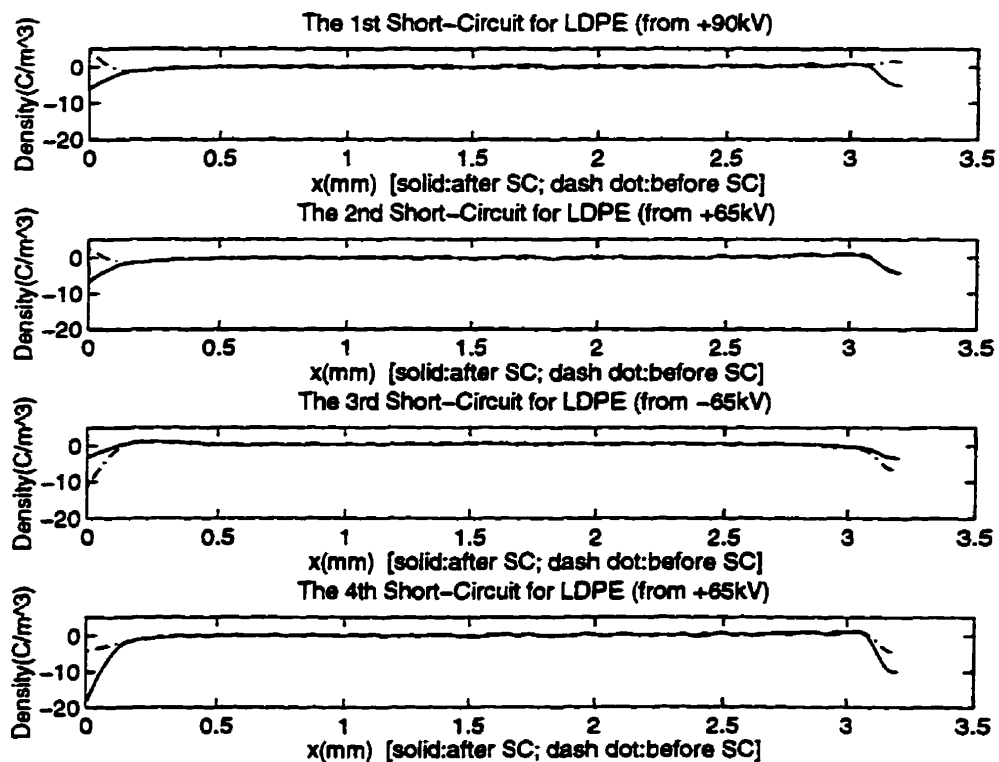


Figure 5.27 Short-circuit experiments for Thin HDPE



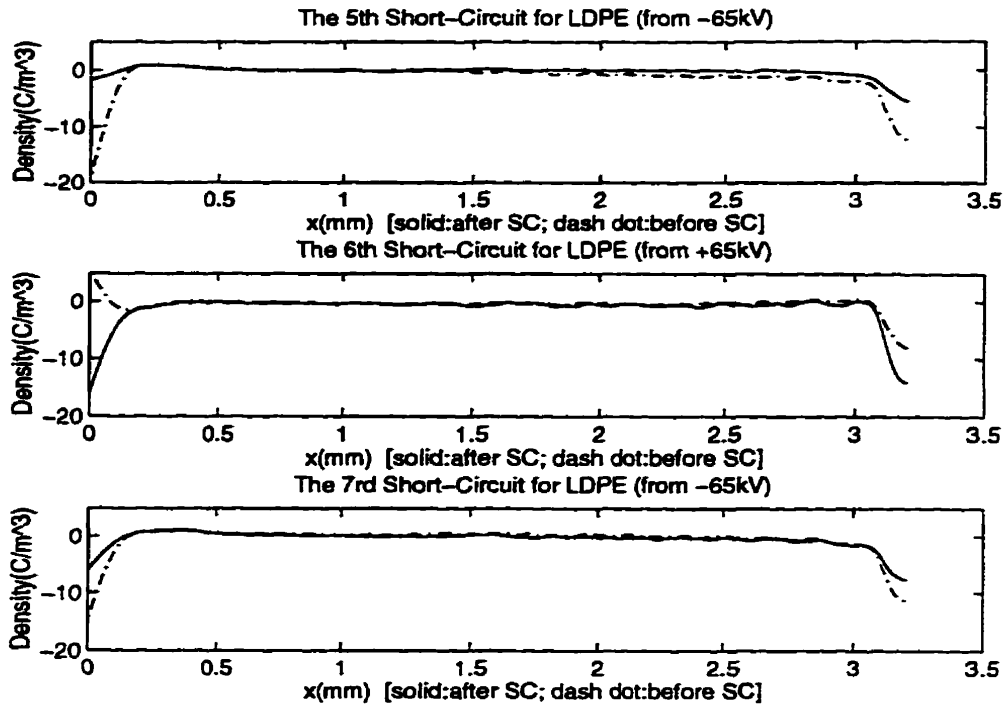


Figure 5.28 Short circuit experimental results for LDPE

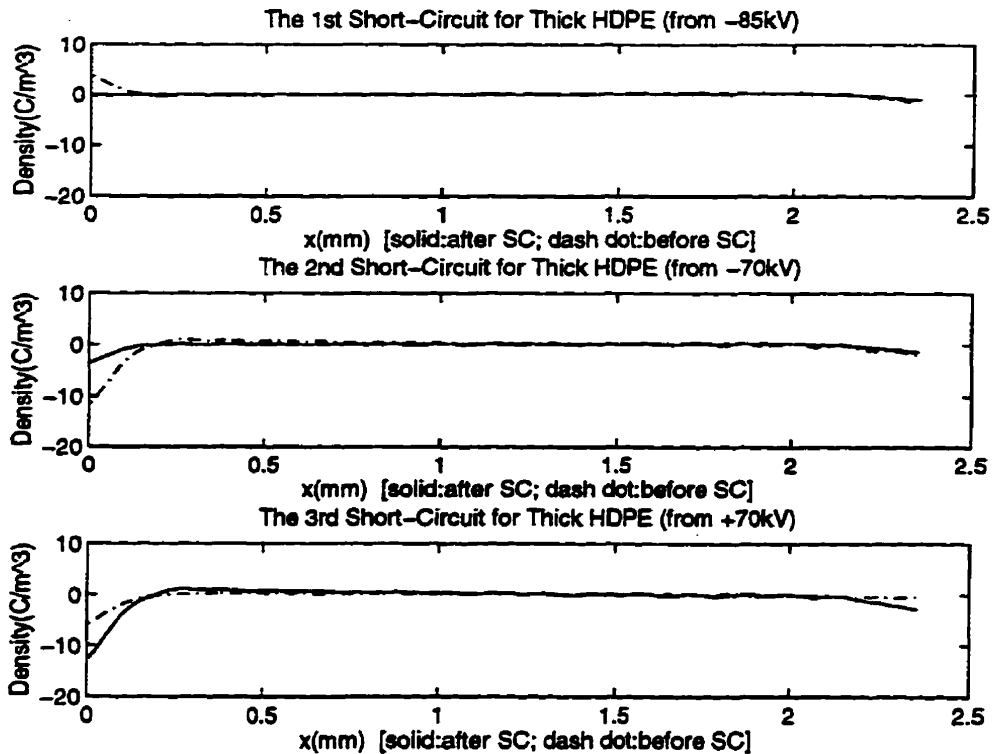


Figure 5.29 Short circuit experimental results for Thick HDPE

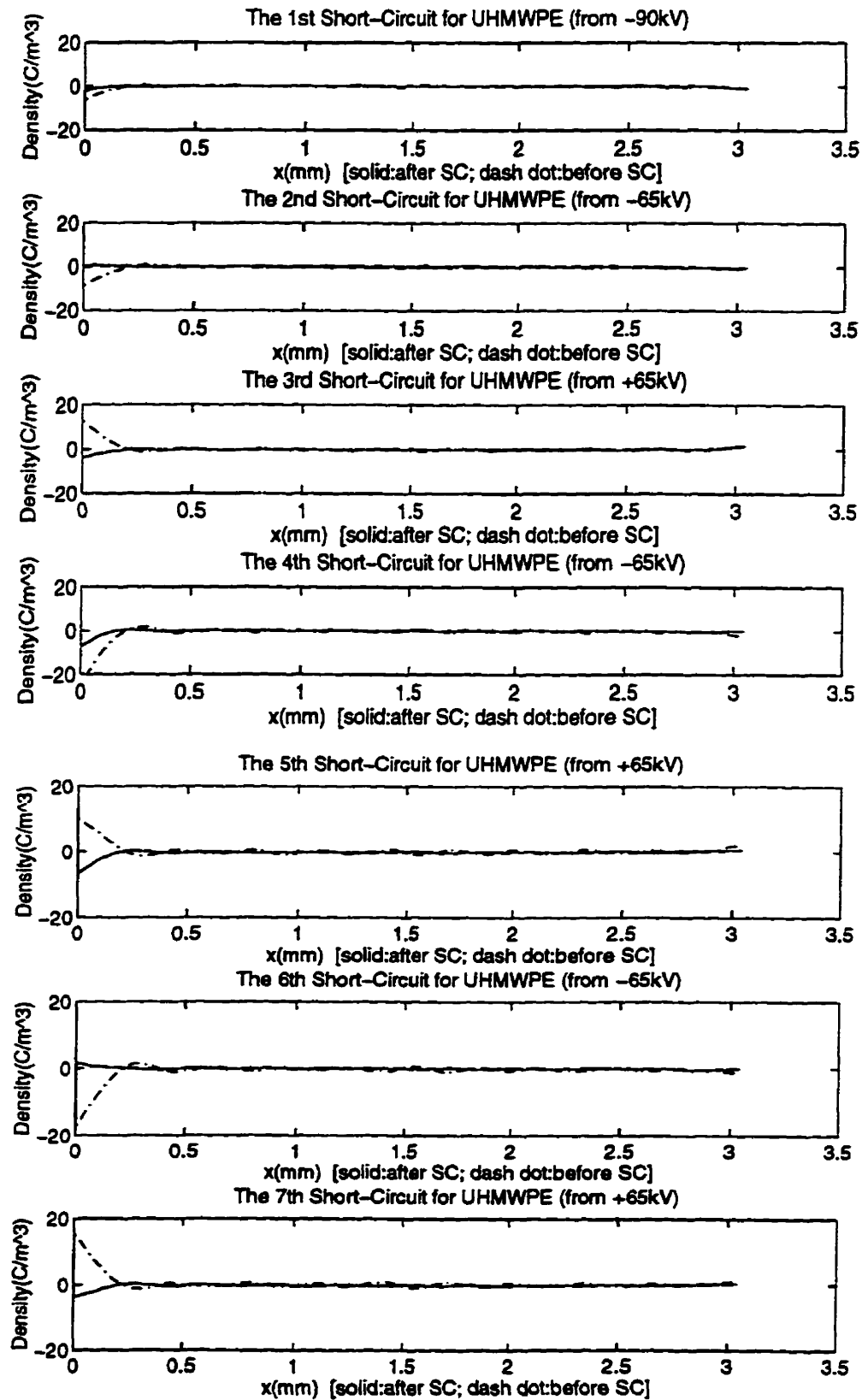


Figure 5.30 Short circuit experimental results for UHMWPE

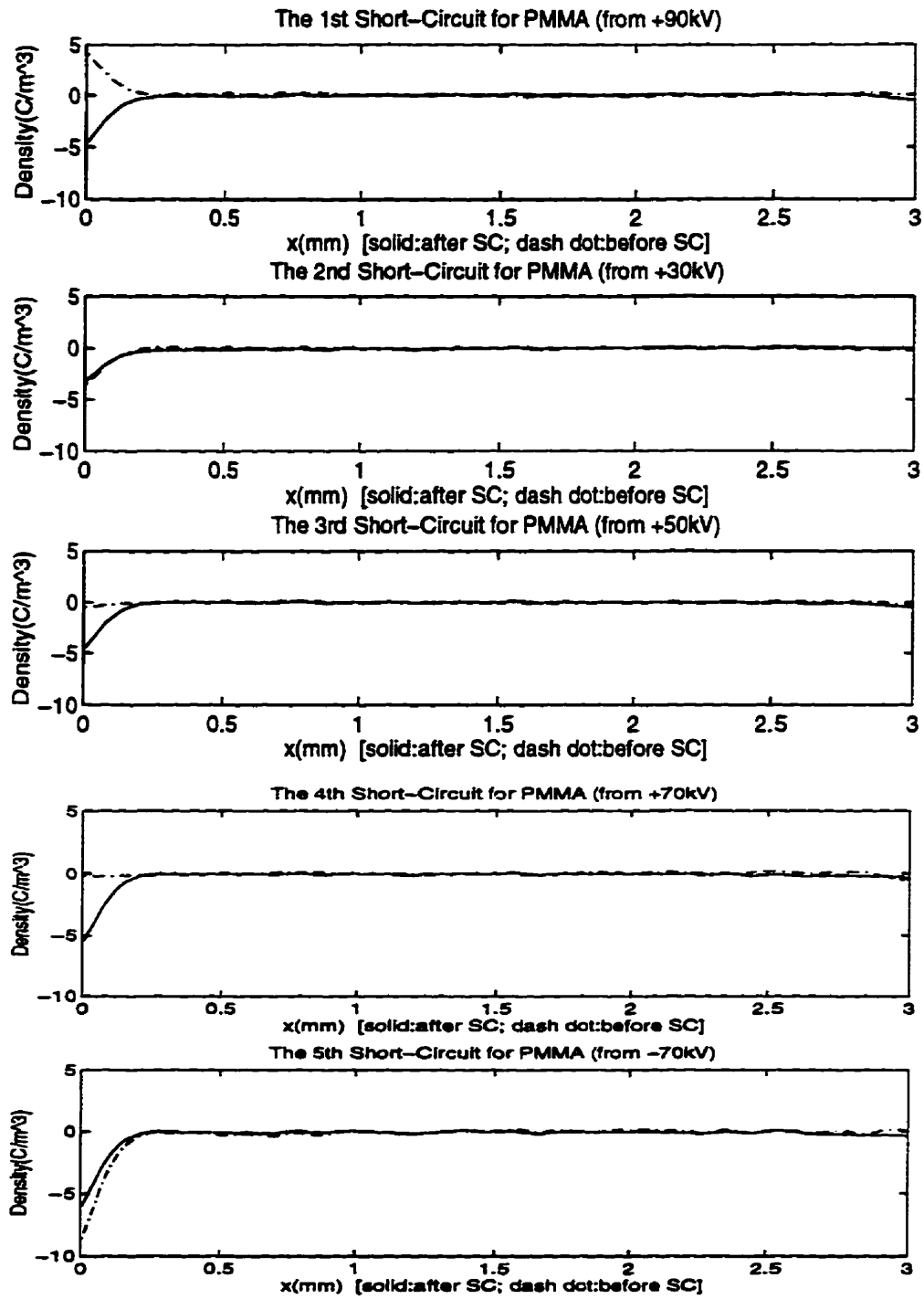


Figure 5.31 Short circuit results for PMMA

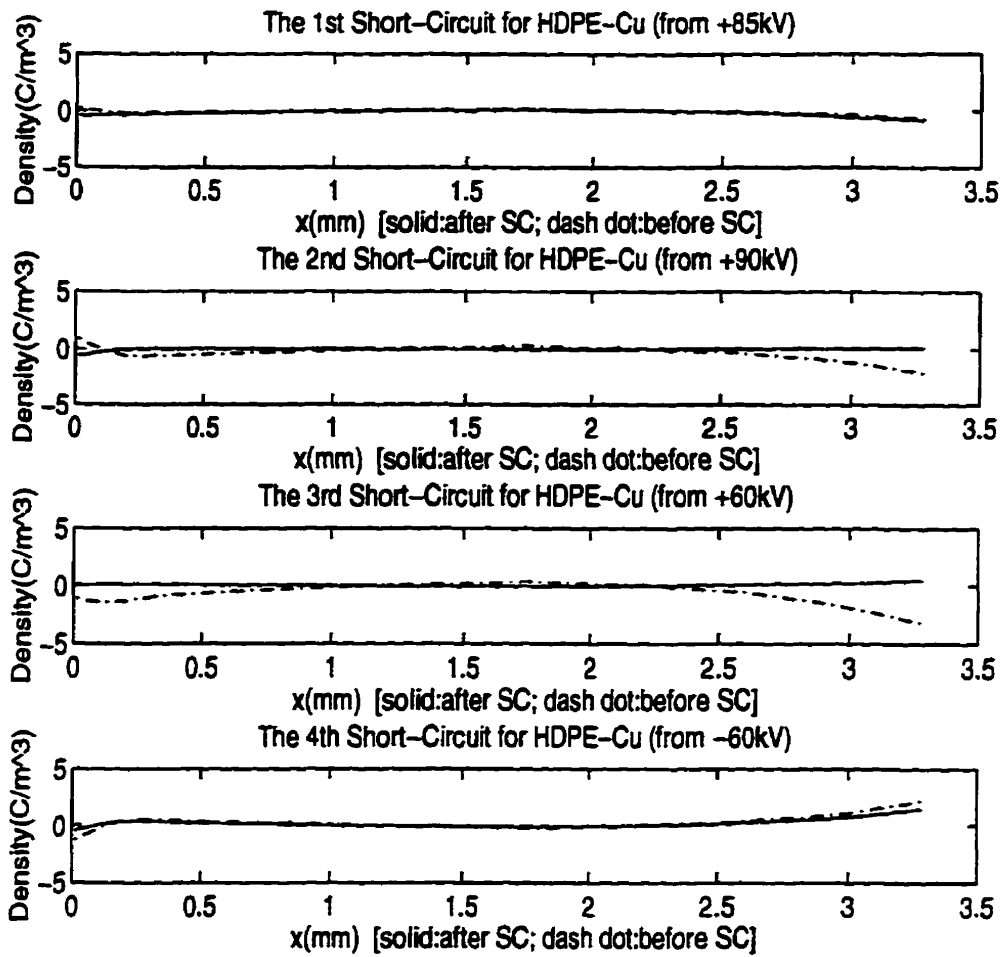
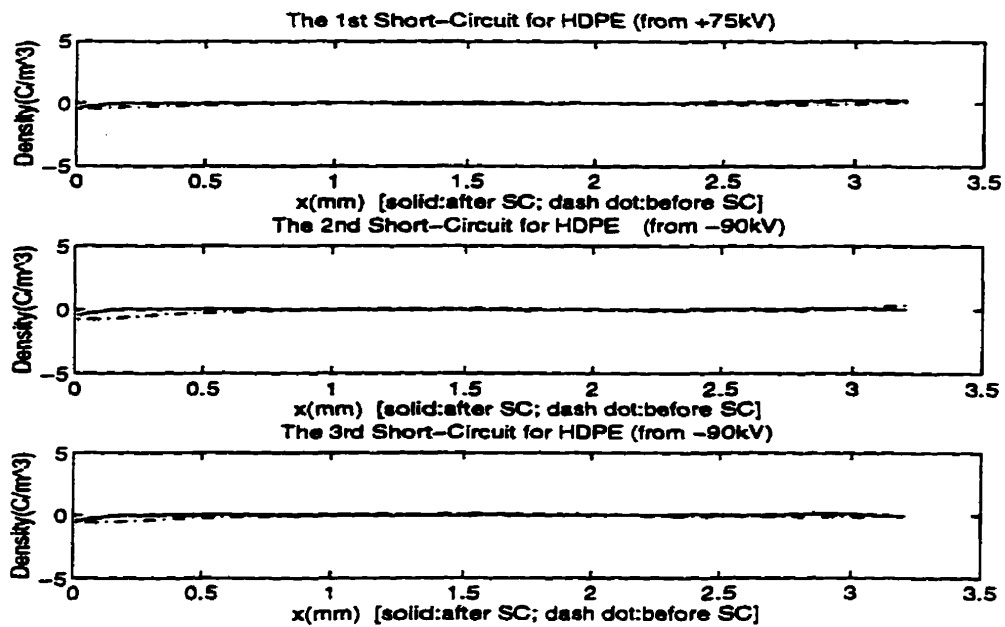


Figure 5.32 Short circuit results for HDPE-Cu



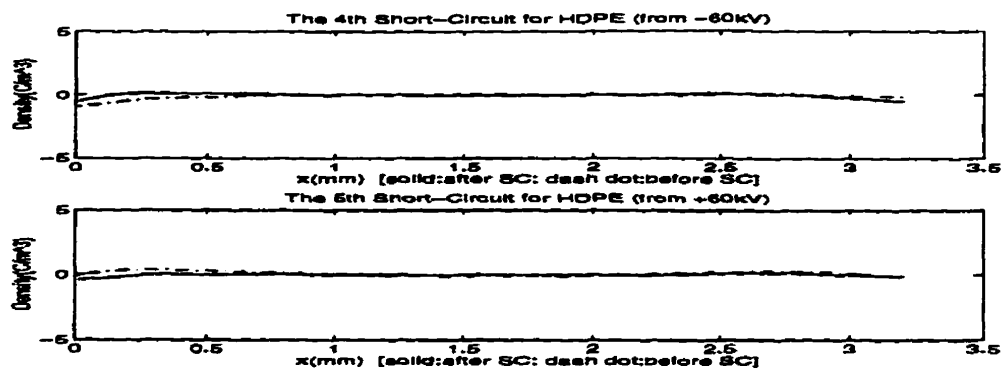


Figure 5.33 Short circuit results for HDPE

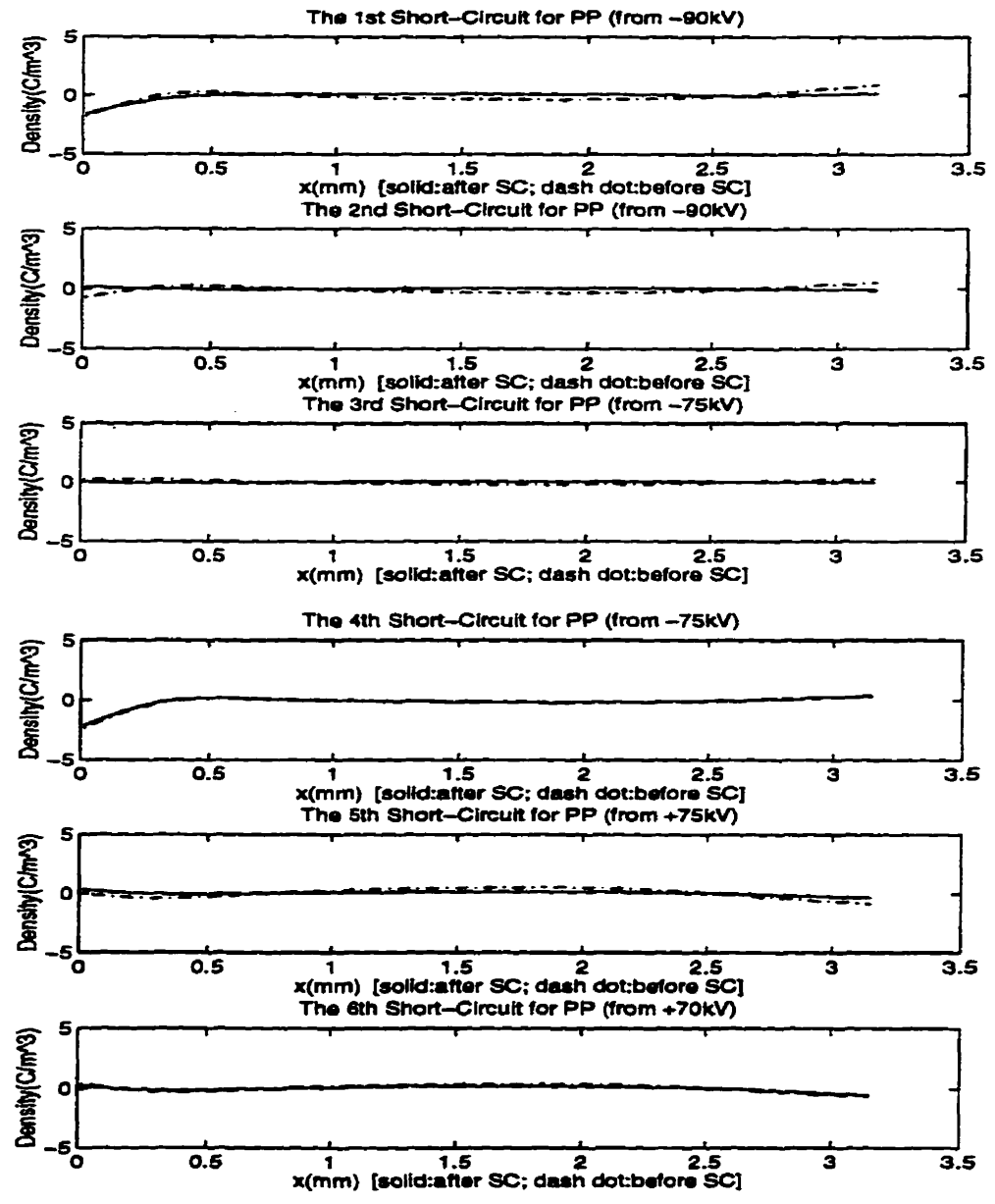


Figure 5.34 Short circuit results for PP

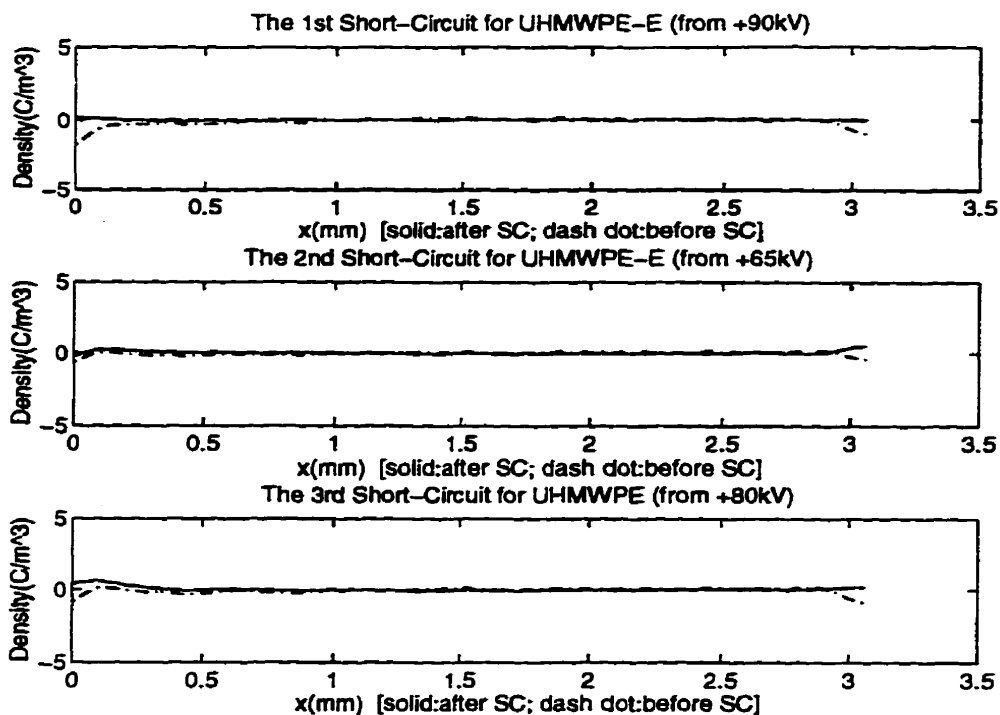


Figure 5.35 Short-circuit results for UHMWPE-E

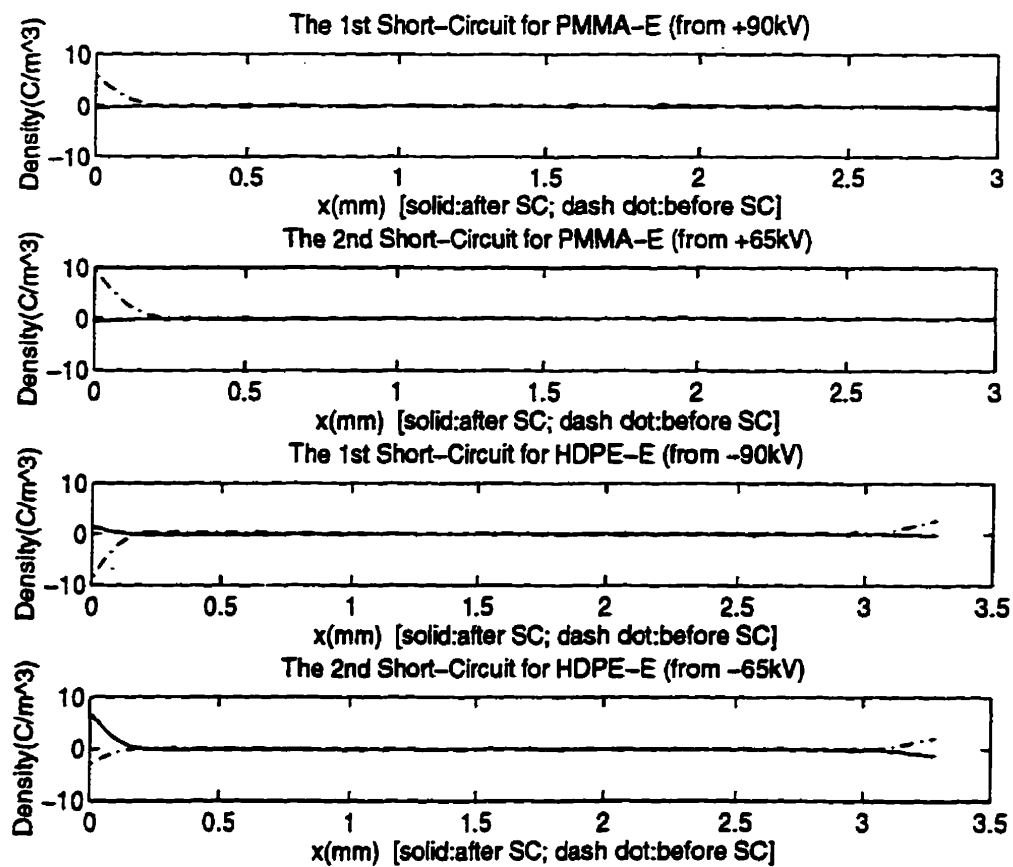


Figure 5.36 Short-circuit results for PMMA-E and HDPE-E

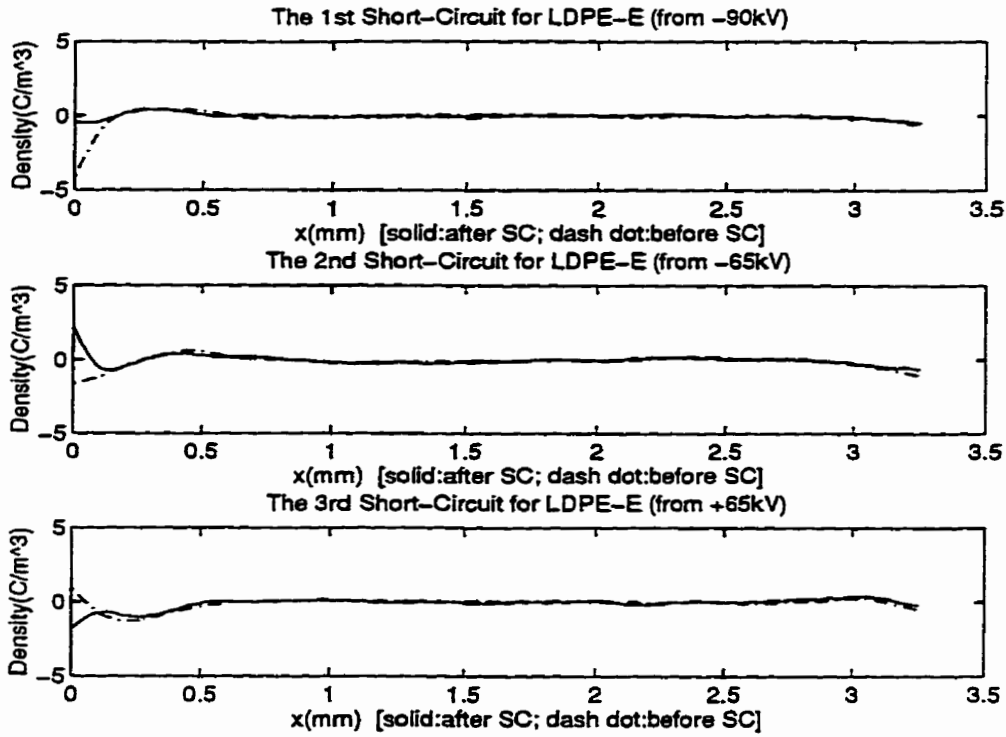


Figure 5.37 Short circuit results for LDPE-E

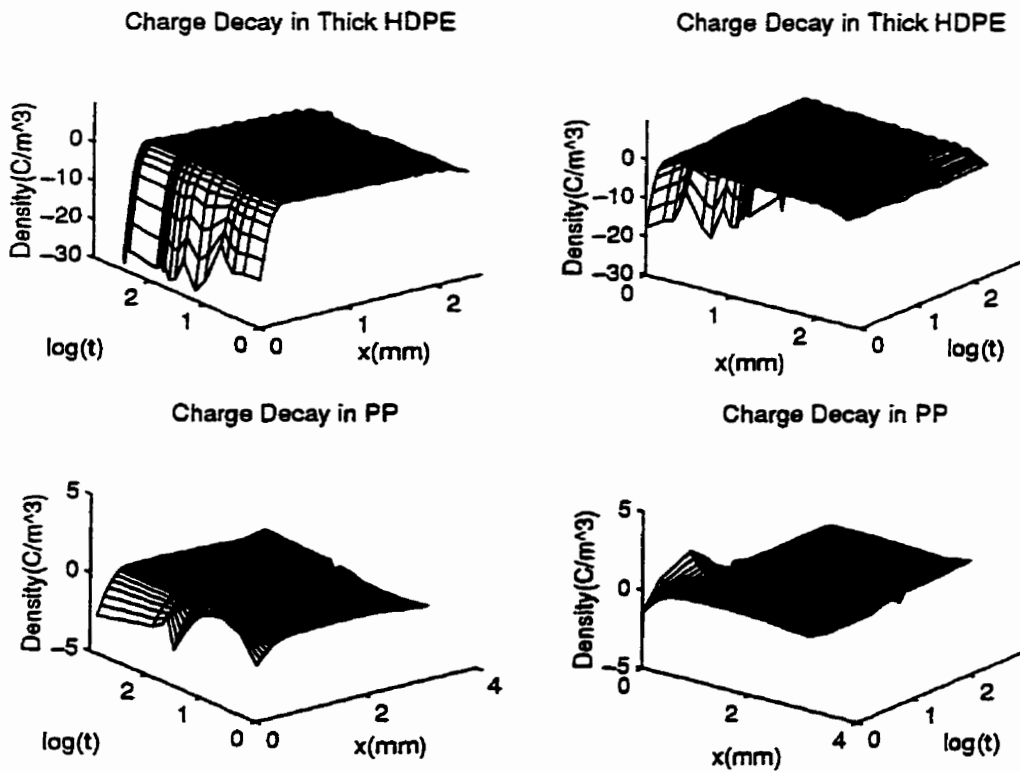


Figure 5.38 Charge dynamics after short circuit in Thick HDPE and PP

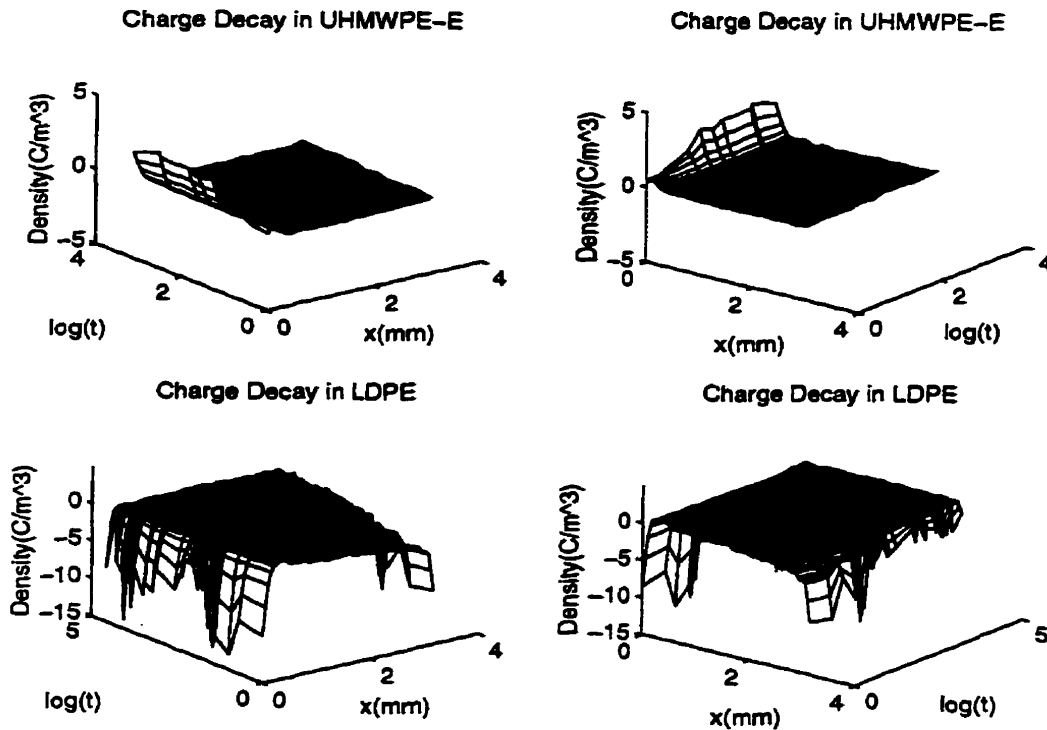


Figure 5.39 Charge decay dynamics in UHMWPE-E and LDPE

5.4.3. Discussion

We can observe two tendencies from the *Type#1* short circuit figures:

1. when the space charges accumulated near interfaces are positive and the short circuit takes place, the space charges accumulated have a greater tendency to change to negative polarity.
2. when space charges accumulated near the interfaces are negative and the applied voltage reduced to zero and the specimen is short-circuited, the space charges accumulated there have a greater tendency to remain negative.

These results seem to indicate that the main charge carriers are electrons and the movement of electrons are the main cause of the changes in the space charge distributions.

From the dynamic changes of charge distribution, it can be seen that short circuit cannot make the charge inside polymers decay immediately and completely. The amount of

charge in Thick HDPE after being short-circuited for 300 minutes, in PP after 780 minutes, or in UHMWPE after 1360 minutes does not seem to decrease. The significant decay of total space charges in LDPE seems to happen after 40 minutes as shown in Figure 5.40. However, even after more than 20 days, space charges still exist in LDPE. The internal charge will move to the interfaces, and the total number of charges will decrease, but there will still be some residue of charges inside the specimen distributed, mainly near the interfaces.

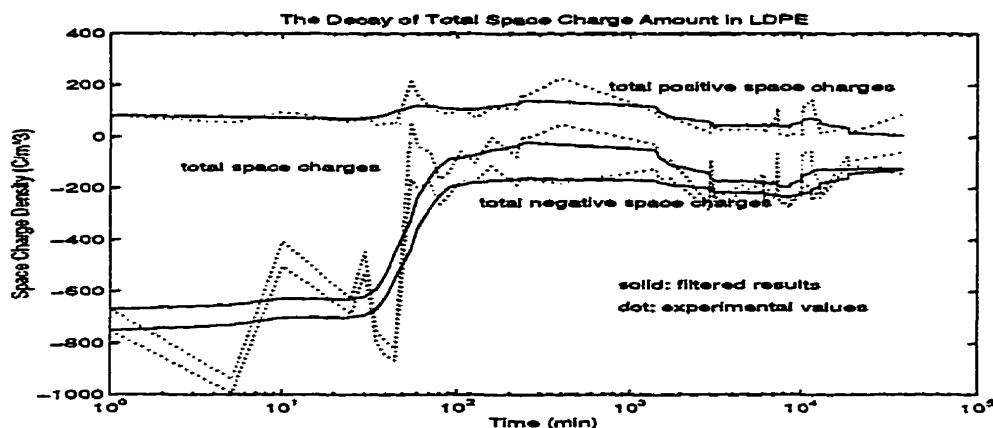


Figure 5.40 The decay of total amount of space charges in LDPE

5.6 SUMMARIES AND DISCUSSIONS

Although every specimen is not the same even if they are cut from the same sheet, the space charge dynamic characteristics of different materials can still be illustrated from the results of the three categories of the discussed experiments.

1. The charge injection field for LDPE is obviously lower than the other specimen materials. From the step increased voltage experiments, the charge injection voltage is around 25-35kV, corresponding to a electrical field stress around 10kV/mm. The LDPE material demonstrates less ability to sustain space charge injection since space charges can grow into the material and preserve a certain depth, depending on the applied voltages and application time.
2. The charge injection electrical field stress of HDPE is more than two times that of LDPE as known from step increased voltage experiments of Thin HDPE, Thick HDPE, HDPE-Cu, and HDPE specimens. The results of *the first step increased*

voltage application shows more charge accumulation for HDPE-E than the other HDPE specimens. However, it seems that the behavior can be explained: the Al evaporation process has resulted in some charge being injected. As one can see from the second negative step increased voltage experiment of Thick HDPE, the tendency of negative charge increases with voltage, near the ground electrode. This result, the same as for the HDPE-Cu, suggests that the charge injection might introduce some degradation of the specimen material near both the ground electrode-sample interface and the HV electrode-sample interface; therefore, it creates more traps for space charge accumulation.

3. Comparing all the specimens under positive HVDC and negative HVDC voltage applications suggest that negative HVDC has more potential to lead to more charge injection and more negative charge accumulation than the positive HVDC. The UHMWPE-E specimen, for example, is subjected only to positive HVDC voltage applications; the amount of charges are very low even when +80 kV is applied to it. Another example is the Thin HDPE. Although there is obvious charge injection for the Thin HDPE specimen at the HV electrode side, the amount of charge accumulated is not as much as the Thick HDPE (when negative HVDC is applied). This can also be seen from PMMA, PMMA-E, HDPE-Cu specimens.
4. The results of PMMA and PMMA-E are consistent. For the step increased voltage experiments, after the application voltage reaches 65kV, the amount of charge seems to increase rapidly to a higher level. A hypothesis is that some changes happen to some polar molecules at this voltage level.
5. Comparing the space charge distributions inside PP with HDPE and UHMWPE and PMMA, it seems that charge distribution of PP is not due to charge carriers such as electrons and holes but rather to polarization. For HDPE etc., the space charge distributions in the inner part of the specimen are about zero and remain zero when the applied voltage is increased. For PP, on the contrary, as one can see from Figure 5.15 and 5.17, the inner becomes concave and, as the voltage increases, this concave shape become more obvious. It is supposed that a kind of orientation of PP molecules may take place when the electric stress is increased.

6. The amount of space charge distributed inside both UHMWPE and UHMWPE-E is little. This result suggests that the bulk materials of the two specimens and their material characteristics are the same. However, the amount of charge distributed near the ground electrode for UHMWPE is much greater than for UHMWPE-E, suggests that the Al-tape connection between ground electrode and the specimen for UHMWPE may introduce some interfacial polarization activities, or provides some defects which encourage space charge injection, accumulation, and transportation.

The different charge dynamic behaviors for different materials, as summarized above, indicate that the ability of a material to sustain the relation of charge injection to the material density is only true for the same material base. The density of PP is the smallest among the five investigated materials; however, PP is much better than LDPE, considering the ability to sustain charge injection. For the three PE type materials, LDPE has the lowest density and is obviously not as good as HDPE and UHMWPE. However, as PE density reaches high density as HDPE, the density effect is saturated. Even if the molecular weight is very high, the ability to sustain charge injection will not improve much. This is not only true for UHMWPE but also true for XLPE. However, the increase of the molecular weight can increase other properties of the material, such as the mechanical strength, the working temperature, which are in that sense useful.

From these experiments, the following charge dynamic behaviors for all the specimens are found to be the same.

1. Negative HVDC application can lead to a larger amount of charge accumulation than the positive HVDC application;
2. Although the charge distribution for different specimens of the same material may not be the same, the charge distribution patterns of these specimens under constant voltage applications may fall into just two patterns, one for positive HVDC application, the other for negative HVDC application, such as *LDPE⁺ pattern* and *LDPE⁻ pattern*, *UHMWPE⁺ pattern* and *UHMWPE⁻ pattern* etc..

3. Frequent reverse of polarity will lead to frequent pattern changes and result in frequent charge injection, which can cause damage to the material near the interface and provide more traps near the interface, and, as a result, more charge accumulation.
4. Short circuit has more potential to cause electron injection than hole injection (or in other words, electron extraction).

From the measurements, despite the two typical charge distributions (i.e. the so-called homocharge distribution and the heterocharge distribution) two special patterns are found for LDPE. One is for negative HVDC application, the *LDPE⁻ pattern*, with negative charges near both electrodes and some positive charges distributed beside the negative charges near the ground electrode. The other is for positive HVDC application, the *LDPE⁺ pattern* with negative charges near the HVDC side and a small amount of inner positive charge beside them. A slight number of positive charges sometimes appear and sometimes disappear near the ground electrode, and a large amount of negative charges distributed with some depth inside the specimen near the ground electrode. From the two charge distribution patterns, one can observe that two processes exist and compete with each other: the homo-charge injection and the heterocharge collection. It seems that all the space charge distributions come from the balance of the two processes. The injection is not continuous; once an injection happens, the field stress decreases near the interfaces. Then the injection stops, and the collection process starts. When more heterocharges are collected, the field stress increases near the interfaces; then, another injection starts. From the constant voltage application experiments, we can observe that, though sometimes the number of charges may increase as the constant voltage application time increases, the overall tendency is for the number of charges near the interfaces to decrease. One can predict that, if there is no sudden changes in the applied voltage, such as a short-circuit, voltage reversal, lightning, or other fault situations, the presence of space charges will not reduce the lifetime of the insulation. However, if fault situations happen, the lifetime will reduce since the rapid movement of space charges can cause the degradation of the insulation material and result in more space charges. It can be predicted that after the internal space charge reaches a certain amount, a fault situation will lead to the initiation of treeing or breakdown processes.

CHAPTER 6

CONCLUSIONS AND FURTHER WORK

6.1 CONCLUSIONS AND CONTRIBUTIONS

The urgent need to investigate the dynamic behaviors of space charges inside polymers was identified by the review of solid breakdown mechanisms and space charge effects in Chapter 2(Section 2.3). Following the review presented in Chapter 2 (Section 2.4), it becomes apparent that the PEA method is well suited to the space charge dynamic investigation. The advantages of the PEA method lie in simple relationships between output signals and space charge distributions and the simple experimental setup. However, the resolution of charge distribution obtained by the PEA method is low compared to the other techniques. This research aimed to overcome this deficiency using the improved PEA method.

Previous work on the PEA method was reviewed in detail in Chapter 2 (Section 2.5) and reanalyzed in Chapter 3 (Section 3.2). The methods used to obtain space charge distributions from measured output signals seemed to need improvement. The two previously used signal processing methods, the deconvolution procedure(DCON) and the direct method(DM), each have difficulty in providing charge distributions with high resolution and accuracy. A novel application of stochastic principles and nonlinear operations is employed in the proposed simulation model to handle both the bandwidth and signal-to-noise-ratio effects; therefore, to provide high resolution. The point-matching simulation model approach was attempted and presented in Chapter 3(Section 3.3). The key contributions of the proposed point matching simulation model to the space charge distribution measurements can be identified as:

1. the ability to identify the presence of surface charges;

2. the ease of processing space charge distribution information separate from surface charge information; and the ease of combining space charge distribution with surface charges to form the whole charge distribution;
3. the improvement of system resolution to at least the rise time of the system transfer function up to the sampling intervals (depending on the used simulation step and delay) which is usually much smaller than the width of the system IR.
4. the judgment of whether the obtained charge distribution is correct by examining the difference between the simulated output signal generated from the obtained charge distribution, and the original measured output signal.
5. the introduction of a nonlinear detection and optimization for even better results.

In addition, the principle of the PEA method was further extended to nonuniform fields (needle-plane electrode configurations) in Chapter 3 (Section 3.4). With the simulation model, the charge distribution in nonuniform field can be obtained. The difference from the uniform field is designed only to obtain a correction factor sequence, which can be calculated when the electric fields of the electrode configuration without space charges can be obtained.

A comparison of the processed results for four sets of synthetic signals by the DM, the DCON, and the point matching simulation model (PMSM) is presented in Chapter 4 (Section 4.2). It was illustrated from the analytic point of view that:

- 1) the DM has the lowest resolution among the three methods but has the most requirements for application to the system (transfer function (IR) to be short duration pulse with no ringing effect). Much more information of space charge distribution can be gathered if the PMSM is applied to the signals obtained for the DM method. A serious shortcoming of the DM method is the inability to identify the presence of surface charges.
- 2) the DCON is the most sensitive to noise and therefore the least stable method among the three. A small disturbance can lead to a messy result. A well-designed filter may help to get rid of the high frequency noises and recover the charge distribution. However, the obtained charge distribution may or may not be the correct profile. Even if the charge

distribution profile is correct, the surface charges are smeared and mixed with the space charge distribution after the filtering process.

- 3) the PMSM uses the prior knowledge of the charge distribution (i.e. surface charges are present at the ground and the HV electrode interfaces). Therefore, surface charges are expected to be present at $\sigma(0)$ and $\sigma(N+1)$ of the σ sequence. When two σ sequences corresponding to two simulation steps are obtained, the two surface charges can be calculated. The surface charges can then be taken out of the space charge distribution. One can apply a filter to the space charge distribution instead of the whole charge distribution. This is the main advantage of the PMSM over the DM and the DCON methods. Moreover, the PMSM allows one to adjust the delay and the noise reduction process; therefore, its ability to handle the signal-noise-ratio effects is better than the DCON.
- 4) the judgment of whether the charge distribution is acceptable can be based on whether the obtained charge distribution profile is reasonable and also on whether the difference between the simulated output signal (using the obtained charge distribution profile) and the original measured output signal is small enough compared to the noise. The point matching principle is actually an attempted to obtain a σ sequence, that when convoluted with the system IR-model, it generates a simulated output signal $SV(k)$ that matches every step point of the original measured output signal $v_{sm}(k)$ or $v_{sm}'(k)$. Therefore, the difference is guaranteed to be small if the simulation is stable. One can roughly know whether the simulation is stable from the two σ sequence results.

Chapter 4 (Section 4.3) used two sets of experimental signals and demonstrated the signal processing procedures used by the PMSM to process the real signals. One contribution in this part is the proposal of a pre-processing procedure; another contribution is the proposal of a self testing algorithm. Although there are many experimental approaches to obtain space charge distributions in solids, one cannot check the validity of the results in any of the existing methods. The self testing algorithm provides a way to test whether the obtained charge distribution satisfies the experimental conditions.

Dynamic changes of charge distributions in the sheets of LDPE, HDPE, UHMWPE, PP and PMMA were investigated through a series of experiments: *Step Increased Voltage* experiments, *Constant Voltage* experiments, and *Short Circuit* experiments. The experimental results were presented and summarized in Chapter 5. The main contributions and experimental findings are as follows:

1. for the first time the simulation model is used to process experimental signals. Surface charges can be calculated and the changes of surface charges can be used as an indication of the internal space charge distributions. When the measured surface charges are lower than the theoretical charges calculated under uniform field (i.e. surface charges are decreasing), it indicates either homocharges are injected or homocharges are distributed near that interface. When experimental surface charges are higher than the theoretical uniform field charges (i.e. surface charges are increasing), it indicates either heterocharges are collected or heterocharges are distributed near that interface.
2. two different space charge distribution patterns exist for HVDC positive and HVDC negative voltage application[94].
3. polarity reversal will result in more charge accumulation and that short-circuits will initiate the rapid electron injection process when the positive charges exist before the short circuit.
4. due to polarity reversal (because of the short circuit), there will be more charge accumulation, which will lead to the electric treeing and eventually breakdown of the material.

6.2 FURTHER WORK

Further work will head mainly in two directions: improving the simulation model method and clarifying space charge dynamics in polymers with more designed experiments and experiments under needle-plane electrode configurations.

The nonlinear detection and optimization process(NDOP) has not been applied to experimental signals because the process is quite time consuming. It is therefore hoped that further work

can find a way to reduce the computation time. One possible way is to use the ARMA(auto-regressive moving average) model in place of the MA(moving average) model for the system I/R in order to reduce the amount of calculation. Further, it may be worth to apply recursive minimum variance deconvolution and the maximum likelihood deconvolution to the simulation model.

With the application of the simulation model, more information of the charge distributions can be obtained. It is therefore hoped that the simulation model can be used to obtain the charge dynamics for some more designed experiments, especially experiments under nonuniform field, and for some more polymeric materials. Also, it is hoped that the space charge distribution measurement can be combined with other relevant measurements such as the measurement of energy storage and relaxation, thermally stimulated current, and high field conductivity, etc..

The application of the simulation model to simulated signals and experimental signals demonstrates that the simulation model principle can separate surface charges from space charges and provide more accurate space charge distribution results and higher resolution. It seems that the simulation model can also be applied to the PWP (Pressure Wave Propagation) signal processing. With the separation of surface charges, the accuracy and the system resolution can also be improved.

REFERENCES

- [1] Martin T. Goosey, *Plastics for Electronics*, Elsevier Applied Science Publishers Ltd, 1985
- [2] W.Tillar Shugg, *Handbook of Electrical and Electronic Insulating Materials*, Van Nostand Reinhold, 1986
- [3] R. Bartnikas and R.M. Eichhorn, *Engineering Dielectrics, Vol IIA, Electrical Properties of solid Insulating Materials: Molecular Structure and Electrical Behavior*, Chapter 4, "Treeing in solid organic dielectric materials", (Publication STP 783), ASTM Press, Philadelphia, 1983
- [4] T. Takada, "Space Charge Formation in Dielectrics", *IEEE Trans. Electr. Insul.*, Vol. 21, No.6, pp.873-879, 1986
- [5] R. Bartnikas and K.D. Srivastava, *Power Cable Engineering*, Sandford Educational Press, 1987
- [6] M. Ieda, "Dielectric Breakdown Process of Polymer", *IEEE Trans. Elect. Ins.* Vol.15, No.3, pp.206-224, 1980
- [7] Z. Liu, R. Liu, H. Wang and W. Liu, "Space Charge and Initiation of Electrical Trees", *IEEE Trans. Electr. Insul.*, Vol. 24, No.1, pp.83-89, 1989
- [8] J. Chen and Z. Liu, "Theory of Dielectrics", MIP, 1982 (in Chinese)
- [9] J.J. O'Dwyer, "The Theory of Electrical Conduction and Breakdown in Solid Dielectrics", Clarendon Press, Oxford, 1973
- [10] J.J. O'Dwyer, "Breakdown in Solid Dielectrics", *IEEE Trans. Elect.Insul.*, Vol.17, No.6, pp 484-487, 1982

- [11]J.J. O'Dwyer, "The role of Space Charge in the Theory of Solid-Dielectric Breakdown", IEEE Trans. Electr. Insul., Vol.19, No.1, pp 1-9 ,1984
- [12]R. Patsch, "Space Charge Phenomena in Polyethylene at High Electric Fields", J.Phys. D: Appl. Phys. Vol. 23, pp.1497-1505, 1990
- [13]N. Klein, "Electrical Breakdown of Insulators by One-carrier Impact Ionization", J. Appl. Phys., Vol.53, No.8, pp.5828-5839, 1982
- [14]N. Klein and M. Albert, "Electrical Breakdown of Aluminum Oxide Films Flanked by Metallic Electrodes", J. Appl. Phys., Vol.53, No.8, pp.5840-5850, 1982
- [15]H. R. Zeller, "Breakdown and Prebreakdown Phenomena in Solid Dielectrics", IEEE Trans. Electr. Insul., Vol.22, No.2, pp.115-122, 1987
- [16]M. Ieda, "Carrier Injection, Space Charge and Electrical Breakdown in Insulating Polymers", IEEE Trans. Electr. Insul., Vol. 22, No. 3, pp.261-267, 1987
- [17]I. Kitani and K. Arii, "DC Tree Associated with Space Charge in PMMA", IEEE Trans. Electr. Insul., Vol. 22, No. 3, pp.303-307, 1987
- [18]T. Tanaka and A. Greenwood, "Effects of Charge Injection and Extraction on Tree Initiation in Polyethylene", IEEE Tran. Power App. Syst., Vol. 97, pp.1749-1757, 1978
- [19]D.K.Das-Gupta, K. Doughty, D.E. Cooper and E.O. Forster, "Role of Atmospheric Gases in the Space Charge Polarization of Low-density Polyethylene in a Divergent AC Field", IEEE Trans. Electr. Insul., Vol. 22, No.3, pp.325-331, 1987
- [20]M. Iwamoto, M. Fukuzawa and T. Hino, "Analysis of Space Charge in Insulating Materials under Non-uniform Electric Fields", IEEE Trans. Electr. Insul., Vol. 22, No.4, pp.419-424, 1987
- [21]A. Hadid and C. Laurent, "An Experimental Technique to Study Space Charge Injection in Polymeric Materials under ac Voltage", IEEE Trans. Electr. Insul., Vol.27, No.6, pp.1095-1100, 1992

- [22]Th. Baumann, B. Fruth, F. Stucki and H.R. Zeller, "Field-enhancing Defects in Polymeric Insulators Causing Dielectric Aging", *IEEE Trans. Electr. Insul.*, Vol. 24, No.6, pp.1071-1076, 1989
- [23]H.J. Wiesmann and H.R. Zeller, "A Fractal Model of Dielectric Breakdown and Prebreakdown in Solid dielectrics", *J.App.Phys.* Vol. 60, No.5, pp. 1770-1773, 1986
- [24]T. Hibma and H.R. Zeller, "Direct Measurement of Space-charge Injection from a Needle Electrode into Dielectrics", *Vol.59, No.5*, pp.1614-1620, 1986
- [25]H.R. Zeller and W.R. Schneider, "Electrofracture Mechanics of Dielectric Aging", *J.App. Phys.* Vol.56, No.2, pp.455-459, 1984
- [26]H.R. Zeller, P. Pfluger and J. Bernasconi, "High-mobility States and Dielectric Breakdown in Polymeric Dielectrics", *IEEE Trans. Electr. Insul.*, Vol. 19, No. 3, pp.200-204, 1984
- [27]H.R. Zeller, "Thermodynamics of Water Treeing", *IEEE. Tran. Electr. Insul.*, Vol.22, No.6, pp677-681, 1987
- [28]E.O. Forster, "The Search for Universal Features of Electrical Breakdown in Solids, Liquids and Gases", *IEEE Trans. Electr. Insul.*, Vol. 17, No.6, pp.517-521, 1982
- [29]P.P. Budenstein, "On the Mechanism of Dielectric Breakdown of Solids", *IEEE Trans. Electr. Insul.*, Vol. 15, No.3, pp. 225-240, 1980
- [30]S. Whitehead, "Dielectric Breakdown of Solids", Clarendon Press, Oxford, 1951
- [31]G.M.Sessler, "Electrets", Springer, Berlin, 1987
- [32]Bozena Hilczer and Jerzy Malecki, "Electrets", PWN-Polish Scientific Publishers- Warszawa, 1986
- [33]D.K. Walkeer and O.Jefimenco, "Volume charge distribution in carnauba wax electrets", *J.Appl. Phys.*, vol.44, pp.3459-3464, 1973

- [34] M. Salah Khalil and Bo Svarrer Hansen, "Investigation of Space Charge in Low-Density Polyethylene Using a Field Probe Technique", *IEEE Trans. on Electr. Insu.*, Vol.23, No.3, pp.441-445, 1988
- [35] T.R. Foord, "Measurement of the Distribution of Surface Electric Charge by Use of a Capacitive Probe", *J.Phys. E:Sci. Instrum.*, Vol.2, pp.411-413, 1969
- [36] H.J. Wintle, "Theory of the Potential Probe Used in Static Electrification Measurements on Insulators", *J.Phys. E:Sci. Instrum.*, Vol.3, pp.334-336, 1970
- [37] G.M.Sessler, J.E.West, and D.A.Berkley, "Determination of Spatial Distribution of Charges in Thin Dielectrics", *Phys.Rev.Lett.*, Vol.38, pp.368-371, 1977
- [38] M.Falk, G.Dreyfus, and J.Lewiner, "Vapour-induced Depolarization Currents", *Phys. Rev. B*, Vol.25, pp.5509-5514, 1982
- [39] J.B. Bernstein, "Improvements to the Electrically Stimulated Acoustic Wave Method for Analysing Bulk Space Charge", *IEEE Trans. on Electr. Insul.* Vol. EI-27, No.1, pp.152-161, 1992
- [40] R.E. Collins, "Analysis of Spatial Distributions of Charges and Dipoles in Electrets by a Transient Heating Technique" *J.Appl. Phys.*, Vol.47, pp.4804-4808, 1976
- [41] F.I. Mopsik and A.S. DeReggi, "Poling Behaviour of Polyvinylidene Flouride at Room Temperature", *Appl. Phys.Lett.*, Vol.44, pp.65-67, 1984
- [42] F.I. Mopsik and A.S. DeReggi, "Numerical Evaluation of the Dielectric Polarization Distribution from Thermal Pulse Data", *J.Appl.Phys.*, Vol.53, pp.4333-4339, 1982
- [43] A.S. De Reggi, C.M. Guttman, F.I.Mopsik, G.T.Davis and M.S. Broadhurst, "Determination of Charge of Polarization Distribution Across Polymer Electrets by the Thermal Pulse Method and Fourier Analysis", *Phys.Rev.Lett.* Vol.40, pp.413-416, 1978
- [44] M. Ieda, T. Mizutani, Y. Suzuoki, and Y. Yokota, "Study of Space Charge Effects in Polyethylene by Thermal Pulse Current Technique", *IEEE Trans. Electr. Insul.*, Vol.25, pp.509-514, 1990

- [45]P. Laurenceau, G. Dreyfus and J. Lewiner, "New Principle for the determination of Potential Distributions in Dielectrics", *Phys. Rev. Lett.* Vol.38, pp.46-49, 1977
- [46]C.Alquie, G.Dreyfus and J.Lewiner, "Stress-Wave Probing of Electric Field Distributions in Dielectrics", *Phys.Rev.Lett.* Vol.47, pp.1483-1487, 1981
- [47]R. Gerhard-Multhaupt, "Analysis of Pressure-Wave Methods for the Nondestructive Determination of Spatial Charge and Field Distributions in Dielectrics", *Phys. Rev.* Vol. B27, pp2494-2503, 1983
- [48]Y. Suzuoki, T. Furuta, et al, "Study of Space Charge in Polyethylene by Direct Probing", *IEEE Trans. on Electr. Insul.*, Vol.26, pp.1073-1079, 1991
- [49]S.B. Lang and D.K. Das Gupta, "A Technique for Determining the Polarization Distribution in Thin Polymer Electrets using Periodic Heating", *Ferroelectrics* Vol.39, pp.1249-1252, 1981.
- [50]D.K. Dass-Gupta and J.S.Hornsby,"Laser-intensity Modulation Method(LIMM), An Analytical and Numerical Modification", *IEEE Trans on Elect. Insul.*, Vol.26 No.1, pp.63-68,1991
- [51]S.B.Lang and D.K.Das-Gupta,"Laser-Intensity Modulation Method:A Technique for Determination of Spatial Distributions of Polarization and Space Charge in Polymer Electrets", *J.Appl.Phys.*, Vol.59, pp.2151-2160, 1986
- [52]T. Takada and T. Sakai, "Measurement of Electric Fields at a Dielectric/Electrode Interface using an Acoustic Transducer Technique", *IEEE Trans. Elect. Ins.* Vol.18, pp.619-628, 1983
- [53]T. Takada, T. Maeno and H. Kushibe, "An Electric Stress Pulse Technique for the Measurement of Charges in a Plastic Plate Irradiated by an Electron Beam", *IEEE Trans. on Electr. Insul.*, Vol.22, No.4, pp.497-501, 1987
- [54]T.Takada, T.Maeno, and H.Kushibe, "An Electric Stress Pulse Technique for the Measurement of Charges in a Plastic Plate Irradiated by an Electron Beam", *Fifth International Symposium on Electrets, Heidelberg*, pp.451-456,1985

- [55] T. Maeno, T. Futami, H. Kushibe, T. Takada, and C. M. Cooke, "Measurement of Spatial Charge Distribution in Thick Dielectrics Using the Pulsed Electro-acoustic Method", *IEEE Trans. Electr. Insul.*, Vol.23, pp.433-439, 1988
- [56] C. M. Cooke, K. A. Wright, T. Maeno, H. Kushibe and T. Takada, "Pulsed Electro-acoustic Determination of MeV Energy Electron Implanted Charge in PMMA", *Proc. 2nd IEEE Internat. Conference on Conduction and Breakdown in Solid Dielectrics, Erlangen*, pp.318-324, 1986
- [57] J. B. Bernstein and C. M. Cooke, "Electrical Poling Behaviour of Poly (methylmeth-acrylate)", *IEEE Trans. Electr. Insul.*, Vol.26, pp.1087-1093, 1991
- [58] J. B. Bernstein and C. M. Cooke, "Bulk Space Charge Behaviour in Poly(methyl-methacrylate) under an Imposed Virtual Cathode Condition", *IEEE Trans. Electr. Insul.*, Vol.26, pp.1080-1086, 1991.
- [59] J. B. Bernstein, "Analysis of the Electrically Stimulated Acoustic-Wave Method for Observing Space Charge in Semi-insulating Films", *Phys. Rev. B*, Vol.44, pp.10804-10814, 1991
- [60] S. B. Lang and D. K. Das-Gupta, "Complex Polarization Distributions in PVDF Samples", *Ferroelectrics*, Vol.55, pp.151-154, 1984
- [61] S. B. Lang and D. K. Das-Gupta, "A New Technique for Determination of the Spatial Distribution of Polarization in Polymer Electrets", *Ferroelectrics*, Vol.60, pp.23-36, 1984
- [62] S. B. Lang and D. K. Das-Gupta, "Space Charge Distribution in thermally Poled Polyethylene and a Comparison with Polyvinylidene fluoride", *IEEE Trans. Electr. Insul.*, Vol.21, pp.399-403, 1986
- [63] S. B. Lang and Q. R. Yin, "Spatial Distributions of Polarization and Space Charge in Tin-substituted Lead Zirconate Titanate Ceramics Using Laser Intensity Modulation Method (LIMM)", *Ferroelectrics*, Vol.74, pp.357-368, 1987
- [64] J. Lewiner, "Evolution of Experimental Techniques for the study of the Electrical Properties of Insulating Materials", *IEEE Trans. Electr. Insul.* Vol.21, No.3, pp.351-360, 1986
- [65] R. A. Anderson and S. R. Kurtz, "Direct Observation of Field-injected Space Charge in a Metal/Insulator/Metal Structure", *J. Appl. Phys.*, Vol.56, pp.2856-2863, 1984

- [66]C.Alquie, C. Laburthe Tolra, J. Lewiner, and S.B. Lang "Comparison Study of the Polarization Distribution Measurement by the LMM and PWP Methods", *IEEE Trans. Electr. Insul.*, Vol. 27, No.4, pp.751-757, 1992
- [67]T. Mizutaani, Y.Suzuoki, T.Furuta, M.Ieda, T.Suzuki, "Direct Observation of Space Charge Distribution in Polyethylene", *CEIDP 1989 Annual Report*, pp.309-314, 1989
- [68]T.Ditchi, C.Alquie and J.Lewiner, "Electrical Properties of Electrode /Polyethylene / Electrode Structures", *IEEE Trans. Elect. Ins.* Vol.24, No.3, pp.403-408, 1989
- [69]Z. Croitoru, "Space Charges in Dielectrics", *Progress in Dielectrics*, vol.6, pp.105-145,1965
- [70]S.Mahdavi, C.Alquie and J. Lewiner, "Measurement of Charge Distributions in Coaxial Structures Application to HV Cables", *CEIDP 1989 Annual Report*, pp.296-302,1989
- [71]C. Alquie, T.Ditchi and J.Lewiner, "Measurement of Charge Distributions in Insulating Materials for HV Cables", *Proc. 2nd Intern. Conf. on Properties and Applications of Dielectric Materials*, pp.434-437, 1988
- [72]T. Takada and Y. Li, "Pulsed Electroacoustic Techniques to Characterize Charge Accumulation Properties", *IEE, Six International Conference of Dielectric Materials, Measurements and applications*, Conf. Pub. No. 363, pp.104-107, 1992
- [73]Y. Liu, Master Thesis, Xi'an Jiaotong University, 1992 (in Chinese)
- [74]Y. Liu, Y. Zhu and D. Tu, "The Pulsed Electro-acoustic Method by Frequency Domain Analysis for Measuring Space charge Distributions in Solid Dielectrics", *Trans. of China Electrotechnical Society*, No.1, pp.44-49, 1994 (in Chinese)
- [75]Y. Li and T. Takada, "Progress in Space Charge Measurement of Solid Insulating Materials in Japan", *IEEE Electr. Insul Magazine*, Vol.10, No.5, pp.16-28, 1994
- [76]Y. Li, M. Yasuda, and T. Takada, "Pulsed Electroacoustic Method for Measurement of Charge Accumulation in Solid Dielectrics", *IEEE Trans on Dielectrics and Electrical Insulation*, Vol.1, No.2, pp.188-195, 1994

- [77] S. Mahdavi, Y. Zhang, C. Alquié & J. Lewiner, "Determination of Space Charge Distributions in Polyethylene Samples Submitted to 120kV dc Voltage", *IEEE Trans. Elect. Insul.*, Vol. 26, No. 1, pp.57-61, 1991
- [78] N. Hozumi, H. Suzuki, T. Okamoto, K. Watanabe, and A. Watanabe, "Direct Observation of Time-dependent Space Charge Profiles in XLPE Cable under High Electric Fields", *IEEE Trans on Dielectrics and Electrical Insulation*, Vol.1, No.6, pp.1068-1076, 1994
- [79] R. Liu, T. Takada and N. Takasu, "Pulsed Electro-acoustic Method for Measurement of Space Charge Distribution in Power Cables under Both DC and AC Electric Fields", *J. Phys. D: Appl. Phys.* 26, pp.986-993, 1993
- [80] K.S. Suh, S.J. Hwang, J.S. Noh, and T. Takada, "Effects of Constituents of XLPE on the Formation of Space Charge", *IEEE Trans on Dielectrics and Electrical Insulation*, Vol.1, No.6, pp.1077-1083, 1994
- [81] F. Coulon, *Signal Theory and Processing*, Artech House, Inc., 1986
- [82] J.M. Mendel, *Maximum-likelihood Deconvolution: A Journey into Model-Based Signal Processing*, Springer-Verlag New York Inc., 1990
- [83] Y. Li, M. Aihara, K. Murata, Y. Tanaka, and T. Takada, "Space Charge Measurement in Thick Dielectric Materials by Pulsed Electroacoustic Method", *Review of Scientific Instruments*, Vol.66, No.7, pp.3909-3916, July 1995
- [84] L. Ljung and T. Glad, *Modeling of Dynamic Systems*, PTR Prentice Hall, 1994
- [85] L.E. Kinsler and A.R. Frey, *Fundamentals of Acoustics*, John Wiley & Sons, Inc., 1962.
- [86] J. Krautkrämer and H. Krautkrämer, *Ultrasonic Testing of Materials*, Springer-Verlag Berlin Heidelberg New York, 1983
- [87] J.M. Mendel, "Minimum-variance and Maximum-Likelihood Recursive Waveshaping", *IEEE Trans. on Acoustics, Speech, and Signal Processing*, Vol. ASSP-31, No.3, pp.599-604, 1983

- [88]I.I. Hirschman and D.V. Widder, *The Convolution Transform*, Princeton University Press, Princeton, New Jersey, 1955
- [89]William D. Stanley, *Digital Signal Processing*, Reston Publishing Company, Inc. A Prentice-Hall Company, Reston, Virginia, 1975
- [90]A.E. Taylor, *Advanced Calculus*, Blaisdell Publishing Company, 1955
- [91]Y. Liu and M.M.Salama, "Applying Simulation Model to Uniform Field Space Charge Distribution Measurements by the PEA Method", 1996 IEEE International Symposium on Electrical Insulation, Vol. 2, pp466-469, Montreal, 1996
- [92]L. Ljung, *System Identification-Theory for the User*, Prentice Hall, Englewood Cliffs, 1987
- [93]Y. Liu and M.M. Salama, "Space Charge Distribution Measurements in Polymers under Needle-Plane Electrode Configurations by Pulsed Electro-acoustic Method", CEIDP 1995 Annual Report, Vol.1, pp.294-297, Virginia Beach, 1995
- [94]Y. Liu and M.M.Salama, "Investigating Space Charge Dynamics in Polymers by the Improved Pulsed Electro-acoustic Method", CEIDP 1996 Annual Report, Vol.1, pp.169-173, Millrae, 1996

APPENDIX-A

RELEVANT CONCEPTS

A-1 Electric Pulse Fields

As it is known, for a uniform field electrode setup (i.e. plane-plane electrode configuration), when there is no space charge distributed inside a specimen, the electric field at any point, x , in the specimen, when a voltage V is applied, can be written as:

$$E(x) = \frac{V}{d}, \quad (\text{A-1-1})$$

where d is the thickness of the specimen.

When space charges are distributed inside the specimen, the uniform field will become nonuniform. Suppose the electric field generated by the distributed space charges is $E_\rho(x)$, using the superposition principle, the total electric field then is,

$$E_t(x) = E_\rho(x) + E(x) = E_\rho(x) + \frac{V}{d}. \quad (\text{A-1-2})$$

If the applied voltage increases a ΔV , under the condition that this change will not change the space charge distribution (i.e. $E_\rho(x)$ remains the same) the total electric field then is:

$$E_t'(x) = E_\rho(x) + E'(x) = E_\rho(x) + \frac{V + \Delta V}{d}. \quad (\text{A-1-3})$$

Therefore, the additional field due to the increase in voltage is:

$$\Delta E(x) = E_t'(x) - E_t(x) = \frac{\Delta V}{d}. \quad (\text{A-1-4})$$

Obviously, $\Delta E(x)$ is related to the voltage difference and the electrode configuration, and it has nothing to do with the space charge distribution. Therefore, one can say that the electric pulse field is related only to the electric pulse voltage and the electrode configuration under the condition that the short duration small pulse voltage application will not change the existing space charge distribution.

A-2 Convolution[88]

When two Laurent series

$$A(z) = \sum_{k=-\infty}^{\infty} a_k z^k, \quad B(z) = \sum_{k=-\infty}^{\infty} b_k z^k \quad (\text{A-2-1})$$

are multiplied together formally, a new series of the same type results

$$A(z)B(z) = \sum_{k=-\infty}^{\infty} c_k z^k \quad (\text{A-2-2})$$

where the new coefficients c_k are related to the old ones as follows:

$$c_n = \sum_{k=-\infty}^{\infty} a_{n-k} b_k, \quad n=0, \pm 1, \pm 2, \pm 3, \dots \quad (\text{A-2-3})$$

The sequence $\{c_n\}_{-\infty}^{\infty}$ is called the *convolution* of the sequences $\{a_n\}_{-\infty}^{\infty}$ and $\{b_n\}_{-\infty}^{\infty}$. When two bilateral Laplace integrals are multiplied together, the continuous analogue of this operation is obtained,

$$A(s) = \int_{-\infty}^{\infty} e^{-st} a(t) dt, \quad B(s) = \int_{-\infty}^{\infty} e^{-st} b(t) dt. \quad (\text{A-2-4})$$

The result is an integral of the same form,

$$A(s)B(s) = \int_{-\infty}^{\infty} e^{-st} c(t) dt, \quad (\text{A-2-5})$$

where

$$c(x) = \int_{-\infty}^{\infty} a(x-t)b(t) dt. \quad (\text{A-2-6})$$

This combination of functions occurs so frequently that it may be regarded as one of the fundamental operations of analysis. The function $c(x)$ is called the *convolution* of $a(x)$ and $b(x)$, and the integral in (A-2-6) is commonly abbreviated as $a(x)*b(x)$ or as $a*b$.

Alternatively, the equation may be thought of as an integral transform. The usual notation will be

$$f(x) = \int_{-\infty}^{\infty} G(x-t)\varphi(t) dt, \quad (\text{A-2-7})$$

and this will be called the *convolution transform with kernel $G(x)$ of the function $\varphi(x)$ into $f(x)$* .

Convolution is by far the most important operation that describes the behavior of a linear time-invariant (LTI) dynamic system. It is the operation of convolution that tells us how to compute the *output* of a LTI system from its *input* and *impulse response (IR)*, i.e.,

$$\text{output} = \text{input} * \text{IR} \quad (\text{A-2-8})$$

Convolution is associated with the “forward problem” of generating the response of a LTI system from the known values of its *input* and *IR*[82]. Deconvolution is the unraveling of convolution. It is associated with the ‘inverse problem’ of generating the input to the LTI system from the known values of its *output* and *IR*.

A-3 Transfer Function

Consider a continuous-time, linear, time-invariant (CTLTI) system with a single input $x(t)$ and a single output (response) $y(t)$ as illustrated in block form in Figure A-3-1. The output-input relationship of such a system can always be described by a differential equation of the form.

$$b_k \frac{d^k y}{dt^k} + b_{k-1} \frac{d^{k-1} y}{dt^{k-1}} + \dots + b_0 y = a_l \frac{d^l x}{dt^l} + a_{l-1} \frac{d^{l-1} x}{dt^{l-1}} + \dots + a_0 x \quad (\text{A-3-1})$$

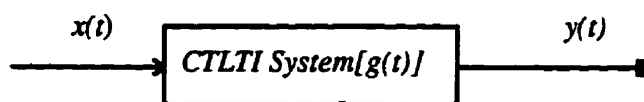


Figure A-3-1 Input-output form for CTLTI system

In most cases, $k \geq l$, and the integer k specifies the order of the system.

The output may also be expressed in terms of the convolution integral and the impulse response. The impulse response $g(t)$ is the response of the system when the input is a unit impulse function $\delta(t)$.

Assuming that the impulse response is known, the response due to any input $x(t)$ can be expressed as

$$y(t) = x(t) * g(t) = \int_{-\infty}^{\infty} x(t - \tau) g(\tau) d\tau = \int_{-\infty}^{\infty} x(\tau) g(t - \tau) d\tau \quad (\text{A-3-2})$$

Assume that the system is initially relaxed (i.e. no energy is stored in the system). Apply the Laplace transform to (A-3-1). It can be shown that all initial condition terms resulting from application of the Laplace transform are canceled on both sides of the equation. The transformed equation is

$$(b_k s^k + b_{k-1} s^{k-1} + \dots + b_0)Y(s) = (a_l s^l + a_{l-1} s^{l-1} + \dots + a_0)X(s) \quad (\text{A-3-3})$$

Therefore,

$$Y(s) = \frac{(a_l s^l + a_{l-1} s^{l-1} + \dots + a_0)}{(b_k s^k + b_{k-1} s^{k-1} + \dots + b_0)} X(s) \quad (\text{A-3-4})$$

A transfer function (or system function) $G(s)$ is defined as:

$$G(s) = \frac{N(s)}{D(s)} = \frac{a_l s^l + a_{l-1} s^{l-1} + \dots + a_0}{b_k s^k + b_{k-1} s^{k-1} + \dots + b_0} \quad (\text{A-3-5})$$

where $N(s)$ is the numerator polynomial and $D(s)$ is the denominator polynomial. Using the transfer function, the input-output relationship simply becomes

$$Y(s) = G(s)X(s) \quad (\text{A-3-6})$$

The time-domain response $y(t)$ can then be determined by inversion of $Y(s)$.

The impulse response can now be readily determined by letting $x(t) = \delta(t)$ or $X(s) = 1$. In this case the output transform is identical with the transfer function, so we have for the impulse response

$$g(t) = \mathcal{L}^{-1}[G(s)] \quad (\text{A-3-7})$$

Now consider a discrete-time, linear, time-invariant(DTLTI) system consisting of a single input $x(n)$ and a single output $y(n)$. Such a system can be described by a linear difference equation with constant coefficients of the form

$$y(n) + b_1 y(n-1) + b_2 y(n-2) + \dots + b_k y(n-k) = a_0 x(n) + a_1 x(n-1) + a_2 x(n-2) + \dots + a_k x(n-k) \quad (\text{A-3-8})$$

This equation describes an ordinary difference equation of order k with constant coefficients. This equation has certain features similar to the differential equation input-output relationship of a continuous-time system. If (A-3-8) is solved for $y(n)$, the result is

$$y(n) = \sum_{i=0}^k a_i x(n-i) - \sum_{i=1}^k b_i y(n-i) \quad (\text{A-3-9})$$

A very interesting feature of (A-3-9) is that it can be completely solved by the basic arithmetic operations of multiplication, addition, and subtraction. All that is required to start a solution is to specify the input function $x(n)$ and the first k values of the output $y(n)$. The algorithm of (A-3-9) is then applied step by step. The solution of a difference equation is seen to be considerably simpler in concept than that of the corresponding differential equation.

Consider a relaxed system (i.e. one with no initial values stored in the system). If we take the z -transforms of both sides of (A-3-8), we obtain after factoring

$$(1+b_1z^{-1}+b_2z^{-2}+\dots+b_kz^{-k})Y(z)=(a_0+a_1z^{-1}+a_2z^{-2}+\dots+a_kz^{-k})X(z) \quad (\text{A-3-10})$$

Solving for $Y(z)$ we obtain

$$Y(z)=\frac{(a_0+a_1z^{-1}+a_2z^{-2}+\dots+a_kz^{-k})}{(1+b_1z^{-1}+b_2z^{-2}+\dots+b_kz^{-k})}X(z) \quad (\text{A-3-11})$$

The transfer function $H(z)$ of the discrete-time system is defined as

$$H(z)=\frac{N(z)}{D(z)}=\frac{a_0+a_1z^{-1}+a_2z^{-2}+\dots+a_kz^{-k}}{1+b_1z^{-1}+b_2z^{-2}+\dots+b_kz^{-k}} \quad (\text{A-3-12})$$

where $N(z)$ is the numerator polynomial and $D(z)$ is the denominator polynomial.

The expression of (A-3-12) is arranged in negative powers of z , which is usually the most natural form in which the function occurs. On the other hand, it is frequently desirable to express $H(z)$ in positive powers of z , particularly when we wish to factor the polynomials or to perform a partial fraction expansion. This is done by multiplying numerator and denominator by z^k , and the result is

$$H(z)=\frac{a_0z^k+a_1z^{k-1}+a_2z^{k-2}+\dots+a_k}{z^k+b_1z^{k-1}+b_2z^{k-2}+\dots+b_k} \quad (\text{A-3-13})$$

Using the transfer function concept, the input-output relationship becomes

$$Y(z) = H(z)X(z) \quad (\text{A-3-14})$$

Thus, a discrete-time system can be represented by the same type of transfer function relationship as for a continuous-time system. As in the case of a continuous-time system, we may define the impulse response by assuming that the input is simply $x(n)=\delta(n)$. In the case of a continuous-time system, the impulse response is often somewhat difficult to implement physically. However, for a discrete-time system, the “impulse function” is simply a number (usually unity) applied at a single sampling instant, which is readily implemented in an actual system. Since $Z[\delta(n)]=1$, the impulse response $h(n)$ is seen to be

$$h(n) = Z^{-1}[H(z)] \quad (\text{A-3-15})$$

A-4 Discrete-Time Signals

A discrete-time signal may represent either a purely digital signal as would be employed in a computer or a sampled-data signal which occurs in certain hybrid systems. A sampled-data signal can be considered as arising from sampling a continuous-time signal at periodic intervals of time T . The sampling rate or sampling frequency is $f_s = 1/T$. In order to avoid aliasing, it is necessary that $f_s - f_h \geq f_h$, where f_h is the highest possible frequency. This leads to the important inequality:

$$f_s \geq 2f_h \quad (\text{A-4-1})$$

Equation(A-4-1) is a statement of Shannon’s Sampling Theorem, which states that a signal must be sampled at a rate at least as high as twice the highest frequency in the spectrum. In practice, the sampling rate must be chosen to be somewhat greater than $2f_h$ to ensure recovery with practical hardware limitations.

A convenient definition that is useful in sampling analysis is the folding frequency f_0 . It is given by $f_0 = f_s/2 = 1/2T$. The folding frequency is simply the highest frequency that can be processed by a given discrete-time system with sampling rate f_s . Any frequency greater than f_0 will be “folded” and cannot be recovered. In addition, it will obscure data within the correct frequency range; therefore, it is important to clearly limit the frequency content of a signal before sampling. The highest frequency f_h in the signal is called the Nyquist frequency, and the minimum sampling rate $2f_h$, at which the signal could theoretically be recovered, is called the Nyquist rate.

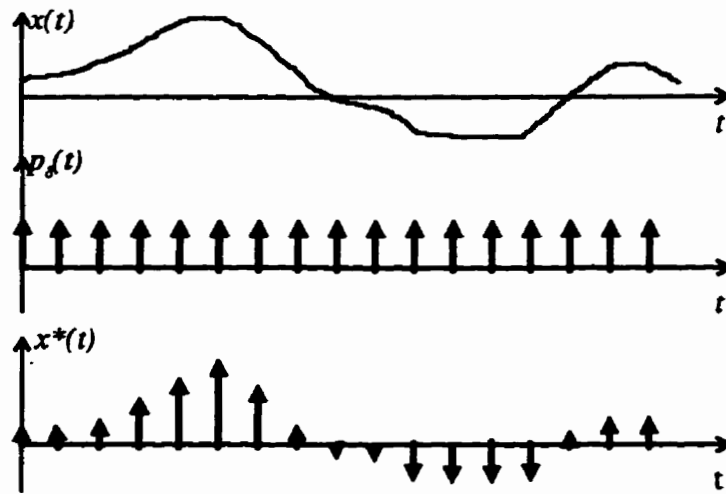


Figure A-4-1 Development of sampled-data signal using ideal impulse sampling

Consider the ideal impulse sampling as shown in Figure A-4-1. The pulse function is designated as $p_s(t)$, and it is assumed to be a train of impulse functions of the form

$$p_s(t) = \sum_{-\infty}^{\infty} \delta(t - nT) \quad (\text{A-4-2})$$

The sampled-data signal $x^*(t)$ can be expressed as

$$x^*(t) = x(t)p_s(t) = x(t) \sum_{-\infty}^{\infty} \delta(t - nT) \quad (\text{A-4-3})$$

The only values of $x(t)$ having significance in (A-4-3) are those at $t=nT$. Hence, an alternate form for the sampled-data signal is

$$x^*(t) = \sum_{-\infty}^{\infty} x(nT)\delta(t - nT) \quad (\text{A-4-4})$$

It turns out that a sequence of numbers which appears in a computer can be conveniently represented as weights of an impulse train for purposes of mathematical analysis. The main point to remember is that the weight of a given impulse represents the value(or digital number) at the instant that the impulse occurs.

A continuous-time signal could be recovered from its sampled-data form by passing the sampled-data signal through a low-pass filter having a cutoff somewhere between f_h and $f_s - f_h$. This process of reconstruction can be aided by the use of a holding device, which actually performs a portion of the

filtering required, thus permitting the use of a less complex filter for the final smoothing. There are a number of holding devices, the zero-order hold is the simplest one, which simply accepts the value of the pulse at the beginning of a sampling interval and holds it to the beginning of the next interval, at which time it changes to the new value. The resulting function is, of course, not normally the same as the original signal before sampling, but it is in the form of a continuous-time function, and it will be easier to perform subsequent processing on it in this form.

Consider now the case of a general discrete-time signal which is defined only at integer multiples of a basic interval T . This signal differs from the sampled-data signal $x^*(t)$ only in the sense that it may not necessarily have arisen from sampling a continuous-time signal. Instead, it may have arisen from some purely discrete or digital process. Nevertheless, we can still interpret the signal in the form of (A-4-4) whenever desirable. Except where it is desirable to use the sampled-data interpretation, the most straightforward notation for a discrete-time signal is simply $x(n)$, where n is an integer defined over some range $n_1 \leq n \leq n_2$. The integer n defines the particular location in the sequence corresponding to a given sample. If the discrete-time signal is derived from sampling a continuous-time signal $x_1(t)$, the signals are related by

$$\begin{aligned} x(n) &= x_1(nT) \text{ for } n \text{ an integer} \\ &= 0 \text{ otherwise} \end{aligned} \tag{A-4-5}$$

In effect, (A-4-5) states that the discrete-time signal is equal to the continuous-time signal at sample points and is zero elsewhere.

APPENDIX-B

FORMULAS FOR TRANSDUCER AT AN ARBITRARY POSITION ON THE PLANE ELECTRODE

This section shows the formulas that are developed in this research for transducer at an arbitrary position on the plane electrode. Figure B-1 shows the case when transducer is put at an arbitrary position where the needle tip is not within the detectable area of the transducer. Figure B-2 shows the case when transducer is put at an arbitrary position where the needle tip is within the detectable area of the transducer. For either of the two cases, since the active area of the transducer is chosen to be small, as mentioned in Section 3.4, after generation, only the pressure waves transmitted perpendicular to the ground electrode sample interface can reach the transducer and be detected; and the space charges can be assumed to be uniformly distributed within the detectable area at each x layer. Therefore, the three dimension space charge distribution $\rho(x,r,\theta)$ is simplified to one dimension $\rho(x)$ within the detectable area S for each layer at x .

The source strength for a simple acoustic source is equal to the surface integral of the scalar product of the vector velocity amplitude and its corresponding surface element[85]. Then, it can be deduced that the amplitude of pressure wave $p_x(t)$ due to $\rho(x)$ detected by the transducer is proportional to the surface integral of the x component of the electric stress due to pulse that space charges are subjected to.

$$p_x(t) = \frac{k}{l + \frac{c_2}{c_1}x} \left[\frac{1}{\pi r_a^2} \iint_{S_x} e_{px}(x,r,\theta,t - \frac{x}{c_2} - \frac{l}{c_1}) dA \right] \rho(x) dx \quad (\text{B-1})$$

where k is a constant, r_a is the radius of transducer active area, l is the length of the lower electrode, c_1 , c_2 are the sound velocity of the lower electrode and the dielectric respectively, S_x represents the detectable area for the x layer, dA represents a small increment in area, and $e_{px}(x,r,t)$ is the x component of the electric field due to pulse at an arbitrary (x,r,θ) point.

The same as the case mentioned in Section 3.4, the electric field due to pulse $e_p(x,r,\theta,t)$ contains both space and time variables. It is more convenient to separate them. This can be done under the assumption that the application of an electric pulse would not cause any change of the space charge distribution[Appendix A-1]. If $Ce(x,r,\theta)$ stands for the electric field at a general point (x,r,θ) due to the

application of a unit voltage ($V_c = 1 \text{ Volt}$) in the needle-plane configuration, $e_p(x, r, \theta, t)$ can then be written as:

$$e_p(x, r, \theta, t) = \frac{v_p(t)Ce(x, r, \theta)}{V_c} = v_p(t)Ce(x, r, \theta) \tag{B-2}$$

or

$$e_{px}(x, r, \theta, t) = \frac{v_p(t)C_{e_x}(x, r, \theta)}{V_c} = v_p(t)C_{e_x}(x, r, \theta) \tag{B-3}$$

where $e_{px}(x, r, t)$ and $C_{e_x}(x, r)$ stand for the x component of $e_p(x, r, t)$ and $Ce(x, r)$.

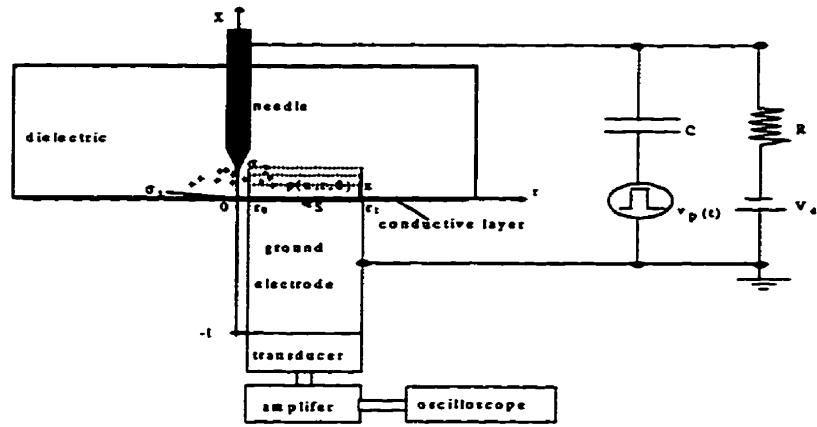


Figure B-1 Principle set-up *Case 1* for transducer at an arbitrary position

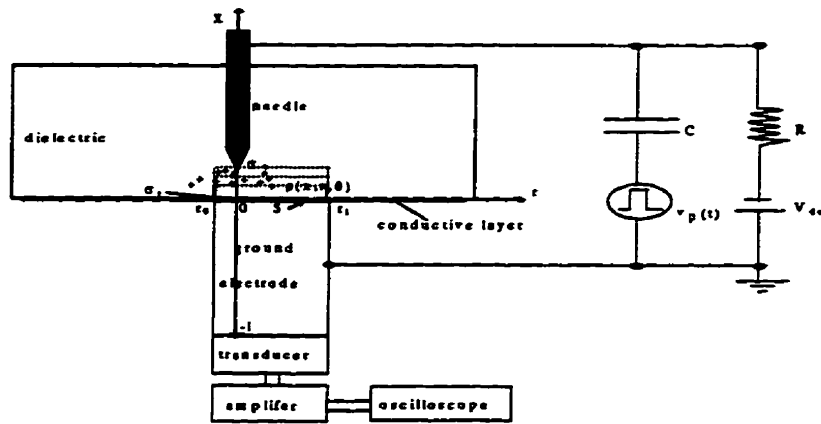


Figure B-2 Principle set-up *Case 2* for transducer at an arbitrary position

Equation (B-1) can then be written as:

$$p_x(t) = \frac{k}{l + \frac{c_2}{c_1}x} \left[\frac{1}{\pi a^2} \iint_{S_x} C e_x(x, r, \theta) dA \right] v_p \left(t - \frac{x}{c_2} - \frac{l}{c_1} \right) \rho(x) dx \quad (\text{B-4})$$

Now just let $\mu(x)$ stands for the double integral and leave how to calculate $\mu(x)$ for the two transducer at arbitrary cases later,

$$\mu(x) = \frac{1}{\pi a^2} \iint_{S_x} C e_x(x, r, \theta) dA \quad (\text{B-5})$$

Then, equation (B-4) becomes

$$p_x(t) = \frac{k}{l + \frac{c_2}{c_1}x} \mu(x) v_p \left(t - \frac{x}{c_2} - \frac{l}{c_1} \right) \rho(x) dx. \quad (\text{B-6})$$

For surface charges $\sigma_2(d)$, its pressure wave $p_d(t)$ is:

$$\begin{aligned} p_d(t) &= \frac{k k}{l + \frac{c_2}{c_1}d} \left[\frac{r^2}{r_a^2} e_{px} \left(d, t - \frac{d}{c_2} - \frac{l}{c_1} \right) \sigma_2(d) + \frac{1}{2} \epsilon_0 \epsilon_r [e_{px} \left(d, t - \frac{d}{c_2} - \frac{l}{c_1} \right)]^2 \right] \\ &= \frac{k k}{l + \frac{c_2}{c_1}d} \left[\frac{r^2}{r_a^2} C e_x(d) v_p \left(t - \frac{d}{c_2} - \frac{l}{c_1} \right) \sigma_2(d) + \frac{1}{2} \epsilon_0 \epsilon_r [C e_x(d) v_p \left(t - \frac{d}{c_2} - \frac{l}{c_1} \right)]^2 \right] \end{aligned} \quad (\text{B-7})$$

where r , is the radius of the needle tip, k' is a constant.

For surface charges $\sigma_1(0)$, its pressure wave $p_0(t)$ is:

$$\begin{aligned} p_0(t) &= \frac{k}{l} \left\{ \frac{1}{\pi a^2} \iint_{S_0} e_{px} \left(0, r, \theta, t - \frac{l}{c_1} \right) dA \sigma_1(0) - \frac{1}{2} \epsilon_0 \epsilon_r \left[\frac{1}{\pi a^2} \iint_{S_0} e_{px} \left(0, r, \theta, t - \frac{l}{c_1} \right) dA \right]^2 \right\} \\ &= \frac{k}{l} \left[\mu(0) v_p \left(t - \frac{l}{c_1} \right) \sigma_1(0) - \frac{1}{2} \epsilon_0 \epsilon_r [\mu(0) v_p \left(t - \frac{l}{c_1} \right)]^2 \right] \end{aligned} \quad (\text{B-8})$$

Applying the superposition principle, the total pressure wave $p(t)$ detected by the transducer is:

$$p(t) = p_0(t) + p_p(t) + j_k p_d(t) \quad (\text{B-9})$$

where,

$$p_p(t) = \int_0^d \frac{k}{l + \frac{c_2}{c_1}x} \mu(x) v_p \left(t - \frac{x}{c_2} - \frac{l}{c_1} \right) \rho(x) dx \quad (\text{B-10})$$

$$j_k = \begin{cases} 0 & \text{for Case 1} \\ 1 & \text{for Case 2} \end{cases} \quad (\text{B-11})$$

When the total pressure wave $p(t)$ reaches the transducer, the same as the uniform field case, the pressure wave will be changed by the transducer into a voltage signal. The voltage signal will be amplified and recorded as $v_s(t)$. Suppose the system that transfers $p(t)$ to $v_s(t)$ is linear time-invariant, in the time domain; then there is the convolution relationship:

$$v_s(t) = p(t) * h(t) \quad (\text{B-12})$$

where $h(t)$ is the system transfer function.

It can also be processed using three approaches for the uniform field case to get rid of the second term in equations (B-7) and (B-8).

- 1) Omit the terms when they are negligible compared to the surface charges response and denote them as $v_s^{(1)}(t)$;
- 2) subtract signals $v_s(t)$ by the signal $v_{s0}(t)$ which is obtained when no dc voltage is applied and no space charge is distributed inside the sample, and denote the subtraction as $v_s^{(2)}(t)$; and
- 3) for general cases, apply a positive electric pulse first and get an output $v_{s+}(t)$; then change pulse polarity to negative and get an output $v_{s-}(t)$, let $v_s^{(3)}(t) = 1/2[v_{s+}(t) - v_{s-}(t)]$,

It can be deduced that:

$$v_{ss}(t) = \left\{ \begin{array}{l} v_s^{(1)}(t) = v_s(t) \\ \text{or} \\ v_s^{(2)} = v_s(t) - v_{s0}(t) \\ \text{or} \\ v_s^{(3)} = \frac{1}{2}[v_{s+}(t) - v_{s-}(t)] \end{array} \right\} = p'(t) * h(t) \quad (\text{B-13})$$

$$p'(t) = p_0'(t) + p_\rho'(t) + j_k p_d'(t) \quad (\text{B-14})$$

where,

$$p_0'(t) = \frac{k}{l} [\mu(0)\sigma_1(0)v_p(t - \frac{l}{c_1})] \quad (\text{B-15})$$

$$p_\rho'(t) = \int_0^d \frac{k}{l + \frac{c_2}{c_1}x} \mu(x)v_p(t - \frac{x}{c_2} - \frac{l}{c_1})\rho(x)dx \quad (\text{B-16})$$

$$p_d'(t) = k' k \frac{1}{l + \frac{c_2}{c_1} d} \frac{r_r^2}{r_a^2} [\sigma_2(d) C e_x(d) v_p(t - \frac{l}{c_1} - \frac{d}{c_2})] \quad (\text{B-17})$$

If we Compare equations (B-15)-(B-17) with equations (3-66)-(3-68) in Chapter 3, the only difference is to change C_f into μ . Therefore, the similar nonuniform simulation model can be set up and we can obtain the nonuniform field space charge distribution when the transducer is put at an arbitrary position on the plane electrode. The only important thing is to obtain $\mu(x)$ for the two cases.

As it is known from calculus[90], the use of polar co-ordinates in evaluating the double integral is,

$$\iint_R F(r, \theta) dA = \int_{\alpha}^{\beta} d\theta \int_{R_1}^{R_2} F(r, \theta) r dr = \int_a^b dr \int_{\Theta_1}^{\Theta_2} F(r, \theta) r d\theta. \quad (\text{B-18})$$

where α, β are the extreme values of θ , and a, b are the extreme values of r , in the region R . The inner limits $R_1, R_2, \Theta_1, \Theta_2$ are read off from the appropriate one of the two figures, as shown in Figure B-3 [(a) or (b)].



Figure B-3 The inner limits $R_1, R_2, \Theta_1, \Theta_2$

Due to the axial symmetry of the electric pulse field, $C e_x(x, r, \theta)$ is not a function of θ ; therefore, the Figure B-3 (b) case is considered easier to implement. Let $C e_x(x, r)$ denote $C e_x(x, r, \theta)$, the equation (B-5) can be written as:

$$\begin{aligned} \mu(x) &= \frac{1}{\pi r_a^2} \iint_{S_x} C e_x(x, r) dA = \frac{1}{\pi r_a^2} \int_a^b C e_x(x, r) r dr \int_{\Theta_1}^{\Theta_2} d\theta \\ &= \frac{1}{\pi r_a^2} \int_a^b C e_x(x, r) r (\Theta_2 - \Theta_1) dr \end{aligned} \quad (\text{B-19})$$

Case 1: Needle point is not within the detectable area

Figure B-4 shows an arbitrary detectable area S_x for *Case 1*.

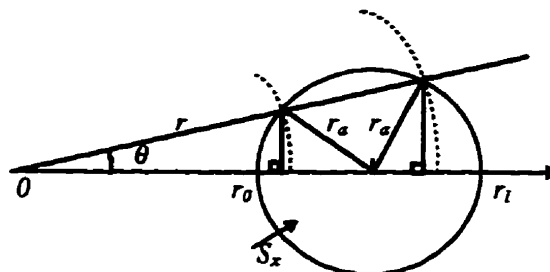


Figure B-4 Diagram used for setting up $\mu(x)$ for *Case 1*

Using the symmetrical situation, one can obtain

$$\mu(x) = \frac{2}{\pi r_a^2} \int_{r_0}^{r_1} C e_x(x, r) r \Theta_2 dr \tag{B-20}$$

where Θ_1 , are chosen as zero, while,

$$\Theta_2 = \cos^{-1} \left(\frac{r_0^2 + 2r_0 r_a + r^2}{2(r_0 + r_a)r} \right) \tag{B-21}$$

Therefore, $\mu(x)$ can be calculated as long as $C e_x(x, r)$ from $r=r_0$ to $r=r_1=r_0+2r_a$ is known.

Case 2: Needle point is within the detectable area

Figure B-5 shows an arbitrary detectable area S_x for *Case 2*.

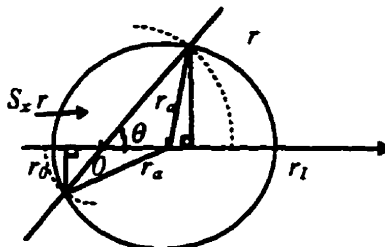


Figure B-5 Diagram used for setting up $\mu(x)$ for *Case 2*

Using the symmetrical situation, one can obtain

$$\mu(x) = \frac{2}{\pi r_a^2} \left[\int_0^{r_0} C e_x(x, r) r \Theta_2^{(1)} dr + \int_0^{r_1} C e_x(x, r) r \Theta_2^{(2)} dr \right] \quad (\text{B-22})$$

where Θ_i , are chosen as zero, while,

$$\begin{cases} \Theta_2^{(1)} = \cos^{-1} \left(\frac{r_0^2 - 2r_0 r_a + r^2}{2(r_0 - r_a)r} \right) \\ \Theta_2^{(2)} = \cos^{-1} \left(\frac{r_1^2 - 2r_1 r_a + r^2}{2(r_1 - r_a)r} \right) \end{cases} \quad (\text{B-23})$$

Therefore, $\mu(x)$ can be calculated as long as $C e_x(x, r)$ from $r=0$ to $r=r_1$, ($r_1 > r_0$) is known.

There have been a few commercial software packages that can do the electric field calculation. Microflux, for example, uses the finite element method to calculate the electric field. Microflux is very easy to apply. It allows one to assign any path, line or circle, within the calculated region. It let user choose the number of data points on the assigned path and generate data files regarding to the potential, the electric field components (x and r components for axis-symmetrical case) along the base coordinate at each point. Therefore, using Microflux, $C e_x(x, r)$ from $r=r_0$ to $r=r_1$, or $C e_x(x, r)$ from $r=0$ to $r=r_1$ can be obtained within a certain error limit.

APPENDIX-C

OTHER SIMULATION MODEL APPROACHES

Since the basic idea of the simulation model is to simulate the charge distribution in the discrete-time domain such that the difference between the simulated output signal(using the simulated charge distribution) and the original output signal is at a minimum, many algorithms can be applied to obtain the simulated charge distribution. The mathematical expressions for all the simulation model approaches are the same as equation (3-41). The only difference among the algorithms are the models that are set-up for their algorithms to apply and the methods they use to obtain the σ sequence.

C-1 Minimum Variance Deconvolution(MVD) Simulation Model

As already mentioned in Chapter 3, the MVD approach prefers to use the ARMA model for system IR , $g(k)$ and equation (3-37) as the input model, assuming the σ sequence to have a white and Gaussian nature with a variance of Var_{σ} . The noise model is the same as the PMSM. Many approaches in literature can be used to conduct the MVD. Some are based on batch formulas and some are based on recursive algorithms. The important feature for an ARMA model is its recursive nature. With this nature, the recursive signal processing algorithms can be applied which can expedite the computation. This section is attempted to present a recursive MVD algorithm (adopted from literature[82]) to obtain the σ sequence.

For the ARMA model in equation as described in equation (3-40), a state-variable representation can be set-up as:

$$\begin{bmatrix} x_1(k+1) \\ x_2(k+1) \\ \cdot \\ \cdot \\ x_n(k+1) \end{bmatrix} = \begin{bmatrix} 0 & 1 & 0 & \cdot & \cdot & 0 \\ 0 & 0 & 1 & \cdot & \cdot & 0 \\ \cdot & \cdot & \cdot & \cdot & \cdot & \cdot \\ \cdot & \cdot & \cdot & \cdot & \cdot & \cdot \\ -a_n & -a_{n-1} & -a_{n-2} & \cdot & \cdot & -a_1 \end{bmatrix} \begin{bmatrix} x_1(k) \\ x_2(k) \\ \cdot \\ \cdot \\ x_n(k) \end{bmatrix} + \begin{bmatrix} 0 \\ 0 \\ \cdot \\ \cdot \\ 1 \end{bmatrix} \sigma(k) \quad (C-1-1)$$

and

$$v_{sr}(k) = (b_n, b_{n-1}, \dots, b_1) \mathbf{x}(k) \quad (C-1-2)$$

where $x_1(k), x_2(k), \dots, x_n(k)$ are state variables,

$$\mathbf{x}(k) = \begin{bmatrix} x_1(k) \\ x_2(k) \\ \cdot \\ \cdot \\ \cdot \\ x_n(k) \end{bmatrix} \quad (\text{C-1-3})$$

is the state vector. Equation (C-1-1) is called a state equation, and equation (C-1-2) is called an output equation. They can be written in the more compact notation:

$$\mathbf{x}(k+1) = \Phi \mathbf{x}(k) + \gamma \sigma(k) \quad (\text{C-1-4})$$

and

$$v_{sm}(k) = v_{ss}(k) + n(k) = \mathbf{h}' \mathbf{x}(k) + n(k) \quad (\text{C-1-5})$$

where $\mathbf{x}(k)$ is always an $n \times 1$ state vector; Φ is an $n \times n$ state transition matrix; γ is an $n \times 1$ input distribution vector; and, \mathbf{h} is an $n \times 1$ observation vector. Φ , γ , and \mathbf{h} can be deduced by comparing equations (C-1-4) and (C-1-5) with equations (C-1-1) and (C-1-2), respectively. The recursive MVD algorithm consists of four component as shown in Figure C-1-1[83]. The equations used for the four computational subsystems are described below.

Kalman Predictor:

Let $\underline{\mathbf{x}}(k|k)$ and $\mathbf{P}(k|k)$ denote an $n \times 1$ mean-squared filtered estimate of state vector $\mathbf{x}(k)$, one that is based on the measurements $v_{sm}(1), v_{sm}(2), \dots$, and $v_{sm}(k)$, and, its associated $n \times n$ covariance matrix. Matrix $\mathbf{P}(k|k)$ describes the estimation error between $\underline{\mathbf{x}}(k|k)$ and $\mathbf{x}(k)$.

$$\underline{\mathbf{x}}(k+1|k) = \Phi \underline{\mathbf{x}}(k|k) \quad (\text{C-1-6})$$

and

$$\mathbf{P}(k+1|k) = \Phi \mathbf{P}(k|k) \Phi' + \text{Var}_{\sigma} \gamma \gamma' \quad (\text{C-1-7})$$

where

$$\underline{\mathbf{x}}(k+1|k+1) = [\mathbf{I} - \mathbf{K}(k+1)\mathbf{h}'] \underline{\mathbf{x}}(k+1|k) + \mathbf{K}(k+1)v_{sm}(k+1) \quad (\text{C-1-8})$$

$$\mathbf{K}(k+1) = \mathbf{P}(k+1|k)\mathbf{h}[\mathbf{h}'\mathbf{P}(k+1|k)\mathbf{h} + \text{Var}_n]^{-1} \quad (\text{C-1-9})$$

$$\mathbf{P}(k+1|k+1) = [\mathbf{I} - \mathbf{K}(k+1)\mathbf{h}'] \mathbf{P}(k+1|k) \quad (\text{C-1-10})$$

and $k=0, 1, \dots, N+1$. The Kalman predictor can be initialized by $\underline{x}(0|0)=0$ and $\mathbf{P}(0|0)=0$.

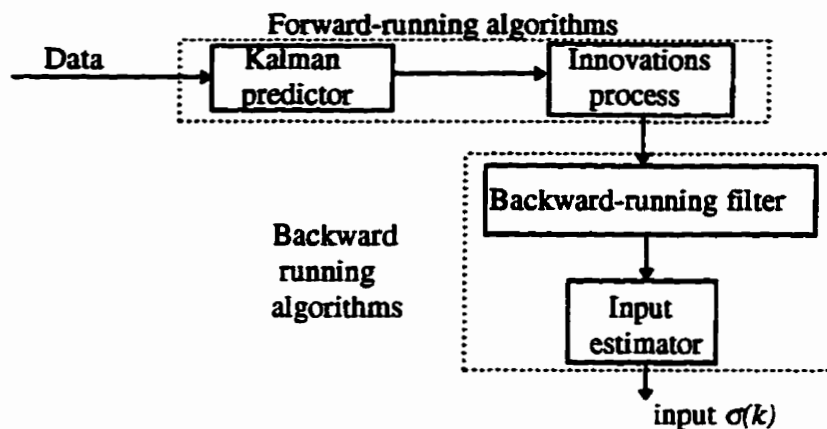


Figure C-1-1 Interconnection of the four computational subsystems that comprise the recursive MVD algorithm[82]

Innovations Process:

The innovations and its variance are the outputs of a forward-running *Kalman predictor*, i.e.,

$$\overline{v_{sm}(k+1|k)} = v_{sm}(k+1) - \mathbf{h}' \underline{\hat{x}}(k+1|k) \quad (\text{C-1-11})$$

and

$$\text{Var}[\overline{v_{sm}(k+1|k)}] = \mathbf{h}' \mathbf{P}(k+1|k) \mathbf{h} + \text{Var}_n \quad (\text{C-1-12})$$

where $k=0, 1, \dots, N+1$. $\underline{\hat{x}}(k+1|k)$ denotes an $n \times 1$ mean-squared prediction of state vector $\mathbf{x}(k+1)$, based on the measurements $v_{sm}(1), v_{sm}(2), \dots$, and $v_{sm}(k)$; and, $\mathbf{P}(k+1|k)$ is the $n \times n$ covariance matrix that describes the estimation error between $\underline{\hat{x}}(k+1|k)$ and $\mathbf{x}(k+1)$.

Backward-Running Filter:

The backward-running state and covariance equations are

$$\mathbf{r}(j|N+2) = [\mathbf{I} - \mathbf{K}(j)\mathbf{h}'] \Phi \mathbf{r}(j+1|N+2) + \mathbf{h} \overline{v_{sm}(j|j-1)} / \text{Var}[\overline{v_{sm}(j|j-1)}] \quad (\text{C-1-13})$$

and

$$S(j|N+2) = [I - K(j)h']' \Phi' S(j+1|N+2) \Phi [I - K(j)h'] + hh' Var[\overline{v_{sm}}(j|j-1)] \quad (C-1-14)$$

where $j=N+2, N+1, \dots, 1$, $r(N+3|N+2)=0$ and $S(N+3|N+2)=0$. In these equations $\overline{v_{sm}}(j|j-1)$ is a scalar process known as the innovations and $K(k)$ is an $n \times 1$ gain matrix, known as the Kalman gain matrix.

Input Estimator:

Let $r(j|N+2)$ denote an $n \times 1$ backward-running (i.e., $j=N+2, N+1, \dots, 0$) state vector, and $S(j|N+2)$ denote $r(j|N+2)$'s associated $n \times n$ covariance matrix. Then,

$$\sigma^{MV}(k|N+2) = Var_{\sigma} \gamma' r(k+1|N+2) \quad (C-1-15)$$

$$Var[\sigma_{ERR}(k|N+2)] = Var_{\sigma} - Var_{\sigma} \gamma' S(k+1|N+2) \gamma Var_{\sigma} \quad (C-1-16)$$

where $\sigma^{MV}(k|N+2)$ denotes the recursive minimum variance results of the σ sequence, $k=N+2, N+1, \dots, 1$. With $\sigma^{MV}(k|N+2)$ as the obtained σ sequence, the simulated charge distribution can be constructed as discussed in Chapter 3, Section 3.3.3.

C-2 Maximum Likelihood Deconvolution(MLD) Simulation Model

In the MLD simulation model, the input σ sequence is considered as the product of an amplitude sequence $d(k)$ and event sequence $q(k)$ as shown in equation (3-37). The amplitude sequence $d(k)$ is assumed to be a Gaussian sequence characterized by variance Var_d , while the event sequence $q(k)$ is assumed to be a Bernoulli sequence characterized by the probability parameter λ . There are also many ways to perform the maximum likelihood deconvolution[82]. Only a simple way is presented here as shown in Figure C-2-1[87].

Let $\sigma^{ML}(k|N+2)$ denote the maximum likelihood estimate of $\sigma(k)$ that uses all the measurements $v_{sm}(1), v_{sm}(2), \dots$, and $v_{sm}(k)$. By means of separation principle[87],

$$\sigma^{ML}(k|N+2) = d^{ML}(k|N+2) q^{ML}(k|N+2). \quad (C-2-1)$$

It was shown in [88] that the overall maximum-likelihood estimate of $\sigma(k)$ could be obtained by first computing $q^{ML}(k|N+2)$ and then computing $d^{ML}(k|N+2)$. Quantity $q^{ML}(k|N+2)$ can be obtained via

maximum likelihood detection. When $q^{ML}(k|N+2)$ is known, one can estimate $d(k)$ from equations (C-1-4) and (C-1-5), written here as:

$$\mathbf{x}(k+1) = \Phi\mathbf{x}(k) + \gamma q^{ML}(k|N+2)d(k) \quad (\text{C-2-2})$$

$$v_{sm}(k) = \mathbf{h}'\mathbf{x}(k) + n(k) \quad (\text{C-2-3})$$

When all uncertainties in (C-2-2) and (C-2-3) are jointly Gaussian, the maximum-likelihood estimates of $d(k)$ and $\mathbf{x}(k)$ equal minimum-variance estimates of these quantities[89], thus,

$$d^{ML}(k|N+2) = d^{MV}(k|N+2) \quad (\text{C-2-4})$$

and

$$\sigma^{ML}(k|N+2) = d^{MV}(k|N+2)q^{ML}(k|N+2) \quad (\text{C-2-5})$$

To summarize, the MLD contains performing ML detection to obtain $q^{ML}(k|N+2)$, $k=1, 2, \dots, N+2$; performing MVD to obtain $d^{ML}(k|N+2)$; and subsequently, $\sigma^{ML}(k|N+2)$. The recursive MLD algorithm is demonstrated in Figure C-2-1.

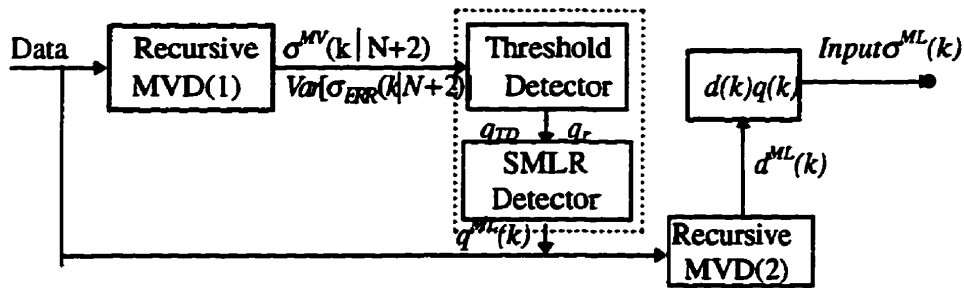


Figure C-2-1 A simple maximum likelihood deconvolution algorithm

Recursive MVD(1):

This block is the same as in recursive minimum variance deconvolution approach discussed in Section C-1. The out put from this block is $\sigma^{MV}(k|N+2)$ and $Var[\sigma_{ERR}(k|N+2)]$.

Threshold detector:

The threshold detector decision strategy is:

$$\text{If } \left[\sigma^{MV}(k|N+2) \right]^2 > t(k) \text{ decide } q(k) = 1 \quad (\text{C-2-6})$$

$$\text{If } \left[\sigma^{MV}(k|N+2) \right]^2 < t(k) \text{ decide } q(k) = 0 \quad (\text{C-2-7})$$

where

$$t(k) = \left\{ A_0(k)A_1(k) / [A_1(k) - A_0(k)] \right\} \left\{ \ln[A_1(k) / A_0(k)] - 2 \ln[\lambda / (1 - \lambda)] \right\} \quad (\text{C-2-8})$$

and for $q=0$ and 1 ,

$$A_q(k) = \left\{ 1 - \text{Var}[\sigma_{\text{ERR}}(k|N+2)] / \text{Var}_\sigma \right\}^2 [q \text{Var}_d] + \text{Var}[\sigma_{\text{ERR}}(k|N+2)] \left\{ 1 - \text{Var}[\sigma_{\text{ERR}}(k|N+2)] / \text{Var}_\sigma \right\} \quad (\text{C-2-9})$$

A threshold detector is a shot detector. It initializes the q parameters and provides a reference q_r to the SMLR detector.

SMLR detector:

A SMLR(single most-likely replacement) detector is recursive. The SMLR detector decision strategy is designed to examine all the values of k for which $\ln D(v_{sm};k) > 0$ and to find the value of k at which $\ln D(v_{sm};k)$ is a maximum. This time point is then the single time point at which a change is made in the reference sequence q_r .

The test q , $q_{t,k}$, and the reference q_r differ at only one time point, the k th, i.e.,

$$\begin{cases} q_{t,k}(i) = q_r(i) & \text{for all } i \neq k \\ q_{t,k}(i) = 1 - q_r(i) & \text{for all } i = k \end{cases} \quad (\text{C-2-10})$$

The detector rule for choosing between sequences $q_{t,k}$ and q_r is given by

$$\begin{cases} \text{If } \ln D(v_{sm};k) > 0 & \text{choose } q_{t,k} \text{ over } q_r \\ \text{If } \ln D(v_{sm};k) < 0 & \text{choose } q_r \text{ over } q_{t,k} \end{cases} \quad (\text{C-2-11})$$

and

$$\ln D(v_{sm};k) = \frac{\left[\sigma^{MV}(k|N+2) / \text{Var}_\sigma(k) \right]^2}{\text{Var}_r^{-1} [q_{t,k}(k) - q_r(k)]^{-1} + \left\{ \text{Var}_\sigma(k) - \text{Var}[\sigma_{\text{ERR}}(k|N+2)] \right\} / \text{Var}_\sigma^2(k)} + 2[q_{t,k}(k) - q_r(k)] \ln[\lambda / (1 - \lambda)] \quad (\text{C-2-12})$$

After the SMLR detector, the $q^{ML}(k)$ is obtained.

Recursive MVD(2):

This block is to obtain $d^{ML}(k)$ after $q^{ML}(k)$ is available. The four computational subsystems that comprise the recursive MVD algorithm can be applied with only a very small correction that is to replace γ with $\gamma^{ML}(k)$. When $d^{ML}(k)$ is obtained, $\sigma^{ML}(k|N+2)$ sequence can be obtained right away using equation (C-2-1).

As has been discussed in Section 4.4, the maximum likelihood deconvolution requires the σ sequence to have a spike-like nature. In the words of charge distribution, this means that the sequence should be the surface charge sequence. Since most parts inside our σ sequence are pseudo surface charges, which do not have the spike-like nature. The question of whether MLD can be applied to provide accurate charge distributions needs more investigations. It may be worth applying if it can just clearly indicate the presence of surface charges. For with this information, one may use other methods to obtain the inside space charge distribution. However, more studies are necessary before considering the application of the MLD simulation model.

APPENDIX-D

NONLINEAR DETECTION AND OPTIMIZATION PROCESS(NDOP): PROCEDURES AND SOME APPLICATION RESULTS

A nonlinear detection and optimization process (NDOP) is proposed for the PMSM to obtain “More Improvements” of the charge distribution results in this research. The proposed procedures are discussed in D-1. The idea of the threshold detection and the single most-likely replacement detection from the maximum likelihood deconvolution (Appendix C-2) are borrowed to construct a proposed detection process for the PMSM and to combine the detection process with a nonlinear least square optimization process to set up the NDOP. The advantage of the NDOP is that it can further improve the resolution and accuracy of the obtained charge distribution and minimize the sum of the squared $F(k)$, where $F(k)$ is denoted as the difference between the simulated signal output $SV(k)$ (using the obtained simulated charge distribution) and the original measured output signal $v_{sm}(k)$ or $v_{sm}'(k)$. However, the disadvantage of the NDOP lies obviously in that the application of this process is quite time-consuming. As mentioned in Chapter 4, it takes about 11 hours to obtain the improved charge distribution results for the first set of synthetic signals with both σ and F accuracy set at 0.01 through only the nonlinear least squared optimization. When output signals are corrupted with noises, a nonlinear detection process must be combined with the nonlinear least squared optimization; the computation time is then further increased. Due to this disadvantage, the NDOP has been applied to the 2nd, the 3rd, and the 4th sets of the synthetic signals instead of the experimental signals. As the results of one run of the NDOP to the 2nd, the 3rd, and the 4th sets of signals show respectively in D-2, D-3, and D-4, the ability of the NDOP to recover the surface charges, improve the resolution and accuracy of the obtained charge distribution, and minimize the difference $F(k)$ is well demonstrated.

D-1 Procedures of A Nonlinear Detection and Optimization Process

The procedures of the developed NDOP consist of three steps: threshold detection, SMLR detection, and the nonlinear least squared optimization, as described below. The initial value of $\sigma^{(0)}(k)$ comes from the PMSM after the reconstructing of the charge distribution from the point matching

deconvolution and discretizing the charge distribution by step $\Delta=1$. With $\sigma^{(0)}(k)$, it is possible to calculate the initial difference $F^{(0)}(k)$ and the sum of the squared difference $D^{(0)}$.

$$\begin{cases} F^{(0)}(k) = SV^{(0)}(k) - v_{sm}'(k) = \sum_{i=1}^{N_s} \sigma^{(0)}(k) g_{m'}(k-i) - v_{sm}'(k) \\ D^{(0)} = \sum_{k=1}^{N_s} [F^{(0)}(k)]^2 = \sum_{k=1}^{N_s} \left[\sum_{i=1}^{N_s} \sigma^{(0)}(k) g_{m'}(k-i) - v_{sm}'(k) \right]^2 \end{cases} \quad (D-1)$$

1) Threshold detection:

According to the noise level of the original measured output, a simple strategy for a threshold detector is set up as:

$$\begin{cases} \text{If } |\sigma^{(0)}(k)| > t(k) \text{ decide } q(k) = 1 \\ \text{If } |\sigma^{(0)}(k)| < t(k) \text{ decide } q(k) = 0 \end{cases} \quad (D-2)$$

where

$$t(k) = \alpha |\sigma^{(0)}|_{\max}. \quad (D-3)$$

If there is no noise in the signals, the detection process is not necessary. This is equivalent to set $\alpha=0$; the third step, the nonlinear least-square optimization, can be directly applied as for the 1st set of the synthetic signals(Chapter 4). When signals are corrupted with noise, the detection process becomes important. The choice of α can start at as large a value as 0.1, and then decrease by halves, until the obtained $D^{(TD)}$ using the q sequence is less than $D^{(0)}$ or is around a minimum.

$$\begin{cases} F^{(TD)}(k) = SV^{(TD)}(k) - v_{sm}'(k) = \sum_{i=1}^{N_s} \sigma^{(0)}(k) q g_{m'}(k-i) - v_{sm}'(k) \\ D^{(TD)} = \sum_{k=1}^{N_s} [F^{(TD)}(k)]^2 = \sum_{k=1}^{N_s} \left[\sum_{i=1}^{N_s} \sigma^{(0)}(k) q g_{m'}(k-i) - v_{sm}'(k) \right]^2 \end{cases} \quad (D-4)$$

The threshold detector is used to initialize the q parameters and provides a reference q_r to the SMLR detector. If $D^{(TD)}$ is less than $D^{(0)}$, we let $D^{(0)} = D^{(TD)}$.

2) SMLR detection:

A SMLR (single most-likely replacement) detector is recursive. The purpose of the SMLR detector decision strategy is to examine all the values of k for $D(v'_{sm};k) < D^{(0)}$ and find the value of k at which $D(v'_{sm};k)$ is a minimum. This time point, designated k' , is then the single time point at which a change is made in the reference sequence q_r . The test q , $q_{t,k}$, and the reference q_r differ at only one time point, the k th, i.e.,

$$\begin{cases} q_{t,k}(i) = q_r(i) & \text{for all } i \neq k \\ q_{t,k}(i) = 1 - q_r(i) & \text{for all } i = k \end{cases} \quad (D-5)$$

$$D(v'_{sm};k) = \sum_{k=1}^{N_m} [F(v'_{sm};k)]^2 = \sum_{k=1}^{N_m} \sum_{i=1}^{N_m} \sigma^{(0)}(k) q_{t,k} g'_m(k-i) - v'_{sm}(k)]^2 \quad (D-6)$$

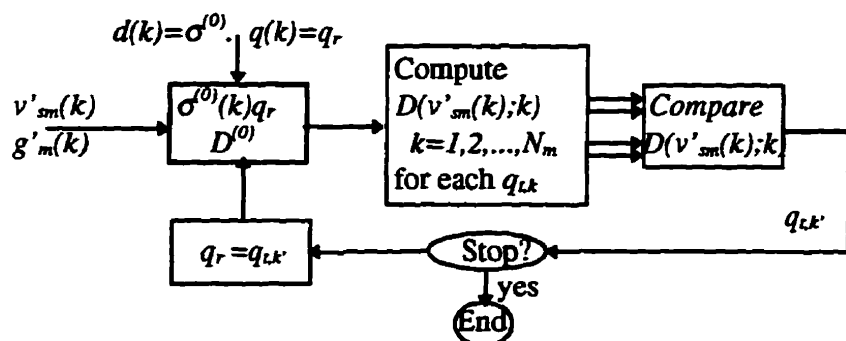


Figure D-1-1 Single most likely replacement detector search algorithm

Figure D-1-1 shows the SMLR search algorithm used in the research. After the SMLR detector, the most significant event sequence $q^s(k)$ is obtained.

3) Nonlinear least-square optimization:

The last step is an optimization process to obtain the most significant amplitude sequence $d^s(k)$. Mathematically, it can be stated as:

$$D^s = \text{minimize} \sum_{k=1}^{N_m} [F(k)]^2 = \text{minimize} \sum_{k=1}^{N_m} \sum_{i=1}^{N_m} d(k) q^s(k) g'_m(k-i) - v'_{sm}(k)]^2 \quad (D-7)$$

Eventually, one can obtain the most significant $\sigma^f(k) = d^f(k)q^f(k)$ that minimizes a nonlinear function composed of squared terms, starting at an initial estimate $d(k) = \sigma^{(0)}$. The obtained σ^f may not be the global minimum, but it is good enough if it is just a local minimum.

Then, one can output this σ^f sequence and reconstruct the simulated charge distribution using equations (3-51) and (3-53). Or one can discrete the obtained simulated charge distribution again, using $\Delta=1$, denote the obtained sequence as $\sigma^{(1)}(k)$, and apply the second run of the NDOP for even better results. One can repeat the NDOP until one is satisfied with the i th results or the difference between $D^{(i)}$ and $D^{(i-1)}$ is not much. The more often the NDOP is repeated, the more computation time is needed. The following section D-2, D-3 and D-4 shows the results of applying only one run of the NDOP to the 2nd, the 3rd, and the 4th sets of the synthetic signals.

D-2 NODP For the 2nd Set of Signals

Figure 4.49 charge distribution is used as the initial charge distribution $\sigma^{(0)}$ for the 2nd set of signals to the NDOP. The total initial sum of the squared difference of Figure 4.51 $[D^{(0)}]$ is 0.2668. A threshold detector is applied. With α setting at 0.05, after the threshold detector, a q sequence is obtained, and sum of the squared difference $[D^{(TD)}]$ is reduced to 0.2119. $[D^{(0)}]$ is then set to $[D^{(TD)}]=0.2119$. A single most-likely replacement detector is then applied. Figure D-2-1 shows the sequences $q_{i,k}$ that makes the sum of the squared difference $D(v'_{sm};k)$ is less than $[D^{(0)}] = 0.2119$. Obviously a test sequence exists which can minimize the squared difference to 0.1556. Then, we can replace the original q_r by the best test sequence, and apply the SMLR again.

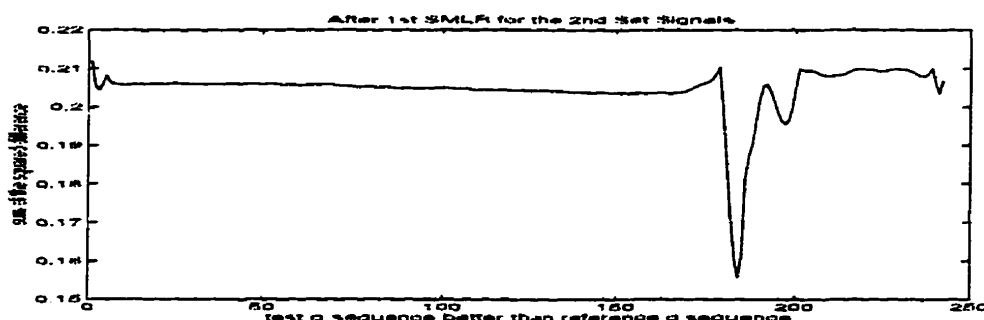


Figure D-2-1 The 1st application of the SMLR detector

After the 9th application of the SMLR detector, the minimum $D(v'_{sm};k)$ among the test sequences q_{tk} that make $D(v'_{sm};k)$ less than 0.2119 is 0.1206. After the 10th application of the SMLR detector, the minimum $D(v'_{sm};k)$ among the test sequences q_{tk} that make $D(v'_{sm};k)$ less than 0.2119 is 0.1204. The sequence that provides the minimum $D(v'_{sm};k)$ after the 10th SMLR detector is then denoted as the most significant q sequence, $q'(k)$. Figure D-2-2 plots the $D(v'_{sm};k)$ as less than 0.2119 for the 10th application of the SMLR detector.

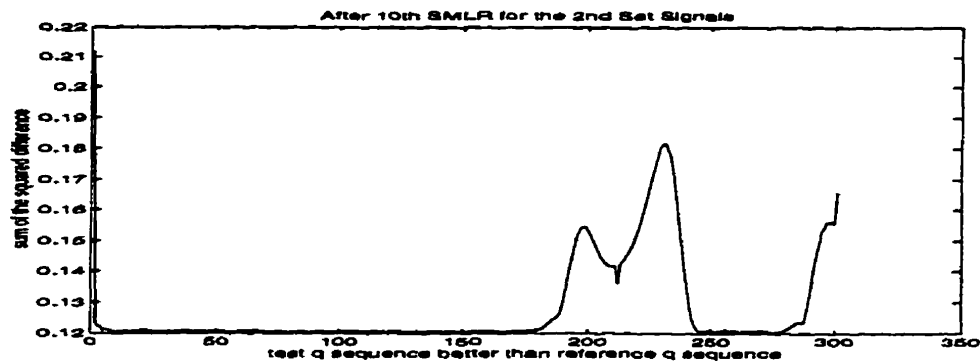


Figure D-2-2 The 10th application of the SMLR detector

Then, the nonlinear least square optimization process is applied, with both σ and F accuracy being set at 0.1. After 20 hours, the optimization process hasn't stopped itself. Therefore, the optimization process is forced to stop. The D^f at the stop time is 0.0229. The obtained most significant σ sequence, σ^f , is shown in Figure D-2-3.

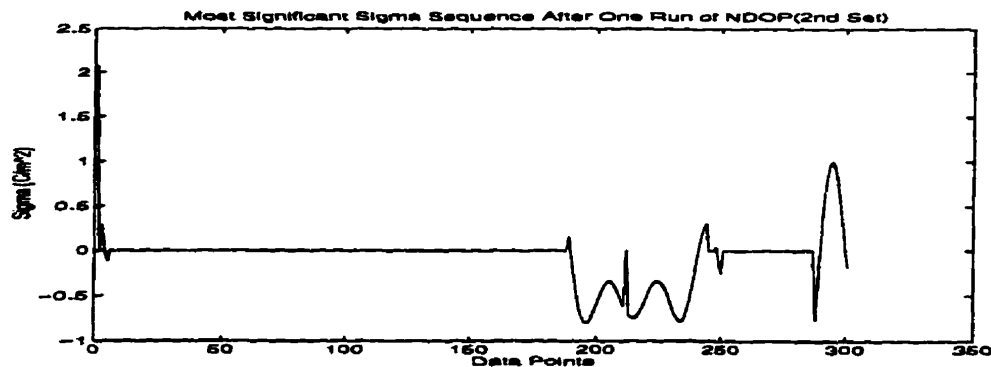


Figure D-2-3 The σ^f obtained after one run of NDOP for the 2nd set of signals

Applying equation (3-53) and equation (3-51) to the σ^f sequence and applying a zero-phase 5 point average filter to the internal space charge distribution, we obtain Figure D-2-4 charge distribution.

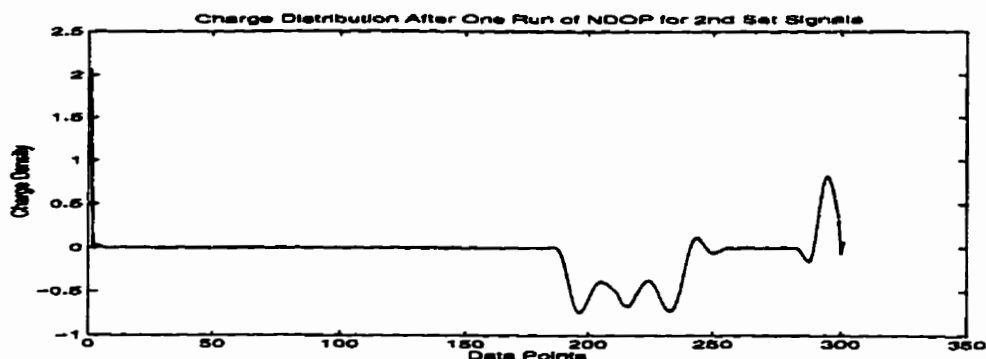


Figure D-2-4 Charge distribution obtained after one run of the NDOP for the 2nd set of signals

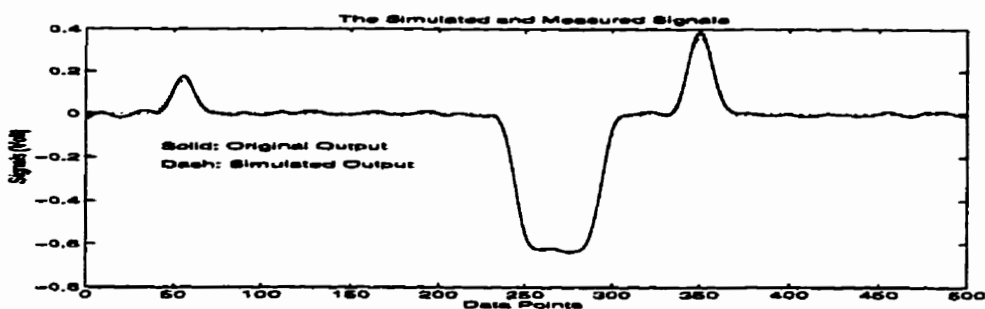


Figure D-2-5 Comparison between $v_{sm}^{2'}(k)$ and $SV(k)$ (using Figure D-2-4 charge distribution)

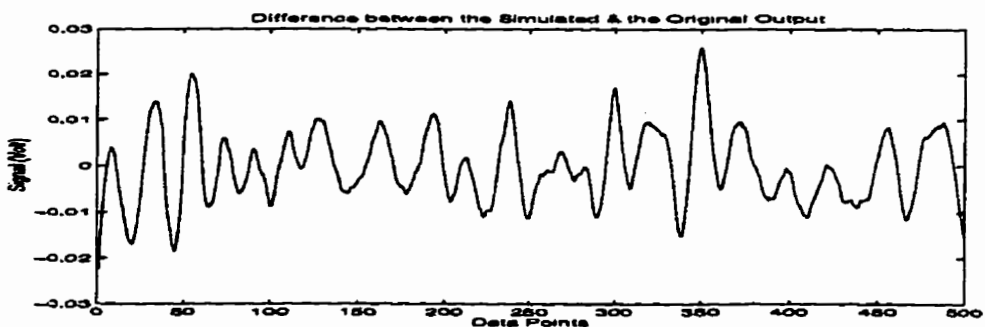


Figure D-2-6 Difference between $v_{sm}^{2'}(k)$ and $SV(k)$ of Figure D-2-5

Figures D-2-5 and D-2-6 compare the difference between $v_{sm}^{2'}(k)$ and $SV(k)$ (using Figure D-2-4 charge distribution). The sum of squared difference of Figure D-2-6 is minimized to 0.0308. One can discrete Figure D-2-4 charge distribution by $\Delta=1$, and regards the obtained σ sequence as $\sigma^{(1)}$. Since $\sigma^{(1)}$ sequence is better than $\sigma^{(0)}$, another run of the NDOP process will generate further improved charge distribution results.

D-3 NODP For the 3rd Set of Signals

Figure 4.93 charge distribution is used as the initial charge distribution $\sigma^{(0)}$ for the 3rd set of signals to the NDOP. The total initial sum of the squared difference of Figure 4.95 $[D^{(0)}]$ is 0.0156. A threshold detector is applied. With α setting at 0.05, after the threshold detector, a q sequence is obtained, and sum of the squared difference $[D^{(TD)}]$ is 0.0766. Then, α is halved and set at 0.025, after the threshold detector, a q sequence is obtained, and sum of the squared difference $[D^{(TD)}]$ is reduced to 0.0134. This q sequence is chosen as the initial reference sequence q_r . Then $[D^{(0)}]$ is set to $[D^{(TD)}]=0.0134$. A single most-likely replacement detector is then applied. Figure D-3-1 shows the sequences $q_{r,k}$ that make the sum of the squared difference $D(v'_{sm};k)$ less than $[D^{(0)}] = 0.0134$. Obviously a test sequence exists which can minimize the squared difference to 0.0121. Then, we can replace the original q_r by the best test sequence, and apply the SMLR again.

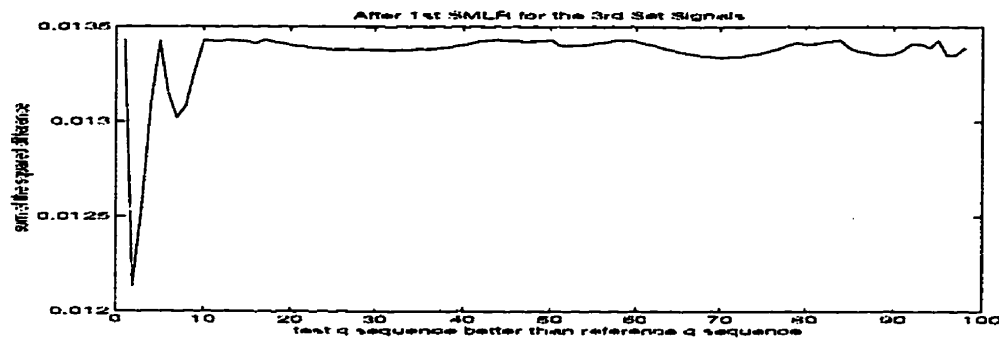


Figure D-3-1 The 1st application of the SMLR detector

After the 6th application of the SMLR detector, the minimum $D(v'_{sm};k)$ among the test sequences $q_{r,k}$ that makes $D(v'_{sm};k)$ less than 0.0134 is 0.0112. After the 7th application of the SMLR detector, the minimum $D(v'_{sm};k)$ among the test sequences $q_{i,k}$ that make $D(v'_{sm};k)$ less than 0.0134 is still 0.0112. The sequence that provides the minimum $D(v'_{sm};k)$ after the 7th SMLR detector is then denoted as the most significant q sequence, $q^s(k)$. Figure D-3-2 plots the $D(v'_{sm};k)$ as less than 0.0134 for the 7th application of the SMLR detector.

Then, the nonlinear least square optimization process is applied. Both σ and F accuracy are set at 0.1. After about 7 hours, the optimization process has stopped itself. The D^s at the stop time is 0.0036. The most significant σ sequence is obtained, σ^s , is shown in Figure D-3-3.

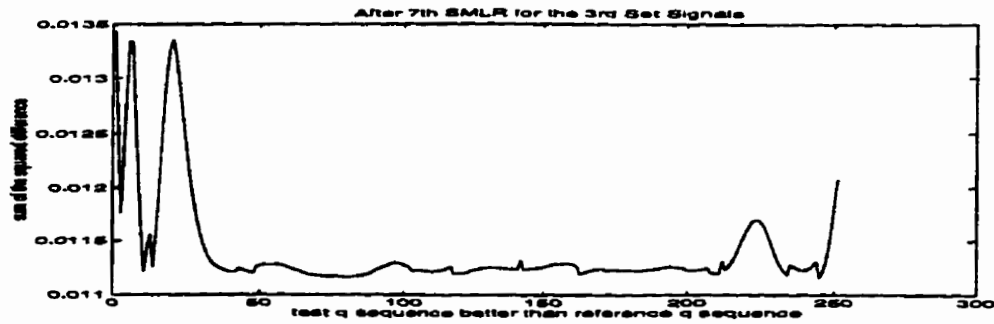


Figure D-3-2 The 7th application of the SMLR detector

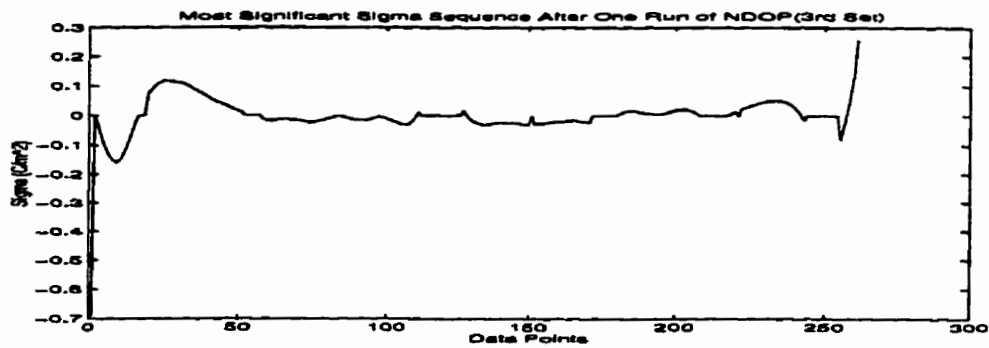


Figure D-3-3 The σ obtained after one run of NDOP for the 3rd set of signals

By applying equation (3-53) and equation (3-51) to the σ sequence and applying a zero-phase 5 point average filter to the internal space charge distribution, we obtain Figure D-3-4 charge distribution.

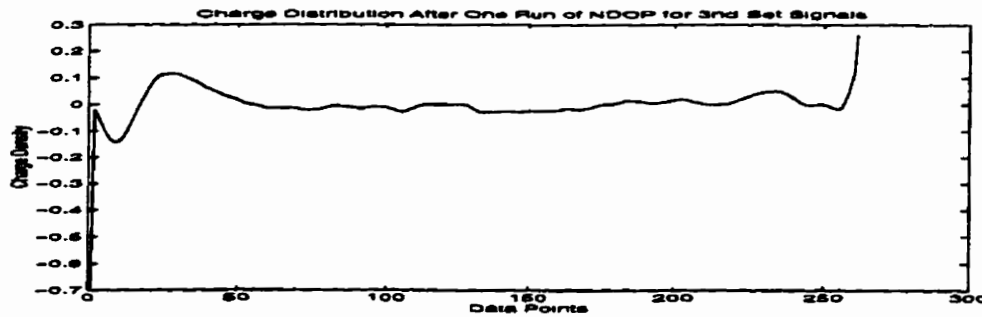


Figure D-3-4 Charge distribution obtained after one run of the NDOP for the 3rd set of signals

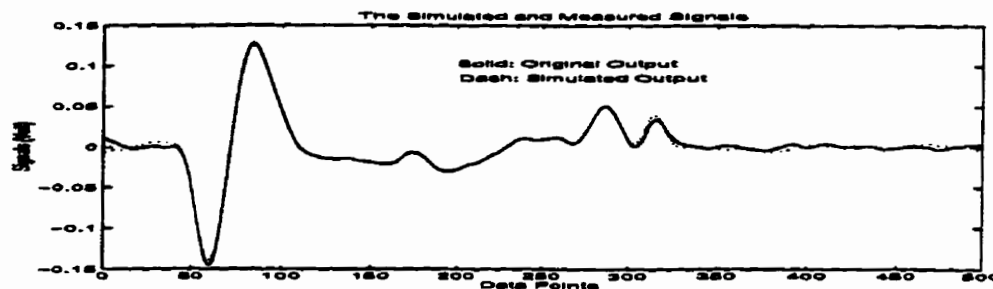


Figure D-3-5 Comparison between $v_{sm}^{j'}(k)$ and $SV(k)$ (using Figure D-3-4 charge distribution)

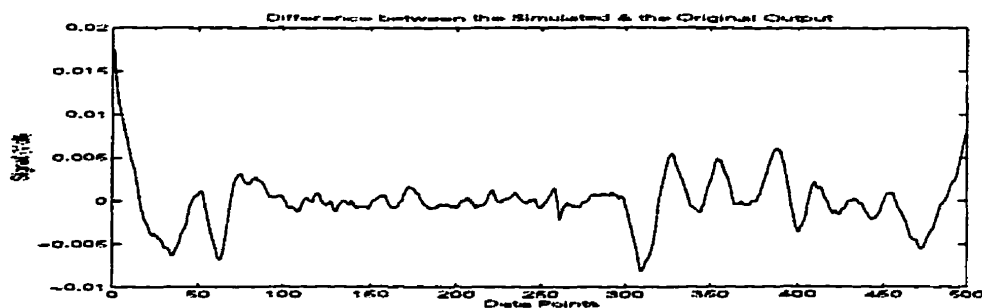


Figure D-3-6 Difference between $v_{sm}^{j'}(k)$ and $SV(k)$ of Figure D-3-5

Figures D-3-5 and D-3-6 compare the difference between $v_{sm}^{j'}(k)$ and $SV(k)$ (using Figure D-3-4 charge distribution). The sum of the squared difference of Figure D-3-6 is minimized to 0.0044. The surface charges are better recovered. One can discrete Figure D-3-4 charge distribution by $\Delta=1$, and regards the obtained σ sequence as $\sigma^{(1)}$. Due to the fact that $\sigma^{(1)}$ sequence is better than $\sigma^{(0)}$, another run of the NDOP process will generate further improved charge distribution results.

D-4 NODP For the 4th Set of Signals

Figure 4.126 charge distribution is used as the initial charge distribution $\sigma^{(0)}$ for the 3rd set of signals to the NDOP. The total initial sum of the squared difference of Figure 4.128 $[D^{(0)}]$ is 16.2910. A threshold detector is applied. With α setting at 0.01, after the threshold detector, a q sequence is obtained, and sum of the squared difference $[D^{(TD)}]$ is 19.9132. Then, α is halved and set at 0.005, after the threshold detector, a q sequence is obtained, and sum of the squared difference $[D^{(TD)}]$ is 17.1658. Then, α is again halved and set at 0.0025, after the threshold detector, a q sequence is obtained, and sum of the squared difference $[D^{(TD)}]$ is 16.3625. This q sequence is chosen as the initial reference sequence q_r because when α is set at 0.00125, the sum of the squared difference is even more than 16.3625. Then, $[D^{(0)}]$ is not changed and $[D^{(0)}]=16.2910$. A single most-likely replacement detector is then applied. Figure D-4-1 shows the sequences $q_{t,k}$ that make the sum of the squared difference $D(v'_{sm};k)$ less than $[D^{(0)}]=16.2910$. Obviously, a test sequence exists which can minimize the squared difference to 14.0384. Then, we can replace the original q_r by the best test sequence and apply the SMLR again.

After the 9th application of the SMLR detector, the minimum $D(v'_{sm};k)$ among the test sequences $q_{t,k}$ that makes $D(v'_{sm};k)$ less than 16.2910 is 8.2539. After the 10th application of the SMLR detector, the

minimum $D(v'_{sm};k)$ among the test sequences q_{tk} that make $D(v'_{sm};k)$ less than 16.2910 is 7.9022. Since it takes about 4 hours for each SMLR detection, the sequence that provides the minimum $D(v'_{sm};k)$ after the 10th SMLR detector is denoted as the most significant q sequence, $q^f(k)$. Figure D-4-2 plot the $D(v'_{sm};k)$ that less than 16.2910 for the 10th application of the SMLR detector.

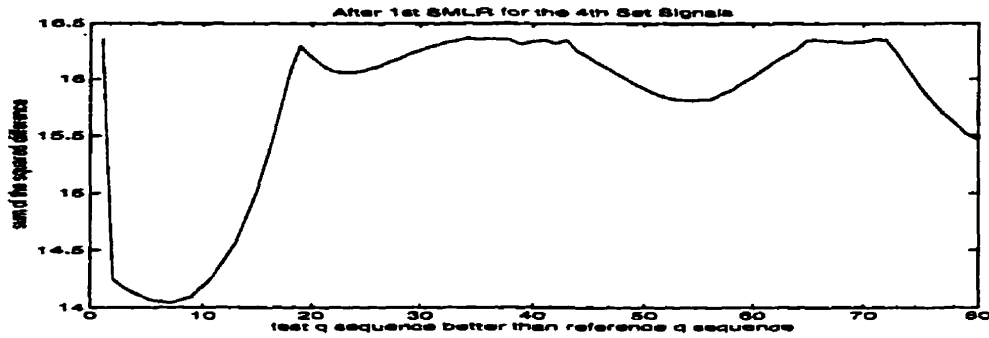


Figure D-4-1 The 1st application of the SMLR detector

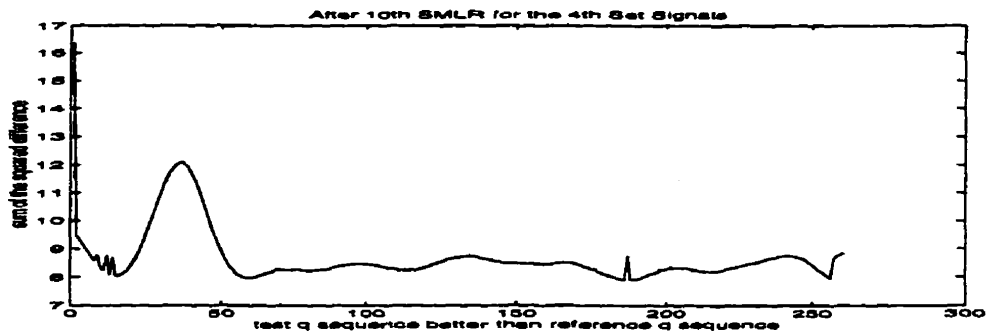


Figure D-4-2 The 10th application of the SMLR detector

Then, the nonlinear least square optimization process is applied with both σ and F accuracy being set at 0.1. After nearly 15 hours, the optimization process has stopped itself. The D^f at the stop time is 2.5896. The most significant σ sequence obtained, σ^f , is shown in Figure D-4-3.

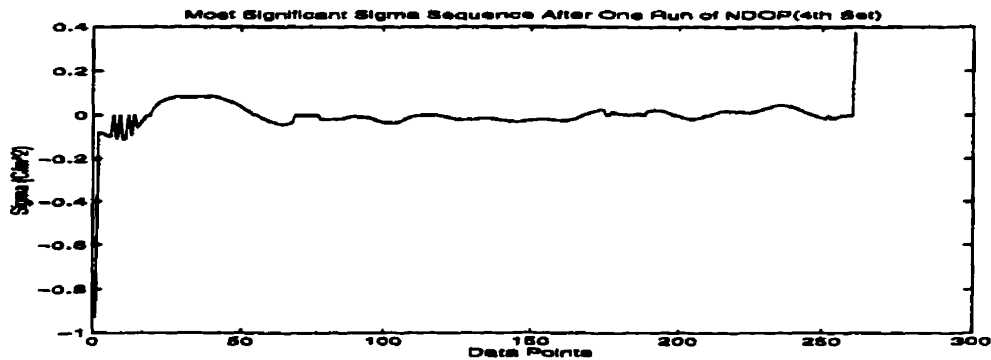


Figure D-4-3 The σ^f obtained after one run of NDOP for the 4th set of signals

By applying equation (3-53) and equation (3-51) to the σ^r sequence and applying a zero-phase 5 point average filter to the internal space charge distribution, we obtain Figure D-4-4 charge distribution.

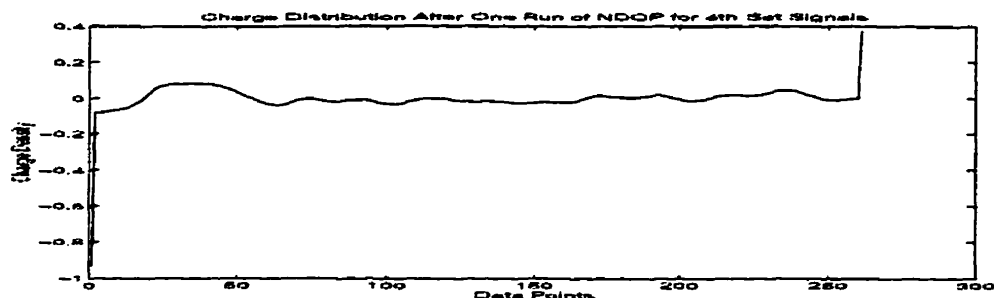


Figure D-4-4 Charge distribution obtained after one run of the NDOP for the 4th set of signals

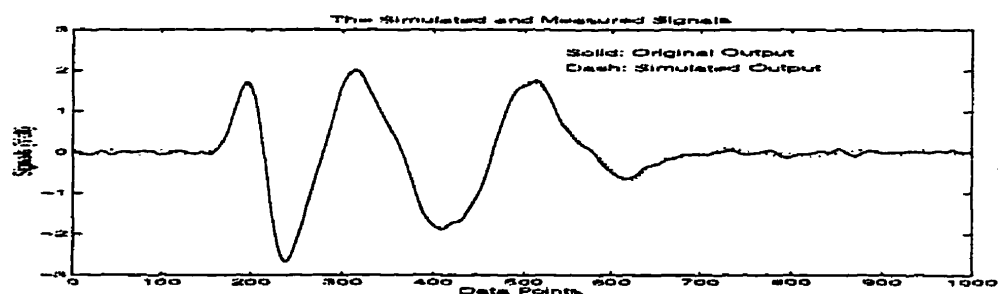


Figure D-4-5 Comparison between $v_{sm}^{4'}(k)$ and $SV(k)$ (using Figure D-4-4 charge distribution)

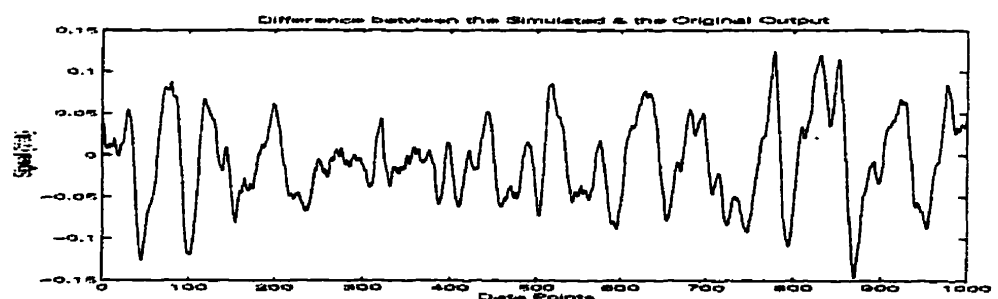


Figure D-4-6 Difference between $v_{sm}^{4'}(k)$ and $SV(k)$ of Figure D-4-5

Figures D-4-5 and D-4-6 compare the difference between $v_{sm}^{4'}(k)$ and $SV(k)$ (using Figure D-4-4 charge distribution). The sum of the squared difference of Figure D-4-6 is minimized to 2.6252. The surface charges are better recovered. Comparing results obtained with the application of NDOP to the 3rd and the 4th set of signals with those obtained without the application of NDOP for the 3rd and 4th set of signals, we can observe that the NDOP is less sensitive to the bandwidth effect than the linear PMSM without applying NDOP. Similarly, one can discrete Figure D-4-4 charge distribution by $\Delta=1$ and regards the obtained σ sequence as $\sigma^{(1)}$. Owing to the fact that $\sigma^{(1)}$ sequence is better than $\sigma^{(0)}$, another run of the NDOP process will generate further improved charge distribution results.